The University Of Sheffield.

The role of refractory metals in controlling properties of Nb-silicide based *in-situ* composites

By:

Jiang Zhao

A thesis submitted in partial fulfilment of the requirements for the degree of Doctor of Philosophy

The University of Sheffield
Faculty of Engineering
Department of Materials Science and Engineering

August 2017

Abstract

The cast and heat treated microstructures and the isothermal oxidation behaviour at 800 ˚C and 1200 ˚C of the alloys Nb-12Ti-18Si-6Ta-2.5W-2Sn-2Ge-1Hf (JZ1), Nb -12Ti-18Si-6Ta-2.5W-5Sn-5Ge-1Hf (JZ2), Nb-12Ti-18Si-6Ta-2.5W-5Sn-5Ge-1Hf -5Al-5Cr (JZ3), Nb-12Ti-18Si-6Ta-2.5W-7.5Sn-5Ge-1Hf-5Al-5Cr (JZ3+), Nb-12Ti -18Si-6Mo-2.5W-7.5Sn-5Ge-1Hf-5Al-5Cr (JZ4) and Nb-12Ti-18Si-6Mo-2.5W-7.5Sn -5Ge-1Hf-5Al-5Cr (JZ5) (at.%) were studied in this work.

The Nb_5Si_3 + Nb_{ss} eutectic was stable in the cast alloys JZ1 and JZ2 but was suppressed in other four alloys. The βNb_5Si_3 was stabilised to a larger extent at 1500 ˚C in the alloys JZ4 and JZ5 owing to the addition of Mo and W. The increase of the Sn concentration in JZ2, JZ3, JZ3+, JZ4 and JZ5 stabilised the A15-Nb_3X phase in their microstructures. The Nb_{ss} was stable in these alloys but was very rich in refractory metals in the alloys JZ3+, JZ4 and JZ5. The addition of 5 at.% Cr with Al, Ge, Sn, Ti, Hf, Ta and W stabilised the C14-Cr_2Nb Laves phase in the alloys JZ3 and JZ3+. The TM_5Sn_2X compound formed in the cast alloys with Mo (JZ4-AC and JZ5-AC) but was not stable after the heat treatment.

Alloying with Mo instead of Ta in the alloys JZ4 and JZ5 led to good oxidation behaviour at 800 ˚C, with the formation of thin scales ($\approx 3\ \mu m$ thick) and no pesting. The increase of the Ti content in the alloy JZ5 and the A15 compound led to better oxidation resistance of the latter in the alloy JZ5 at 800 ˚C. The parabolic oxidation rate constants of the alloys JZ3+, JZ4 and JZ5 at 1200 ˚C were one order of magnitude higher than that of the single crystal Ni superalloy CMSX-4. Good adherence of the oxide scale at 1200 ˚C was observed in the alloys JZ2, JZ3, JZ3+, JZ4 and JZ5, with the thinnest scale formed on the latter alloy, which is probably attributed to the formation of Sn and Ge containing intermetallic phases in the diffusion zone due to the segregation of Ge and Sn to the substrate just below the scale/substrate interface.

Acknowledgement

First of all, I would like to express my sincere gratitude to my supervisor Prof. Panos Tsakiropoulos for his motivated, patient and knowledgeable support throughout the research and writing of the thesis. Without his guidance and help this thesis would not have been possible.

Also, I am deeply grateful to Dr. Claire Utton for the help with the oxidation experiments and my sincere thanks also goes to Dr. Conor McCaughey, Dr. Mohammad Hossein Ghadyani and other colleagues-in our research group who helped me during the experimental work. I would also like to thank Dr. Le Ma, Dr. Peng Zeng and Mr Kyle Arnold who gave me the training for the equipment used in the research.

Finally, I would like to thank my family for their encouragement and support during my study.

Table of Contents

Introduction

The performance of gas turbine engines at high temperatures has improved greatly due to the development of Ni-based superalloys. Turbine blade temperatures have increased by approximately 125 ˚C in the past decades and metal surface temperatures on the hottest part of engines approach 1150 ˚C. Thermal barrier coatings protect the blade from the hot gas that can have temperatures about 1500 ˚C (Bewlay *et al.* 2003). However, it will be difficult to substantially improve the temperature capability of Ni-based superalloys to meet requirements for applications in advanced turbine engines operating at higher temperatures, as Ni-based superalloys melt at temperatures above 1350 ˚C. Chemical segregation in alloys during processing and heat treatment can result in incipient melting at 1270 ˚C and the interaction zones between the bond coat and the airfoil can melt below 1250 ˚C. Hence, the desired improved high-temperature performances of gas turbine engines necessitate the development of new materials that can survive above the current temperature limit of the presently used Ni-based superalloys.

Nb-silicide based in-situ composites that consist of Nb solid solution (Nb_{ss}) and Nb_5Si_3 with/without the Cr_2Nb Laves phase have been developed. The Nb_{ss} can provide the room-temperature ductility and fracture toughness, and the Nb_5Si_3 is beneficial for the required high strength, creep resistance and high-temperature oxidation resistance. The Cr_2Nb Laves phase is introduced due to its positive effect on the high-temperature oxidation resistance. Although properties of Nb-silicide based in-situ composites have been successfully enhanced significantly, a further improvement in oxidation resistance is required and how to achieve a balance of mechanical and environmental properties is still a critical issue.

Alloying elements in Nb-silicide based in-situ composites mainly include free electron metals, transition metals and metalloid elements. Refractory metals are good

solid solution strengtheners in the Nb_{ss} and possess ultra-high melting points, and therefore are expected to be beneficial to the strength and the creep resistance of composites. In addition, refractory metals such as W and Mo have been identified as beneficial additions for the oxidation resistance of conventional Nb-Si alloys. In the group's research, it has been shown that alloying with Ge and Sn can compensate the negative effect of W and Mo on oxidation behaviour and that the addition of the aforementioned elements with Al and Cr improves oxidation behaviour further and at no expense of high temperature properties. However, there are limited studies on the effects of Ta and its effects together with other additions to date.

In this research, the aim is to understand the role of specific refractory metals in controlling the properties of Nb-silicide based in-situ composites. The objectives include:

(1) To understand the effect of refractory metals W and Ta or Mo with Ti, Hf, Sn, Ge, Al and Cr on the microstructure and oxidation behaviour of Nb-silicide based in-situ composites.
(2) To explore the effect of the Sn/Ge ratio on the oxidation behaviour of Nb-silicide based in-situ composites.

The above objectives are expected to be achieved as follows:

(1) Design of appropriate alloy compositions.
(2) Use of a series of experimental techniques, including XRD. SEM/EDS and TGA, to examine the microstructure of alloys in the as cast and heat treated conditions and the isothermal oxidation behaviour of alloys at 800 ˚C and 1200 ˚C.

The thesis includes 7 chapters. In chapter 1, a literature review on phase equilibria, processing techniques, mechanical properties and oxidation behaviour of Nb-silicide based in-situ composites is summarised. The experimental procedures adopted in the research are described in chapter 2. Chapters 3 to 5 give the results and discussion of the microstructures of alloys. The research on the oxidation behaviour of alloys is

given in chapter 6. Chapter 7 presents the conclusion of the research and gives suggestions for future work. Details of X-ray diffraction data of the studied alloys are given in appendices.

Chapter 1

Literature review

1.1 Nb-silicide based in-situ composites

The development of advanced gas turbine engines is strongly dependent on the development of new materials that can survive at elevated temperatures of above 1200 ˚C, as the efficiency of turbine engines is limited by the turbine entry temperature, which is restricted by the capability of presently used Ni-based superalloys.

In the 1990s, intermetallic compounds were considered due to low density, high melting points and high stiffness, but their application in turbine engine components was not possible because of the poor fracture toughness and/or creep resistance. This problem has been solved by combining intermetallic compounds with metallic phase(s) to form composites that exhibit appropriate toughness for structural applications (Jackson *et al.* 1996). Nb-Si binary alloys that consist of Nb solid solution (Nb_{ss}) and Nb_5Si_3 have been considered as the basis for the development of potential candidate alloys to replace currently used Ni-based superalloys. The element Nb has an inherent ductility at room temperature and lower density (8.56 g/cm^3) than Ni. The Nb_5Si_3 has a high melting point (2515 ˚C), low density (7.16 g/cm^3), high strength and exceptional creep behaviour, and is also able to provide the required high-temperature oxidation resistance owing to its high Si concentration. In addition, a large two phase field between Nb_{ss} and αNb_5Si_3 in the binary Nb-Si phase diagram (Schlesinger *et al.* 1993) indicates that a microstructure of coexisting Nb_{ss} and αNb_5Si_3 can be obtained in a large composition range, and can be morphologically and chemically stable at temperatures up to 1770 ˚C (see below section 5.3).

Unfortunately, composites from the binary Nb-Si system cannot be used in advanced turbine engines because they have very poor oxidation resistance and insufficient

fracture toughness. Thus, alloying strategies have been explored and Nb_{ss}/Nb_5Si_3 multi-component composites with/without the Cr_2Nb Laves phase are developed currently. It is reported that the fracture toughness of Nb-silicide based in-situ composites at room temperature has exceeded 20 MPa $m^{0.5}$ (Bewlay and Jackson 2003).

1.2 Processing techniques

A range of processing techniques have been used to produce Nb-silicide based in-situ composites, mainly including arc melting (for example, Grammenos and Tsakiropoulos 2010, Li and Tsakiropoulos 2010), directional solidification (Bewlay *et al.* 1999, Bewlay and Jackson 2003), investment casting (Bewlay *et al*. 2003), and powder metallurgy.

Arc melting

Consumable and non-consumable arc melting techniques are widely used to fabricate Nb-silicide based in-situ composites from binary Nb-Si alloys to higher order alloys as they are suitable for materials with high melting temperatures and can produce uncontaminated ingots with inert gas processing. Ingots produced by arc melting are generally with diameters up to 75 mm and lengths up to 150 mm and therefore large enough for manufacturing prototype components. However, according to previous studies and experiences in the research group in the production of Nb-silicide based in-situ composites, arc melting has disadvantages as follows (Bewlay *et al.* 1999, Geng and Tsakiropoulos 2007, Li and Tsakiropoulos 2011):

(1) Microcracks could form within the intermetallic phases because of the high thermal gradients.

(2) Evaporation of low melting point elements cannot be avoided which meant that control of the alloy composition might be difficult.

(3) Poor solidification control, which is typical in arc melting, might result in macro-segregation in the ingots.

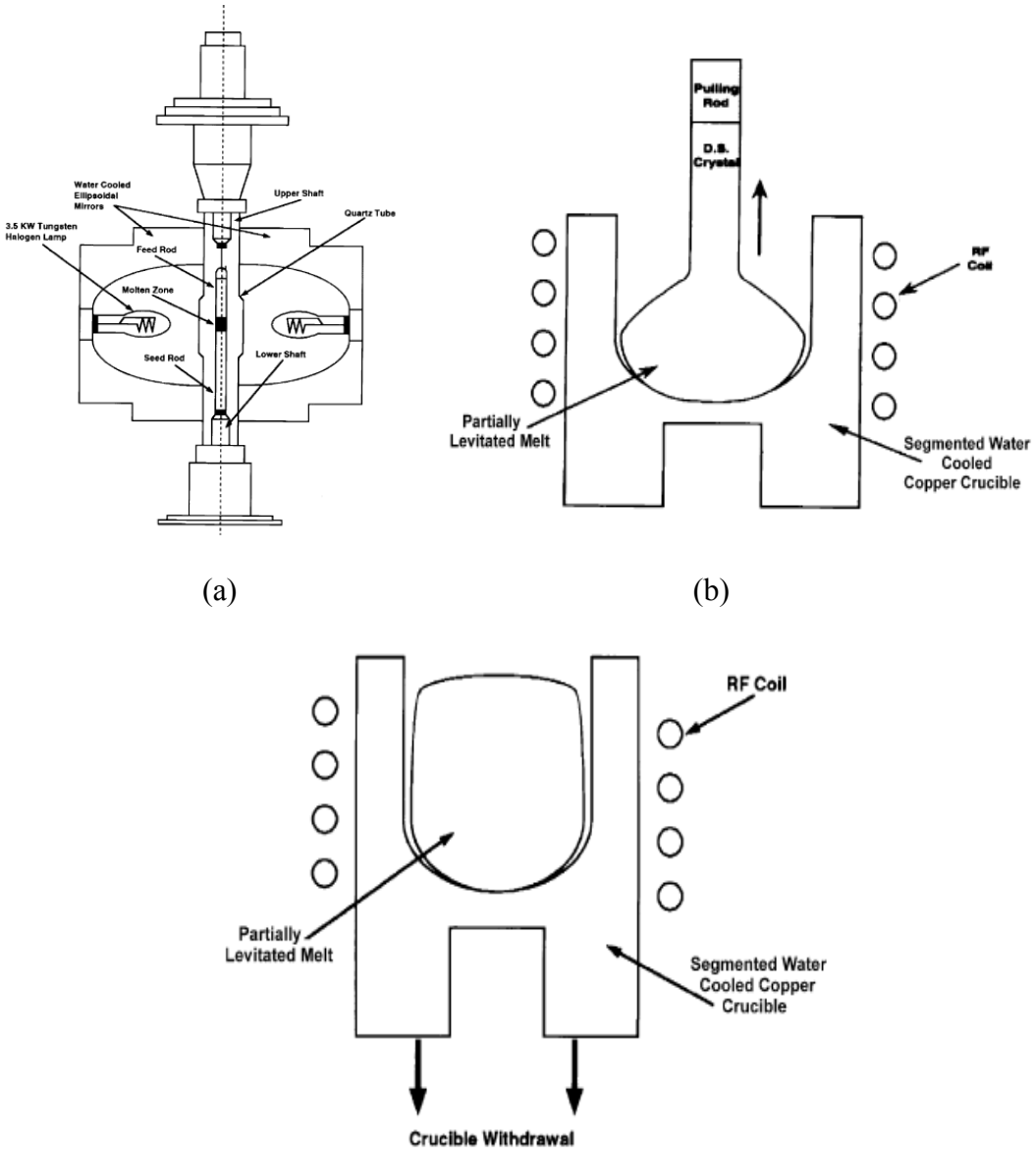

Figure 1.2.1 Diagrams of directional solidification by techniques (a) optical imaging float zone processing (Pope *et al.* 1994), (b) the Czochralski method (Bewlay *et al.* 1999) and (c) the Bridgman method (Bewlay and Jackson 2003).

Directional solidification

Three directional solidification techniques that have been used for fabricating Nb-silicide based in-situ composites are optical imaging float zone (OFZ) processing, the Czochralski method, and the Bridgman method.

Pope *et al.* (1994) used the optical imaging float zone technique to produce refractory metal in-situ composites. A schematic diagram is shown in Figure 1.2.1(a). This method comes from the zone melting technique, in which a small melted zone of material in a rod-type charge is translated along the rod. A crucible is not needed in this technique because the molten zone can be retained in position by surface tension between two co-linear rods. Optical imaging float zone solidification processing is green and clean and can be used to produce different materials. However, there are strict requirements with regard to the materials, that can be pressed using OFZ and their size is limited. High level of homogeneity is not always achieved. In addition, evaporation of volatile elements, such as Cr, can result in attenuation of the heat input from the optical source. Optical imaging float zone processing is essentially used for producing laboratory-scale volumes of alloys.

Induction heating and electron beam heating sources have also been used for directional solidification of Nb-silicide based in-situ composites. The former requires samples to be conducting but allows the growth of samples with a large diameter and the latter is not suitable for producing alloys containing elements with high vapor pressures as a high vacuum is needed for this method.

A schematic diagram of the Czochralski process is shown in Figure 1.2.1(b) (Bewlay *et al.* 1999). A range of Nb-silicide based in-situ composites with liquidus temperature of up to 2300 ˚C have been successfully produced using this method (Chang *et al.* 1992, Bewlay *et al.* 1997). Samples with diameters of no more than 15 mm and lengths of more than 100 mm can be directional solidified using this approach. The microstructure and chemistry of ingots produced by the Czochralski process can be controlled effectively, with low defect concentration and size in the products.

The Bridgman method is shown schematically in Figure 1.2.1(c) (Bewlay and Jackson 2003). This method adopts segmented copper crucibles cooled by water and is effective to produce ingots with diameters of no more than 35 mm, but the structure of

products using this method is not as homogeneous as those produced by the Czochralski method.

(a)

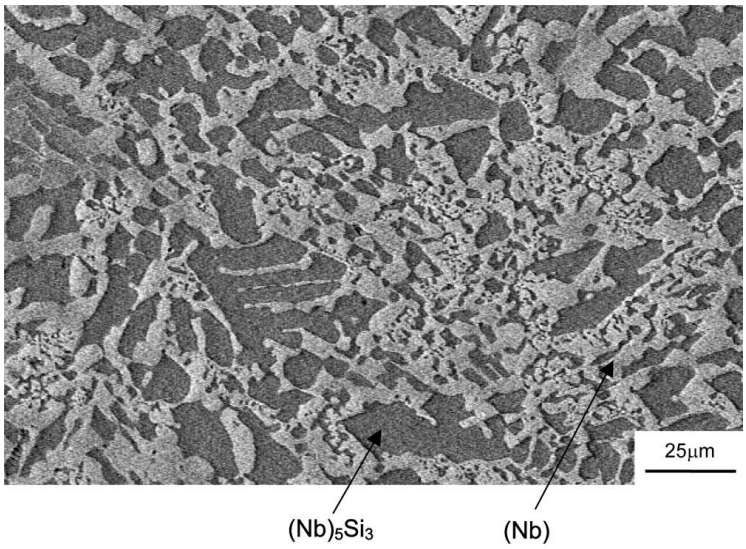

(b)

Figure 1.2.2 Typical investment-cast (a) prototype airfoil of a Nb-silicide based in-situ composite based on the composition of Nb-22Ti-16Si-2Hf-3Al-4Cr (with small additions of Sn and Ge), which is also known as the MASC alloy and (b) the microstructure of the transverse section (Bewlay *et al*. 2003).

Investment casting

Investment casting has the potential to produce near-net-shape Nb-silicide based in-

situ composites but has not received much attention because the development of ceramic muld materials resistant to the very high melt temperatures is difficult. A hybrid arc-melting and drop-casting technique has been performed to explore the feasibility of fabricating thin sheets of selected Nb-silicide based in-situ composites, in which the composites were arc melted and drop cast into heated ceramic mulds with appropriate face coats.

Simple prototype airfoil shapes of Nb-silicide based in-situ composites based on ternary Nb-Si-Ti and Nb-Si-Ti-Hf-Al-Cr compositions have been produced using this process. A typical example is given in Figure 1.2.2(a) and the microstructure of the alloy is shown in Figure 1.2.2(b) (Bewlay *et al*. 2003). The phase distribution in investment cast alloys was similar to those produced using other casting techniques and there was no evidence of any macrosegregation.

Powder metallurgy

Spark plasma sintering (SPS) has been used to fabricate Nb_{ss}/Nb_5Si_3 alloys (Murakami *et al.* 2001, Chen and Tan 2006, Liu and Sha 2016). In this process, a mixture of fine powders prepared by ball miling of charge is placed in a BN-coated graphite die and sintered using a spark plasma sintering furnace. Compared with the casting methods, a homogeneous and controlled microstructure (volume fraction, size, morphology and distribution of constituent phases) can be obtained in Nb_{ss}/Nb_5Si_3 alloys fabricated by SPS.

1.3 Phase equilibria of Nb-silicide based in-situ composites

The Nb-Si system

The phase diagram of the Nb-Si system is shown in Figure 1.3.1 (Schlesinger *et al.* 1993). Pure Nb has the melting temperature of 2469 ˚C. The solubility of Si in Nb_{ss} is very small, up to 3.5 at.%. There is an eutectic reaction Liquid → Nb_{ss} + Nb_3Si

occurring at 1920 ˚C and an eutectoid reaction $Nb_3Si \rightarrow Nb_{ss} + Nb_5Si_3$ at 1770 ˚C. The Nb_3Si has the *tP*32 crystal structure and the Nb_5Si_3 exists as two forms which are the high temperature form (βNb_5Si_3) and the low temperature form (αNb_5Si_3). The βNb_5Si_3 and the αNb_5Si_3 both have the *tI*32 structure but differ in lattice parameters. Schachner *et al*. (1994) have reported that a metastable phase γNb_5Si_3 with the *hP*16 structure was formed in some composites.

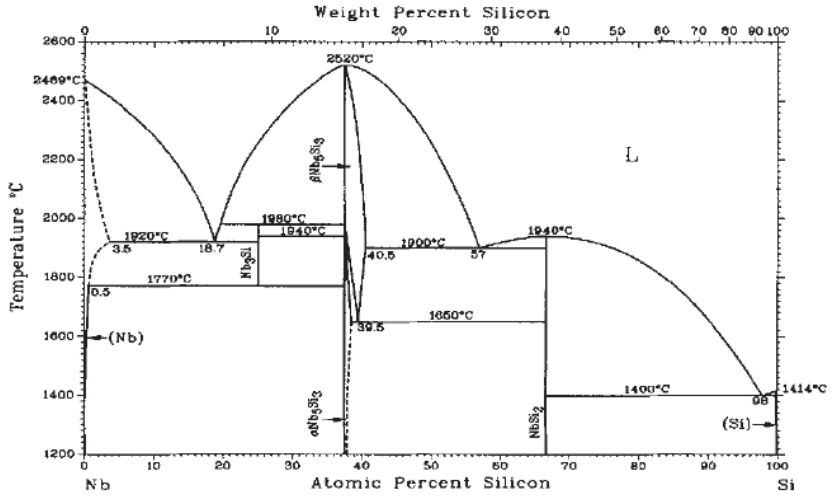

Figure 1.3.1 The Nb-Si binary phase diagram (Schlesinger *et al.* 1993).

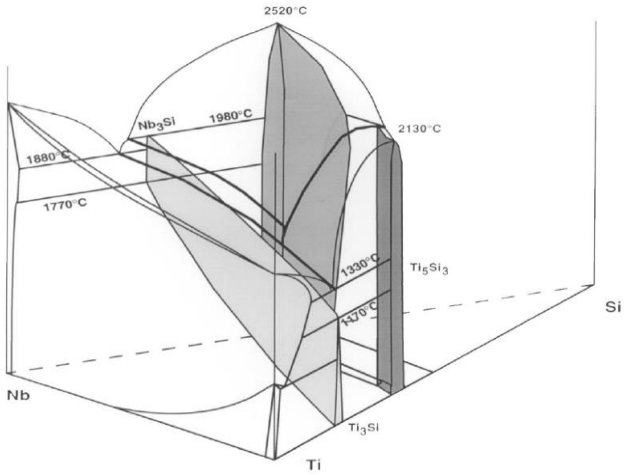

Figure 1.3.2 Metal-rich area of the Nb-Ti-Si ternary phase diagram (Bewlay *et al.* 1997).

The Nb-Ti-Si system

Bewlay *et al.* (1997) have reported a metal-rich area of the Nb-Ti-Si ternary phase

diagram, shown in Figure 1.3.2. A eutectic transformation Liquid → Ti_{ss} + Ti_5Si_3 occurs at 1330 ˚C in the Ti-rich side, and the Ti_3Si exists at temperatures below 1170 ˚C. The Ti_5Si_3 has the *hP*16 structure that is different from that of the Nb_5Si_3 but the same as the metastable γNb_5Si_3 phase. The Ti_3Si and the Nb_3Si are isomorphous, with *tP*32 crystal structure. From figure 1.3.2, it can be seen that Ti addition would reduce the temperature of the eutectic reaction Liquid → Nb_{ss} + Nb_3Si and stabilise the Nb_3Si to lower temperatures. In addition, the solubility of Ti in Nb_5Si_3 is very large and can be up to 34 at.% according to Bewlay *et al.* (1997).

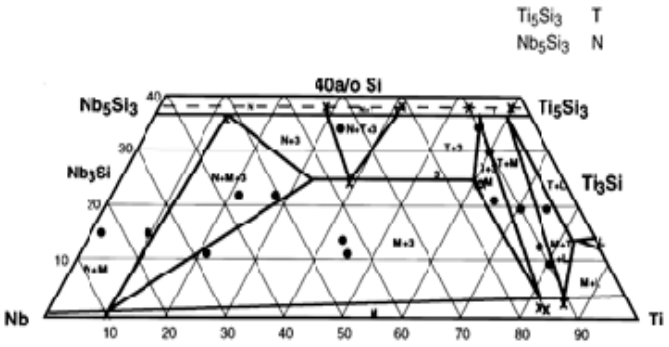

(a)

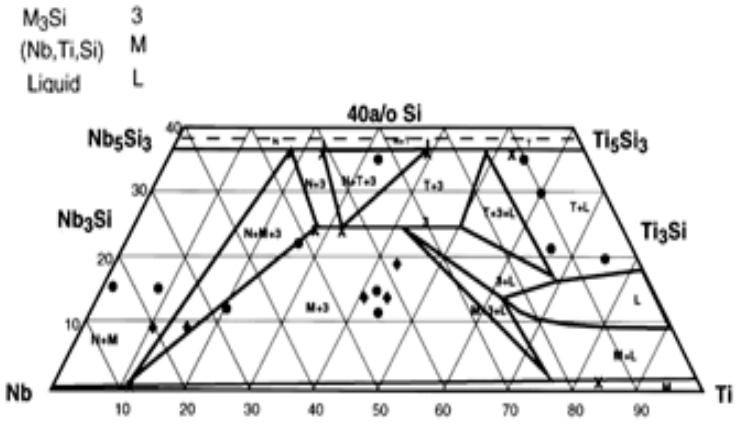

(b)

Figure 1.3.3 Partial isothermal sections of the Nb-Ti-Si ternary phase diagram at (a) 1340 ˚C and (b) 1500 ˚C (Bewlay *et al.* 1999).

Partial isothermal sections of the Nb-Ti-Si ternary phase diagram at 1340 ˚C and 1500 ˚C have been investigated, see Figure 1.3.3(a) and (b) (Bewlay *et al.* 1999). Zhao *et al.*

(2004) have also reported isothermal sections at 1000 ˚C, 1150 ˚C and 1200 ˚C using diffusion multiples, see Figure 1.3.4.

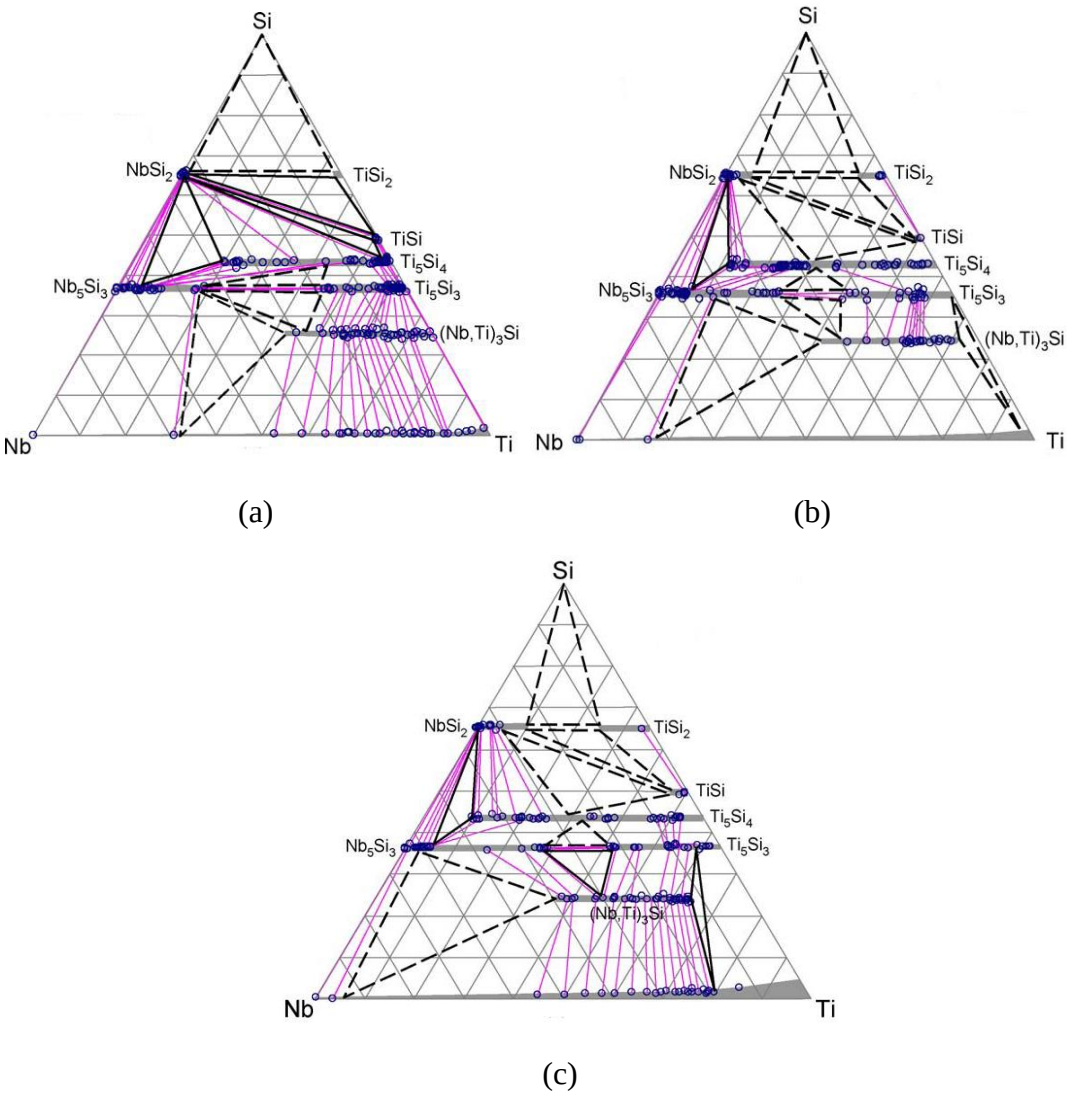

Figure 1.3.4 Isothermal sections of the Nb-Ti-Si ternary phase diagram at (a) 1000 ˚C, (b) 1150 ˚C and (c) 1200 ˚C (Zhao *et al.* 2004).

The Nb-Hf-Si system

A metal-rich region of the Nb-Hf-Si ternary phase diagram has been reported by Bewlay *et al.* (1999), and is shown in Figure 1.3.5. In the Hf-Si binary the Hf_5Si_3 has the *hP*16 crystal structure and is a product of peritectic reaction and not stable at temperatures below 2080 ˚C. It can be seen that the Hf addition reduces the temperature of the eutectic reaction Liquid → Nb_{ss} + Nb_3Si but does not stabilise the

Nb_3Si to lower temperatures.

Zhao *et al.* (2001) have reported the isothermal section of the Nb-Hf-Si ternary diagram at 1500 ˚C, as shown in Figure 1.3.6. Four three phase regions were defined, including Nb_{ss} + Nb_5Si_3 + Hf_2Si, Nb_5Si_3 + Hf_2Si + Hf_5Si_3, Nb_{ss} + Hf_{ss} + Hf_2Si and $NbSi_2$ + Hf_5Si_3 + HfSi. At 1500 ˚C, the solubility of Hf in Nb_5Si_3 is about 16 at.% and the Nb_3Si phase was unstable.

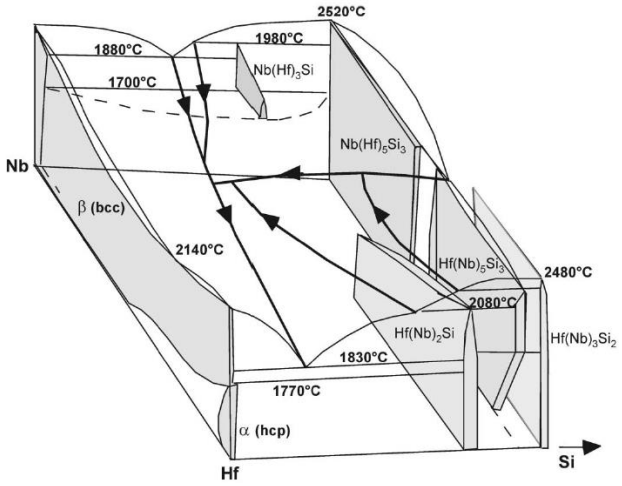

Figure 1.3.5 Metal-rich region of the Nb-Hf-Si ternary phase diagram (Bewlay *et al.* 1999).

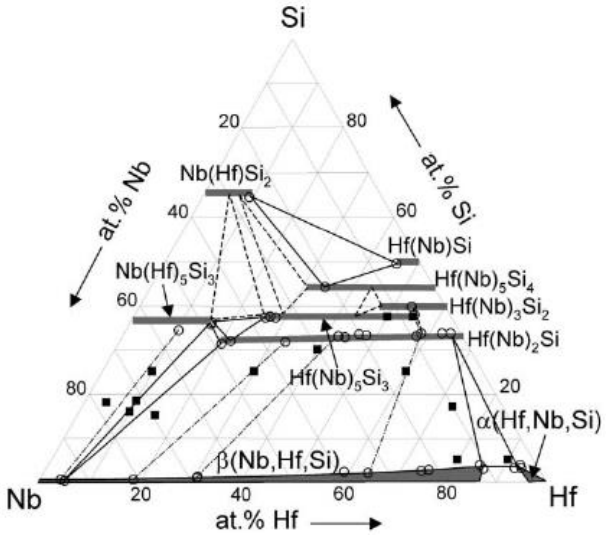

Figure 1.3.6 The isothermal section of the Nb-Hf-Si ternary diagram at 1500 ˚C (Zhao *et al.* 2001).

The Nb-W-Si system

The liquidus surface projection in the Nb-W-rich area of the Nb-W-Si ternary system has been given by Ma *et al.* (2002), and is shown in Figure 1.3.7. It can be seen that alloying with W would significantly shrink the three phase region Nb_{ss} + Nb_5Si_3 + Nb_3Si and promote the eutectic reaction Liquid → Nb_{ss} + βNb_5Si_3 that does not exist in the Nb-Si system. The W_5Si_3 is isomorphous with the βNb_5Si_3 and therefore would stabilise the latter to low temperatures.

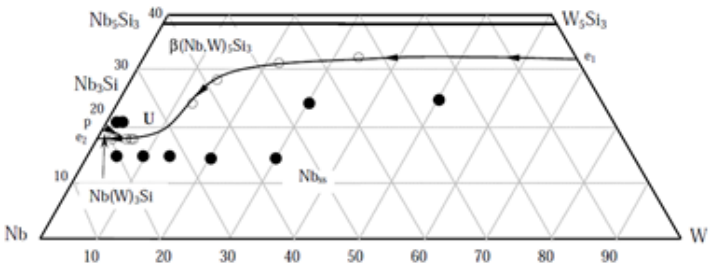

Figure 1.3.7 The liquidus surface projection in the Nb-W-rich area of of the Nb-W-Si ternary system (Ma *et al.* 2002).

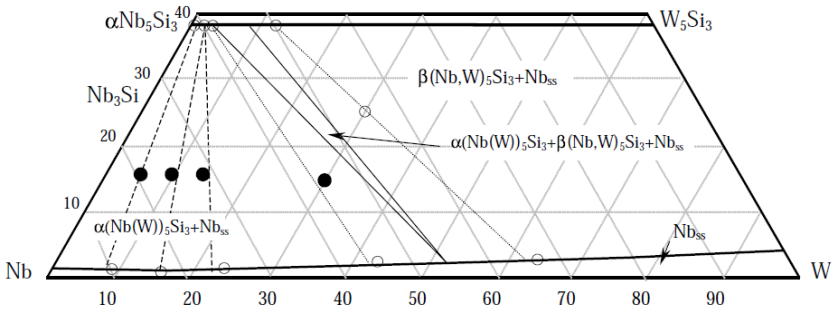

Figure 1.3.8 Partial isothermal section of the Nb-W-Si ternary phase diagram at 1700 ˚C (Ma *et al.* 2002).

Ma *et al.* (2002) have also investigated the phase equilibrium in the Nb-W-rich region of the Nb-W-Si system at 1700 ˚C, see Figure 1.3.8. This section consists of one three-phase region and two two-phase regions, with no formation of Nb_3Si. Li *et al.* (2013) have calculated isothermal sections of the Nb-W-Si ternary system at 800 ˚C, 1200 ˚C and 1600 ˚C using the CALPHAD method. They are given in Figure 1.3.9 and are consistent with previous experimental data.

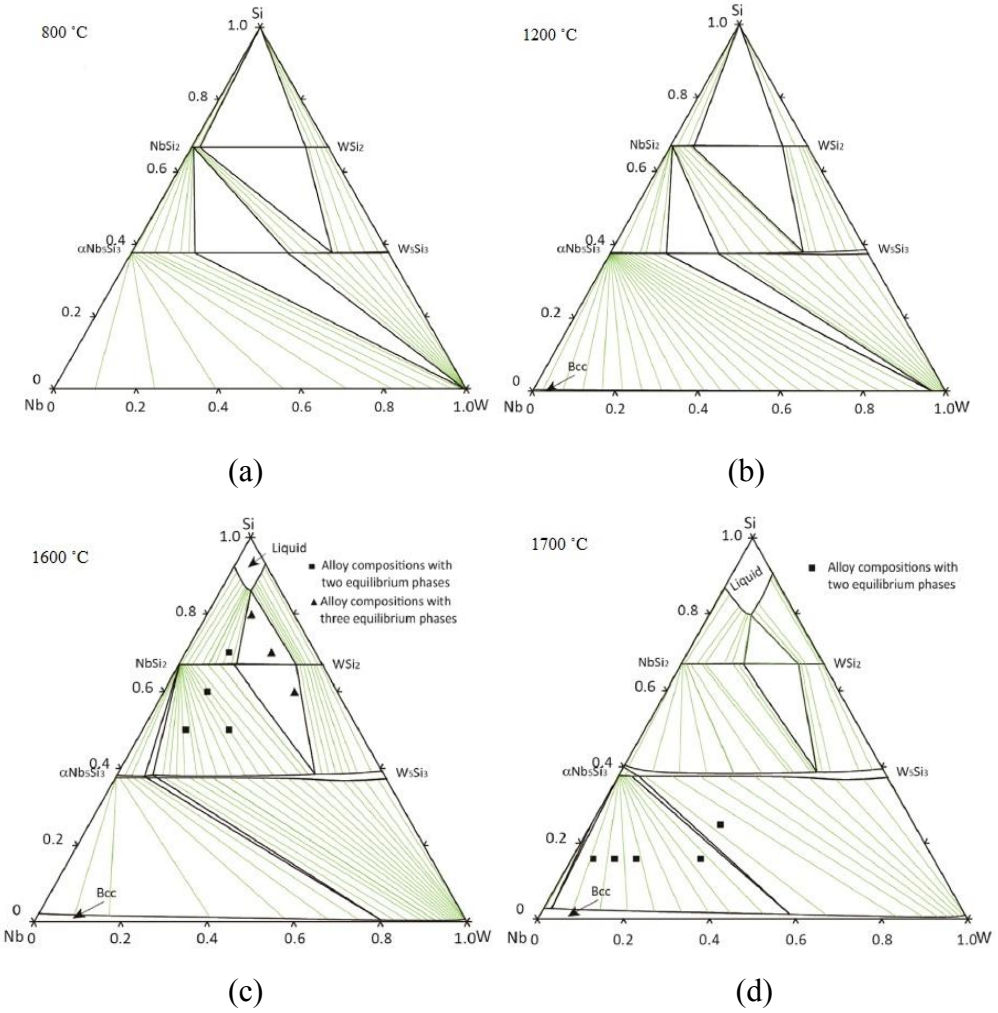

Figure 1.3.9 Calculated isothermal sections of the Nb-W-Si ternary phase diagram at (a) 800 ˚C, (b) 1200 ˚C, (c) 1600 ˚C and (d) 1700 ˚C (Li *et al.* 2013).

The Nb-Al-Si System

Brukl *et al.* (1961) have reported isothermal sections of the Nb-Al-Si ternary phase diagram at 500 ˚C and 1400 ˚C, as shown in Figure 1.3.10(a), and identified the equilibrium between $Nb_3Si_5Al_2$ and $Nb_{10}Si_3Al_3$. Pan *et al.* (1984) have investigated the isothermal section of the Nb-Al-Si ternary phase diagram at 1500 ˚C, as shown in Figure 1. 3.10(b), and found the equilibrium between αNb_5Si_3 and $NbAl_3$, which has been also observed by Murakami *et al.* (2001). Murakami *et al.* have estimated the isothermal section of the Nb-Al-Si ternary phase diagram at temperatures between 1200 ˚C and 1600 ˚C, as shown in Figure 1.3.10(c). The $Nb_3Si_5Al_2$ has also been confirmed by Zhao *et al.* (2003), as shown in Figure 1.3.10(d).

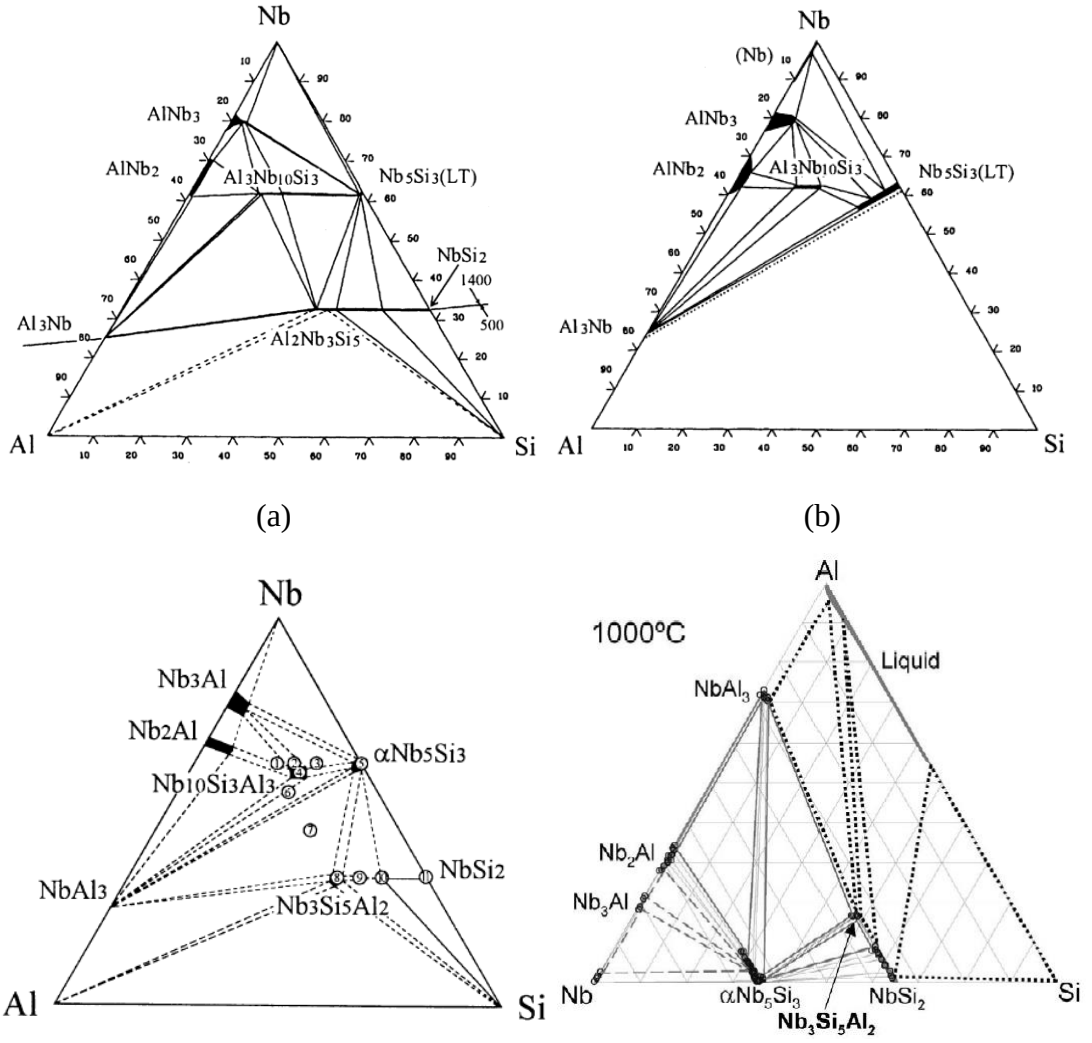

Figure 1.3.10 Isothermal sections of the Nb-Al-Si ternary phase diagram at (a) 500 ˚C (lower part) and 1400 ˚C (upper part) (Brukl *et al.* 1961), (b) 1500 ˚C (Pan *et al.* 1984), (c) estimated section between 1200 ˚C and 1600 ˚C (Murakami *et al.* 2001) and (d) 1000 ˚C (Zhao *et al.* 2003).

The Nb-Cr-Si System

Chromium is an effective addition for benefiting oxidation resistance of Nb-silicide based in-situ composites through introducing the $NbCr_2$-based Laves phase. In the Nb-Cr system the Cr_2Nb exists as a C14 type phase at high temperatures and a C15 type phase at low temperatures but alloying with Si stabilises the hexagonal C14-Cr_2Nb Laves phase. According to the Cr-Si binary system, the αCr_5Si_3 has the same crystal structure as the βNb_5Si_3 (Geng *et al.* 2006). Therefore, the addition of Cr

would be expected to stabilise the βNb_5Si_3 to lower temperatures.

Zhao *et al.* (2003) have reported isothermal sections of the Nb-Cr-Si system at 1000 ˚C and 1150 ˚C, as shown in Figure 1.3.11, and suggested that Nb_{ss} and Nb_5Si_3 are in equilibrium with the CrNbSi phase. However, the equilibrium of $Nb_{ss,}$ Nb_5Si_3 and Cr_2Nb has been identified in the Nb-18Si-16Cr alloy by Geng *et al.* (2006). In addition, Bewlay *et al.* (2009) have reported a new phase $Nb_9(Cr, Si)_5$ in the Nb-Cr-Si system.

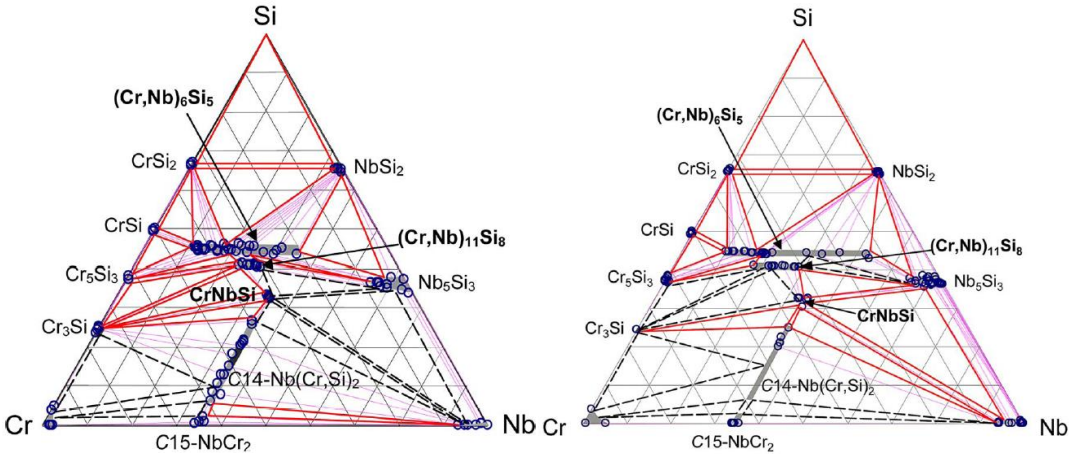

Figure 1.3.11 Isothermal sections of the Nb-Cr-Si ternary diagram at 1000 ˚C and 1150 ˚C (Zhao *et al.* 2003).

The Nb-Sn-Si system

Tin has been regarded as an effective addition to eliminate pest oxidation (Bewlay *et al.* 2003, Geng *et al.* 2007). In the Sn-Sn system, the stability of Nb_3Sn at room temperature has been reported by Matstakova and Lazarev (1973) and confirmed by Toffolon *et al.* (2002). The Nb_3Sn has the *cP*8 (A15) crystal structure.

Sun *et al.* (2012) have calculated isothermal sections of the Nb-Sn-Si system at 900 ˚C, 1200 ˚C, 1500 ˚C and 1600 ˚C using the CALPHAD method, as shown in Figure 1.3.12. The Nb-rich area of these sections contains one three-phase region and three

two-phase regions, and there is no significant change in the three-phase region Nb_{ss} + αNb_5Si_3 + Nb_3Sn at these temperatures. In addition, the existence of a Nb_5SiSn_2 has been found at temperatures between 900 ˚C and 1200 ˚C.

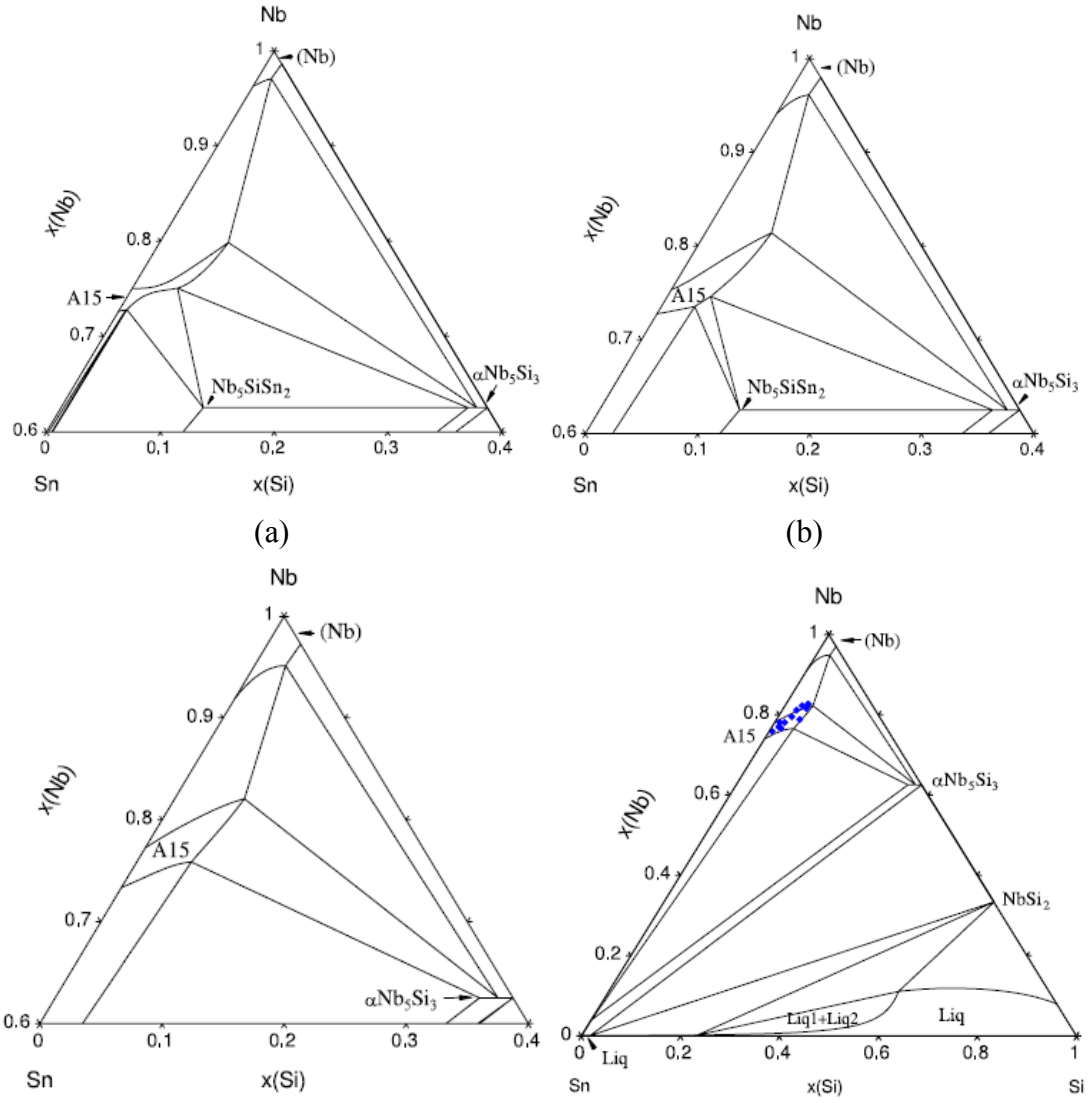

Figure 1.3.12 Calculated isothermal sections of the Nb-Sn-Si ternary system at (a) 900 ˚C, (b) 1200 ˚C, (c) 1500 ˚C and (d) 1600 ˚C (A15 is the symbol of the Nb_3Sn) (Sun *et al.* 2012).

The Nb-Ge-Si system

Pan *et al.* (1982) have reported isothermal sections of the Nb-Ge-Si ternary diagram at 1780 ˚C, 1800 ˚C and 1820 ˚C, based on the experimental data, as shown in Figure

1.3.13. The Nb_3Si phase exists in the ternary system at 1820 ˚C and 1800 ˚C but disappears at 1780 ˚C. The solubility of Ge is about 8 at.% in Nb_{ss} and is up to 2 at.% in Nb_3Si. In Nb_5Si_3 the Ge solubility is limited to about 6 at.%, whereas Nb_5Ge_3 can have solubility of Si up to 30 at.%. Li and Tsakiropoulos (2010) have investigated the Nb-18Si-5Ge and Nb-18Si-10Ge alloys and found that the eutectic $Nb_{ss} + \beta Nb_5Si_3$ with no Nb_3Si formed in the ingots of these alloys, which would suggest that the addition of Ge would suppress the eutectic reaction Liquid → Nb_{ss} + Nb_3Si.

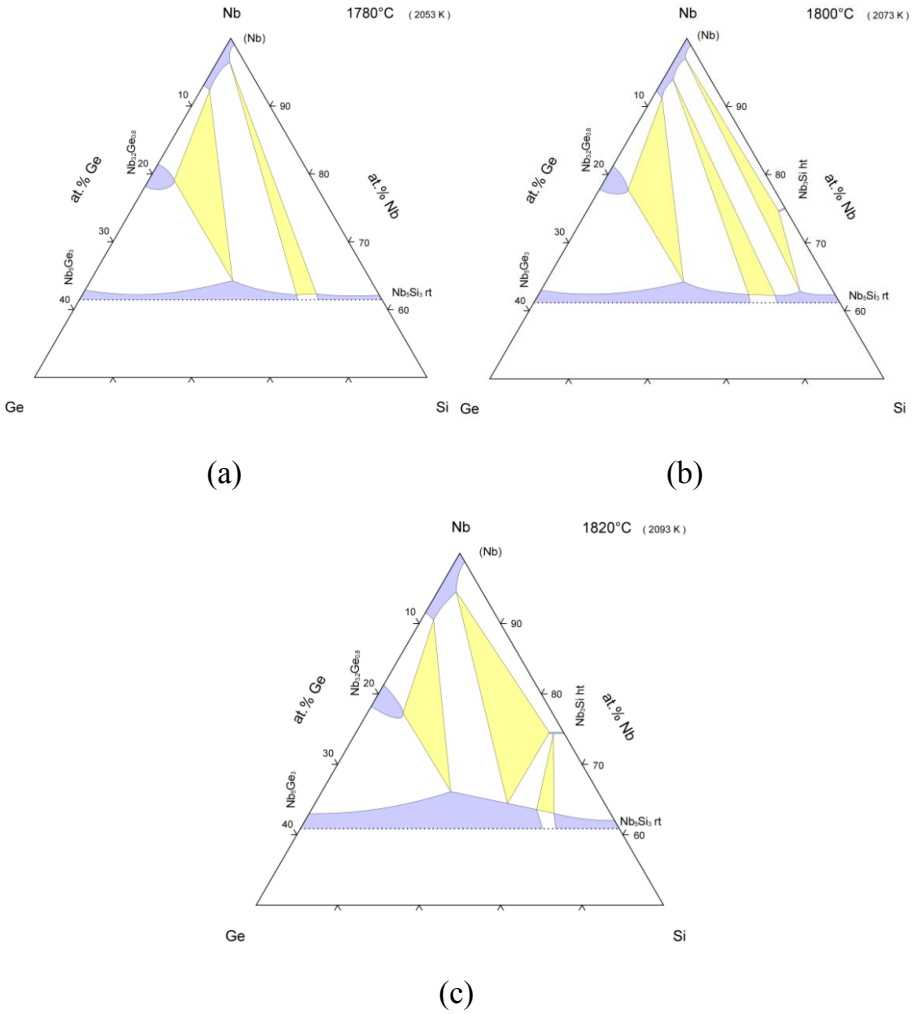

Figure 1.3.13 Isothermal sections of the Nb-Ge-Si ternary diagram at (a) 1780 ˚C, (b) 1800 ˚C and (c) 1820 ˚C (Pan *et al.* 1982).

Utton *et al.* (2017) have calculated isothermal sections of the Nb-Ge-Si system at 1200 ˚C and 1500 ˚C, as shown in Figure 1.3.14, which indicates the formation of the

three phase region Nb_{ss} + αNb_5Si_3 + $Nb_5(Ge,Si)_3$ at these temperatures and that the $Nb_5(Ge,Si)_3$ with the W_5Si_3 prototype can be stabilised to low temperatures when the Ge content exceeds 3.4 at.%.

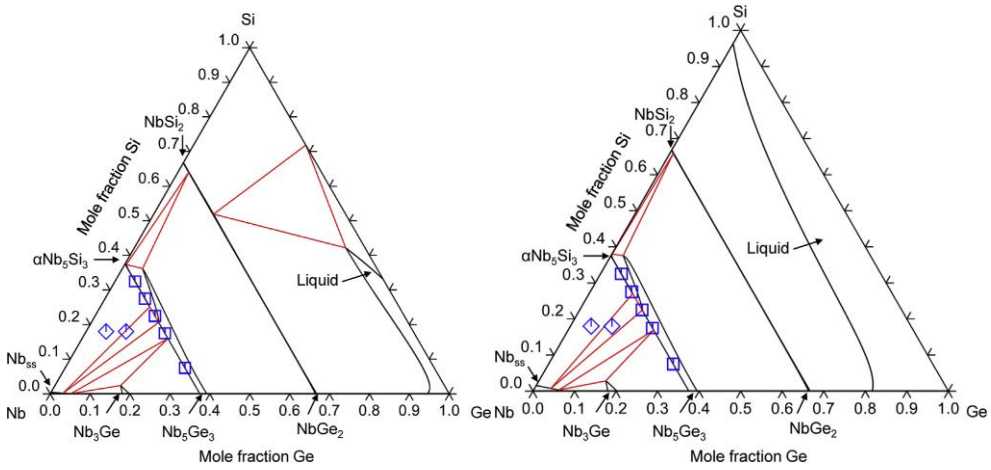

(a) (b)

Figure 1.3.14 Calculated isothermal sections of the Nb-Ge-Si ternary system at (a) 1200 ˚C and (b) 1500 ˚C (Utton *et al.* 2017).

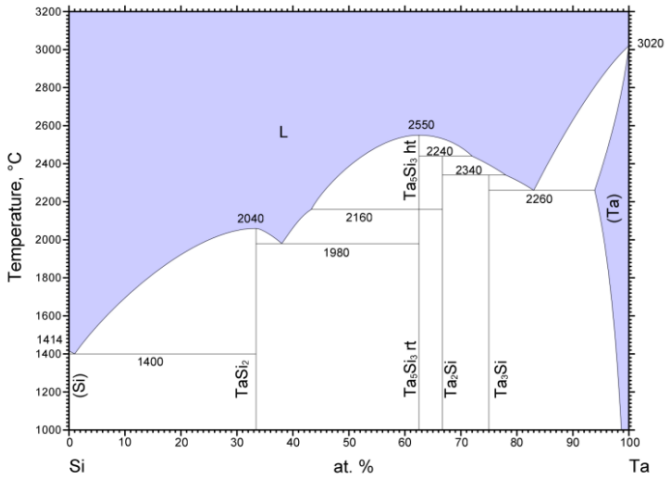

Figure 1.3.15 The Ta-Si binary phase diagram (Schlesinger 1994).

The Nb-Ta-Si system

There is no data on the Nb-Ta-Si ternary system to date. The Nb-Ta and Ta-Si binary systems have been studied. From the Ta-Si phase diagram shown in Figure 1.3.15 (Schlesinger 1994), it can be noted that the Ta_3Si with the *tP32* structure exists below

2200 ˚C to room temperature, and therefore the Ta addition would probably stabilise the Nb_3Si to lower temperatures.

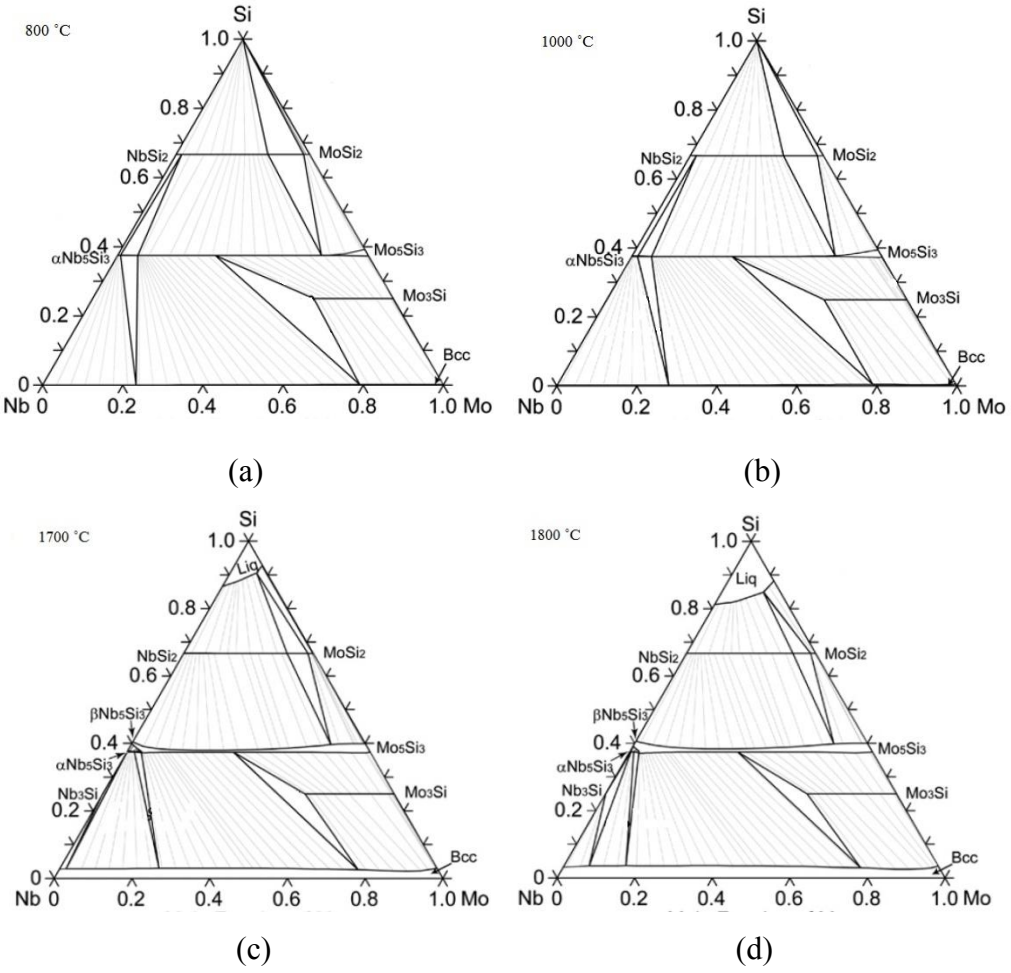

Figure 1.3.16 Calculated isothermal sections of the Nb-Mo-Si ternary phase diagram at (a) 800 ˚C, (b) 1000 ˚C, (c) 1700 ˚C and (d) 1800 ˚C (Geng *et al*. 2010).

The Nb-Mo-Si system

Geng *et al*. (2010) calculated isothermal sections of the Nb-Mo-Si system at 800 ˚C, 1000 ˚C, 1700 ˚C and 1800 ˚C using the CALPHAD approach, see Figure 1.3.16, and indicated that the calculated results was in good agreement with the experimental data. It can be seen that the Nb_3Si is present above 1700 ˚C and that the Nb_3Si region is narrow. Ma *et al*. (2004) and Chattopadhyay *et al*. (2006) reported that the Nb_{ss} + βNb_5Si_3 eutectic formed instead of the Nb_{ss}+ Nb_3Si in their cast alloys.

1.4 Mechanical properties

Fracture toughness

Materials for applications in advanced engines require sufficient fracture toughness to make components fit for the final assembly and to tolerate potential damages in service. A fracture toughness of 20 MPa $m^{0.5}$ is regarded as the minimum value in critical engine components (Bewlay and Jackson 2003). An incorporation of the toughening Nb solid solution phase into silicides to form Nb-silicide based in-situ composites is an effective way to improve the fracture toughness, as silicides are very brittle and are hardly toughened in their monolithic forms.

It is generally accepted that the Nb_{ss} phase provides the majority of the toughness in Nb-silicide based in-situ composites, and that the fracture toughness of composites is very dependent on the volume fraction of the Nb_{ss} phase. However, Chan and Davidson (2003) have reported that the toughening by the Nb_{ss} would be ineffective in composites containing more than 40-50% silicides and the fracture toughness would be determined by silicides when the volume fraction of silicides is in excess of 60%.

Bewlay *et al.* (2003) measured the fracture toughness of a series of Nb-silicide based in-situ composites. They found that the addition of Ti improved the toughness of the Nb-16Si binary alloy by more than 50% and a decrease in Si content from 16 at.% to 12 at.% resulted in a slight reduction in fracture toughness of alloys containing 21 at.% and 27 at.% Ti. Bewlay *et al.* (2003) also indicated that fracture toughness of composites can be slightly increased by adding a low concentration of Hf. Chan (2002) reported that in alloys of the Nb-Cr-Ti system the fracture toughness of the Nb_{ss} can be improved by adding Ti and can reach a maximum value at approximately 37 at.% Ti, as shown in Figure 1.4.1. Kim *et al*. (2001) have measured the fracture toughness of a series of binary and ternary Nb_{ss}/Nb_5Si_3 composites with addition of Mo and found that alloying with Mo improved the fracture toughness of composites at

any Si content except for 10 at.%. However, in the study of Xiong *et al*. (2014) the fracture toughness of the Nb-20Si alloy was not enhanced by alloying with 10 at.% W or Mo but was improved significantly when both were present simultaneously in the alloy. Zhang and Guo (2016) investigated the room-temperature fracture toughness of the Nb-22Ti-16Si-3Al system with additions Cr, Hf or B individually and simultaneously and reported that the alloy with the fine eutectic performed better compared with that containing the coarse eutectic.

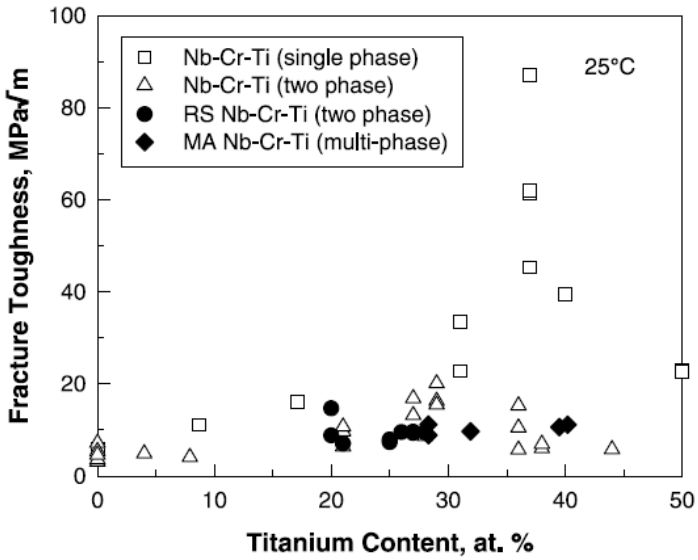

Figure 1.4.1 Fracture toughness of the Nb_{ss} (single phase alloy) and $Nb/NbCr_2$ alloys (two or multiphase) as a function of Ti concentration (Chan and Davidson 2002).

Creep behaviour

The creep resistance of Nb-silicide based in-situ composites is determined by the combined creep performance of the metallic phase(s) and silicide(s) (Subramanian *et al.*1995), and is also dependent on the volume fraction of the metallic phase (Henshall *et al.* 1995). It is expected that the creep must be no more than 1% for 125 hours at high temperatures and stresses (Bewlay *et al.* 2003). The corresponding secondary creep rate under this condition should be 2.2×10^{-8} s^{-1}.

The creep rupture behaviour of Nb-silicide based in-situ composites is shown in the

Larson-Miller plot in Figure 1.4.2 (Bewlay *et al.* 2001). It can be seen that in 2001 the creep behaviour of Nb-silicide based in-situ composites was at least similar to that of Ni-based superalloys. The greater potential for the Nb-silicide based in-situ composites was attributed to their lower densities compared with Ni-based superalloys.

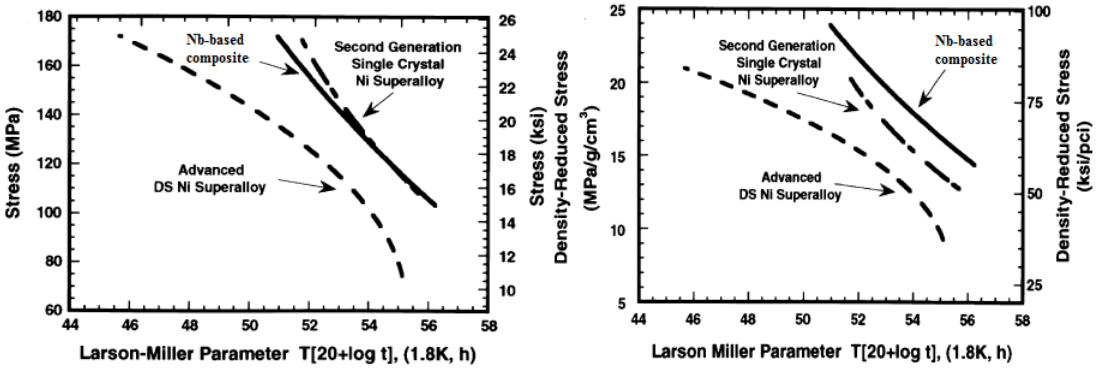

(a) (b)

Figure 1.4.2 Creep rupture behaviour of Nb-silicide based in-situ composites in Larson-Miller plot compared with that of Ni-based superalloys (a) rupture stress (b) rupture stress/density (Bewlay *et al.* 2001).

The effect of alloying with Ti, Hf, Cr, Al, and Mo on the creep resistance of Nb-silicide based in-situ composites has been investigated. Bewlay and Jackson (2003) have measured the secondary creep rates for a number of Nb-silicide based in-situ composites at 1100 ˚C and 1200 ˚C for stresses of 70 to 280 MPa, and suggested that the addition of Ti and Hf has a significant effect on the creep behaviour of composites. At high stresses, an increase in Ti concentration can cause a premature failure. When the Hf content was higher than 7.5 at.%, the secondary creep rate became more sensitive to the stress. This investigation also suggested that the ratio of Ti:Hf must be kept below 3 and Ti concentration must be lower than 21 at.%. A possible reason for the increase in creep rate of Ti and Hf containing composites is that the hexagonal Nb_5Si_3 formed (the Ti_5Si_3 and Hf_5Si_3 are hexagonal and have lower melting point than the tetragonal Nb_5Si_3). The addition of 3 at.% Mo was found to be

beneficial at higher stresses. Furthermore, Al and Cr were considered to be detrimental additions for the creep behaviour of Nb-silicide based in-situ composites.

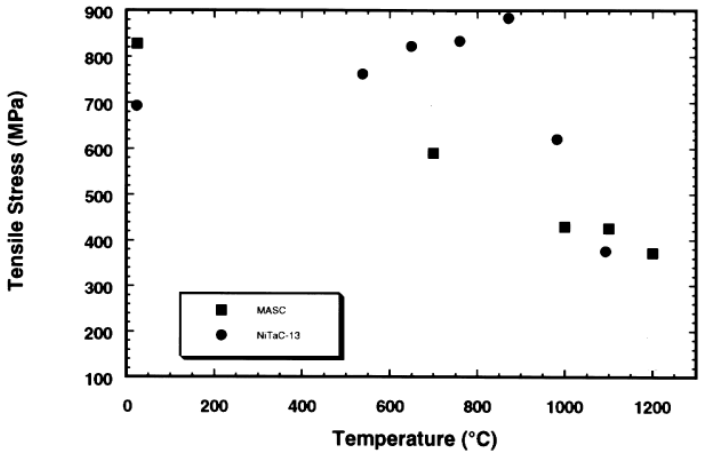

Figure 1.4.3 Tensile fracture stress of the MASC alloy (Nb-24.7Ti-16Si-8.2Hf-2Cr -1.9Al) as a function of temperature in comparison with a Ni-based superalloy (Bewlay *et al.* 1997).

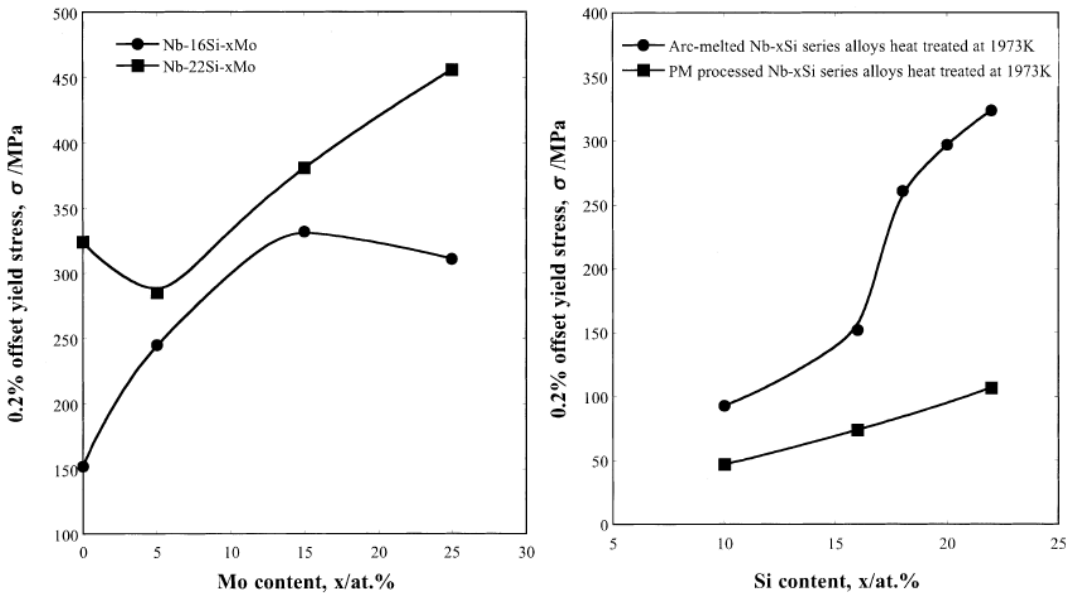

(a) (b)

Figure 1.4.4 (a) Offset yield stress at 1500 ˚C of Nb-16Si-xMo and Nb-22Si-xMo alloys fabricated by arc-melting as a function of Mo content and (b) offset yield stress at 1700 ˚C of Nb-xSi alloys fabricated by arc-melting and powder metallurgy as a function of Si content (Kim *et al.* 2002).

High-temperature strength

Bewlay *et al.* (1997) have investigated the tensile strength of a Nb-silicide based in-situ composite as a function of temperature and compared it with a Ni-based superalloy, as shown in Figure 1.4.3. The tensile fracture stress of the MASC alloy was lower than that of the Ni-based superalloy at intermediate temperatures, but higher at temperatures above 1000 ˚C.

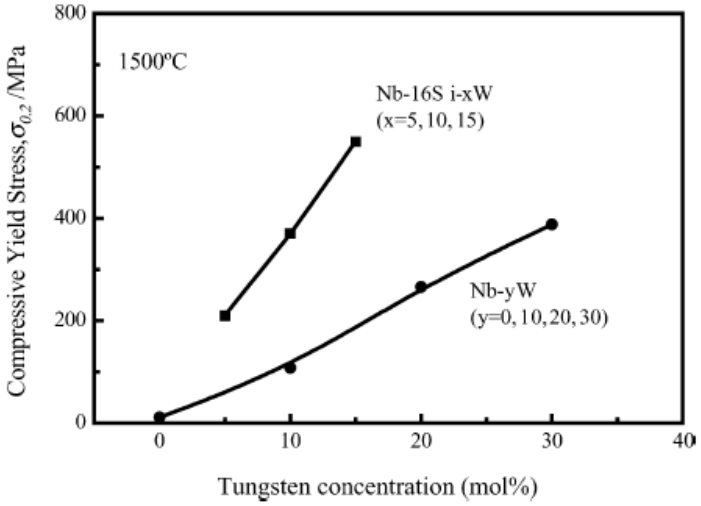

Figure 1.4.5 Compressive yield stress 1500 ˚C of Nb-16Si-xW alloys as a function of W content at (Ma *et al.* 2004).

The effects of a number of potential strengthening additions on the strength of Nb-silicide based in-situ composites have been investigated. Kim *et al.* (2002) have reported a beneficial effect of Mo addition on the yield stress of binary Nb_{ss}/Nb_5Si_3 composites at 1500 ˚C. They found that the yield stress was very dependent on the microstructure of composites at high temperatures, as shown in Figure 1.4.4. Ma *et al.* (2004) have investigated the compressive yield stress of Nb-16Si-xW alloys and found that W is also a very beneficial addition, as shown in Figure 1.4.5. Sha *et al.* (2004) improved the compressive strength of the Nb-10W-10Si alloy by alloying with 2 at.% B. Sha *et al.* (2010) have investigated the room- and high-temperature strength of the Nb-8Si-20Ti-6Hf alloy with addition of Cr and reported strengthening and weakening effects of Cr addition in their Nb-silicide-based alloy. In their work, an

improved strength of the Nb-8Si-20Ti-6Hf alloy with 6 to 14 at.% Cr was observed at room temperature and 1150 ˚C, whereas an opposite effect was noted at 1250 and 1350 ˚C.

1.5 Oxidation behaviour

There are two cyclic-oxidation resistance goals for Nb-silicide based in-situ composites for advanced engine applications, a long-term goal and a short-term goal, as shown in Figure 1.5.1 (Bewlay *et al.* 2001). The long-term goal is to achieve less than 25 μm material loss after an expose of 100 hours at 1315 ˚C. The short-term goal is to achieve less than 200 μm material loss under an exposure of 10 hours at 1370 ˚C. The short-term goal has been fulfilled at present, and developmental alloys have moved closer to the long-term.

The effects of a range of alloying elements on the oxidation behaviour of Nb-silicide based in-situ composites have been investigated. Jackson *et al.* (1996) have suggested that a decrease in the volume fraction of the Nb_{ss} improves the oxidation resistance of composites. They have reported that Ti or Hf is a beneficial addition for oxidation resistance, which also has been observed by Geng and Tsakiropoulos (2006). The Ti addition decreases the oxidation rate of the monolithic Nb_{ss}, but increases the oxidation rate of the monolithic Nb silicides. The Hf addition decreases the solubility and diffusivity of oxygen, and thus retards the embrittlement of composites at high temperatures. Furthermore, Bewlay *et al.* (2001) have suggested that composites with chemistries with ratios of Nb:(Ti+Hf) in the range of 1.8 to 2.1 and with Si content from 17 at.% to 19 at.% possess optimum oxidation resistance and exceptional creep behaviour simultaneously. The Cr addition can help to form the Cr-rich Cr_2Nb Laves phases, and therefore can lead to a substantial increase in the oxidation resistance of composites. Alloying with Al is also beneficial for oxidation resistance of composites, which is probably attributed to the improved oxidation kinetics for the Nb_{ss} and silicides.

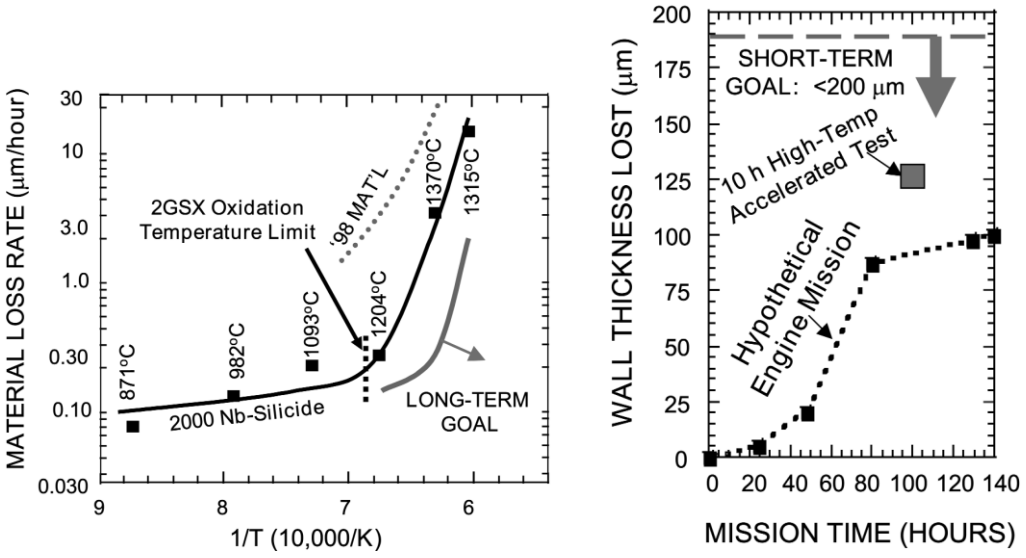

(a) (b)

Figure 1.5.1 Cyclic-oxidation resistance goals for Nb-silicide based in-situ composites for applications in advanced engines (a) the long-term goal (b) the short-term goal (Bewlay *et al.* 2001).

The effects of additions such as B, Ge, Mo, W, and Ta on the oxidation behaviour of Nb-silicide based in-situ composites have also been investigated. Bewlay *et al.* (2001) have reported that alloying with 3 to 6 at.% B may be useful to improve the oxidation performance of composites, which is probably attributed to a change of the kinetics of silica formation or the formation of more stable oxides. They have also found that alloying with up to 4 at.% Ge has a positive effect on the oxidation behaviour. Geng *et al.* (2006) have suggested that Mo content should be kept lower than 2 at.% for oxidation resistance purposes, as alloying with more than 2 at.% Mo had a detrimental effect. Xiong *et al.* (2009) reported that the addition of W in the Nb-20Si alloy was very beneficial to its oxidation resistance. Tantalum addition led to a higher oxidation rate and a lower adherence of oxide scales in the Nb-24Ti-18Si-5Cr-5Al alloy, as reported by Zelenitsas and Tsakiropoulos (2006).

Another key issue is that Nb-silicide based in-situ composites can suffer from pest oxidation (Bewlay *et al.* 2003). Pesting damage is often referred to as self-

pulverization and is observed in materials that are cycled at temperatures from 25 ˚C to intermediate temperatures generally less than 900 ˚C. It has been attributed to preferential oxidation at microstructure features, such as grain boundaries and inclusions. The Hf and Al additions are known to reduce the susceptibility of composites to pesting (Balsone 2001). Zelenitsas and Tsakiropoulos (2006) have found the pest oxidation can be avoided by simultaneously alloying with Ti, Al and Cr. Tin has been shown to be a very effective alloying element in managing the pesting behaviour (Bewlay *et al.* 2003, Geng *et al.* 2006)

The oxidation resistance of Nb-silicide based in-situ composites has increased tenfold in the last decade. Achieving the long-term goal with a balance of mechanical properties requires further research.

Chapter 2

Experimental procedures

2.1 Selection of alloy compositions

The compositions of alloys that were studied in this research are shown in Table 2.1. These compositions were selected based on the consideration of phase equilibria, properties of Nb-silicide based alloys, and data from previous and current research in the group.

Table 2.1 The nominal compositions of the alloys of this project (at.%).

Alloy	Nb	Ti	Si	Ta	Mo	W	Sn	Ge	Hf	Cr	Al
JZ1	56.5	12	18	6	-	2.5	2	2	1	-	-
JZ2	50.5	12	18	6	-	2.5	5	5	1	-	-
JZ3	40.5	12	18	6	-	2.5	5	5	1	5	5
JZ3+	38	12	18	6	-	2.5	7.5	5	1	5	5
JZ4	38	12	18	-	6	2.5	7.5	5	1	5	5
JZ5	30	20	18	-	6	2.5	7.5	5	1	5	5

The Si content was set 18 at.% for achieving optimum oxidation resistance and creep behaviour (Bewlay *et al.* 2001). The choice of the relatively low Ti content compared with previous works was made for creep resistance and high-temperature strength purposes, and the effect of Ti on the oxidation behaviour and fracture toughness was expected to be balanced by other alloying elements, in particular Hf, Sn and Ge for oxidation and Hf and W for toughness. The 20 at.% Ti addition in the alloy JZ5 was designed to find out if it had a very significant effect on oxidation, compared with the alloy JZ4.

The Ta and W are both solid solution strengthening elements, in particular W, and

both are expected to be very beneficial additions regarding the high-temperature strength and the creep resistance of the composites. The addition of Ta was limited to 6 at.% after considering the effects of Ta on oxidation resistance (Balsone *et al.* 2001). The addition of W at 2.5 at.% was also made in order not to affect adversely the oxidation resistance (Xiong et al. 2009). Another reason behind the choice of Ta and W was to confirm whether in the presence of Hf alloying Ta and W affects the solid solubility of Si in the Nb_{ss}, given that Zelenitsas and Tsakiropoulos (2006) reported an increase in the solid solubility of Si in the presence of 6 at.% Ta in Nb-silicide-based alloys without Hf and refractory metals and Grammenos and Tsakiropoulos (2011) reported the formation of Si free Nb_{ss} in Nb-silicide-based alloys with Hf and the refractory metal Mo and W, or only W but not when Hf was added with Ta and Mo (Grammenos and Tsakiropoulos 2010). Another reason for choosing Ta and W was to compare the Ta+W solubility in the Nb_{ss} with the Mo+W solubility, as all these elements are solid solution strengtheners but Mo is more effective than Ta when present at the same concentration in the Nb_{ss}.

The addition of Ge or Sn is known to be beneficial to the oxidation resistance of Nb-silicide based alloys (Balsone *et al.* 2001, Geng *et al.* 2007). In the Nb-Si-Sn and Nb-Si-Ge systems the Nb_5Si_3+Nb_{ss} eutectic forms instead of the Nb_3Si+Nb_{ss} eutectic, and can be used to improve the mechanical properties of the alloys (Vellios and Tsakiropoulos 2007, Li and Tsakiropoulos 2010). The addition of Ge and Sn together at Ge:Sn=1:1 and different concentrations were made in order to study the oxidation of the alloys and in particular the substrate-scale interface where according to Geng *et al.* (2007) Sn-rich intermetallic can form and whether the latter alloyed with Ge can protect the base metal from further oxidation. Furthermore, the changes in the Ge and Sn concentrations were made to investigate the synergetic effects of Ge and Sn on the stability of the eutectic. However, due to significant loss of Sn in the production of the JZ1, JZ2 and JZ3 alloys using arc melting, the Sn contents in the JZ3+, JZ4 and JZ5 alloys were increased to 7.5 at.% to ensure the ratio Sn/Ge=1 was achieved.

The Hf addition improves the oxidation behaviour of Nb-silicide based alloys and can increase their fracture toughness when present at low concentrations (Geng *et al.* 2006). The addition of 1 at.% Hf was made in order to study whether its effect on oxidation property in alloys with (Nb+Ta+W)/(Ti+Hf) ratio in the range 1.9 to 5.0.

The elements Al and Cr are known to affect both the toughness of Nb-silicide based alloys and their high-temperature strength. Both elements in solid solution in Si free Nb affect the fracture toughness depending on the Ti/Nb ratio and the Cr+Al content of the Nb_{ss}. Furthermore, the solid solubility of Cr and Al in Nb_{ss} increase with its Ti solubility (Zelenitsas and Tsakiropoulos 2005). The addition of 5 at.% Cr and 5 at.% Al were made in order to study how their solid solubility in the Nb_{ss} are affected in the presence of Ta or Mo, W, Sn and Ti and thus whether these elements can be used to balance the mechanical properties and oxidation resistance of Nb-silicde based alloys containing refractory metal additions.

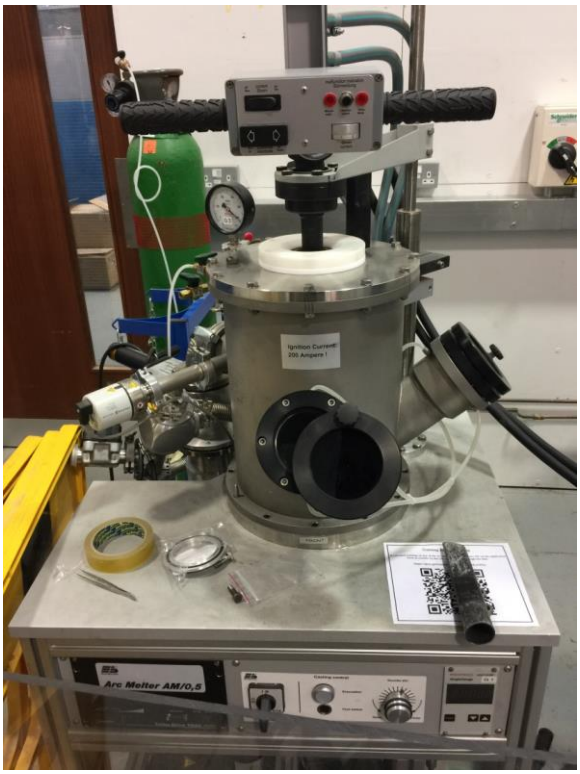

Figure 2.1 The arc melter used in this research.

2.2 Preparation of ingots

All alloys were produced from high purity elements better than 99.99 wt.% using arc melting under an argon atmosphere in a water cooled copper hearth with a non-consumable tungsten electrode, as shown in Figure 2.1. The chamber was evacuated to a pressure less than 10^{-3} Pa and then was filled with argon to a pressure of about 60 KPa before melting. The alloys were melted five times to ensure homogeneity and cooled in the water-cooled copper crucible.

2.3 Specimen preparation for microstructure analysis

Alloy ingots were sectioned to produce specimens containing the top, bulk and bottom areas of the ingots (the bottom refers to the side facing the copper crucible during melting). The specimens were mounted in bakelite, ground using 120, 400, 800 and 1200 grid papers, and polished to 1μm surface finish using 6 μm, 3 μm and 1 μm diamond pastes.

2.4 Heat treatment

Small pieces were cut from the ingots for differential thermal analysis (DTA) before the heat treatment temperatures were decided. Specimens for heat treatment were cut from the bulk of the ingots, wrapped in Ta foil, placed in an alumina crucible, and heat treated at 1500 ˚C for 100 hours in a tube furnace under a flow of argon. Ti sponge was used at the entrance of the argon flow as the oxygen getter. The specimens were cooled in the furnace.

2.5 X-ray diffraction

A Siemens D5000 X-ray diffractometer with monochromatic CuKα radiation (λ =

1.540562 Å) was used to identify the phases in as cast and heat treated specimens. Phase identification was done by matching the characteristic peaks of the XRD diffractogram against PDF (Powder Diffraction File) data using the ICDD PDF-4+ and Sieve+ software.

2.6 Scanning electron microscopy and energy dispersive spectrometry

The microstructures of Nb-silicide based alloys were observed using scanning electron microscopy (SEM). SEM microscopes use a focused beam of electrons to interact with the atoms under the surface of a sample to produce different signals, containing secondary electrons, back-scattered electrons, characteristic X-rays and others which provide information about the surface topography and chemical composition of the sample. Secondary electrons (SE) arise within the region of a few nanometres under the sample surface and are suitable for the analysis of fine surface morphology under high resolution. Back-scattered electrons (BSE) are from a larger and deeper interaction region and provide image contrast as a function of composition. BSE imaging requires a high quality surface finish of the sample.

Energy dispersive X-ray spectrometry (EDS) was used to determine the chemical composition of the microstructure. This technique uses the energy of characteristic X-rays emitted from the sample to obtain a chemical analysis, and was used to do spot, line and area analysis for the Nb-silicide based alloys. The quantitative analytical accuracy of the EDS is generally $\pm 1\%$. Standards and ZAF correction were applied in the analysis. The spatial resolution is a function of the electron beam voltage and density of the spot being analysed. For Nb-silicide based alloys under a voltage of 20 kV, the spatial resolution is about 1 μm, and thus the features subjected to spot analysis were larger than $5\mu m$. X-ray elemental mapping can be used to show the spatial distribution of elements of interest in the sample.

BSE imaging was performed using an Inspect F SEM. Typical areas in the top, centre

and bottom of the as cast specimen and in the bulk and near the surface of the heat treated specimen were selected for the observation of the microstructure. Chemical compositions for large area from top, bulk and bottom, constituent phases and eutectic regions of the specimens were analysed using JEOL 6400 SEM and Philips XL 30S FEG equipped with an EDS under a voltage of 20 kV. A minimum of 5 EDS analyses on large areas and phases were performed with size large than $5\mu m$. The chemical data is given with the average, minimum and maximum values and standard deviation. Calibration using a pure Co was repeated every hour in the EDS analysis. Area fractions of selected phases (Nb_{ss} and/or A15 phase) of the alloys were calculated using the software Image-Pro with images of microstructures taken in the SEM in back scatter electron imaging mode.

2.7 Thermal gravimetric analysis

Thermal gravimetric analysis (TGA) is used to measure changes of physical and chemical properties of materials as a function of time in isothermal condition or as a function of temperature. In this research, the TGA technique was used to study the oxidation kinetics of Nb-silicide based alloys at 800 ˚C and 1200 ˚C by measuring the weight change of a sample as a function of time. The 800 ˚C was chosen to investigate the pesting behaviour of alloys and the 1200 ˚C was for the investigation of the oxidation behaviour of alloys at high temperature. For the oxidation tests, cubic samples of 3×3×3 mm^3 were cut from the as cast alloys and their sides were ground to 1200 grit. The dimensions of each sample were measured using a micrometer and the surface area of each sample was calculated. Each cubic was placed in a small alumina crucible and tested using a NETZSCH STA 449 F3 thermal analyser. The rate of 3 ˚C per minute was applied in both heating and cooling. The oxidised samples then were cold mounted and polished until the base metal appeared. The images, elemental mapping and chemical spot analysis of samples for areas from bulk to oxide scale were investigated using the Inspect F SEM and Philips XL 30S FEG equipped with EDS under a voltage of 20 kV. Pure Co was used to calibrate the EDS detector.

Chapter 3

Alloys without Al and Cr additions

3.1 The alloy Nb-12Ti-18Si-6Ta-2.5W-2Sn-2Ge-1Hf (alloy JZ1): Results

The actual composition of the cast alloy (JZ1-AC) was 55Nb-11.6Ti-22.5Si-5.3Ta -1.7W-1.2Sn-1.8Ge-0.9Hf. Tin was lost in the alloy preparation and the Si concentration was higher than the nominal one. Large area analyses that are given in Table 3.2 indicated that there was macrosegregation of Si in JZ1-AC with the Si content varying between 19 at.% and 24.6 at.%. The XRD and EDS data (Figure 3.1 and Table 3.2) would suggest that the phases in the microstructure of JZ1-AC were the Nb_5Si_3, Nb_3Si, Nb_{ss} and HfO_2. The Nb_5Si_3 existed in both the βNb_5Si_3 and αNb_5Si_3 structures, see Figure 3.1, and the Nb_3Si was observed only in the bottom of the ingot, see below.

BSE images of the typical microstructure of JZ1-AC are given in Figure 3.3. The microstructures in the top and bulk of the ingot were similar, both consisting of irregular large Nb_5Si_3 particles surrounded by fine Nb_5Si_3 + Nb_{ss} eutectic and Nb_{ss} with a small volume fraction of HfO_2, see Figures 3.3a, b and c. The vol% of the Nb_{ss} in the top was slightly lower than in the bulk, see Table 3.1. The partitioning of Ta, W and Sn into the Nb_{ss} and Ge into the Nb_5Si_3 was observed. The Si content in the Nb_{ss} was relatively high, 4.4 at.%, in agreement with reports for Sn or Ta containing alloys (Geng *et al.* 2006, Zelenitsas and Tsakiropoulos 2006, Grammenos and Tsakiropoulos 2010). The areas exhibiting darker contrast in the Nb_5Si_3 and Nb_{ss} were rich in Ti and had lower contents of Ta and W and higher contents of Sn, Ge (only for Nb_5Si_3) and Hf compared with the normal Nb_5Si_3 and Nb_{ss}. In the Nb_5Si_3 and Ti-rich Nb_5Si_3, the Si+Sn+Ge contents were 39.1 at.% and 37.9 at.%, respectively. The average composition of the Nb_5Si_3 + Nb_{ss} eutectic was 58.8Nb-10.8Ti-18.2Si-6.2Ta-2.8W-1.3Sn-1.2Ge-0.7Hf and the Si+Sn+Ge content was 20.7 at.%, slightly higher than the

Si content of the $Nb_3Si + Nb_{ss}$ eutectic of the Nb-Si binary system, and in the range of Si concentration reported for the metastable $Nb_5Si_3 + Nb_{ss}$ eutectic.

The microstructure in the bottom of the ingot was different and contained only Nb_5Si_3 and Nb_{ss} without the fine $Nb_5Si_3 + Nb_{ss}$ eutectic, see Figure 3.3e. The vol% of Nb_{ss} in the bottom was the same as in the bulk, see Table 3.1. Furthermore, there was a small region in the bottom of JZ1-AC where the Nb_3Si was present in the microstructure, surrounded by $Nb_5Si_3 + Nb_{ss}$ lamellar microstructure and Nb_{ss}, see Figure 3.4. In this area, the average composition determined by the large area analysis was 56Nb-11.8Ti-21.2Si-5.6Ta-1.8W-1.3Sn-1.3Ge-1Hf, slightly poor in Si and Ge and richer in Ta and Sn compared with the rest of the ingot. Unlike the Nb_5Si_3, the concentrations of Ta and W were relatively high in the Nb_3Si, respectively at 6.5 at.% and 1.5 at.%, and the Sn solubility in the Nb_3Si was extremely low. The presence of Nb_3Si was also suggested by the XRD data, see Figure 3.1.

The average composition of the alloy JZ1 after the heat treatment at 1500 ˚C for 100 hours (JZ1-HT) is given in Table 3.3. There was still inhomogeneity in the Si content. The microstructure of the heat treated specimen was similar to that in the bottom of JZ1-AC and consisted of Nb_5Si_3, Nb_{ss}, HfO_2 and Ti oxide, see Figures 3.2 and 3.5 and Table 3.3. According to the XRD data, the Nb_5Si_3 existed both in the αNb_5Si_3 and βNb_5Si_3 forms with more peaks corresponding to the former and there was no peak corresponding to the Nb_3Si. The Ti-rich area in the Nb_{ss} had disappeared in JZ1-HT, whereas the Ti-rich areas in the Nb_5Si_3 remained. The volume fraction of the Nb_{ss} had not changed after the heat treatment, see Table 3.1.

Compared with the cast alloy, there were slight changes in the concentration of Si, Ta, W, Sn and Ge in the Nb_{ss} and the content of Hf in the Nb_{ss} was reduced to zero owing to the consumption of Hf to form HfO_2. The Si content in the Nb_{ss} was still high compared with other heat treated Nb-silicide-based alloys without Sn or Ta, but in agreement with Zelenitsas and Tsakiropoulos (2006) and Grammenos and

Tsakiropoulos (2010) for Ta containing alloys. The Ta+W content in the Nb_{ss} was slightly decreased to 12.0 at.% after the heat treatment. The composition of the Nb_5Si_3 was almost unchanged after the heat treatment. The content of W in the Ti-rich Nb_5Si_3 was essentially zero. There was Ti oxide formed just below the surface of the JZ1-HT specimen, which was attributed to the contamination of the specimen during the heat treatment.

Table 3.1 Density of the as cast (AC) alloys and % area of Nb_{ss} in the as cast and heat treated (HT) alloys JZ1 and JZ2.

Alloy	Density (g/cm^3)	% area Nb_{ss} [a]		
		Top	Bulk	Bottom
JZ1-AC[a]	8.24±0.02 8.2-8.26	42.3±0.7 41.3-43	46.5±0.8 45.4-47.6	46.5±1.0 45.4-48.2
JZ1-HT	-	-	46.5±1.5 44-48.2	-
JZ2-AC[a]	8.31±0.02 8.28-8.33	32.9±1.1 32.1-34.1	34.5±1.0 33.9-35.6	21.9±1.1 20.7-22.7
JZ2-HT	-	-	23.5±2.7 20.4-25.4	-

[a] includes the Nb_{ss} and Ti-rich Nb_{ss}.

Table 3.2 The EDS analysis data (at.%) for the alloy JZ1-AC.

	Nb	Ti	Si	Ta	W	Sn	Ge	Hf
Top[a]	55.1±0.8 54.0-55.9	11.9±0.6 11.3-12.7	22.3±1.7 20.4-24.4	5.4±0.3 5.2-5.8	1.6±0.3 1.4-2.0	1.1±0.2 0.9-1.3	1.8±0.1 1.7-2.0	0.8±0.1 0.7-0.9
Bulk[a]	55.1±0.9 53.5-56.0	11.4±0.2 11.1-11.6	22.9±1.6 21.2-23.0	5.1±0.4 4.6-5.7	1.6±0.3 1.3-1.9	1.2±0.1 1.1-1.3	1.8±0.2 1.6-2.1	0.9±0.2 0.8-1.1
Bottom[a]	55.4±2.0 53.5-57.6	11.4±0.2 11.3-11.7	22.3±2.6 19.0-24.6	5.5±0.4 5.1-6.2	1.7±0.4 1.3-2.3	1.1±0.2 0.9-1.3	1.8±0.2 1.6-2.0	0.8±0.1 0.6-0.9
Nb_{ss}	68.2±0.6 67.1-69.4	11.8±1.7 9.4-13.9	4.4±0.9 3.6-5.4	8.5±0.5 7.7-9.2	4.5±0.4 3.8-5.3	1.7±0.3 1.2-2.0	0.5±0.1 0.3-0.7	0.4±0.1 0.2-0.6
Ti-rich Nb_{ss}	61.1±1.6 59.6-64.5	22.7±1.8 21.6-24.8	4.2±1.1 3.1-5.6	5.5±0.7 4.4-6.9	1.8±0.4 1.0-2.4	3.0±0.2 2.7-3.5	0.6±0.1 0.4-0.7	1.1±0.2 0.9-1.4
Nb_5Si_3	48.4±0.3 47.7-48.6	7.8±0.2 7.4-8.0	36.3±0.6 35.4-37.2	3.9±0.2 3.6-4.2	0.3±0.1 0.1-0.5	0.5±0.1 0.4-0.7	2.3±0.1 2.1-2.6	0.5±0.1 0.4-0.6
Ti-rich Nb_5Si_3	46.3±0.7 45.1-47.0	11.9±0.9 10.9-12.9	34.5±0.7 34.0-35.7	2.9±0.2 2.5-3.1	0.1	0.6±0.1 0.5-0.7	2.8±0.2 2.6-3.0	0.9±0.2 0.7-1.1
Nb_3Si[b]	55.9±0.4 55.2-56.1	8.0±0.1 7.8-8.1	26.2±0.5 25.7-26.9	6.5±0.2 6.2-6.8	1.5±0.1 1.3-1.6	0	1.4±0.1 1.4-1.5	0.5±0.1 0.4-0.6
Eutectic	58.8±0.6 58.0-59.8	10.8±0.7 9.9-11.9	18.2±0.6 16.1-18.1	6.2±0.3 6.1-6.8	2.8±0.2 2.7-3.2	1.3±0.1 1.2-1.6	1.2±0.2 0.9-1.5	0.7±0.1 0.4-0.8

[a] Large area analysis.

[b] Only formed in the bottom area.

Table 3.3 The EDS analysis data (at.%) for the alloy JZ1-HT.

	Nb	Ti	Si	Ta	W	Sn	Ge	Hf
Large area	55.0±1.3	12.0±0.4	22.4±1.6	5.2±0.3	1.6±0.3	1.2±0.2	1.8±0.2	0.8±0.1
	53.3-56.9	11.5-12.8	20.1-24.5	4.6-5.5	1.1-2.1	1.0-1.5	1.5-2.1	0.7-0.9
Nb_{ss}	69.3±0.5	12.3±0.2	3.8±0.7	8.0±0.3	4.0±0.2	2.3±0.1	0.3±0.1	0
	68.7-69.8	12.1-12.6	3.1-4.7	7.5-8.3	3.8-4.3	2.2-2.4	0.2-0.3	
Nb_5Si_3	48.3±0.4	7.9±0.2	35.9±0.4	4.1±0.1	0.4±0.1	0.6±0.1	2.3±0.2	0.5±0.1
	47.9-48.8	7.7-8.2	35.4-36.4	3.9-4.2	0.2-0.4	0.5-0.7	2.0-2.4	0.4-0.5
Ti-rich	44.8±0.5	12.5±0.4	35.3±0.6	2.8±0.2	0	0.7±0.1	2.9±0.3	1.0±0.2
Nb_5Si_3	44.0-45.2	12.1-13.0	34.3-35.8	2.4-3.1		0.5-0.8	2.7-3.3	0.8-1.2

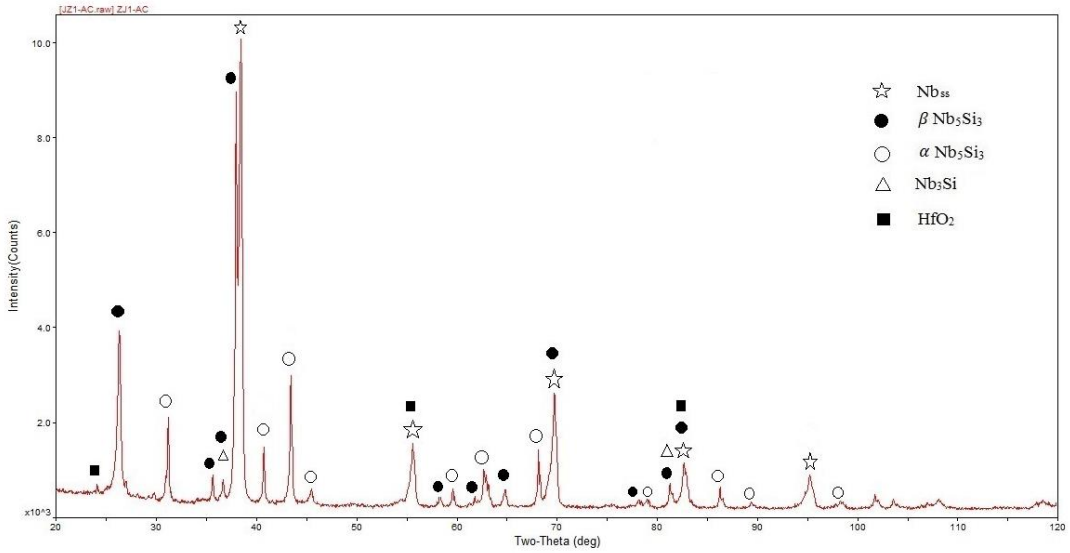

Figure 3.1 The X-ray diffractogram of the alloy JZ1-AC.

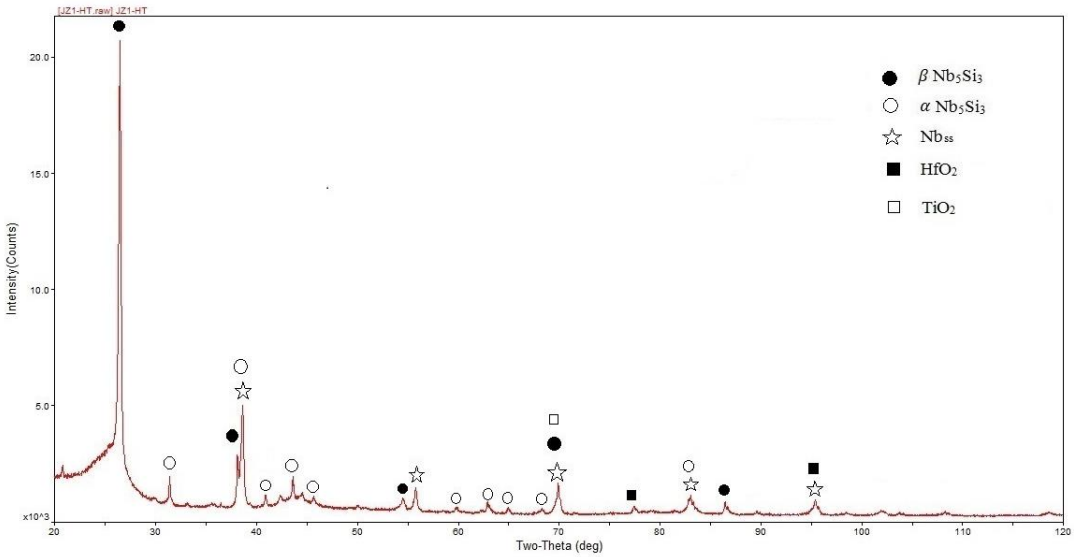

Figure 3.2 The X-ray diffractogram of the alloy JZ1-HT.

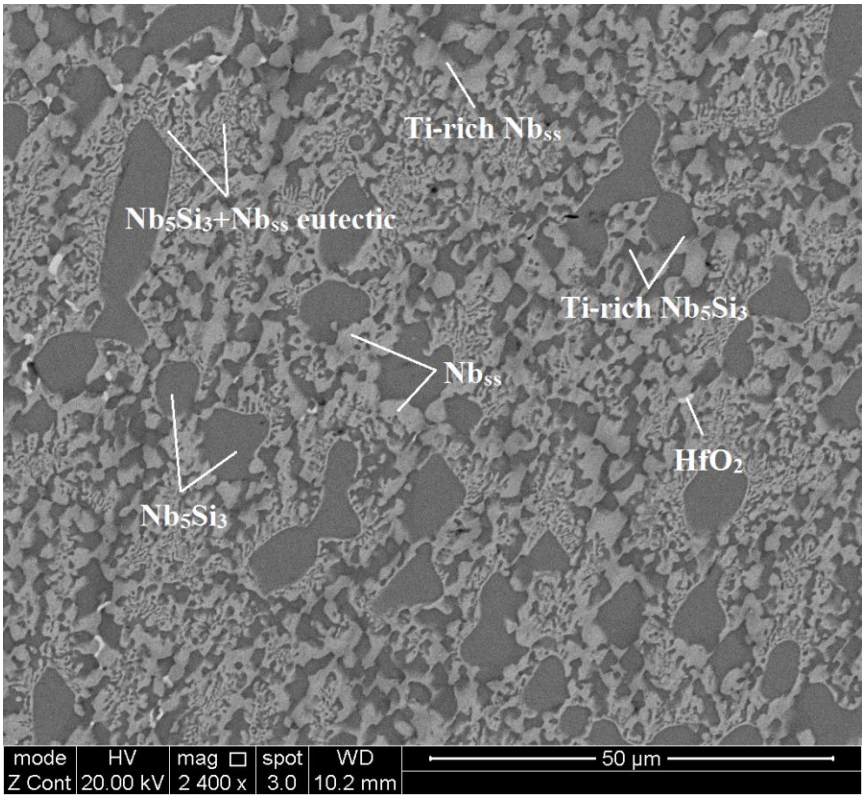
Ti-rich Nbss
Nb5Si3+Nbss eutectic
Ti-rich Nb5Si3
Nbss
HfO2
Nb5Si3
mode HV mag spot WD
Z Cont 20.00 kV 2 400 x 3.0 10.2 mm
50 µm

(a)

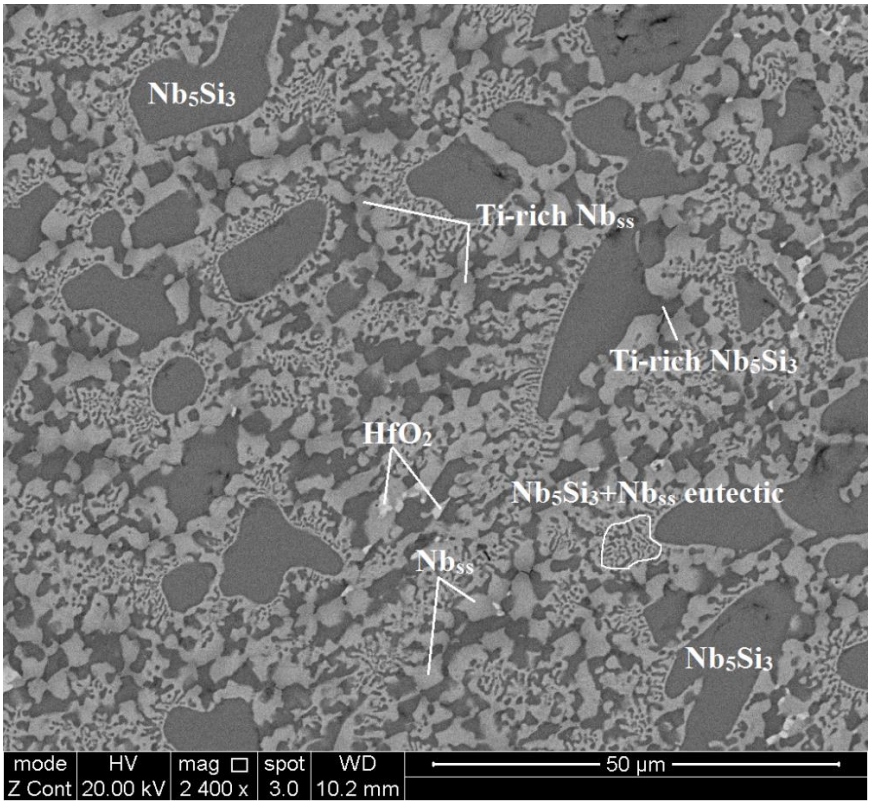
Nb5Si3
Ti-rich Nbss
Ti-rich Nb5Si3
HfO2
Nb5Si3+Nbss eutectic
Nbss
Nb5Si3
mode HV mag spot WD
Z Cont 20.00 kV 2 400 x 3.0 10.2 mm
50 µm

(b)

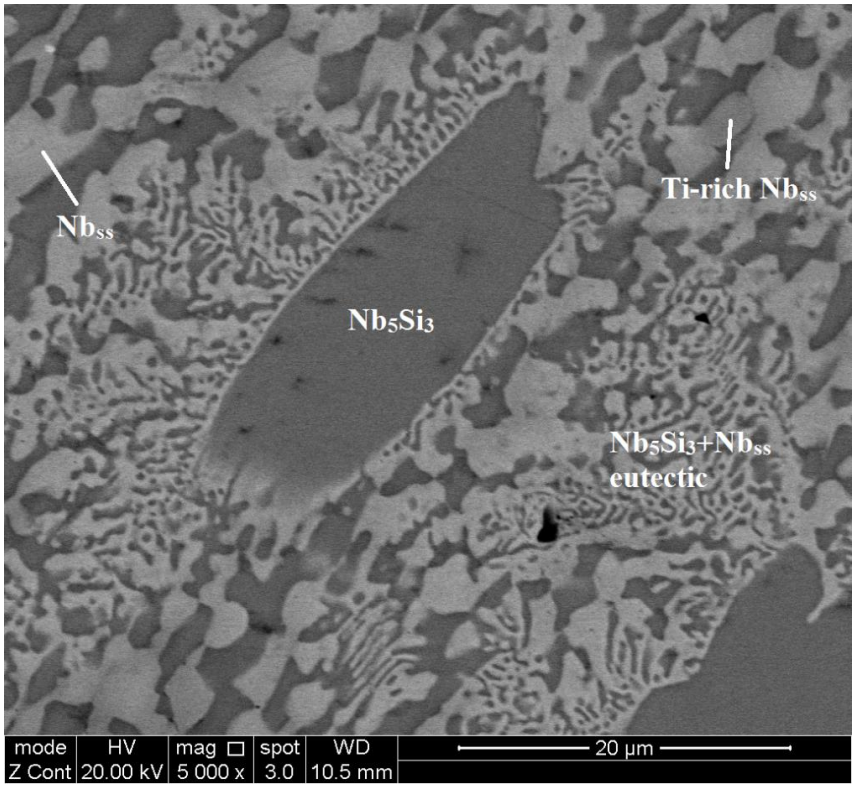
Nbss
Ti-rich Nbss
Nb5Si3
Nb5Si3+Nbss
eutectic
mode
Z Cont
HV
20.00 kV
mag
5 000 x
spot
3.0
WD
10.5 mm
20 µm

(c)

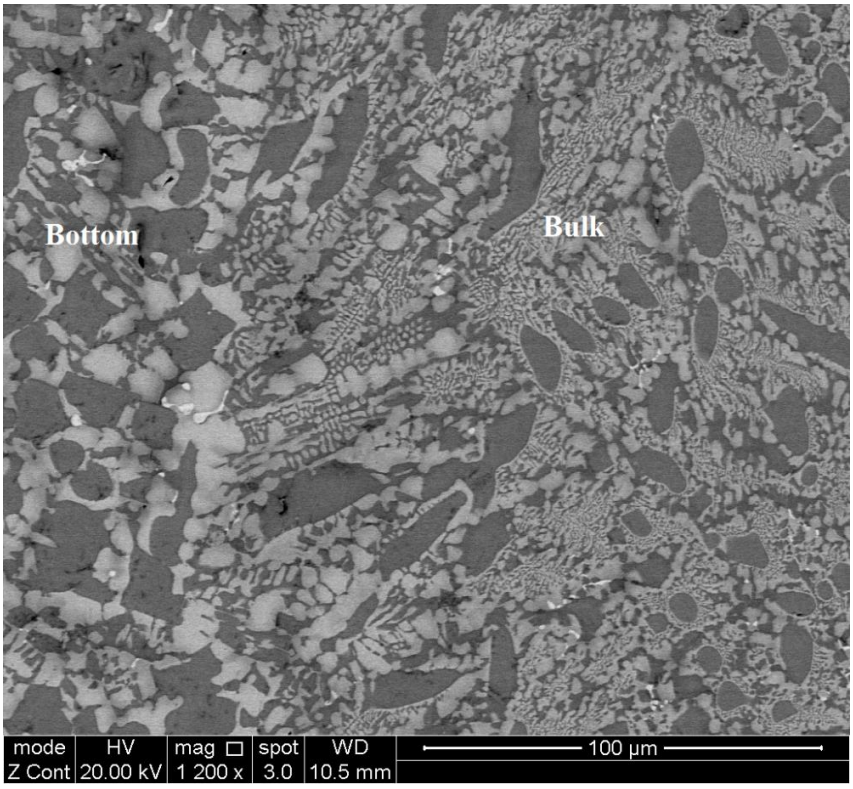
Bottom
Bulk
mode
Z Cont
HV
20.00 kV
mag
1 200 x
spot
3.0
WD
10.5 mm
100 µm

(d)

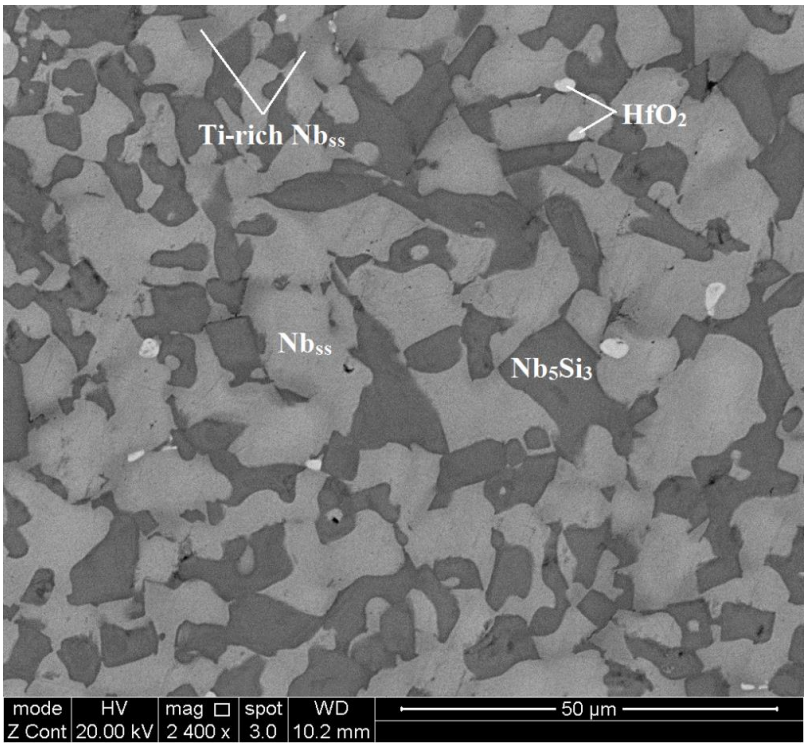

(e)

Figure 3.3 BSE images of the microstructure of JZ1-AC in the (a) top, (b) and (c) bulk, (d) the area showing the transition from the bottom to bulk and (e) bottom.

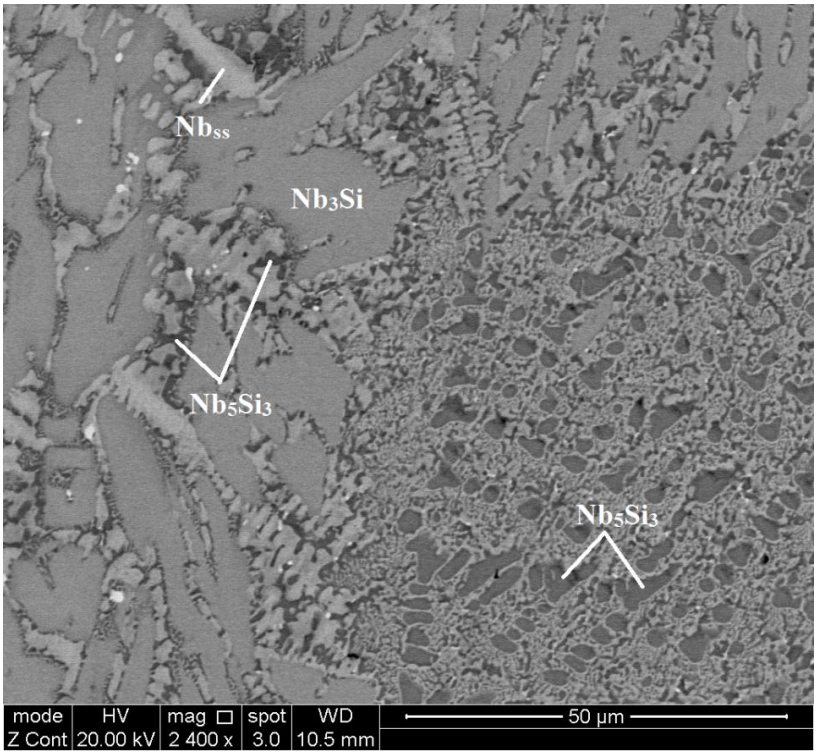

(a)

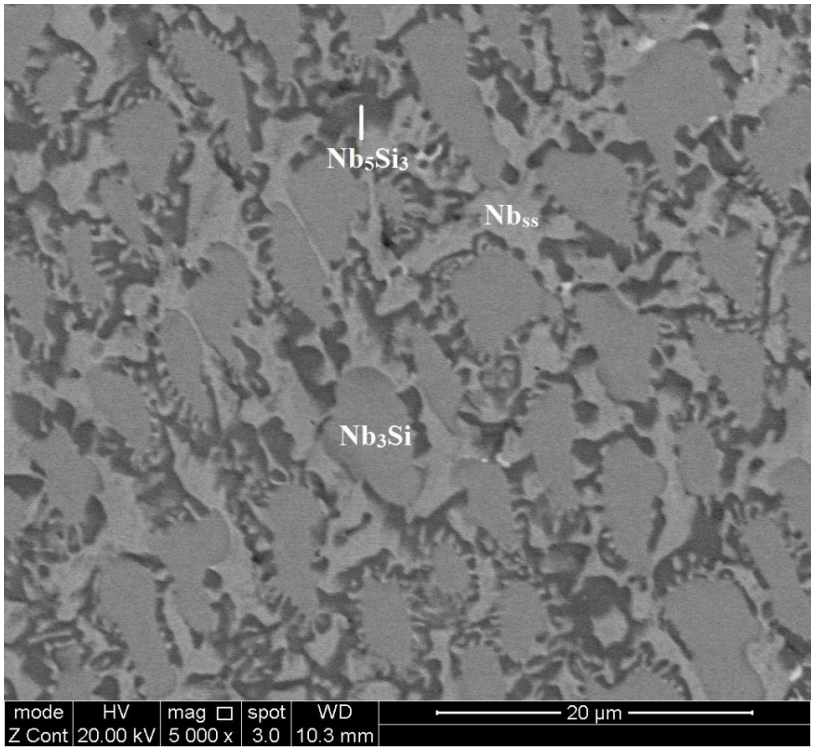

(b)

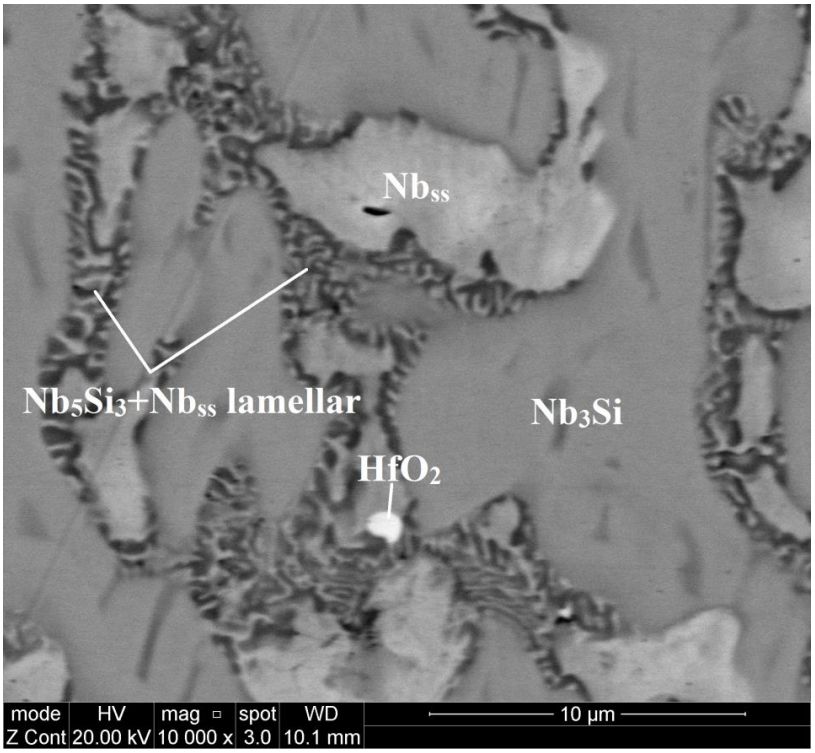

(c)

Figure 3.4 BSE images of the microstructure of the bottom area of JZ1-AC in the region where the Nb_3Si was observed at (a) and (b) low magnification and (c) high magnification.

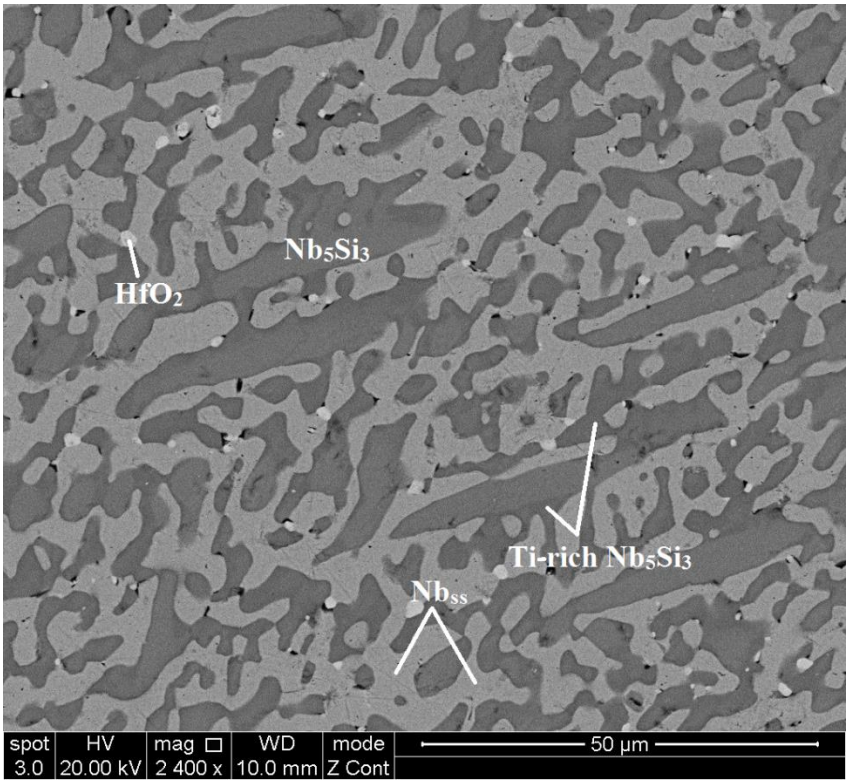

(a)

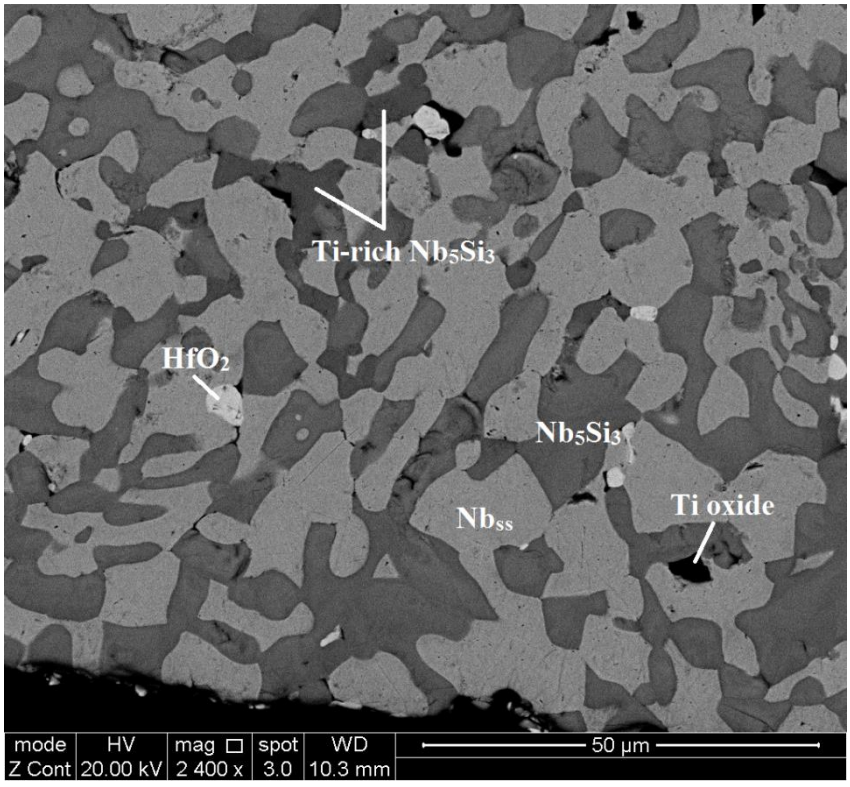

(b)

Figure 3.5 BSE images of the microstructure of JZ1-HT (a) in the bulk and (b) below the surface.

3.2 The alloy Nb-12Ti-18Si-6Ta-2.5W-5Sn-5Ge-1Hf (alloy JZ2): Results

The actual composition of the cast alloy (JZ2-AC) was 50.5Nb-11.8Ti-21.5Si-5.2Ta -2.0W-2.8Sn-5.2Ge-1Hf. Again Sn was lost during the arc melting and the Si concentration was higher than the nominal one. Large area analyses for different parts of the ingot are given in Table 3.4 and show that the macrosegregation of Si in JZ2-AC was as significant as in the JZ1-AC and the Si content was in the range of 18.8 to 23.7 at.%. The XRD and EDS data (Figure 3.6 and Table 3.4) would suggest that the phases in the microstructure of JZ2-AC were Nb_5Si_3, Nb_{ss}, the A15-Nb_3Sn and HfO_2. The XRD data indicated the presence of both the β and αNb_5Si_3 with more peaks corresponding to the former.

BSE images of the microstructure of JZ2-AC are given in Figure 3.8, and show a similar microstructure to that of the alloy JZ1-AC. The microstructure of JZ2-AC in the top and bulk consisted of primary Nb_5Si_3 surrounded by Nb_5Si_3 + Nb_{ss} eutectic, Nb_{ss} and HfO_2 and finer Nb_5Si_3 and Nb_{ss} with no eutectic in the bottom. The top right hand corner of figure 3.8e shows the change from the bottom microstructure to that in the bulk. The partitioning behaviour of elements between the Nb_{ss} and the Nb_5Si_3 in JZ2-AC was the same as in JZ1-AC. Relatively high Si content was found in the Nb_{ss}. Ti enrichment in the outer areas of the Nb_{ss} and the Nb_5Si_3 grains was observed in the top and bulk and no Ti-rich Nb_{ss} formed in the bottom of the ingot. It can be seen that the enrichment of Ti in the solid solution and the silicide “push out” the Ta and W and drew in the Sn in the Nb_{ss} and the Sn, Ge and Hf in the Nb_5Si_3. In the Nb_{ss} and Ti-rich Nb_{ss}, the Ta+W contents were 15.8 at.% and 12.0 at.%, respectively, the latter significantly higher compared with the alloy JZ1-AC. The contents of Si+Sn+Ge in the normal and the Ti-rich Nb_5Si_3 were 39.5 at.% and 38.7 at.%, closer to each other than those in JZ1-AC. The A15-Nb_3Sn only formed in the bottom, exhibiting darker contrast than the Nb_{ss}. The volume fraction of the Nb_{ss} in the bottom was lower than those in the top and bottom (Table 3.1), owing to the formation of the A15-Nb_3Sn. The Si+Sn+Ge and Ta+W contents in the A15-Nb_3Sn were 19.1 at.% and 6.9 at.%,

respectively. Compared with JZ1-AC, the Si+Ge+Sn concentration of the eutectic was 23.3 at.%, owing to the higher Sn and Ge concentrations in the alloy, the Si concentration was lower and the Ta+W content was the same.

The average composition of the alloy JZ2 after the heat treatment at 1500 ˚C for 100 hours (JZ2-HT) is given in Table 3.5. The chemical inhomogeneity of Si was still present in JZ2-HT. BSE images of the typical microstructure of the heat treated specimen are given in Figure 3.9. The XRD (figure 3.7) and EDS data showed that the A15-Nb_3Sn, which only exists in the bottom of the ingot, had formed in the bulk after the heat treatment. The Nb_5Si_3 + Nb_{ss} eutectic microstructure was not stable and the Nb_5Si_3 existed with the β and α structures with fewer peaks corresponding to the former after the heat treatment, see Figure 3.7.

The Si solubility in the Nb_{ss} was still relatively high at 3.5 at.% and the Sn content in the Nb_{ss} of JZ2-HT was decreased to 2.1 at.%. The contents of Ta and W in the Nb_{ss} increased slightly and the Ta+W content was 17.5 at.%. No Ti-rich area was found in the Nb_{ss}. The compositions of the Nb_5Si_3 and the A15 phase did not change significantly, the Ti enrichment in the Nb_5Si_3 was still observed and there were Ti rich sub-grain boundaries in the Nb_5Si_3. The Si+Sn+Ge content in the A15 phase was 18.9 at.% and the solubility of Ta+W in the A15 phase was 7.6 at.%. The Hf concentration in the Nb_{ss} and the A15 phase and the W content in the Ti-rich Nb_5Si_3 were reduced to zero. Ti oxide formed in the area below the surface after the heat treatment, see also Figure 3.7.

Table 3.4 The EDS analysis data (at.%) for the alloy JZ2-AC.

	Nb	Ti	Si	Ta	W	Sn	Ge	Hf
Top[a]	50.7±0.9	11.6±0.2	21.6±1.7	5.4±0.5	1.9±0.2	2.6±0.2	5.3±0.4	0.9±0.1
	49.0-50.5	11.4-12.0	19.2-23.7	4.8-6.2	1.7-2.1	2.3-2.9	4.8-5.9	0.8-1.0
Bulk[a]	50.3±0.2	11.7±0.4	21.7±1.2	5.3±0.3	2.0±0.2	2.5±0.3	5.4±0.7	1.1±0.1
	50.2-50.7	11.3-12.4	20.0-23.0	5.0-5.7	1.8-2.2	2.1-2.8	5.0-6.6	0.9-1.3
Bottom[a]	50.8±0.9	12.1±0.5	21.1±1.7	4.9±0.4	2.0±0.2	3.2±0.3	4.9±0.2	1.0±0.2
	50.1-52.1	11.4-12.7	18.8-22.5	4.5-5.6	1.9-2.4	2.9-3.6	4.7-5.1	0.8-1.3
Nb_{ss}	63.7±0.7	11.5±1.0	3.4±0.4	9.3±0.5	6.5±0.4	4.1±0.4	1.0±0.2	0.5±0.1
	62.9-64.7	10.6-12.9	3.1-4.1	8.7-9.8	5.9-7.0	3.9-4.8	0.8-1.2	0.3-0.6
Ti-rich	61.4±0.9	15.5±1.1	4.0±0.5	7.6±0.5	4.4±0.4	5.5±0.4	1.0±0.1	0.6±0.1
Nb_{ss}	60.3-62.4	14.7-17.4	3.5-4.7	7.0-8.1	3.7-4.7	5.1-6.1	0.8-1.2	0.5-0.7
Nb_5Si_3	46.7±0.2	8.2±0.3	32.5±0.7	4.3±0.1	0.7±0.1	1.0±0.1	6.0±0.2	0.6±0.2
	46.4-47.0	8.1-8.6	31.4-33.2	4.2-4.4	0.6-0.8	0.9-1.1	5.9-6.2	0.4-0.7
Ti-rich	44.0±1.1	13.0±1.2	29.2±0.8	3.1±0.4	0.2	1.9±0.4	7.6±0.6	1.0±0.1
Nb_5Si_3	42.1-45.1	12.2-15.2	28.3-30.4	2.3-3.4		1.5-2.5	7.1-8.7	0.9-1.2
A15[b]	56.5±0.9	16.8±1.3	6.6±0.5	4.7±0.5	2.2±0.4	9.5±0.4	3.1±0.2	0.6±0.2
	55.4-57.8	15.0-18.5	5.8-7.1	4.0-5.2	1.7-2.7	8.9-10.0	2.9-3.4	0.3-0.9
Eutectic	53.2±0.9	13.5±0.6	15.6±0.4	5.9±0.1	3.0±0.2	3.4±0.2	4.3±0.2	1.1±0.3
	52.2-54.3	12.9-14.3	15.1-16.1	5.9-5.9	2.9-3.0	3.2-3.6	4.2-4.6	0.8-1.6

[a] Large area analysis.

[b] Only formed in the bottom area.

Table 3.5 The EDS analysis data (at.%) data for the alloy JZ2-HT.

	Nb	Ti	Si	Ta	W	Sn	Ge	Hf
Large area	51.0±0.6	12.0±0.3	21.1±1.1	5.4±0.3	2.1±0.2	2.7±0.1	4.9±0.2	0.8±0.1
	50.3-51.8	11.8-12.5	19.5-22.6	4.9-5.8	1.8-2.2	2.7-2.8	4.6-5.2	0.7-0.8
Nb_{ss}	65.6±0.3	10.7±0.4	3.5±1.0	10.0±0.4	7.5±0.2	2.2±0.2	0.5±0.1	0
	65.3-66.2	10.4-11.3	2.5-4.9	9.5-10.4	7.3-7.7	1.9-2.4	0.4-0.6	
Nb_5Si_3	46.7±0.4	8.4±0.5	32.3±0.7	4.6±0.2	0.7±0.3	0.8±0.1	5.9±0.2	0.6±0.1
	46.2-47.1	7.9-9.1	31.2-32.8	4.4-4.8	0.2-0.9	0.8-1.0	5.6-6.1	05-0.7
Ti-rich	37.9±4.6	19.4±4.6	28.6±2.4	2.6±0.3	0	0.7±0.4	9.3±2.1	1.5±0.6
Nb_5Si_3	34.3-43.3	14.3-22.8	26.5-31.8	2.2-2.9		0.2-1.2	6.8-10.9	0.7-2.2
A15	58.8±0.4	14.5±0.3	5.7±0.6	5.3±0.2	2.3±0.1	10.4±0.2	2.9±0.1	0
	58.3-59.4	14.2-14.8	5.2-6.6	4.9-5.4	2.2-2.5	10.2-10.7	2.7-3	

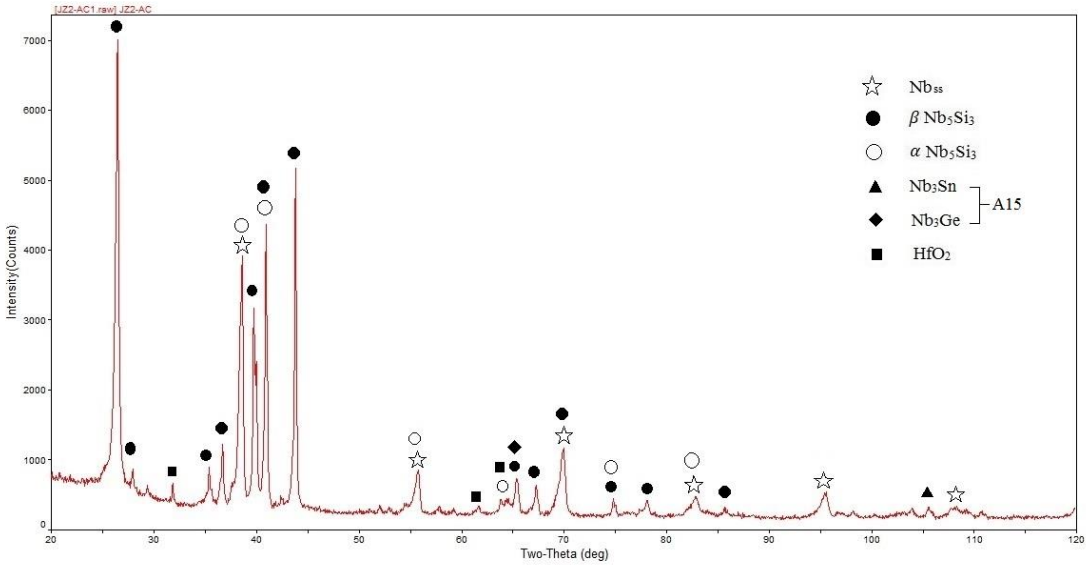

Figure 3.6 The X-ray diffractogram of the alloy JZ2-AC.

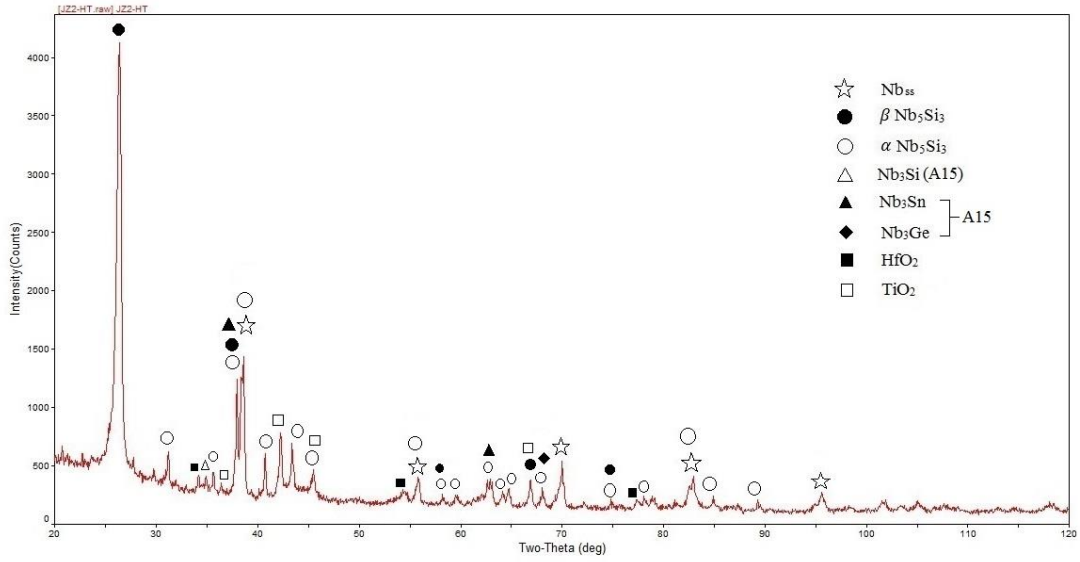

Figure 3.7 The X-ray diffractogram of the alloy JZ2-HT.

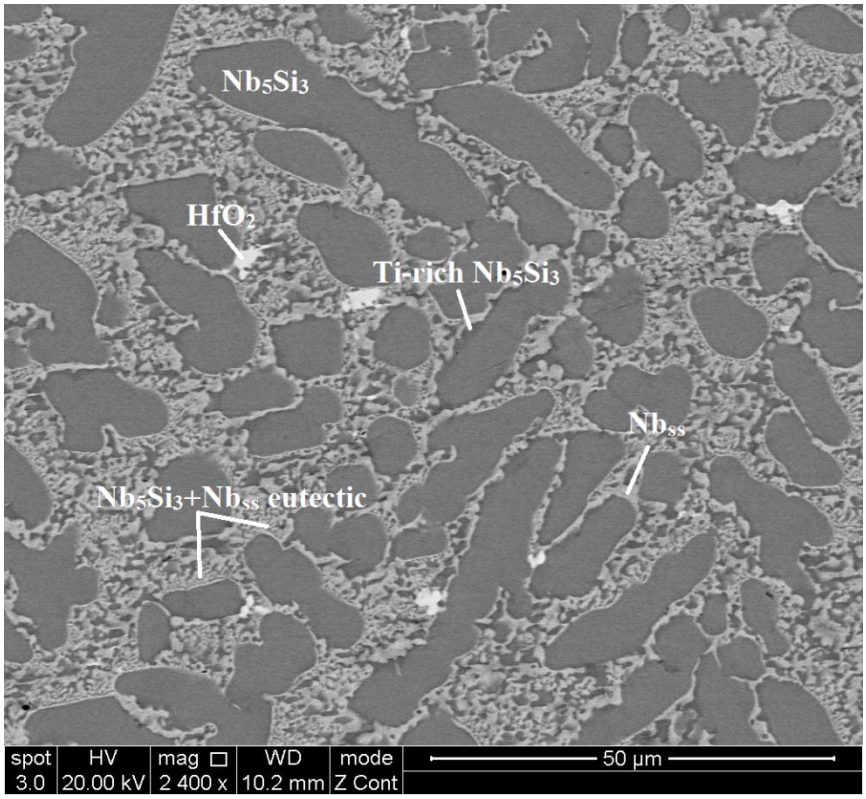
Nb_5Si_3
HfO_2
Ti-rich Nb_5Si_3
Nb_{ss}
Nb_5Si_3+Nb_{ss} eutectic
spot 3.0
HV 20.00 kV
mag 2 400 x
WD 10.2 mm
mode Z Cont
50 µm

(a)

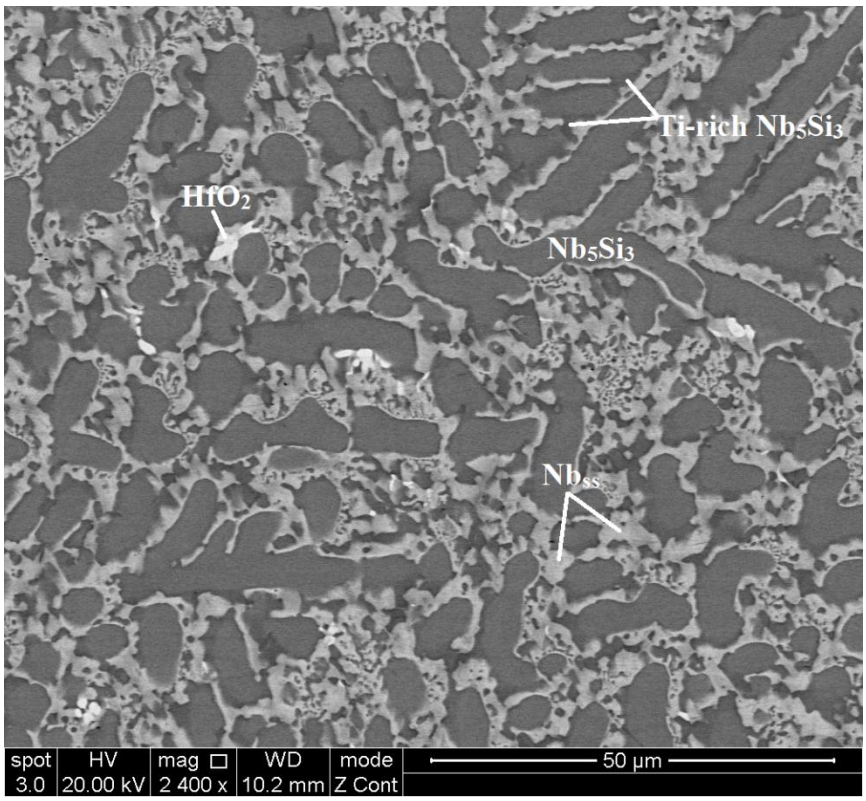
Ti-rich Nb_5Si_3
HfO_2
Nb_5Si_3
Nb_{ss}
spot 3.0
HV 20.00 kV
mag 2 400 x
WD 10.2 mm
mode Z Cont
50 µm

(b)

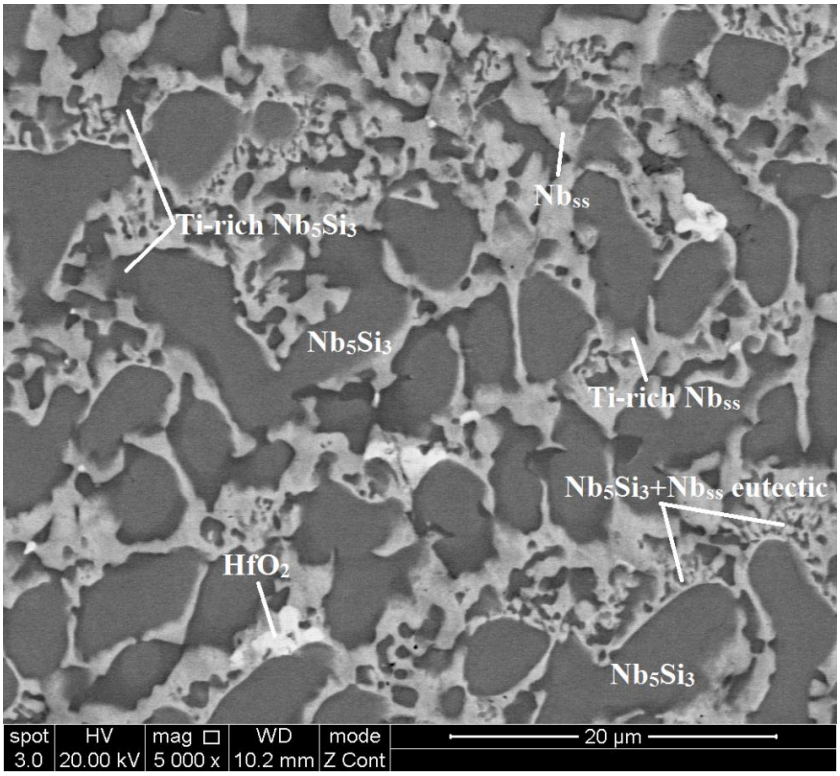
Ti-rich Nb_5Si_3
Nb_{ss}
Nb_5Si_3
Ti-rich Nb_{ss}
Nb_5Si_3+Nb_{ss} eutectic
HfO_2
Nb_5Si_3
spot 3.0
HV 20.00 kV
mag 5 000 x
WD 10.2 mm
mode Z Cont
20 µm

(c)

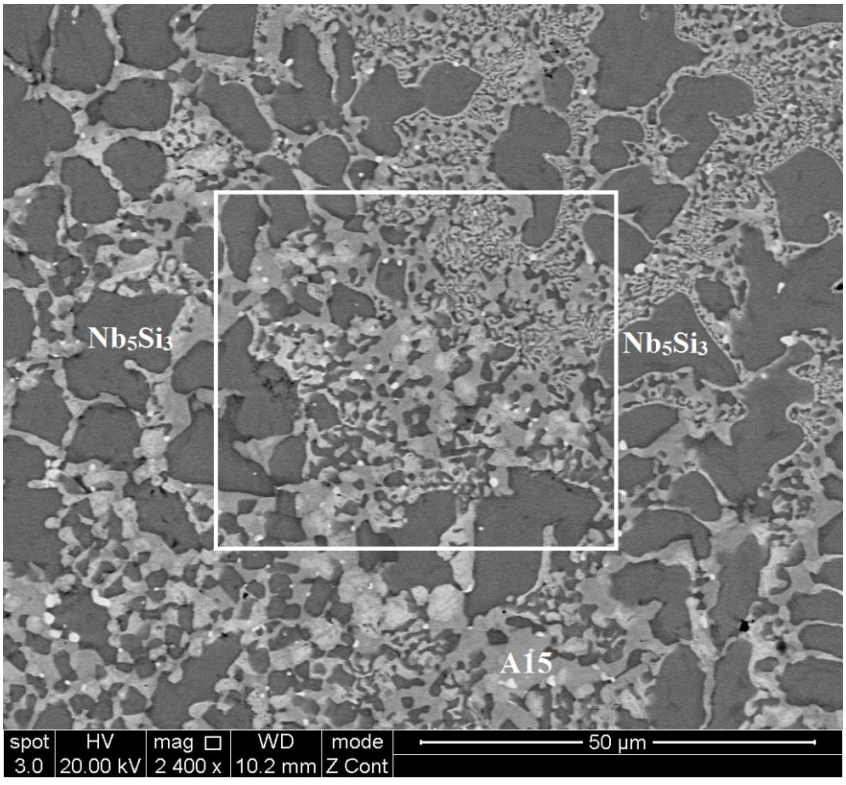
Nb_5Si_3
Nb_5Si_3
A15
spot 3.0
HV 20.00 kV
mag 2 400 x
WD 10.2 mm
mode Z Cont
50 µm

(d)

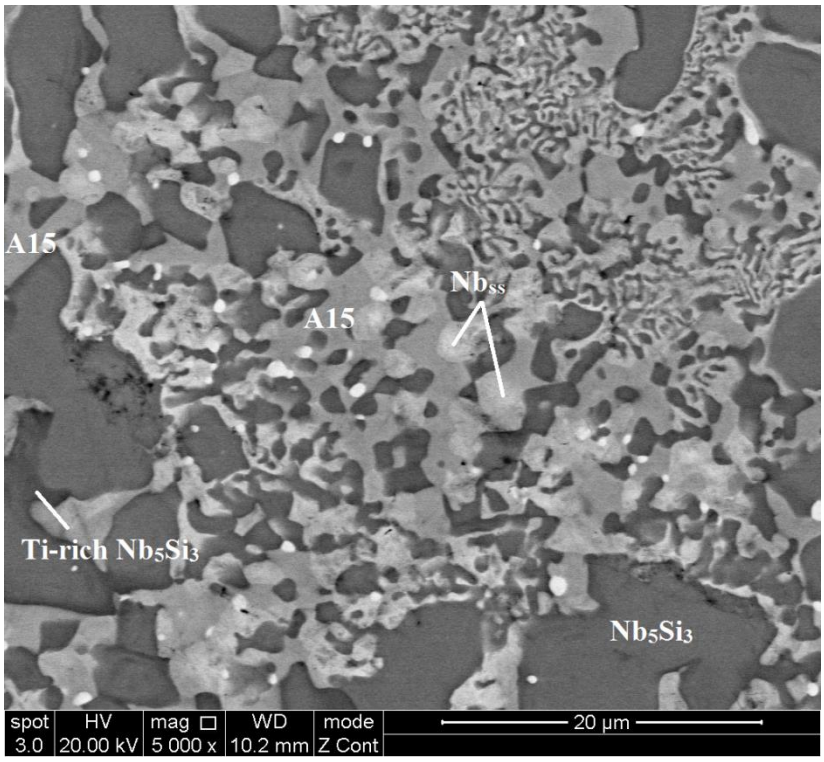

(e)

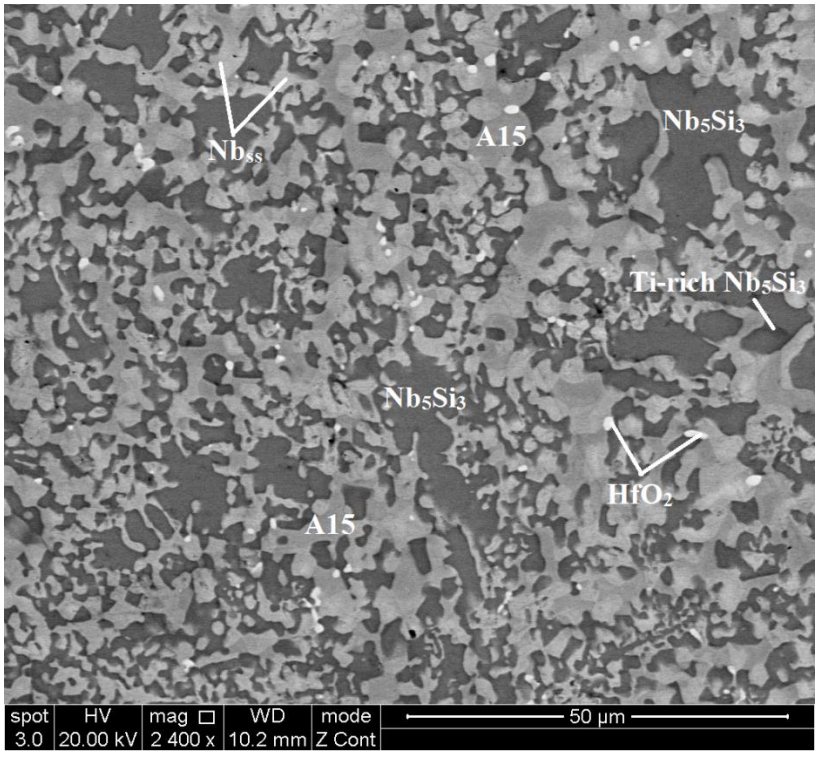

(f)

Figure 3.8 BSE images of the microstructure of the alloy JZ2-AC in the (a) top, (b) and (c) bulk, (d) and (e) the area showing the transition from the bottom to bulk and (f) bottom. (e) is a high magnification image of the area in the square in (d).

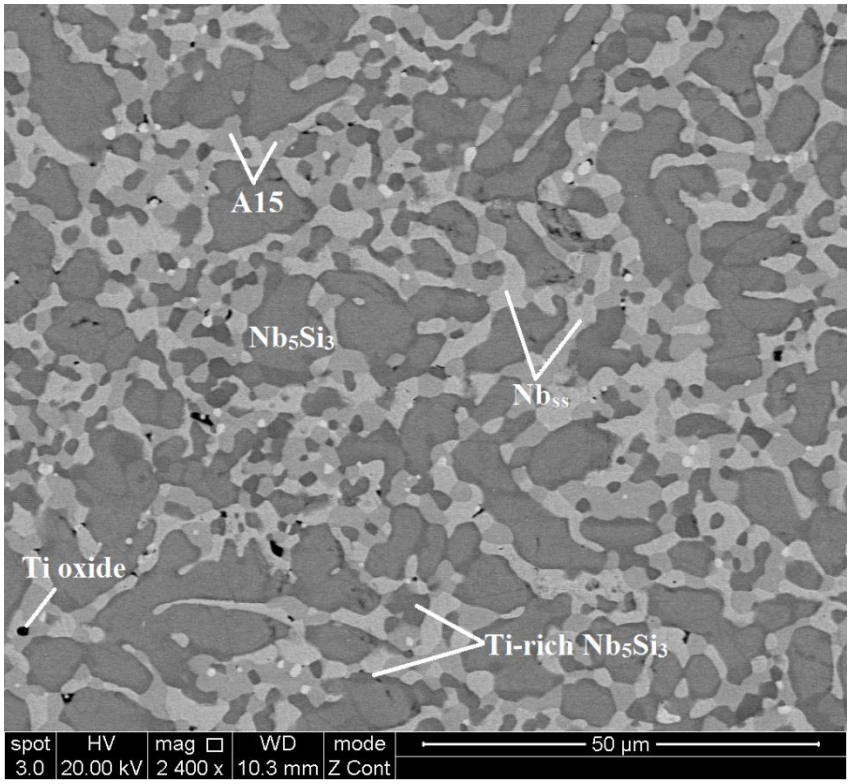
A15
Nb5Si3
Nbss
Ti oxide
Ti-rich Nb5Si3
spot 3.0
HV 20.00 kV
mag 2 400 x
WD 10.3 mm
mode Z Cont
50 µm

(a)

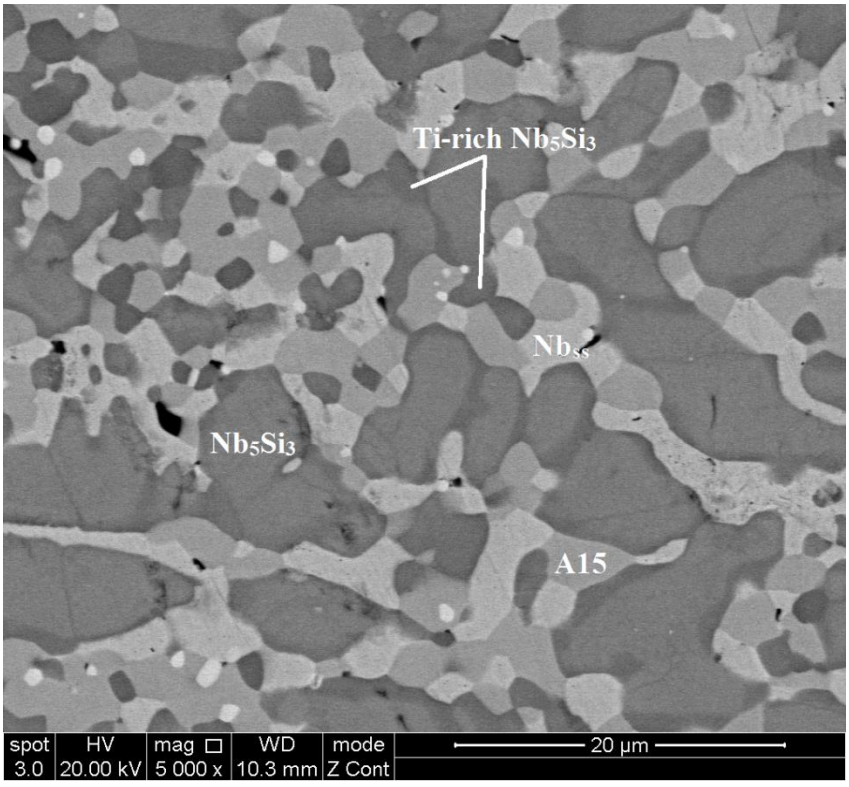
Ti-rich Nb5Si3
Nbss
Nb5Si3
A15
spot 3.0
HV 20.00 kV
mag 5 000 x
WD 10.3 mm
mode Z Cont
20 µm

(b)

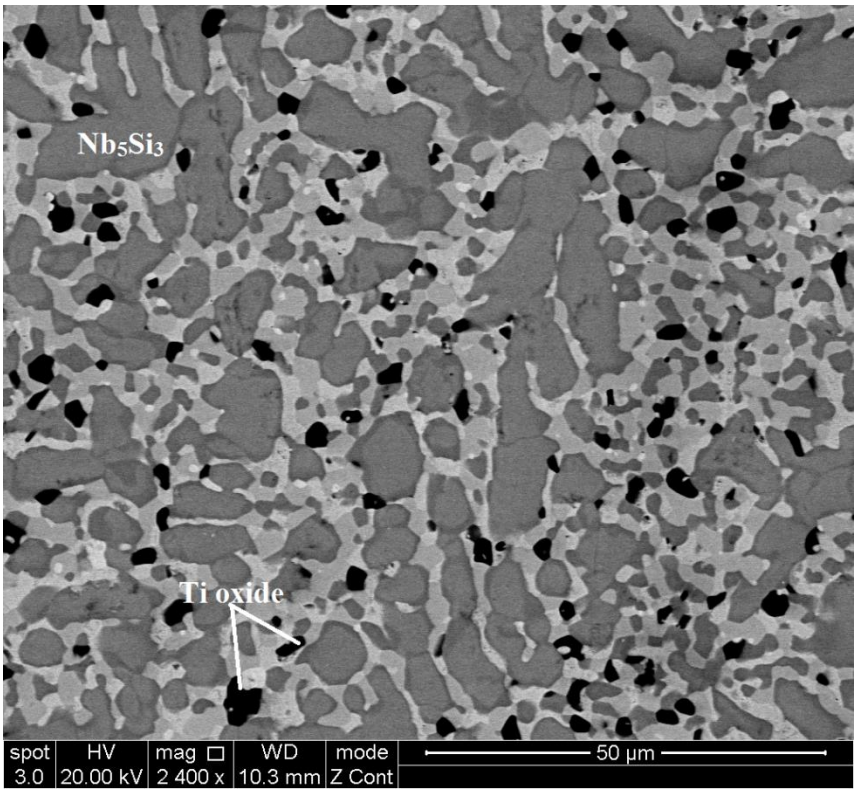

(c)

Figure 3.9 BSE images of the microstructure of the alloy JZ2-HT (a) and (b) in the bulk and (c) below the surface.

3.3 Discussion

There was a Sn loss in the preparation of both alloys, owing to the evaporation of Sn during the arc melting. This is a well-known problem with the production of Nb-silicide based alloys. Macrosegregation of Si existed in both alloys. The latter is defined MACSi = C_{Max}^{Si} - C_{Min}^{Si} where C_{Max}^{Si} and C_{Min}^{Si}, respectively are the maximum and minimum Si concentrations in the ingot. The MACSi values were 5.6 and 4.9 at.% for the alloys JZ1 and JZ2, respectively. These compare well with the average calculated MACSi values using the group's alloy design methodology (Tsakiropoulos 2015), which were 6.2 and 6 at.% for JZ1 and JZ2, respectively. Furthermore, the MACSi values calculated using the parameter ΔH_m^{sd} (Tsakiropoulos 2014) were 5.4 and 5.9 at.% for JZ1 and JZ2, respectively.

In the alloy JZ1, as the primary βNb_5Si_3 formed the surrounding melt became rich in Sn, Ta, Ti and W owing to the partitioning of these solutes. Then the Nb_{ss} and the Nb_{ss} + βNb_5Si_3 eutectic formed as the melt undercooled. The need to nucleate the eutectic of which one phase was the (existing in the melt) βNb_5Si_3 lead to Nb_{ss} halo formation around primary βNb_5Si_3 grains, sometimes surrounding the primary βNb_5Si_3 completely, as can be seen for an unmarked Nb_5Si_3 grain in the right hand bottom side of figure 3.3a or in the top left hand side of the same figure where the Nb_5Si_3 grain (with hafnia particles on the left) can be seen. The halo formation was caused by the pile up of solutes that formed the Nb_{ss} at the βNb_5Si_3/melt interface and would suggest an asymmetric coupled zone, which is expected given the difference in entropies of fusion of the Nb_{ss} and Nb_5Si_3. In other words, the pile up of solutes shifted the melt composition beyond the composition of coupled growth and the halo formation brought the composition back in the coupled zone and the eutectic formed. In the eutectic the Si+Ge+Sn content was 20.7 at.%, which is close to the composition of the metastable Nb_{ss} + βNb_5Si_3 eutectic in the Nb-Si binary (Bendersky *et al.* 1987) and falls within the range (20.5 to 24 at.%) of eutectics in high order Nb-silicide based alloys studied in our group.

The XRD showed evidence of both βNb_5Si_3 and αNb_5Si_3 in JZ1-AC. The αNb_5Si_3 can form on cooling from the β or from the Nb_3Si via a eutectoid transformation. The easiest way to consider this is to use the binary Nb-Si system (figure 1.3.1). Solute additions also tend to stabilise the βNb_5Si_3 or αNb_5Si_3 and to stabilise or destabilise the Nb_3Si. We can understand the latter by considering the crystal structures of M_5Si_3 and M_3Si silicides and the stability of the latter in Nb-Si-M ternaries.

In the top and bulk of JZ1-AC the Si content was in the range 20.4 to 24.4 at.% and 21.2 to 23 at.%, respectively (Table 3.2). Thus, in both cases and according to the Nb-Si binary phase diagram the primary phase should be the βNb_5Si_3 and Nb_3Si would form via L + βNb_5Si_3 → Nb_3Si (at 1986 ˚C in the binary) and then αNb_5Si_3 from βNb_5Si_3 + Nb_3Si → αNb_5Si_3 at 1947 ˚C and then Nb_3Si → Nb_{ss} + αNb_5Si_3 at about

1700 ˚C. No evidence of Nb_3Si was observed in the top and bulk as well as no evidence of microstructures resulting from the above transformations.

The solutes Ta and Ti form M_3Si silicides that have the same crystal structure as Nb_3Si, thus would be expected to encourage formation of the latter. The solutes Hf and W on the other hand do not form M_3Si silicides and thus would be expected to have the opposite effect. Furthermore, Sn suppresses the Nb_3Si on its own and with Ti (Vellios and Tsakiropoulos 2007), meaning that Sn has a very strong effect on the stability of Nb_3Si. Ge can also suppress the Nb_3Si (Nb_3Ge has the A15 structure, the same as Nb_3Sn and Nb_3Al) (Li and Tsakiropoulos 2010) but its effectiveness is compromised when it was added with Ti (Li and Tsakiropoulos 2011). The solutes Ge, Ta, W form 5-3 silicides that have the same crystal structure as the βNb_5Si_3, and thus would be expected to stabilise the latter but Sn stabilises the αNb_5Si_3 on its own or with Ti (Vellios and Tsakiropoulos 2007). The solutes Ge, Sn and W promote the Nb_{ss} + Nb_5Si_3 eutectic in ternary Nb-Si-X alloys. In the case of W the Nb_{ss} + Nb_3Si eutectic is suppressed and replaced by the Nb_{ss} + βNb_5Si_3 eutectic when W ≥ 3 at% in the ternary.

Thus, it is suggested that in the top and bulk of JZ1-AC the solidification path was L $\rightarrow$ L + βNb_5Si_3 $\rightarrow$ βNb_5Si_3 + $(Nb_{ss} + \beta Nb_5Si_3)_{eutectic}$ with the latter eutectic stabilised and the Nb_3Si suppressed for the reasons discussed above. The formation of αNb_5Si_3 occurred during solid state cooling and was promoted by Sn.

The solidification path calculated for the alloy JZ1 using the Pandat database and combining Ta with Nb, and Ge and Sn with Si (because of non-availability of phase equilibria data), was as follows: solidification started at 2125 ˚C with Nb_5Si_3 as the primary phase, then at 1912 ˚C the Nb_{ss} formed via L $\rightarrow$ Nb_5Si_3 + bcc A2 (Nb), then at 1861 ˚C the Nb_3Si formed via L + Nb_5Si_3 $\rightarrow$ bcc A2 (Nb) + Nb_3Si, then at 1515 ˚C the Ti_5Si_3 formed via L + Nb_3Si $\rightarrow$ bcc A2 (Nb) + Ti_5Si_3, and the last liquid at 1334 ˚C formed bcc A2 (Nb) + Ti_5Si_3. The mole fractions of phases were predicted to be

0.482 for Nb_5Si_3, 0.239 for Nb_{ss}, 0.274 for Nb_3Si and 0.005 for Ti_5Si_3. The calculation predicted formation of hexagonal 5-3 silicide, which was not observed in JZ1-AC, gave Nb_5Si_3 as the primary phase, in agreement with experiments and also predicted a significant mole fraction of Nb_3Si, which was not observed. The predicted Nb_3Si was observed in the bottom of the ingot of JZ1 and was predicted to form at lower temperature than those according to the Nb-Si binary phase diagram, owing to Ti stabilising the Nb_3Si to lower temperatures.

In the bottom of JZ1-AC the Si content was in the range 19 to 24.6 at.%. Considering the Nb-Si binary phase diagram, for Si content from 19 to 20.2 at.% or to 19.5 at.% (depending on choice of binary phase diagram) the solidification path $L \rightarrow L + Nb_3Si \rightarrow Nb_3Si + (Nb_{ss} + Nb_3Si)_{eutectic} \rightarrow (Nb_{ss} + Nb_3Si)_{eutectic} + (Nb_{ss} + \alpha Nb_5Si_3)_{eutectoid}$ is possible and for Si content exceeding 20.2 at.% (or 19.5 at.%), $L + \beta Nb_5Si_3 \rightarrow Nb_3Si$ at 1986 ˚C (for the binary) and then αNb_5Si_3 from $\beta Nb_5Si_3 + Nb_3Si \rightarrow \alpha Nb_5Si_3$ at 1947 ˚C and then $Nb_3Si \rightarrow Nb_{ss} + \alpha Nb_5Si_3$ at about 1700 ˚C.

In the microstructure in the bottom of JZ1-AC there was no evidence of either of the above solidification paths. Instead, the microstructure was either a mixture of coarse Nb_{ss} and Nb_5Si_3 with a transition to the $\beta Nb_5Si_3 + (Nb_{ss} + \beta Nb_5Si_3)_{eutectic}$ bulk microstructure (figure 3.3d), a mixture of Nb_{ss}, Nb_5Si_3 and Nb_3Si (figure 3.4, not seen in JZ2-AC) with transition to the bulk microstructure, i.e., $\beta Nb_5Si_3 + (Nb_{ss} + \beta Nb_5Si_3)_{eutectic}$ (figure 3.4a, notice limited evidence of Nb_{ss} halos around the Nb_5Si_3 in the $\beta Nb_5Si_3 + (Nb_{ss} + \beta Nb_5Si_3)_{eutectic}$ microstructure in this figure) and evidence of the transformation $Nb_3Si \rightarrow (Nb_{ss} + \alpha Nb_5Si_3)_{eutectoid}$, see figure 3.4c. In the bottom of JZ1-AC the dominant microstructure was the mixture of coarse Nb_{ss} and Nb_5Si_3 followed by a transition to the $\beta Nb_5Si_3 + (Nb_{ss} + \beta Nb_5Si_3)_{eutectic}$ bulk microstructure, see figures 3.3d and e.

In Nb-Si-Ge ternary alloys Li and Tsakiropoulos (2010) reported that the microstructure of the ingot that was in contact with the water cooled crucible

consisted of a mixture of Nb_{ss} and Nb_5Si_3, like the microstructures in figure 3.3e and 3.8c and that there was a transition of the latter (anomalous eutectic) to regular eutectic to $Nb_5Si_3 + (Nb_{ss} + Nb_5Si_3)_{eutectic}$ (as shown in figure 3.3d) further away from the water cooled side towards the bulk of the ingot. The "width" of the former zone (mixture of Nb_{ss} and Nb_5Si_3) increased with Ge content in the alloy. The microstructures seen in figures 3.3d and are attributed to the addition of Ge in the alloy JZ1.

A eutectic that exhibits a transition from anomalous to regular eutectic with decreasing melt undercooling (ΔT_{melt}) usually consists of a solid solution with an intermetallic. The coarse microstructure in the bottom of JZ1-AC was made of Nb_{ss} and the intermetallic Nb_5Si_3. These phases have different crystal structures and the Nb_5Si_3 has higher entropy of fusion (ΔS_f = 14.55 J/molK) than the non-facetted Nb_{ss} (ΔS_f = 9.45 J/molK). Thus, the Nb_5Si_3 would require kinetic undercooling than the Nb_{ss} (high ΔS_f means flat (or facetted or sharp) S/L interface and thus surface nucleation (meaning melt undercooling) is required for growth). In unconstrained solidification of eutectic melts (as is the case of solidification in the water cooled copper crucible, directional solidification (DS) is constrained solidification) a transition from purely anomalous eutectic to a mixture of regular and anomalous eutectic to regular eutectic has been reported with decreasing melt undercooling (Han and Wei 2002).

Thus, it is suggested that in the bottom of the ingot of the alloys JZ1 the undercooling of the melt was $\Delta T_{melt} > \Delta T_{critical}$, with $\Delta T_{critical} \approx 0.25\Delta T_{max}$, where $\Delta T_{critical}$ and ΔT_{max} are respectively the critical undercooling for the formation of anomalous eutectic and the maximum undercooling achievable in the eutectic system (Li and Kuribayashi 2003). The condition $\Delta T_{melt} > \Delta T_{critical}$ meant different growth rates for the Nb_{ss} and Nb_5Si_3 with the former growing faster (low ΔS_f which means diffuse (or rough) S/L interface) than the latter (higher ΔS_f). This caused decoupled growth of the two phases of the eutectic and led to the anomalous microstructure in the bottom. As the latter

grew the released latent heat of solidification increased the temperature of the melt ahead of the S/L interface which led to lower growth rates and eventually coupled growth between the two phases became possible which led to the formation of the regular eutectic.

The three phases Nb_{ss} + Nb_3Si + Nb_5Si_3 microstructure was seen in parts of the bottom of the JZ1-AC, see figures 3.4a and b, where the volume fraction of the Nb_3Si was higher than the other two phases. This microstructure could be a ternary eutectic consisting of the aforementioned phases as the Nb_{ss} and Nb_3Si form a eutectic and it is also possible for Nb_{ss} and Nb_5Si_3 to form a eutectic (see above discussion based on the Nb-Si binary). In parts of this three phase microstructure the Nb_3Si had transformed, as shown in figure 3.4c, and the morphological characteristics of the transformation are typical of the eutectoid reaction $Nb_3Si \rightarrow Nb_{ss} + \alpha Nb_5Si_3$. The αNb_5Si_3 detected by XRD was also from this transformation.

In the Nb-Si system the Nb_3Si can form as the primary phase when the Si content is above the eutectic composition (17.5 at.% or 18.2 at.% depending on choice of phase diagram) and below 20.2 at.% (or 19.5 at.%). As we discussed above, in the bottom of JZ1-AC the lowest Si concentration was 19 at.% (see Table 3.2), but the Nb_3Si did not form in the bottom of JZ2-AC where the lowest Si concentration was 18.8 at.%. That is because in the alloy JZ2 the Sn concentration was higher compared with the alloy JZ1 and Sn has a strong destabilising effect on the Nb_3Si (see above). The Nb_3Si formed in the bottom of JZ1 because of the Si content of the melt that solidified in contact with the water cooled crucible (see above) and because the (large area) chemical composition of the microstructure shown in figure 3.4 was essentially the same as in the bottom of JZ1-AC (see large area EDS data for bottom in Table 3.1) but with Ge/Sn = 1 instead of Ge/Sn = 1.6. This would suggest that at low Sn contents in the alloy the Ge, which, as discussed above, destabilises the Nb_3Si but is not as effective as Sn, is required to “help” the Sn supress the Nb_3Si.

The figure 3.4a shows a transition to the Nb_5Si_3 + $(Nb_{ss}$ + $Nb_5Si_3)_{eutectic}$ microstructure. It shows that the latter "grows" from an Nb_{ss} and Nb_5Si_3 coarse microstructure, see middle of the figure. It is suggested that this transition occurred when the growth of Nb_3Si was destabilised by high Sn concentration in the melt ahead of the ternary eutectic/melt interface (Sn has negligible solubility in Nb_3Si and extremely low solubility in Nb_5Si_3, see Table 3.2, thus the solidification of the ternary was accompanied by partitioning of Sn in the melt) so that only Nb_{ss} and Nb_5Si_3 could form and then while $\Delta T_{melt} > \Delta T_{critical}$ the two phases (Nb_{ss} and Nb_5Si_3) grew as discussed above.

The microstructure in the top and bulk of JZ2-AC was formed with the same solidification path as discussed above for the top and bulk of JZ1-AC. The finer scale of the eutectic in the top and bulk of the alloy JZ2 compared with the alloy JZ1 (figures 3.3a and b and 3.8a and b) is attributed to the higher Ge content in the alloy JZ2 ($1.5 < Ge/Sn < 2.16$) and the higher Ge/Sn in the top and bulk. Li and Tsakiropoulos (2010) showed that Ge refines the Nb_{ss} + Nb_5Si_3 eutectic microstructure. The average Si+Ge+Sn content of the eutectic was 23.3 at.%, and is in the range (20.5 to 24 at.%) of eutectics in high order Nb-silicide based alloys studied in the group.

The solidification path calculated for the alloy JZ2 using the Pandat database and combining Ta with Nb, and Ge and Sn with Si, was as follows: solidification started at 2239 ˚C with Nb_5Si_3 as the primary phase, then at 1939 ˚C the Nb_{ss} formed via $L \rightarrow Nb_5Si_3$ + bcc A2 (Nb), then at 1824 ˚C the Nb_3Si formed via $L + Nb_5Si_3 \rightarrow$ bcc A2 (Nb) + Nb_3Si, then at 1508 ˚C the Ti_5Si_3 formed via $L + Nb_3Si \rightarrow$ bcc A2 (Nb) + Ti_5Si_3, and the last liquid at 1334 ˚C formed bcc A2 (Nb) + Ti_5Si_3. The mole fractions of phases were predicted to be 0.675 for Nb_5Si_3, 0.171 for Nb_{ss}, 0.148 for Nb_3Si and 0.006 for Ti_5Si_3. The calculation predicted formation of Nb_3Si and hexagonal 5-3 silicide, both of which were not observed in JZ2-AC, and gave Nb_5Si_3 as the primary phase, in agreement with experiments. Furthermore, the calculation predicted a lower

mole fraction of Nb_{ss} in JZ2 compared with JZ1, in agreement with the experimental work, see Table 3.1.

The A15-Nb_3Sn was observed only in the bottom of JZ2-AC where the Ge/Sn ratio was 1.5 (i.e., the melt was richer in Sn compared with the bulk and top). Research in the group has shown that formation of Nb_3Sn in Nb silicide based alloys depends strongly on their Sn content and that a minimum Sn concentration is required for the Nb_3Sn to be stabilised in the microstructure. This is further supported by the results for the alloy JZ2.

The case for the microstructure formed in the bottom of the ingot of the alloy JZ2 where the melt was in direct contact with the water cooled crucible is slightly different compared with the alloy JZ1-AC in that the phases formed in JZ2-AC were the Nb_{ss}, A15 and Nb_5Si_3 and there was no Nb_5Si_3+Nb_{ss} eutectic and no Ti-rich Nb_{ss} and Ti-rich Nb_5Si_3. The entropies of fusion of the three phases are 9.45, 11.6 and 14.55 J/molK, respectively for the Nb_{ss}, A15-Nb_3Sn and Nb_5Si_3 (Utton and Tsakiropoulos 2017). Thus, the growth of the former two would be expected to be easier than that of the Nb_5Si_3, which would require kinetic undercooling (see above discussion for JZ1-AC).

Niobium has the bcc structure, which is also the structure of the Nb solid solution. Niobium can form a metastable A15-Nb_3Nb structure with 0.5246 nm lattice parameter (Stewart *et al.* 1980). The lattice parameter of the stoichiometric A15-Nb_3Sn is 0.529 nm (Devantay *et al.* 1981). In the A15 structure the Sn atoms form a bcc lattice, each face of the cube is bisected by orthogonal Nb chains and the distance between the Nb atoms is 0.265 nm. In the A15-Nb_3Nb structure the distance between the Nb atoms is 0.262 nm. In both cases these distances are lower than the shortest distance between Nb atoms in bcc Nb, which is 0.286 nm (for Nb lattice parameter 0.330 nm) (Straumanis and Zyszczynsk 1970). Both Ta and Ti occupy Nb sites in the A15-Nb_3Sn lattice (Tafto *et al.* 1984) and as their concentrations increase the stability

of the cubic phase increases.

The compositions of phases and the eutectic in Table 3.4 and the fact that no Ti rich Nb_{ss} and Ti rich Nb_5Si_3 were observed in the microstructure formed in the bottom of the ingot of the alloy JZ2 show that the partitioning of solutes in Nb_5Si_3 created favourable concentrations for the Ge, Si, Sn, Ta, Ti, W in the eutectic, but the partitioning of solutes in the solid solution and A15 phase, respectively created favourable concentrations for Ge and Si, and Ge, Si and Ta.

In the undercooled melt near the water cooled crucible the Nb_5Si_3 formed first (owing to its higher melting temperature) and then the Nb_{ss}, the growth of which was easier because of its lower entropy of fusion (see above). As solutes partitioned to the melt the formation of A15-Nb_3Sn next to the solid solution became possible due to crystallographic reasons and the availability of Ta and Ti that stabilise the A15-Nb_3Sn. Thus, growth of the three phases became possible and the eutectic did not form because the melt could not reach the eutectic composition owing to the growth of the three phases separately. However, as the latter grew the melt undercooling decreased making it possible for Ti rich Nb_{ss} and Ti rich Nb_5Si_3 to form. Formation of the latter two phases made less Ge, Si and Ti available for the needs of the A15-Nb_3Sn and thus its formation/growth was suppressed and this marked the start of the transition from the microstructure in the bottom of JZ2-AC to that in the bulk, with coupled growth of Nb_{ss} and Nb_5Si_3 resulting to the eutectic between these two phases.

In the microstructures of the heat treated alloys JZ1 and JZ2 the Nb_{ss} and β and αNb_5Si_3 were present with Ti rich areas being present only in the 5-3 silicide where the Ti+Hf content was not high enough to stabilize the hexagonal γNb_5Si_3. This would suggest that the solid solution and the tetragonal 5-3 silicide are stable in both alloys. The presence of both forms of the tetragonal Nb_5Si_3 is attributed to the βNb_5Si_3 stabilisers Ta, W and Ge "controlling" the effect of Sn on promoting the αNb_5Si_3. In JZ2-HT the A15 phase was stabilised owing to the higher Sn content in the alloy

compared with JZ1 as well as the presence of other elements that stabilise this structure. For both alloys the calculation of phase equilibria at 1500 ˚C predicted liquid phase formation which was not observed in the heat treated alloys.

In the alloys JZ1 and JZ2 the typical eutectic microstructure observed in the cast condition was not stable after the heat treatment. This was not observed in the alloys Nb-17.4Si-5.3Hf-3.4Ta-2Mo and Nb-19.7Si-2W-4.5Mo (Grammenos and Tsakiropoulos 2010) with refractory metal additions but no Ti and was attributed (1) to the addition of the refractory metals with Ge and Sn and (2) to the higher homologous heat treatment temperatures for the alloys JZ1 and JZ2 that were ≈ 0.74 and 0.76, respectively, compared with the homologous temperature of ≈ 0.69 for the two aforementioned alloys in which lamellar microstructures consisting of Nb_{ss} and Nb_5Si_3 were present after the heat treatment.

3.4 Conclusions

In this chapter the microstructures of the alloys Nb-12Ti-18Si-6Ta-2.5W-2Sn-2Ge -1Hf (JZ1) and Nb-12Ti-18Si-6Ta-2.5W-5Sn-5Ge-1Hf (JZ2) in the as cast and heat treated conditions were studied. The conclusions of this chapter were as follows:

1. Macrosegregation of Si existed in both alloys.
2. The microstructures in the top and bulk of the as cast alloys JZ1 and JZ2 consisted of primary Nb_5Si_3 surrounded by $Nb_5Si_3 + Nb_{ss}$ eutectic and Nb_{ss} with a small volume fraction of HfO_2. The Nb_5Si_3 existed in the β and α forms in both alloys.
3. The Nb_3Si formed in parts of the bottom of the ingot of JZ1-AC and the A15-Nb_3Sn in the bottom of the ingot of JZ2-AC owing to the higher Sn concentration which has a strong destabilising effect on the Nb_3Si and promotes the formation of the A15 phase.

4. After the heat treatment at 1500 ˚C for 100 h, the microstructure of the alloy JZ1 consisted of βNb_5Si_3, αNb_5Si_3, Nb_{ss} and HfO_2 and the microstructure of the alloy JZ2 consisted of βNb_5Si_3, αNb_5Si_3, Nb_{ss}, A15 phase and HfO_2. The $Nb_5Si_3 + Nb_{ss}$ eutectic microstrucure was unstable in the heat treated microstructures of both alloys.
5. Ti oxide formed in the heat treated microstructures near the surface areas of both alloys.

Chapter 4

Alloy with Al, Cr and Ta additions

4.1 The alloy Nb-12Ti-18Si-6Ta-2.5W-5Sn-5Ge-1Hf-5Al-5Cr (alloy JZ3): Results

The actual composition of the cast alloy (JZ3-AC) was 41.8Nb-12.4Ti-17.7Si-6Ta -2.7W-3.7Sn-4.8Ge-1Hf-4.7Al-5.2Cr. The concentration of Sn was lower after the arc melting, but the Si concentration was very close to the nominal one. Large area analyses (Table 4.2) showed macrosegregation of Si in JZ3-AC. The Si content varied from 15.3 at.% to 19.3 at.%. The XRD and EDS data (Figure 4.1 and Table 4.2) would suggest that the phases present in the microstructure of JZ3-AC were the Nb_5Si_3, A15-Nb_3X, C14-Cr_2Nb and HfO_2 and $Nb_{ss,}$ the existence of which in the ingot was only indicated by the EDS data. The XRD data showed the presence of both the β and αNb_5Si_3.

BSE images of the typical microstructure of JZ3-AC are shown in Figure 4.3. The microstructure in the top and bulk consisted of primary Nb_5Si_3 with A15 phase, Nb_{ss} and Laves phase in the interdendritic regions. The Nb_5Si_3 and the Laves phase exhibited similar contrast under BSE imaging. Ti enrichment was found both in the Nb_5Si_3 silicide and the A15 phase not only at the edge but also in the bulk of their grains. The concentrations of Al and Cr in the Nb_5Si_3 were as expected from previous research and the Si content in Nb_5Si_3 was slightly decreased due to the substitution of Al for Si. The contents of Si+Sn+Ge+Al in the Nb_5Si_3 and Ti-rich Nb_5Si_3 were 38.7 at.% and 36.6 at.%, respectively. The partitioning of the Ta and W into the A15 phase was enhanced compared with the alloy JZ2-AC and in the Ti-rich regions the solubility of Ta and W was decreased. The Ta+W content in the A15 and Ti-rich A15 phases were 16.3 at.% and 12.1 at.%, respectively. Furthermore, a Cr-rich A15 phase was observed in the C14-Cr_2Nb forming regions in the bulk, this was also rich in Ti, Si and Al but lean in Ta and W compared with the normal and Ti-rich A15 phase, see

Figure 4.3(d) and Table 4.2. The content of Si+Sn+Ge+Al in the Cr-rich A15 phase was 24.4 %, higher than those in the normal and Ti-rich A15 phases, which were 19.4 at.% and 19.5 at.%, respectively. The Nb_{ss} existed only with a very small volume fraction and was rich in Ti, Al and Cr. The Si content in the C14 Laves phase was 8.8 at.% Si and the Laves was lean in Sn and Ge. In the bottom of the ingot, the Nb_{ss} rich in Ta, W and Cr and lean in Si, Sn, Ge and Hf was observed. The volume fraction of the C14-Cr_2Nb in the bottom was lower than those in the top and bulk. In JZ3-AC the vol% of the A15 phase was about 27 % (Table 4.1).

The average composition of the alloy JZ3 after the heat treatment at 1500 ˚C for 100 hours (JZ3-HT) is given in Table 4.3. The chemical inhomogeneity of Si still existed. The microstructure had coarsened after the heat treatment and consisted of irregular large Nb_5Si_3 grains surrounded by A15 phase, Nb_{ss} (exhibiting white contrast and confirmed by EDS), C14-Cr_2Nb and HfO_2, see Table 4.3, Figures 4.2 and 4.4. The Nb_5Si_3 existed with both the β and α structures. Ti enrichment was only observed in the Nb_5Si_3 and was relatively more severe in some small Nb_5Si_3 grains adjacent to the Laves phase but was not found in the A15 phase. There were many tiny Nb_{ss} particles dispersed in Ti-rich regions in the large Nb_5Si_3 grains.

According to the EDS data, there was no noticeable change in the composition of the Nb_5Si_3 after the heat treatment. The Ti, Al and Cr contents in the A15 phase of JZ3-HT were increased and the Ta and W contents were decreased. The Si+Sn+Ge+Al and Ta+W contents in the A15 phase were 20.6 at.% and 12.4 at.%, respectively. The content of W in the Nb_{ss} of JZ3-HT was increased to 17 at.% and the Sn and Al contents were reduced by 1.1 at.% and 2.1 at.%, respectively. The Si content in the Laves phase was increased by 2.4 at.% and the Ti content was reduced by 4.8 at.% after the heat treatment. The contents of Hf in the Nb_{ss}, A15 phase and C14-Cr_2Nb Laves were reduced to zero due to the formation of HfO_2. The areas near the surface of specimen were contaminated by oxygen during the heat treatment and Ti oxide formed exhibiting black contrast, see Figures 4.2 and 4.4. The vol% of Nb_{ss} had

increased in JZ3-HT, as did the vol% of the A15 phase, see Table 4.1.

Table 4.1 Density of the as cast (AC) and % area of selected phases in the bulk of the as cast and heat treated (HT) alloys JZ3 and JZ3+.

Alloy	Density (g/cm^3)	Solid solution (%)	A15 (%)
JZ3-AC	7.94±0.01 7.93-7.96	-	26.8±2.3 24.2-28.8
JZ3-HT[a]	-	4.7±0.7 4.1-5.5	31.2±3.4 27.5-34.2
[JZ3+]-AC	7.54±0.01 7.53-7.55	-	13.3±0.3 12.9-13.5
[JZ3+]-HT[a]	-	1.2±0.2 1.1-1.4	13.9±0.9 12.9-14.6

[a] hafnia was counted in as its same contrast to the solid solution.

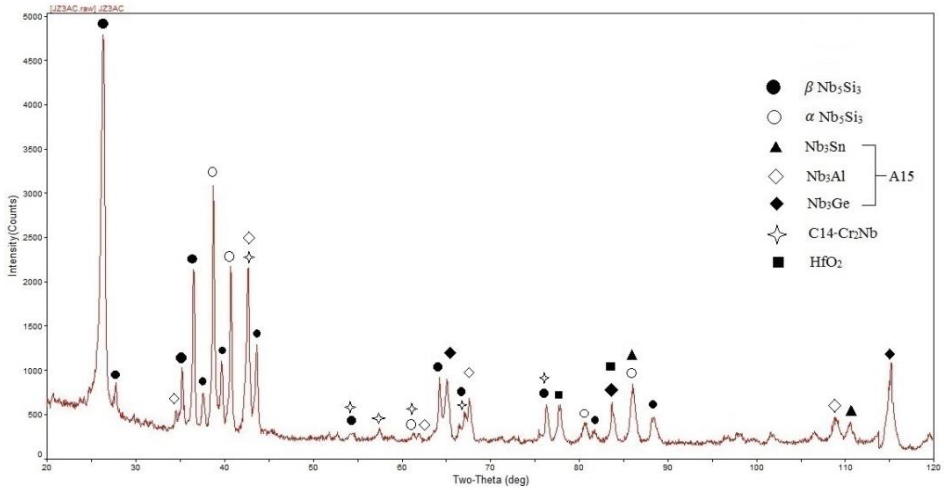

Figure 4.1 The X-ray diffractogram of the alloy JZ3-AC.

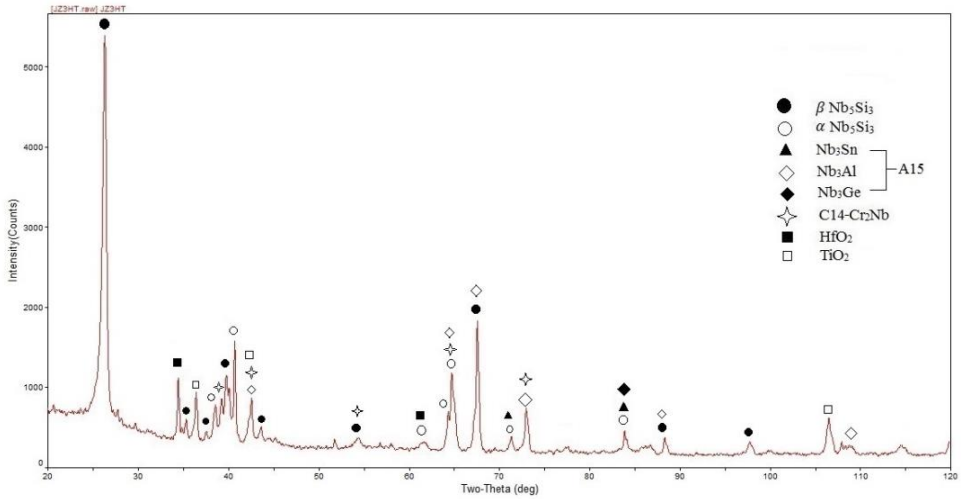

Figure 4.2 The X-ray diffractogram of the alloy JZ3-HT.

Table 4.2 The EDS analysis data (at.%) for the alloy JZ3-AC.

	Nb	Ti	Si	Ta	W	Sn	Ge	Hf	Al	Cr
Top[a]	41.7±0.6	12.9±0.7	17.1±1.5	6.2±0.5	2.9±0.4	3.4±0.3	4.7±0.6	1.0±0.1	4.6±0.4	5.5±1.0
	41.0-42.5	12.2-13.9	15.3-18.8	6.0-6.5	2.5-3.3	2.9-3.5	4.0-5.6	0.9-1.2	4.1-5.1	4.6-6.7
Bulk[a]	41.5±0.7	12.2±0.4	18.5±1.3	5.9±0.5	2.7±0.5	3.5±0.3	4.9±0.4	1.1±0.1	4.7±0.4	5.0±0.5
	40.6-42.4	11.8-12.9	16.4-19.3	5.2-6.5	2.3-3.6	3.1-4.0	4.6-5.5	0.9-1.2	4.3-5.2	4.3-5.5
Bottom[a]	41.8±0.3	12.5±0.3	16.9±1.1	5.9±0.3	2.7±0.2	4.2±0.4	4.7±0.3	1.0±0.2	4.9±0.3	5.4±0.4
	41.0-41.9	12.0-12.7	15.9-18.3	5.6-6.3	2.4-2.9	3.7-4.8	4.1-5.1	0.7-1.2	4.6-5.4	5.0-5.9
Nb_{ss}[b]	26.4±2.4	31.4±1.9	2.4±1.2	3.6±0.3	1.5±0.1	3.5±0.8	1.2±0.3	2.3±0.5	8.6±1.6	19.1±5.3
	22.9-28.8	29.0-33.2	1.6-4.4	3.2-4.0	1.3-1.6	2.2-4.4	0.9-1.5	1.8-3.0	6.3-10.0	14.1-26.9
Nb_{ss}[c]	40.6±0.7	14.1±0.7	2.9±1.1	10.4±0.5	10.9±1.0	2.5±0.1	0.5±0.1	0.3	5.6±0.5	12.2±0.4
	39.5-41.1	13.4-15.0	1.0-3.6	9.9-11.2	9.4-12.3	2.4-2.5	0.3-0.6		5.1-6.3	11.7-12.8
Nb_5Si_3	42.6±0.4	9.5±0.3	27.8±1.5	6.0±0.2	1.2±0.1	1.5±0.3	6.6±0.3	0.6±0.3	2.8±0.6	1.4±0.1
	42.3-43.1	9.2-9.9	26.2-29.8	5.8-6.2	1.0-1.4	1.2-1.9	6.2-7.0	0.3-1.0	2.3-3.5	1.1-1.5
Ti-rich Nb_5Si_3	37.3±2.3	15.9±1.9	23.1±1.6	4.5±0.4	0.6±0.1	2.0±0.1	6.9±0.1	1.6±0.5	4.6±0.2	3.5±1.4
	34.4-39.7	14.1-18.8	20.5-24.8	4.0-5.0	0.3-0.7	1.9-2.1	6.7-7.1	1.1-2.3	4.3-4.8	2.5-5.8
A15 phase	50.9±0.2	9.5±0.3	5.2±0.7	9.2±0.2	7.1±0.2	7.3±0.2	2.2±0.6	0.5±0.1	4.7±0.4	3.4±0.2
	50.6-51.1	9.1-9.9	4.5-6.2	9.0-9.5	6.8-7.2	7.1-7.7	1.7-3.1	0.3-0.6	4.2-5.2	3.1-3.7
Ti-rich A15	45.3±0.4	15.4±0.2	4.2±0.3	7.2±0.3	4.9±0.2	7.0±0.2	1.7±0.2	0.6±0.1	6.5±0.2	7.2±0.3
	45.0-46.0	15.0-15.6	3.8-4.5	6.8-7.4	4.7-5.1	6.8-7.2	1.6-2.0	0.4-0.8	6.2-6.8	6.7-7.5
Cr-rich A15[c]	26.8±1.1	25.6±1.2	9.8±2.4	3.2±0.5	1.0±0.4	3.0±0.4	4.3±1.4	2.6±0.3	7.2±0.7	16.5±3.2
	25.2-29.2	23.5-27.4	6.5-13.3	2.8-3.6	0.6-1.2	2.5-3.3	2.9-6.7	2.1-3.1	6.2-8.3	12.2-21.9
C14-Cr_2Nb	20.1±0.3	9.0±0.7	8.8±1.1	6.4±0.4	3.2±0.2	0.3±0.1	1.1±0.1	1.7±0.1	4.6±0.2	44.8±0.6
	19.8-20.5	8.2-10.0	7.0-9.9	5.8-6.9	2.9-3.4	0.1-0.4	1.0-1.2	1.6-1.9	4.3-4.8	44.0-45.6

[a] Large area analysis.

[b] Solid solution rich in Ti and Cr and present in the top and bulk (very small vol%).

[c] Solid solution present in the bottom.

[d] A15 phase rich in Ti and Cr present in the bulk.

Table 4.3 The EDS analysis data (at.%) for the alloy JZ3-HT.

	Nb	Ti	Si	Ta	W	Sn	Ge	Hf	Al	Cr
Large area	41.7±0.4	12.8±0.1	18.3±1.0	5.7±0.4	2.5±0.2	3.4±0.5	5.2±0.2	0.8±0.2	4.8±0.1	4.8±0.3
	41.2-42.2	12.7-12.8	16.8-19.4	5.4-6.3	2.2-2.7	2.8-2.9	5.0-5.4	0.5-1.1	4.5-4.9	4.3-5.1
Nb_{ss}	43.1±0.5	9.2±0.3	2.1±1.0	12.4±0.4	17.0±0.2	1.4±0.1	0.3	0	3.5±0.1	11.0±0.2
	42.5-43.4	8.8-9.6	1.2-3.3	11.9-12.8	16.0-17.3	1.3-1.6			3.4-3.6	10.7-11.1
Nb_5Si_3	41.8±0.5	9.4±0.6	28.5±1.0	5.7±0.3	1.2±0.2	1.2±0.1	6.2±0.2	0.7±0.1	2.7±0.4	2.6±0.4
	41.1-42.5	8.9-10.2	27.6-29.8	5.4-6.0	0.9-1.4	1.1-1.4	6.0-6.4	0.6-0.7	2.3-3.4	2.1-3.1
Ti-rich Nb_5Si_3	37.4±3.3	16.2±3.4	25.2±0.9	4.2±0.5	0.3	1.4±0.7	7.1±0.4	0.7±0.5	4.7±0.5	2.8±0.1
	33.6-40.2	13.4-20.0	24.3-26.4	3.4-4.8		0.6-2.1	6.5-7.6	0.3-1.6	4.3-5.3	2.6-2.9
A15 phase	49.1±0.4	11.9±0.2	5.2±0.6	7.1±0.3	5.3±0.1	8.0±0.2	1.6±0.2	0	5.9±0.1	5.9±0.2
	48.4-49.5	11.7-12.2	4.6-6.0	6.7-7.4	5.2-5.4	7.7-8.2	1.4-1.9		5.7-6.0	5.6-6.2
C14-Cr_2Nb	20.3±0.3	4.2±0.1	11.2±0.5	8.2±0.2	4.0±0.1	0.2	0.8±0.1	0	3.0±0.2	48.1±0.3
	19.8-20.7	4.1-4.4	10.6-11.2	7.9-8.5	3.8-4.1		0.6-0.9		2.8-3.3	47.7-48.4

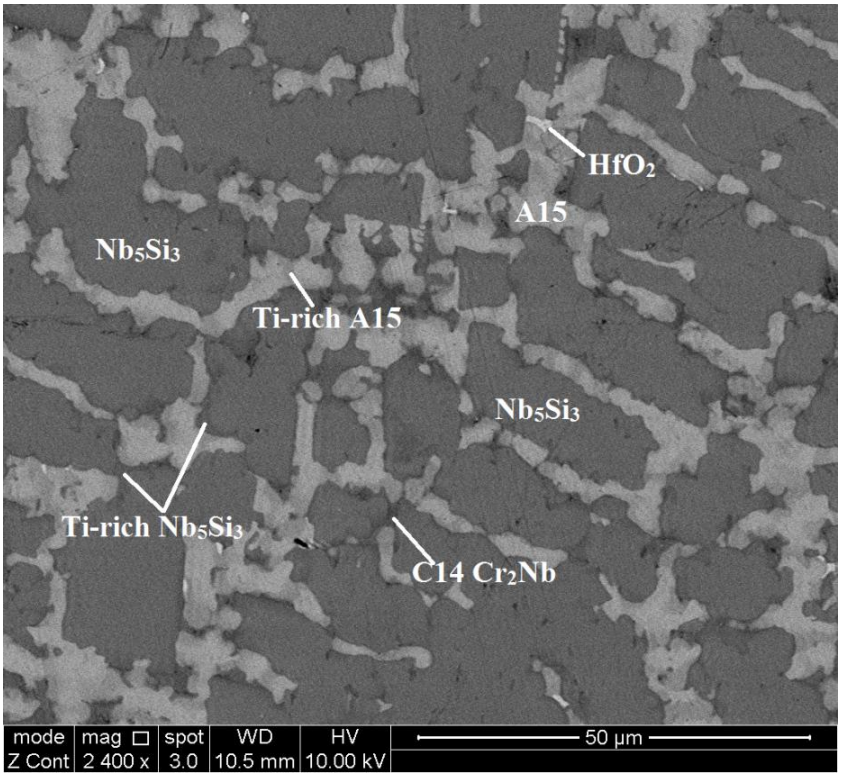
HfO2
A15
Nb5Si3
Ti-rich A15
Nb5Si3
Ti-rich Nb5Si3
C14 Cr2Nb
mode mag spot WD HV
Z Cont 2 400 x 3.0 10.5 mm 10.00 kV
50 µm

(a)

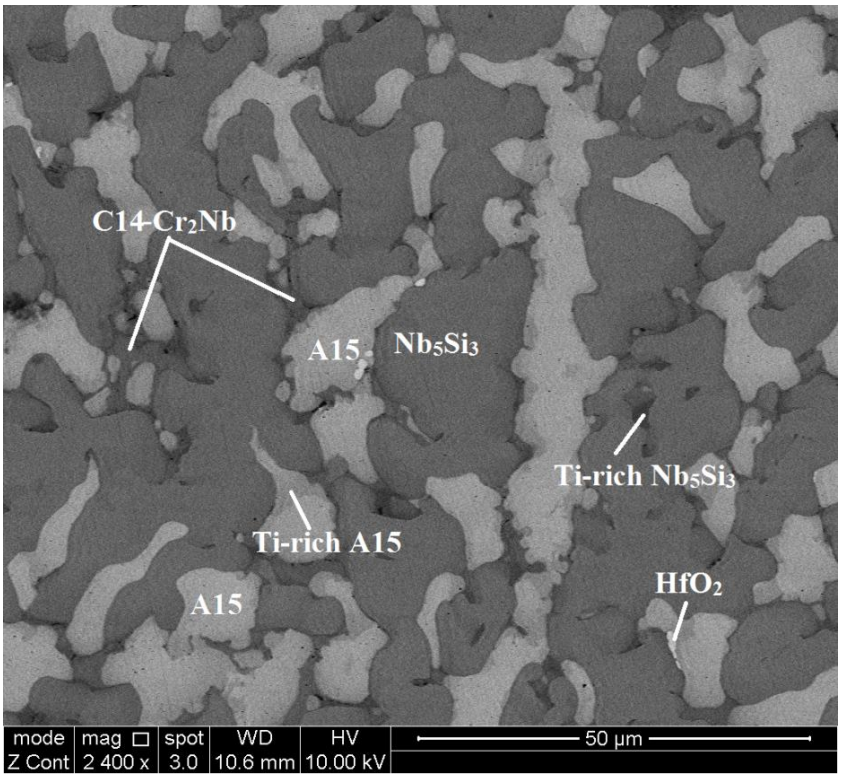
C14-Cr2Nb
A15
Nb5Si3
Ti-rich Nb5Si3
Ti-rich A15
A15
HfO2
mode mag spot WD HV
Z Cont 2 400 x 3.0 10.6 mm 10.00 kV
50 µm

(b)

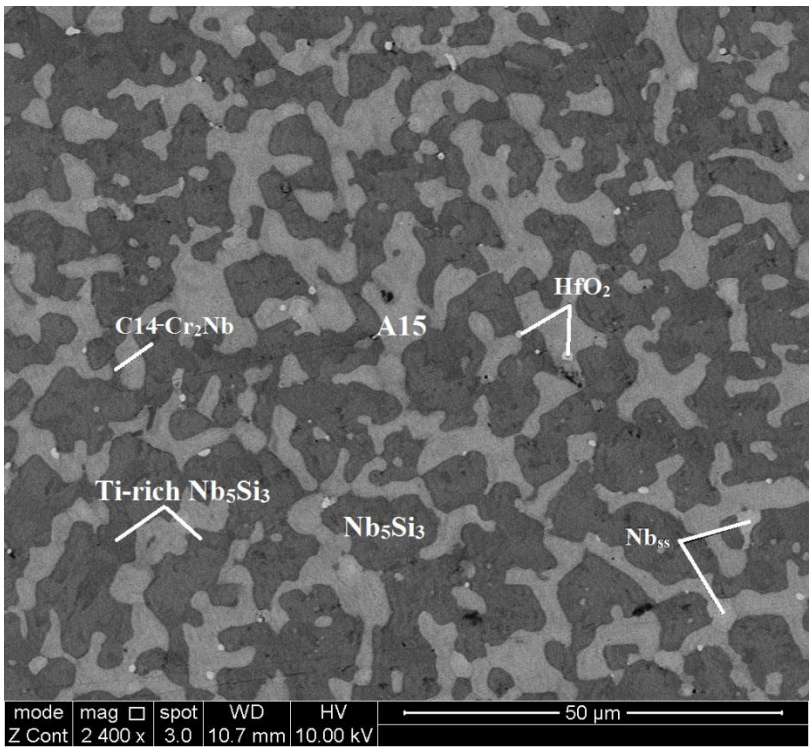

(c)

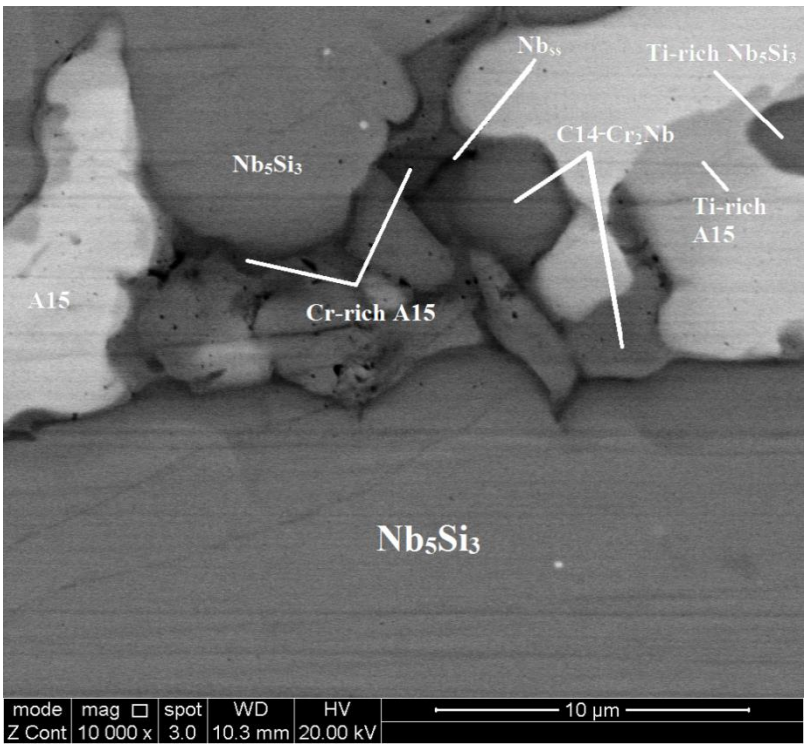

(d)

Figure 4.3 BSE images of the microstructure of the alloy JZ3-AC in the (a) top, (b) bulk, (c) bottom and (d) bulk at high magnification.

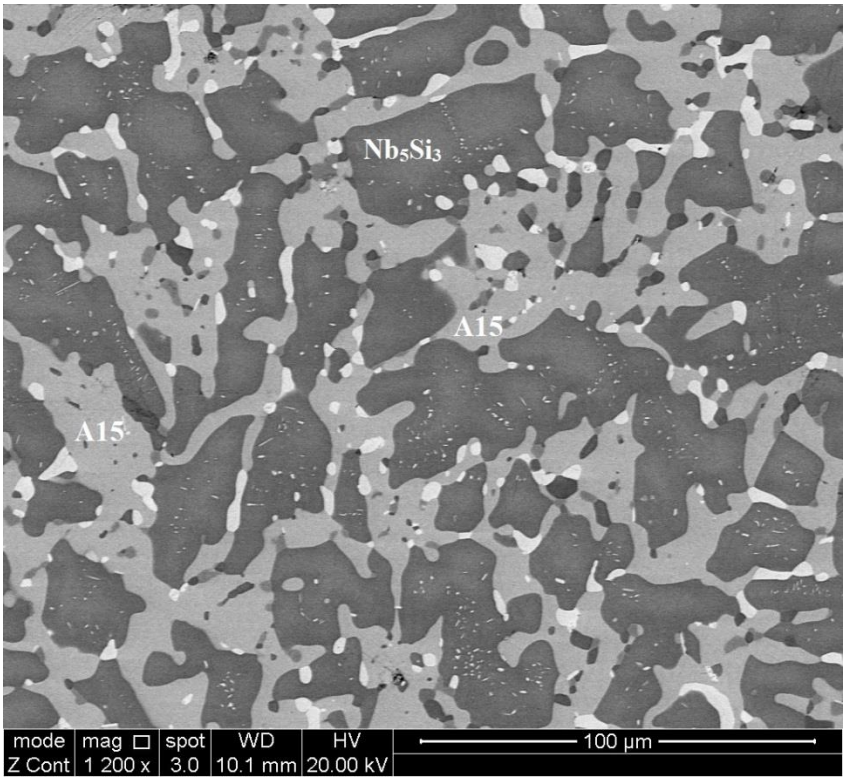
Nb5Si3
A15
A15
mode mag spot WD HV
Z Cont 1 200 x 3.0 10.1 mm 20.00 kV
100 µm

(a)

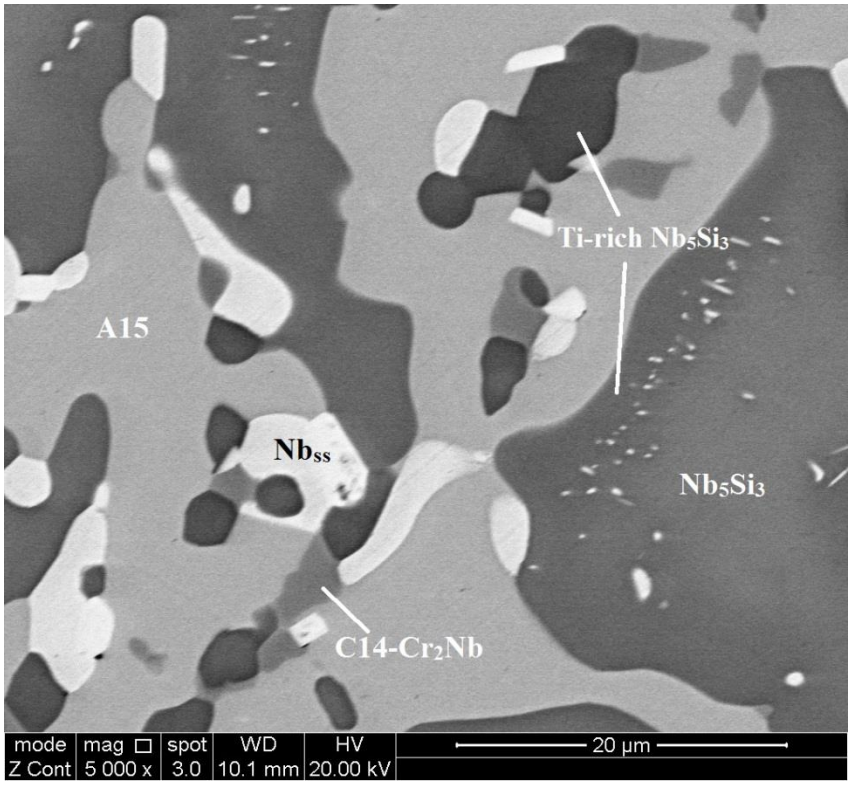
Ti-rich Nb5Si3
A15
Nbss
Nb5Si3
C14-Cr2Nb
mode mag spot WD HV
Z Cont 5 000 x 3.0 10.1 mm 20.00 kV
20 µm

(b)

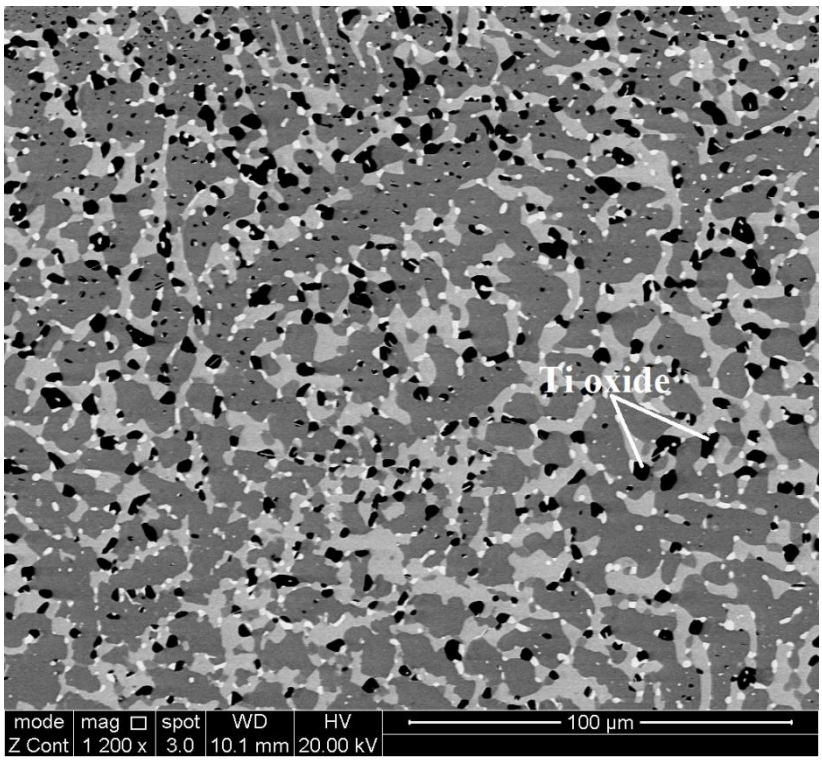

(c)

Figure 4.4 BSE images of the microstructure of the alloy JZ3-HT (a) and (b) in the bulk and (c) below the surface.

4.2 The alloy Nb-12Ti-18Si-6Ta-2.5W-7.5Sn-5Ge-1Hf-5Al-5Cr (alloy JZ3+): Results

The actual composition of the cast alloy ([JZ3+]-AC) was 38.7Nb-12.4Ti-19.7Si -5.7Ta-2.3W-5.7Sn-4.9Ge-0.8Hf-4.6Al-5.2Cr. The ratio Sn/Ge=1 was almost achieved due to the Sn loss in the ingot preparation. Large area analyses (Table 4.4) showed that the macrosegration of Si was reduced slightly and the minimum and maximum concentrations of Si were 17.7 at.% and 20.8 at.%, respectively. On the basis of the XRD and EDS data (Figure 4.5 and Table 4.4), the phases in the cast microstructure were the Nb_5Si_3, A15-Nb_3X, C14-Cr_2Nb, HfO_2 and $(Nb,W)_{ss}$ that only formed in the bottom of the ingot. The XRD data showed that the Nb_5Si_3 existed both in the β and α forms.

The microstructures in the top and bulk of [JZ3+]-AC were slightly coarser than those

of the alloy JZ3-AC, see Figure 4.7(a) and (b), and consisted of the A15 phase and C14-Cr_2Nb Laves that were present between grains of primary Nb_5Si_3. The volume fraction of the A15 phase was lower than that in the alloy JZ3-AC, see Table 4.1. The Ti segregation in the Nb_5Si_3 and A15 phase was more severe compared with the alloy JZ3-AC. The composition of the Nb_5Si_3 was almost identical to that in JZ3-AC with higher concentrations of Si and Al. It should be noticed that the Si content in the Ti-rich Nb_5Si_3 of [JZ3+]-AC was only 14.3 at.% while the Sn solubility was increased to 9.5 at.%, which was not observed in the first three cast alloys. This was attributed to the high addition of the Sn which probably made the further substitution of Sn for Si possible and the fact that Ti and Si form Ti_5Si_3 that has a prototype Mn_5Sn_3, which is the prototype of hexagonal Ti_5Si_3 and γNb_5Si_3. However, in the Sn-rich (and Ti-rich) Nb_5Si_3 the ratio Nb/Ti+Hf was greater than one, meaning the 5-3 silicide was tetragonal, as confirmed by XRD. The concentrations of Si+Sn+Ge+Al in the normal and Ti-rich Nb_5Si_3 were 39.3 at.% and 37.3 at.%, respectively. The Sn contents in the normal and Ti-rich A15 phases were increased with decreased solubility of Si, Ge, Ta and W, compared with the alloy JZ3-AC. The Si+Sn+Ge+Al contents in the A15 and Ti-rich A15 phase were 21.8 at.% and 22.7 at.%, respectively and the contents of Ta+ W were 15.2 at.% and 8.9 at.%, respectively. There was no obvious change in the composition of the C14-Cr_2Nb except of slight changes in the contents of Ti, W and Al.

The microstructure of the bottom of the ingot was slightly different from those of the top and bulk. In the bottom of the ingot, the phase in white contrast could be the $(Nb,W)_{ss}$ solid solution or HfO_2 according to the EDS spot analyses. The $(Nb,W)_{ss}$ exhibited a high Ta solubility of 15.2 at.% while the Si content was relatively low at 1.7 at.%, compared with the Nb_{ss} of the first three cast alloys and other Sn or Ta containing alloys studied in our research group.

The average composition of the alloy JZ3+ after the heat treatment at 1500 ˚C for 100 hours ([JZ3+]-HT) is given in Table 4.5. There was still chemical inhomogeneity of

Si. BSE images of the microstructure of the heat treated specimen are given in Figure 4.8. The XRD data showed the presence of both the β and αNb_5Si_3, see Figure 4.6. No Ti enrichment was found in the large Nb_5Si_3 grains but some small Nb_5Si_3 grains rich in Ti were observed adjacent to the Laves phase. The $(Nb,W)_{ss}$ was observed adjacent to large 5-3 silicide grains, which was also dispersed in large Nb_5Si_3 grains in the form of small particles. The volume fractions of the A15 and solid solution in the alloy [JZ3+]-HT were lower than those in JZ3-HT, see Table 4.1.

According to the EDS data (Table 4.5), there were small changes in the Ti, Ta, W and Cr contents in the Nb_5Si_3 while the Si content was reduced to 23.8 at.% together with the increases in the contents of Sn and Al after the heat treatment. In Ti-rich Nb_5Si_3 grains the Si content was slightly higher with deceased Sn content and the Hf content was increased to 3.2 at.% compared with the normal 5-3 silicide. The contents of Si+Sn+Ge+Al in the normal and Ti-rich Nb_5Si_3 were 38.3 at.% and 38.4 at.%, respectively. In the A15 phase the Si content was reduced to 2.8 at.% and the Sn content was increased to 12.2 at.%. The contents of Si+Sn+Ge+Al and Ta + W in the A15 phase were 20.4 at.% and 14.7 at.%, respectively. The W solubility of the $(Nb,W)_{ss}$ was increased by 4.5 at.% after the heat treatment and some grains with no Si were found. No contamination was observed in the alloy JZ3+ after the heat treatment.

Table 4.4 The EDS analysis data (at.%) for the alloy [JZ3+]-AC.

	Nb	Ti	Si	Ta	W	Sn	Ge	Hf	Al	Cr
Top[a]	39.2±0.7	12.5±0.2	20.0±1.0	5.6±0.4	2.1±0.3	5.0±0.3	5.1±0.1	0.8±0.1	4.6±0.3	5.1±0.4
	38.0-39.8	12.1-12.7	18.3-20.6	5.0-6.0	1.9-2.6	4.6-5.2	4.9-5.3	0.6-1.0	4.3-5.1	4.5-5.6
Bulk[a]	39.8±0.3	12.3±0.4	19.1±0.9	5.8±0.3	2.6±0.3	5.3±0.4	4.6±0.2	0.8±0.1	4.5±0.2	5.2±0.2
	39.3-40.1	11.9-12.8	17.7-19.9	5.6-6.0	2.2-3.1	4.6-5.8	4.5-5.0	0.7-0.9	4.3-4.7	4.9-5.2
Bottom[a]	37.7±0.4	12.6±0.2	20.1±0.7	5.6±0.1	2.2±0.3	6.0±0.3	4.8±0.1	0.9±0.1	4.7±0.2	5.4±0.7
	37.4-38.0	12.2-12.8	19.0-20.8	5.4-5.7	2.0-2.8	5.7-6.3	4.7-5.0	0.8-1.0	4.5-5.0	4.9-6.4
$(Nb,W)_{ss}$[b]	31.2±1.5	4.9±0.3	1.7±1.3	15.2±0.2	35.3±1.4	1.8±0.2	0.3±0.3	0.1±0.1	2.4±0.2	7.1±0.5
	29.4-32.8	4.5-5.3	0.6-3.6	14.8-15.5	33.8-37.5	1.5-2.1	0.0-0.8	0.0-0.3	2.1-2.7	6.3-7.5
Nb_5Si_3	42.0±0.3	9.2±0.2	30.6±0.6	6.3±0.2	1.3±0.1	1.3±0.0	5.5±0.2	0.5±0.1	1.9±0.1	1.4±0.2
	41.7-42.3	8.9-9.4	29.8-31.3	6.1-6.6	1.3-1.4	1.2-1.5	5.2-5.6	0.4-0.7	1.8-2.0	1.2-1.6
Ti-rich Nb_5Si_3	32.7±2.0	21.4±3.0	16.7±2.0	2.9±0.4	0.4±0.1	8.1±0.9	5.3±0.5	1.6±0.2	7.3±1.1	3.6±0.3
	29.4-34.1	18.6-26.2	14.3-19.4	2.3-3.3	0.3-0.6	7.3-9.5	4.6-5.7	1.4-1.8	6.5-9.1	3.0-3.9
A15 phase	46.3±0.4	11.3±0.2	5.2±0.5	7.8±0.3	7.3±0.2	10.4±0.2	1.3±0.1	0.3±0.1	4.8±0.0	5.3±0.4
	45.4-46.6	11.1-11.6	4.5-5.6	7.4-8.1	7.0-7.6	10.0-10.7	1.2-1.5	0.2-0.5	4.8-4.9	5.0-5.9
Ti-rich A15	39.9±01.9	19.3±3.5	2.8±0.5	4.9±0.3	4.0±1.1	12.6±0.9	0.9±0.2	0.5±0.2	6.4±0.6	8.7±1.0
	37.3-42.2	13.9-23.3	2.1-3.2	4.1-7.0	3.1-5.9	11.2-13.5	0.6-1.2	0.3-0.8	5.7-6.9	7.8-9.8
C14-Cr_2Nb	20.5±0.6	6.6±0.6	8.7±0.5	6.9±0.5	4.4±0.5	0.6±0.2	1.0±0.1	1.1±0.1	6.0±0.6	44.2±0.7
	20.0-21.4	5.8-7.2	8.2-9.5	6.3-7.7	3.9-5.1	0.3-0.8	0.9-1.1	1.1-1.2	5.2-6.7	43.5-45.1

[a] Large area analysis.

[b] Solid solution only formed in the bottom, very rich in W and XRD data suggested the presence of $(Nb_{0.5},W_{0.5})_{ss}$.

Table 4.5 The EDS analysis data (at.%) for the alloy [JZ3+]-HT.

	Nb	Ti	Si	Ta	W	Sn	Ge	Hf	Al	Cr
Large area	39.3±0.3	12.3±0.2	20.7±1.1	5.7±0.2	2.0±0.3	4.8±0.3	5.1±0.1	0.8±0.1	4.6±0.3	4.7±0.2
	39.1-39.9	12.2-12.5	19.4-21.9	5.5-6.0	1.7-2.3	4.5-5.1	5.0-5.2	0.6-0.8	4.2-4.9	4.4-4.9
$(Nb,W)_{ss}$	29.9±0.7	3.9±0.4	1.9±0.1.3	15.1±0.6	39.8±0.6	0.4±0.2	0.1±0.1	0.2±0.1	1.5±0.2	7.1±0.4
	29.0-30.8	3.4-4.3	0.0-3.1	14.3-16.0	38.8-40.2	0.3-0.7	0.0-0.2	0.0-0.4	1.4-1.8	6.7-7.4
Nb_5Si_3	39.2±0.4	13.0±0.2	23.8±0.9	4.9±0.3	0.8±0.1	4.2±0.2	5.6±0.2	0.9±0.1	4.6±0.3	3.0±0.2
	38.5-39.6	12.7-13.3	22.7-25.0	4.6-5.3	0.7-1.0	3.9-4.4	5.4-5.9	0.7-1.0	4.2-5.0	2.9-3.4
Ti-rich Nb_5Si_3	34.2±0.2	16.0±0.5	25.5±0.9	4.9±0.5	0.5±0.1	1.3±0.5	6.5±0.3	3.2±0.4	5.1±0.2	2.8±0.2
	33.8-34.5	15.4-16.6	24.0-26.4	4.4-5.6	0.4-0.6	1.0-2.2	6.2-6.9	2.5-3.6	4.8-5.3	2.6-3.1
A15 phase	48.0±0.4	11.6±0.2	2.8±0.6	8.2±0.2	6.5±0.2	12.2±0.3	0.8±0.2	0.1±0.1	4.7±0.1	5.1±0.3
	47.6-48.9	11.4-11.8	1.8-3.5	8.0-8.5	6.3-6.9	11.9-12.6	0.6-1.0	0.0-0.2	4.7-4.9	4.9-5.5
C14-Cr_2Nb	19.2±0.6	3.4±0.3	11.4±0.3	9.6±0.2	5.2±0.3	0.4±0.3	0.7±0.1	0.5±0.1	3.1±0.2	46.5±1.2
	18.7-20.3	3.1-3.7	11.2-11.9	9.4-9.8	4.7-5.3	0-0.7	0.6-0.9	0.3-0.5	2.8-3.4	44.7-48.1

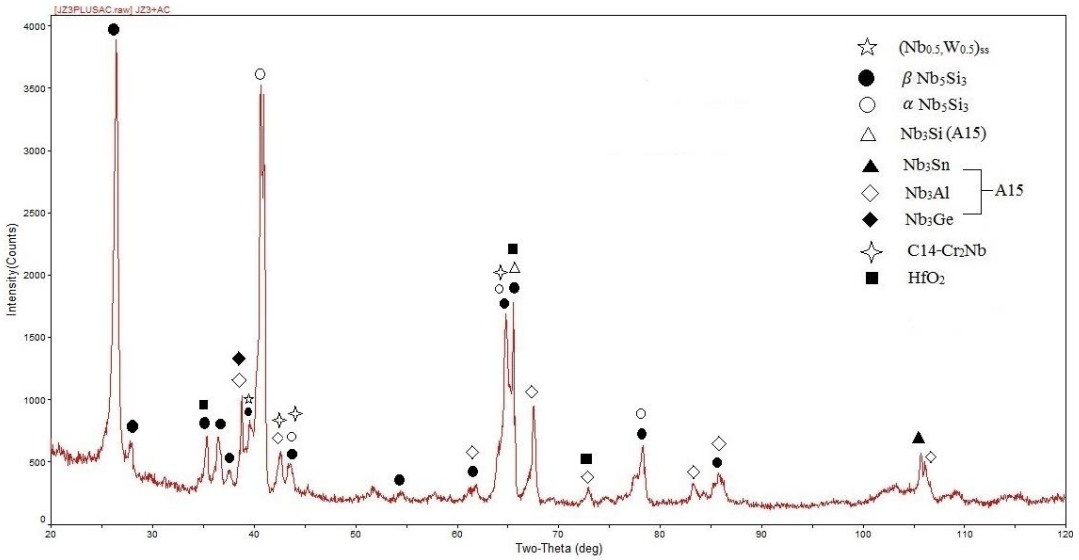

Figure 4.5 The X-ray diffractogram of the alloy [JZ3+]-AC.

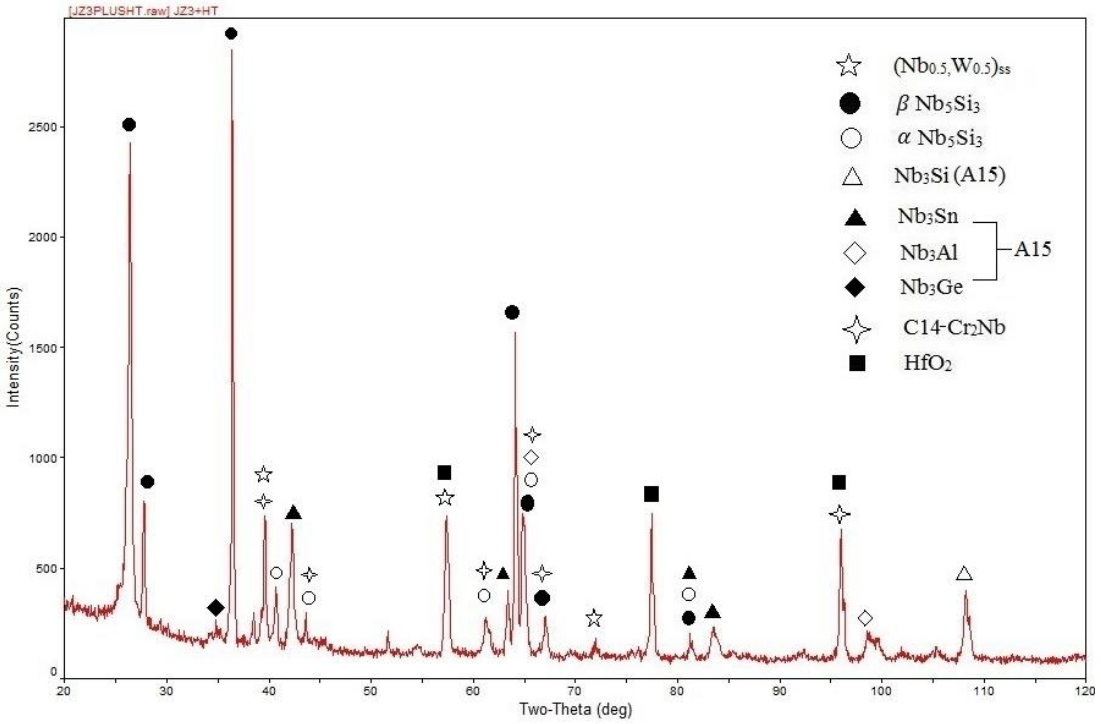

Figure 4.6 The X-ray diffractogram of the alloy [JZ3+]-HT.

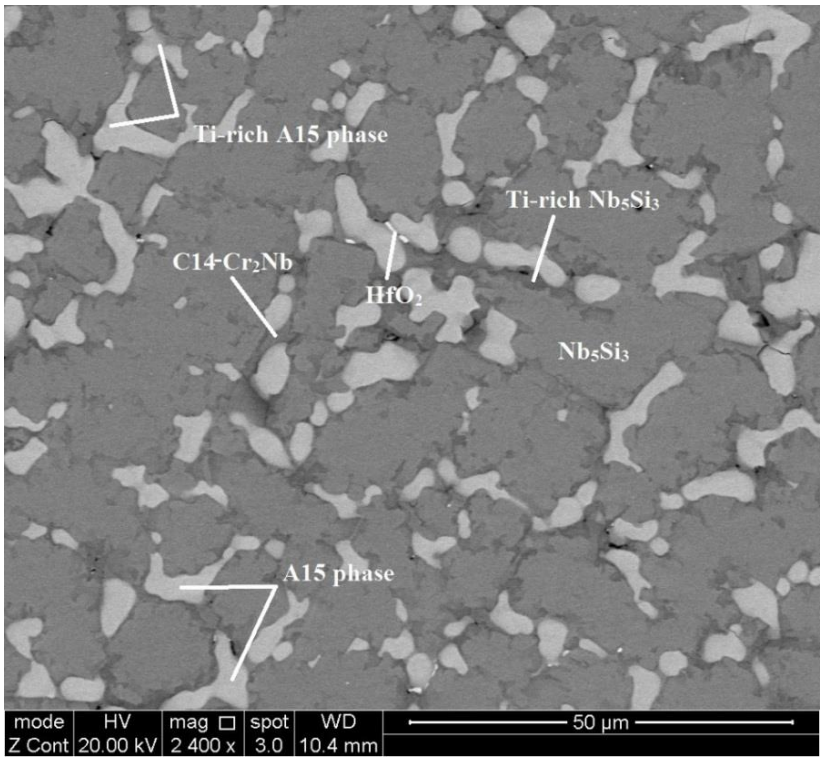
Ti-rich A15 phase
Ti-rich Nb_5Si_3
C14-Cr_2Nb
HfO_2
Nb_5Si_3
A15 phase
mode HV mag spot WD
Z Cont 20.00 kV 2 400 x 3.0 10.4 mm
50 µm

(a)

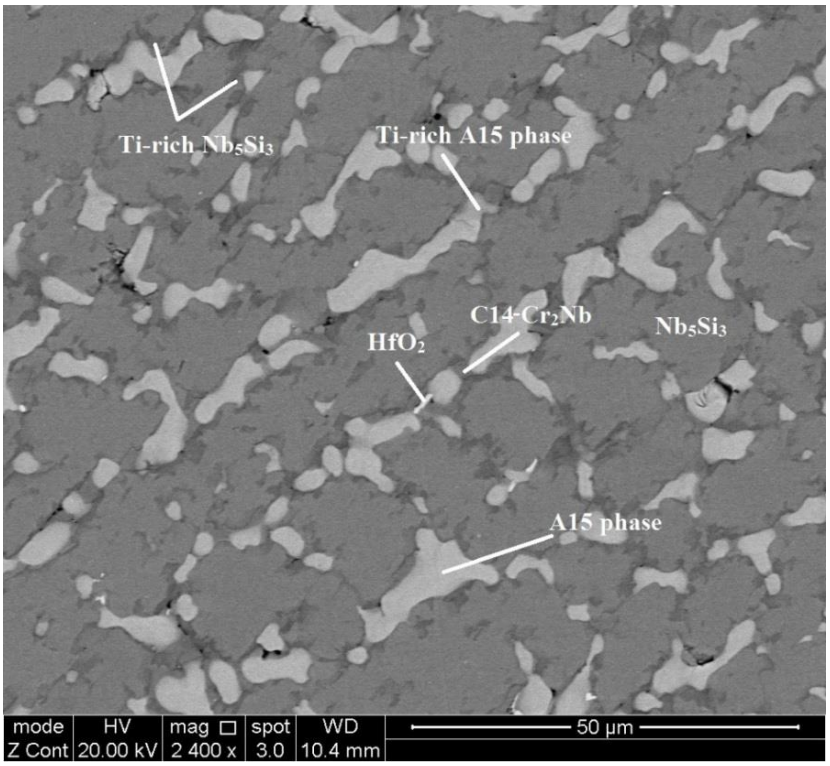
Ti-rich Nb_5Si_3
Ti-rich A15 phase
C14-Cr_2Nb
HfO_2
Nb_5Si_3
A15 phase
mode HV mag spot WD
Z Cont 20.00 kV 2 400 x 3.0 10.4 mm
50 µm

(b)

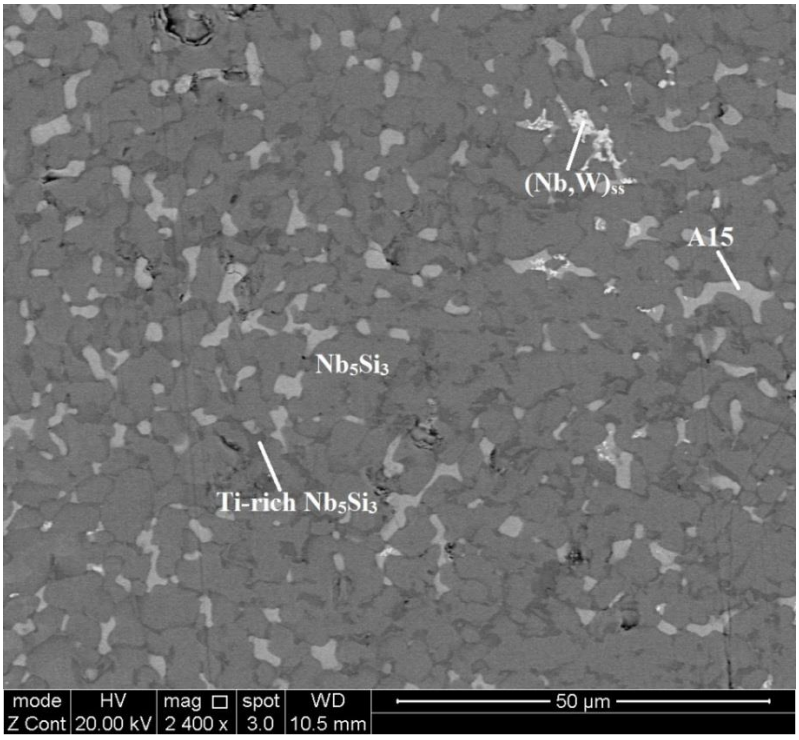

(c)

Figure 4.7 BSE images of the microstructure of the alloy [JZ3+]-AC in the (a) top, (b) bulk and (c) bottom.

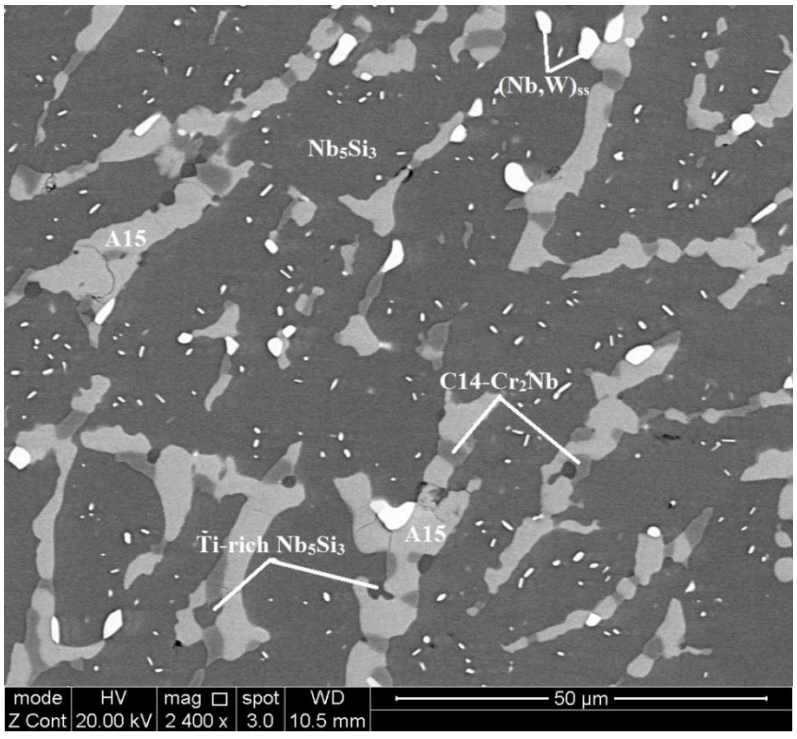

(a)

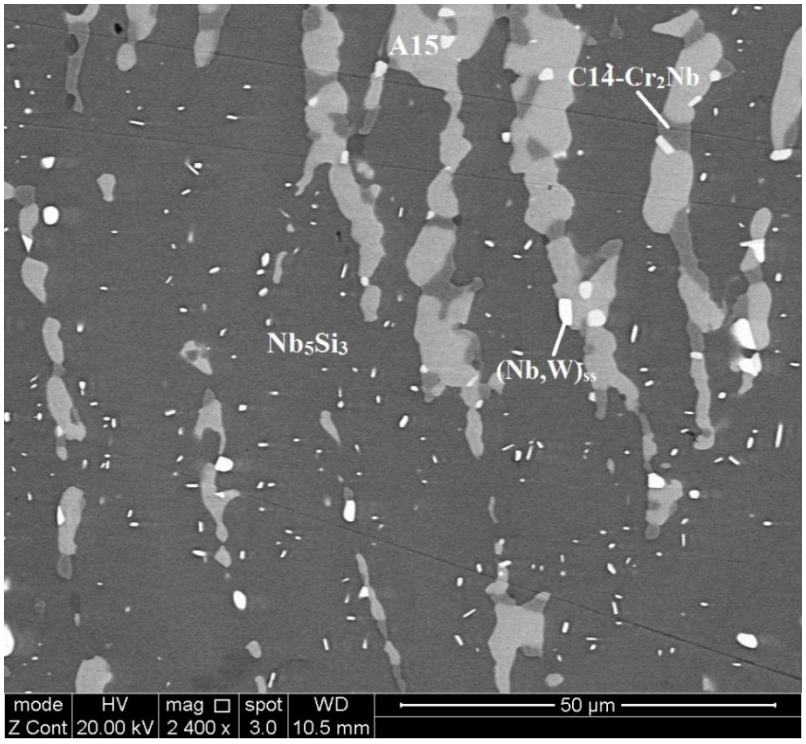

(b)

Figure 4.8 BSE images of the microstructure of the alloy [JZ3+]-HT (a) in the bulk and (b) below the surface.

4.3 Discussion

Similar to the alloys JZ1 and JZ2, there was Sn loss in the preparation of the alloys JZ3 and JZ3+ because of the evaporation of Sn during the arc melting. There was macrosegregation of Si with MACSi of 4 at.% and 3.1 at.%, respectively in JZ3 and JZ3+. The predicted MACSi values using the group's alloy design methodology were 6.1 and 6.4 at.% for the alloys JZ3 and JZ3+, respectively.

In the alloy JZ3 the addition of Al and Cr and the increase in the concentrations of Ge and Sn resulted to a dramatic change in the microstructure as the Nb_{ss} + Nb_5Si_3 eutectic was completely suppressed. Previous research in the group on Nb-Si-Ti-Al-Cr-Ge and Nb-Si-Ti-Al-Cr-Sn alloys with similar Si concentration (but with no refractory metal additions) has shown that Ge did not completely suppress the Nb_{ss} + Nb_5Si_3 eutectic (Li 2012) but Sn did and with the latter element microstructure

architectures similar to those in figure 4.3 were formed (Xu and Tsakiropoulos 2016). Thus, the increased Sn concentration in the alloy JZ3 and the addition of Sn (and to a lesser extent that of Ge) with Al and Cr were the reasons for the different microstructures seen in the alloy JZ3. Owing to the higher concentration of Sn in the alloy JZ3 the A15 compound based on the Nb_3Sn was expected to be stable in the microstructure. This was confirmed by the experimental results. In the alloy JZ3, as the primary Nb_5Si_3 formed the surrounding melt became richer in Al, Cr, Sn, Ti and W owing to the partitioning of these solutes (Zelenitsas and Tsakiropoulos 2005, 2006, Vellios and Tsakiropoulos 2007, Grammenos and Tsakiropoulos 2010). Between the Nb_5Si_3 dendrites the A15, Laves and Nb_{ss} phases formed.

The solutes Al, Cr, Ge, Si and Sn can form the A15 compounds Nb_3Al, Nb_3Ge, Nb_3Si (metastable), Nb_3Sn, Cr_3Si and Cr_3Ge. The Ti_3Sn is not an A15 compound (DO_{19} structure). Ti however can substitute Nb in A15 compounds. Nb forms the C14-Cr_2Nb Laves phase as do Hf, Ta and Ti that form $HfCr_2$, $TaCr_2$ and $TiCr_2$ Laves phases, respectively. If we consider the melting temperatures of the aforementioned A15 compounds and of the Nb_{ss} in the top and bulk (Nb_{ss}^{b} in Table 4.2) and that the phase with the highest melting temperature should form first, then the ranking is Nb_3Sn (2130 ˚C), Nb_3Al (2060 ˚C), Nb_3Ge (1900 ˚C), Nb_{ss}^{b} (1866 ˚C), Cr_2Nb (1730 ˚C). Thus, in the melt surrounding the Nb_5Si_3 the A15 phase formed first followed by the Nb_{ss}^{b} and then the C14-Cr_2Nb Laves phase that formed in the last to solidify Cr rich melt (Zelenitsas and Tsakiropoulos 2005). As the A15 compound formed the surrounding melt became richer in Ti, Si, Ge, Cr and poorer in Sn, Ta, W and Ti rich A15 and Cr rich A15 formed, which made the melt rich in Ge and Si, and poor in Ti, Al, Cr, Hf, Sn and then the Nb_{ss}^{b} formed making the surrounding melt rich in Si, Ta, W, Ge and poor in Ti, Hf, Al, Cr. Thus, it is suggested that in the top and bulk of the alloy JZ3-AC the solidification path was $L \rightarrow L + \beta Nb_5Si_3 \rightarrow L + \beta Nb_5Si_3 + A15 \rightarrow L + \beta Nb_5Si_3 + A15 + Nb_{ss}^{b} \rightarrow \beta Nb_5Si_3 + A15 + Nb_{ss}^{b} +$ C14-Cr_2Nb. The formation of αNb_5Si_3 occurred from the solid state transformation $\beta Nb_5Si_3 \rightarrow \alpha Nb_5Si_3$, as discussed for the alloys JZ1-AC and JZ2-AC.

In the bottom of JZ3-AC the vol% of the C14-Cr_2Nb Laves phase was reduced and there was also formation of a Cr, Ta and W rich solid solution (Nb_{ss}^c in Table 4.5) that exhibited brighter contrast than the solid solutions in the alloys JZ1 and JZ2 under BSE imaging, owing to the atomic numbers of Ta and W. If we consider the melting temperatures of the aforementioned A15 compounds and of the Nb_{ss} in the bottom (Nb_{ss}^c in Table 4.2) and that the phase with the highest melting temperature should form first, then the ranking is Nb_{ss}^c (2255 ˚C), Nb_3Sn (2130 ˚C), Nb_3Al (2060 ˚C), Nb_3Ge (1900 ˚C), Cr_2Nb (1730 ˚C). Thus, in the bottom of the alloy JZ3 in the melt surrounding the Nb_5Si_3 the Nb_{ss}^c formed first, and then the A15 phase followed by the C14-Cr_2Nb Laves phase that formed in the last to solidify Cr rich melt. As the Nb_{ss}^c was rich in Cr, Ta and W (all three elements are constituents of the $NbCr_2$ Laves phase, see Table 4.2) a lower vol% of the Cr_2Nb Laves formed in the last to solidify melt. The high concentrations of Cr, Ta and W in the Nb_{ss}^c also affected the partitioning of solutes in the A15 and the formation of the Ti rich and Cr rich A15. Thus, it is suggested that in the bottom of JZ3-AC the solidification path was $L \rightarrow L + \beta Nb_5Si_3 \rightarrow L + \beta Nb_5Si_3 + Nb_{ss}^c \rightarrow L + \beta Nb_5Si_3 + Nb_{ss}^c + A15 \rightarrow L + \beta Nb_5Si_3 + Nb_{ss}^c + A15 + C14\text{-}Cr_2Nb$.

The solidification path, calculated for the alloy JZ3 using the Pandat database and combining Ta with Nb, and Ge and Sn with Si (because of non-availability of phase equilibria data), was as follows: solidification started at 2161 ˚C with Nb_5Si_3 as the primary phase, then at 1874 ˚C the Nb_{ss} formed via $L \rightarrow Nb_5Si_3$ + bcc A2 (Nb), then at 1474 ˚C the C14-Cr_2Nb Laves phase formed via $L \rightarrow Nb_5Si_3$ + bcc A2 (Nb) + C14-Cr_2Nb, then at 1453 ˚C the Ti_5Si_3 formed via $L + Nb_5Si_3 \rightarrow$ bcc A2 (Nb) + C14-Cr_2Nb + Ti_5Si_3, then at 1344 ˚C the Hf_2Si formed via $L + Ti_5Si_3 \rightarrow$ bcc A2 (Nb) + C14-Cr_2Nb + Hf_2Si, then at 1313 ˚C solid solution and C14 Laves formed via $L \rightarrow$ bcc A2 (Nb) + C14-Cr_2Nb, then at 1213 ˚C the C15-Cr_2Nb Laves phase formed via $L \rightarrow$ bcc A2 (Nb) + C14-Cr_2Nb + C15-Cr_2Nb, then at 1122 ˚C hcp A3 (Ti) solid solution formed via $L \rightarrow$ bcc A2 (Nb) + C14-Cr_2Nb + C15-Cr_2Nb + hcp A3 (Ti), then at 1114 ˚C DO22 tri-aluminide intermetallic formed via $L \rightarrow$ bcc A2 (Nb) + C14-Cr_2Nb + hcp

A3 (Ti) + DO22-Al_3X, then at 1102 ˚C the Hf_2Si formed gain via L + C14-Cr_2Nb → bcc A2 (Nb) + hcp A3 (Ti) + DO22-Al_3X + Hf_2Si, and from the last liquid at 653 ˚C formed bcc A2 (Nb) + hcp A3 (Ti) + DO22-Al_3X + Hf_2Si.

The mole fractions of phases were predicted to be 0.694 for Nb_5Si_3, 0.291 for Nb_{ss}, 0.002 for Ti_5Si_3 and 0.013 for the C14-Cr_2Nb Laves, with negligible mole fractions for Hf_2Si, C15-Cr_2Nb, DO22-Al_3X and hcp A3 (Ti). The calculation predicted formation of hexagonal 5-3 silicide and Hf_2Si, C15-Cr_2Nb, DO22-Al_3X and hcp A3 (Ti), which were not observed in JZ3-AC, gave Nb_5Si_3 as the primary phase, in agreement with experiments and also predicted the formation of C14-Cr_2Nb Laves phase, which was observed in JZ3-AC. The calculation did not give the A15 phase, which was expected since the Ge and Sn (that stabilize the A15) were combined with Si and the database does not include metastable A15-Nb_3Si.

The content of Sn was increased to 5.7 at.% in alloy JZ3+ of which the cast microstructure condition was very similar to that of the alloy JZ3 with the only difference that no solid solution formed in the top and bulk but still existed in the bottom and exhibited a white contrast (the same as that of hafnia). The solid solution was identified as the $(Nb,W)_{ss}$ by the XRD and EDS data. Thus, it is concluded that by increasing the Sn concentration in the alloy the formation of the Nb_{ss} can be suppressed. In the alloy [JZ3+]-AC, this was the come in the top and bulk, where the maximum Sn concentration was 6 at.%, compared with 5.7 at.% in the bottom.

The microstructure of [JZ3+]-AC was similar to that of JZ3-AC. In the top and bulk as primary Nb_5Si_3 formed, the surrounding melt became rich in Ti, W, Sn, Al and Cr. Considering the melting temperature of the phases and that the phase with highest melting temperature should formed first, in the melt surrounding the 5-3 silicide the A15 compound form first followed by the C14-Cr_2Nb. Thus, it is suggested that in the top and bulk of [JZ3+]-AC the solidification path was L → L + βNb_5Si_3 → L + βNb_5Si_3 + A15 → βNb_5Si_3 + A15 + C14-Cr_2Nb. In the bottom of the JZ3+, the

melting temperature of the $(Nb,W)_{ss}$ was estimated at 2200 ˚C, higher than those of the A15 and Laves phase. Thus, it is suggested that in the bottom of JZ3+-AC the solidification path was $L \rightarrow L + \beta Nb_5Si_3 \rightarrow L + \beta Nb_5Si_3 + (Nb,W)_{ss} \rightarrow L + \beta Nb_5Si_3 + (Nb,W)_{ss} + A15 \rightarrow \beta Nb_5Si_3 + (Nb,W)_{ss} + A15 + C14\text{-}Cr_2Nb$.

The solidification path, calculated for the alloy JZ3+ using the Pandat database and combining Ta with Nb, and Ge and Sn with Si, was as follows: solidification started at 2233 ˚C with Nb_5Si_3 as the primary phase, then at 1811 ˚C the Nb_{ss} formed via $L \rightarrow Nb_5Si_3$ + bcc A2 (Nb), then at 1456 ˚C the Ti_5Si_3 formed via $L + Nb_5Si_3 \rightarrow$ bcc A2 (Nb) + Ti_5Si_3, then at 1317 ˚C the Hf_2Si formed via $L + Ti_5Si_3 \rightarrow$ bcc A2 (Nb) + Hf_2Si, then at 1145 ˚C DO22 tri-aluminide intermetallic formed via $L \rightarrow$ bcc A2 (Nb) + Hf_2Si + DO22-Al_3X, then at 1111 ˚C hcp A3 (Ti) solid solution formed via $L \rightarrow$ bcc A2 (Nb) + Hf_2Si + DO22-Al_3X + hcp A3 (Ti) and from the last liquid at 656 ˚C formed bcc A2 (Nb) + hcp A3 (Ti) + DO22-Al_3X + Hf_2Si.

The mole fractions of phases were predicted to be 0.798 for Nb_5Si_3, 0.197 for Nb_{ss}, 0.005 for Ti_5Si_3, with negligible mole fractions for Hf_2Si, DO22-Al_3X and hcp A3 (Ti). The calculation predicted formation of hexagonal 5-3 silicide and Hf_2Si, DO22-Al_3X and hcp A3 (Ti), which were not observed in [JZ3+]-AC, gave Nb_5Si_3 as the primary phase, in agreement with experiments but did not predict the formation of C14-Cr2Nb Laves phase, which was observed in [JZ3+]-AC. The calculation did not give the A15 phase, which was expected since the Ge and Sn (that stabilize the A15) were combined with Si and the database does not include metastable A15-Nb_3Si.

The partitioning behaviour of elements between the Nb_5Si_3 and A15 phase in the alloys JZ3 and JZ3+ showed that Ge partitioned to the 5-3 silicide and Ta, W, Sn, Al and Cr to the A15 compound. The Al and Cr contents in the Nb_5Si_3 were increased apparently in the Ti-rich regions, which confirmed the effect of Ti on the solubility of Al and Cr in the Nb_5Si_3 reported in other alloys. Unlike the alloy JZ1-AC, JZ2-AC and JZ3-AC, the concentration of Si in the Ti-rich Nb_5Si_3 of [JZ3+]-AC was low at

16.7 at.% with significantly increased contents of Sn and Al, which were 8.1 at.% and 7.3 at.%, respectively, this was also not observed in the previous alloys in our group. Thus, the presence of this Ti-rich Nb_5Si_3 in [JZ3+]-AC was attributed to the synergetic effect of (the increased content of) Sn with Ge, Al, Cr and refractory metals, promoting the substitution of Sn and Al for Si in the Ti-rich regions of the 5-3 silicide. The strong partitioning of Ta and W into the A15 phase observed in the alloys JZ3-AC and JZ3+-AC was not observed in the alloys JZ2-AC because of the high solubility of Ta and W in the Nb_{ss}. Thus, it is concluded that the Ta and W partitioned to the Nb_{ss} rather than in the A15 compound and exhibited the lowest solubility in the Nb_5Si_3. The solid solution rich in Ta and W only existed in the bottom of the ingot of JZ3-AC and [JZ3+]-AC with extremely high content of W in the latter, which would suggest that in the as cast microstructures of the alloys JZ3 and JZ3+ the formation of this solid solution was sensitive to the cooling rate and the solubility of Ta and W was significantly affected by the content of Sn with the other elements in the alloys.

In the microstructures of the heat treated alloys JZ3 and JZ3+ the solid solution, C14-Cr_2Nb Laves phase, A15 phase and β and αNb5Si3 were present with Ti rich regions being present only in the 5-3 silicide. Thus, it is suggest that the solid solution, C14 Laves, A15 compound and tetragonal 5-3 silicide were stable in both alloys. The reason of the presence of both forms of the tetragonal Nb_5Si_3 was the same as discussed for the alloys JZ1 and JZ2. The Cr can form the Cr_5Si_3 which also has the W_5Si_3 prototype and can be a stabiliser of the βNb_5Si_3. The low solubility of Sn and the high content of Ge in the Nb_5Si_3 were exhibited by JZ3-HT, in agreement with JZ1-HT, JZ2-HT and Sn or Ge containing alloys (Vellios and Tsakiropoulos 2007 and 2010, Li and Tsakiropoulos 2012), whereas in [JZ3+]-HT the Sn concentration in the Nb_5Si_3 was increased to 4.2 at.% together with a slightly increased content of Al. Thus, it is suggested that Sn (more than 5 at.%) with the other elements in the alloy JZ3 widened the solubility of Sn and Al other than Si in the Nb_5Si_3. In JZ3-HT the Si content in the solid solution varied between 1.2 and 3.3 at.% while in [JZ3+]-HT it varied from 0 to 3.1 at.% and their values were lower than those in the alloys JZ1, JZ2

and Ta containing alloys KZ6 and KZ8 (Zelenitsas and Tsakiropoulos 2006). This was attributed to the very high content of W in the solid solution of JZ3-HT and [JZ3+]-HT lessening the effect of Ta on the solubility of Si in the solid solution.

The C14-Cr_2Nb Laves phase was still present in both JZ3-HT and [JZ3+]-HT, which would suggest that as little as 5 at.% Cr is capable of stabilising the Laves when Cr is added with Al (which also stabilises the C14-Cr_2Nb), Ge, Sn, Ti, Hf, Ta and W. It should be noted that in alloys without Ge, Sn and refractory metals concentrations Cr $\geq$ 8 at% seems to be required for the C14-Cr_2Nb to be stable in the microstructure (Zelenitsas and Tsakiropoulos 2005 and 2006).

For both alloys the calculation of phase equilibria at 1500 ˚C predicted only the Nb_5Si_3 and the Nb_{ss} as stable phases. The mole fractions of Nb_5Si_3 and Nb_{ss} were 0.7 and 0.3 for JZ3-HT and 0.803 and 0.197 for [JZ3+]-AC.

4.4 Conclusions

In this chapter the microstructures of the alloys Nb-12Ti-18Si-6Ta-2.5W-5Sn-5Ge -1Hf-5Al-5Cr (JZ3) and Nb-12Ti-18Si-6Ta-2.5W-7.5Sn-5Ge-1Hf-5Al-5Cr (JZ3+) in the as cast and heat treated conditions were studied. The conclusions of this chapter were as follows:

1. Macrosegregation of Si existed in both alloys.
2. The phases in the microstructures of the as cast alloys JZ3 and JZ3+ were the Nb_5Si_3, A15-Nb_3X, C14-Cr_2Nb, HfO_2 and Nb_{ss}, and the latter only formed in the bottom area of the [JZ3+]-AC. The Nb_5Si_3 was present in the β and α forms in both alloys.
3. The increase of the Sn concentration supressed the formation of the solid solution and stabilised the A15 phase in the solidified microstructures of both alloys.
4. After the heat treatment at 1500 ˚C for 100 h the phases in the microstructures of

both alloys were the βNb_5Si_3, αNb_5Si_3, A15 phase, C14-Cr_2Nb, HfO_2 and solid solution.

5. Ti oxide formed in the heat treated microstructure near the surface areas of the alloy JZ3.
6. Ta and W partitioned to the solid solution rather than in the A15 compound and exhibited the lowest solubility in the Nb_5Si_3.
7. The solubility of W in the solid solution was high and up to 40.2 at.% in the [JZ3+]-HT.
8. The addition of 5 at.% Cr was capable of stabilising the Laves phase in the alloys JZ3 and JZ3+ where Cr was added together with Al, Ge, Sn, Ti, Hf, Ta and W.

Chapter 5

Alloys with Al, Cr and Mo additions

5.1 The alloy Nb-12Ti-18Si-6Mo-2.5W-7.5Sn-5Ge-1Hf-5Al-5Cr (alloy JZ4): Results

The actual composition of the alloy (JZ4-AC) was 38.9Nb-12.5Ti-17.8Si-6.2Mo -2.3W-5.8Sn-5.2Ge-1.1Hf-5.0Al-5.2Cr. There was loss of Sn in the alloy preparation and macrosegregation of Si. The concentration of Si was in the range 16.1 to 19.1 at.%. The XRD data in Figure 5.1 would suggest the presence of the Nb_5Si_3, Nb_5Sn_2Si, A15 phase, C14-Cr_2Nb and HfO_2. The 5-3 silicide existed in both the β and α forms with more peaks corresponding to the βNb_5Si_3.

BSE images of the typical microstructure of JZ4-AC from top to bottom of the ingot are shown in Figure 5.3 and the EDS data for phase analyses are given in Table 5.2. The microstructures in the top and bulk of JZ4-AC were similar. The Nb_5Si_3 was the primary phase with no apparent difference in composition. The Mo solubility in the silicide was 4.5 at.%, different from those in the alloys JG4 (without Ge and Sn) and JG6 (without Ge) (Geng *et al.*, 2007). The areas exhibiting lighter contrast at the edge of the Nb_5Si_3 grains were rich in Ti with relatively low content of Si at about 20.8 at.% and high content of Sn at about 5.0 at.%. The contents of Si+Sn+Ge+Al in the normal and Ti-rich Nb_5Si_3 were 37 at.% and 36.2 at.%, respectively. The A15 phase formed between the Nb_5Si_3 grains and had Ti-rich areas in some regions, with the same solubility of Mo (14.2 at.% and 14.4 at.%) in the normal and the Ti-rich regions of A15. The Si+Sn+Ge+Al contents in the A15 phase and its Ti-rich areas were 19.8 at% and 23.8 at.%, respectively. There was a new phase formed in the interdendritic regions, exhibiting a similar contrast to that of the Ti-rich A15 phase. According to the EDS data, the average composition of this phase corresponded to the Nb_5Sn_2Si intermetallic with Si+Sn+Ge+Al content of 36.9 at.%. The analysis data of this phase had large standard deviations for Nb, Ti, Si and Sn. Considering its relatively high

concentrations of Ti, Ge and Al and the fact that Nb_5Sn_2Si, Nb_5Sn_2Ge, Nb_5Sn_2Al and Ti_5Sn_2Si all have the same W_5Si_3 prototype, this phase is written as TM_5Sn_2X in Table 5.2 where TM = Nb, Ti and X = Si, Ge, Al. The composition of the Laves phase was close to that in [JZ3+]-AC (with Ta) and reported by others and with higher contents of Hf and Al. The microstructure in the bottom of JZ4-AC was slightly finer, consisting of the same phases as in the top and bulk but with no Nb_5Sn_2Si. Ti-rich areas in the Nb_5Si_3 and A15 phase were not observed in the bottom of the ingot. Also no solid solution was observed in the bottom of JZ4-AC.

The average composition of the alloy JZ4 after the heat treatment at 1500 ˚C for 100 hours (JZ4-HT) is given in Table 5.3. There was no chemical inhomogeneity of Si in JZ4-HT. BSE images of the microstructure of JZ4-HT are shown in Figure 5.4. The XRD data (Figure 5.2) would suggest that the heat treated microstructure consisted of Nb_5Si_3, A15 phase(s), $(Nb_{0.5},Mo_{0.5})$ solid solution and HfO_2. The 5-3 silicide was present with both the β and α structures with only one peak corresponding to the αNb_5Si_3. The vol% of the A15 phase was reduced after the heat treatment (Table 5.1). The solid solution, which was not observed in the cast alloy, formed at a small volume fraction after the heat treatment (Table 5.1).

After the heat treatment, the Si concentration in the Nb_5Si_3 was reduced to 20.8 at.% while the solubility of Ti, Sn, Al and Cr was increased. Ti-rich Nb_5Si_3 was observed as small grains adjacent to the A15, in which the solubility of Sn was lower and the solubility of Si and Hf was higher compared with the normal silicide. The Si+Sn+Ge+Al contents of the normal and Ti-rich Nb_5Si_3 were 36.7 at.% and 38 at.%, respectively. Considering the high concentration of W (29.4 at.%) in the solid solution, the solid solution was given as $(Nb,Mo,W)_{ss}$ in Table 5.2. The solid solution was observed not only around the 5-3 silicide but was also dispersed in silicide grains in the form of tiny particles. According to EDS analysis, no Si was present in the solid solution. A very small volume fraction of the C14-Cr_2Nb Laves phase was present. The Laves phase exhibited the same contrast as the Ti-rich Nb_5Si_3. The Si content in

the Laves phase was increased by 2.5 at.% and the Al was reduced by 5 at.% after the heat treatment. No TM_5Sn_2X intermetallic was detected in the heat treated specimen. The contamination by oxygen was not severe and Al oxide formed just below the surface.

Table 5.1 Density of the as cast (AC) and % area of selected phases in the bulk of the as cast and heat treated (HT) alloys JZ4 and JZ5.

Alloy	Density (g/cm^3)	Solid solution (%)	A15 (%)
JZ4-AC	7.28±0.01	-	19.8±3.2
	7.28-7.29		17.3-23.4
JZ4-HT[a]	-	3.3±0.5	12.2±2.0
		2.7-3.6	10.9-14.5
JZ5-AC	6.91±0.06	-	12.7±1.1
	6.87-7.01		11.4-13.4
JZ5-HT[a]	-	2.3±0.3	10.6±0.3
		2.1-2.6	10.4-10.9

[a] hafnia was counted in as its same contrast to the solid solution.

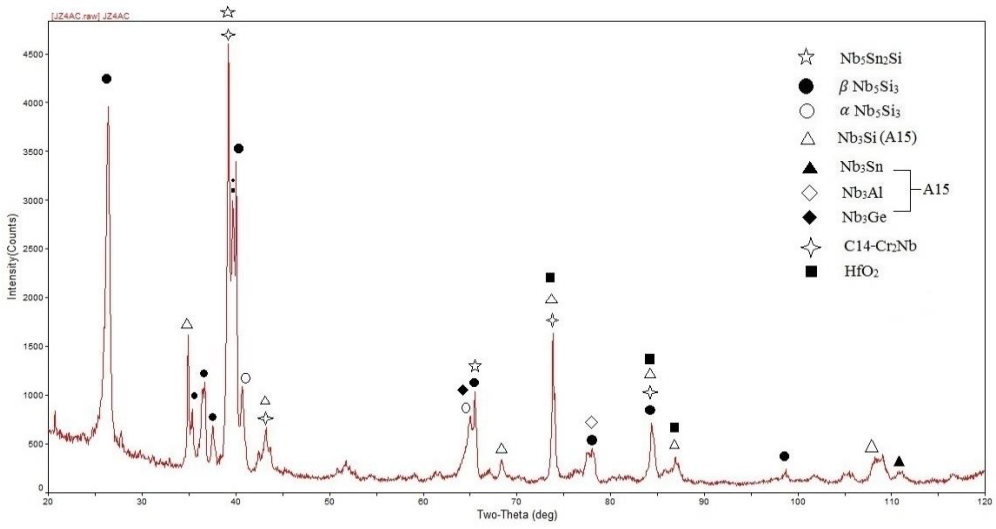

Figure 5.1 The X-ray diffractogram of the alloy JZ4-AC.

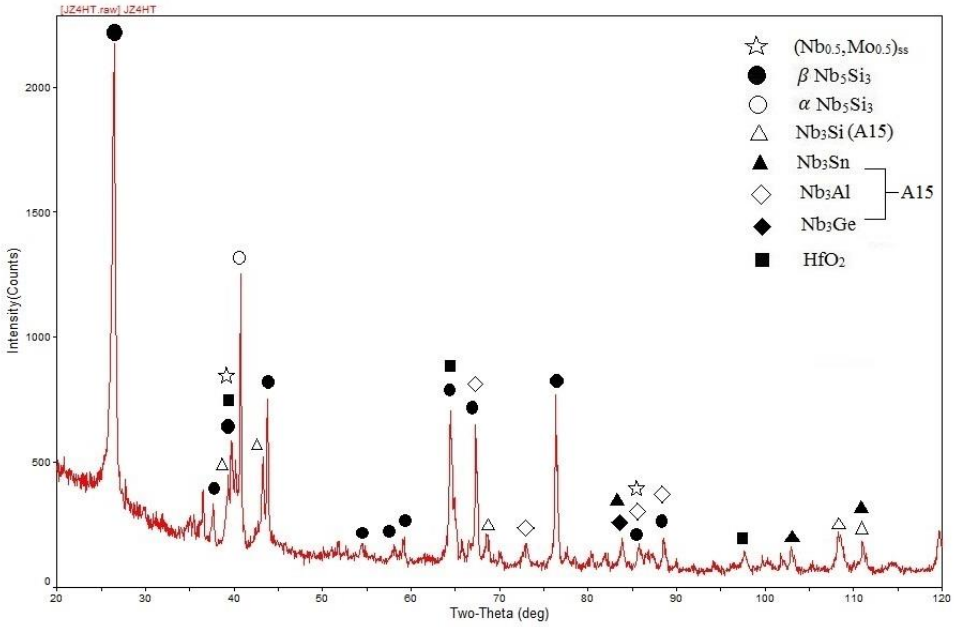

Figure 5.2 The X-ray diffractogram of the alloy JZ4-HT.

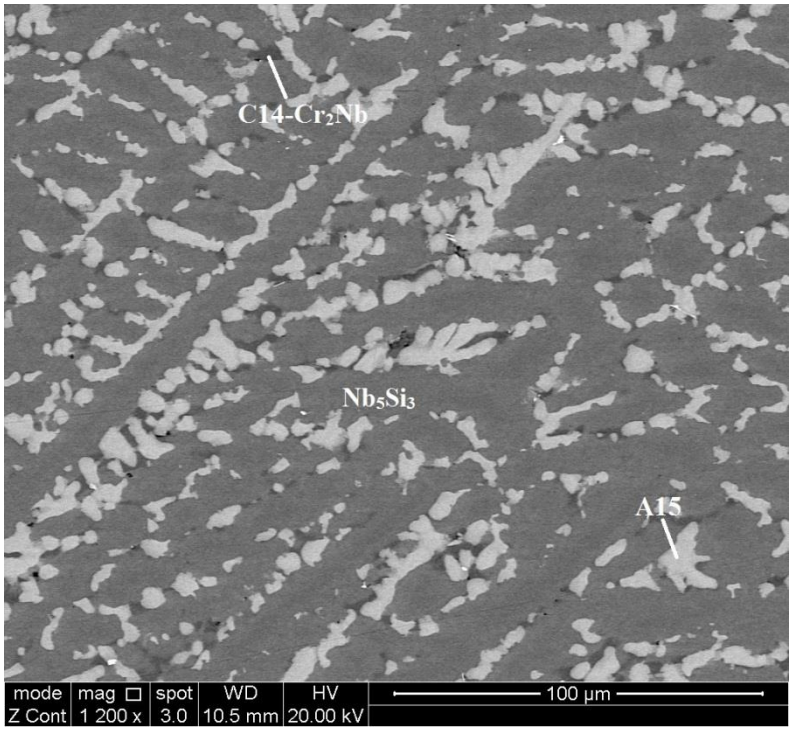

(a)

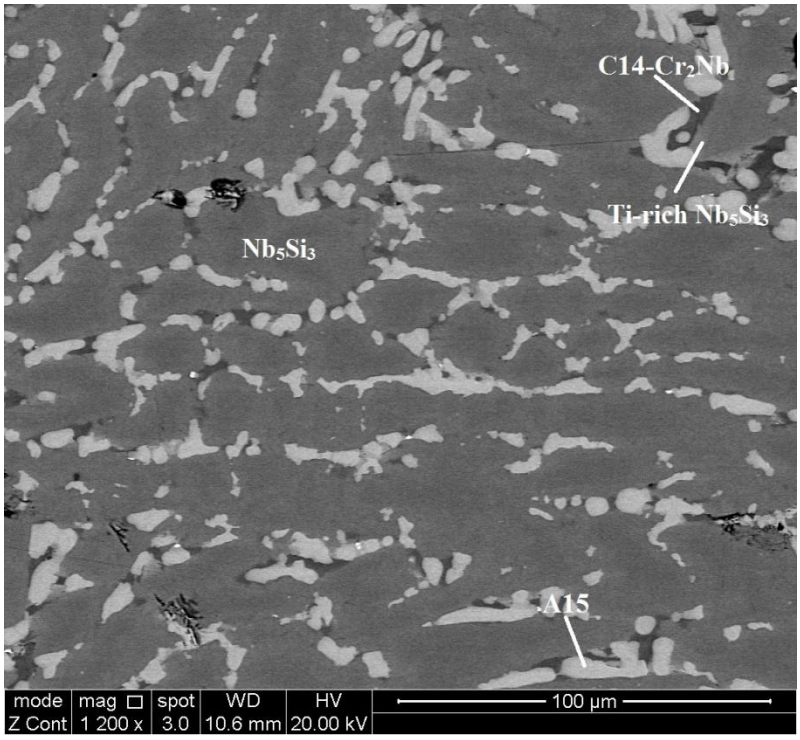
C14-Cr2Nb
Ti-rich Nb5Si3
Nb5Si3
A15
mode mag spot WD HV
Z Cont 1 200 x 3.0 10.6 mm 20.00 kV
100 µm

(b)

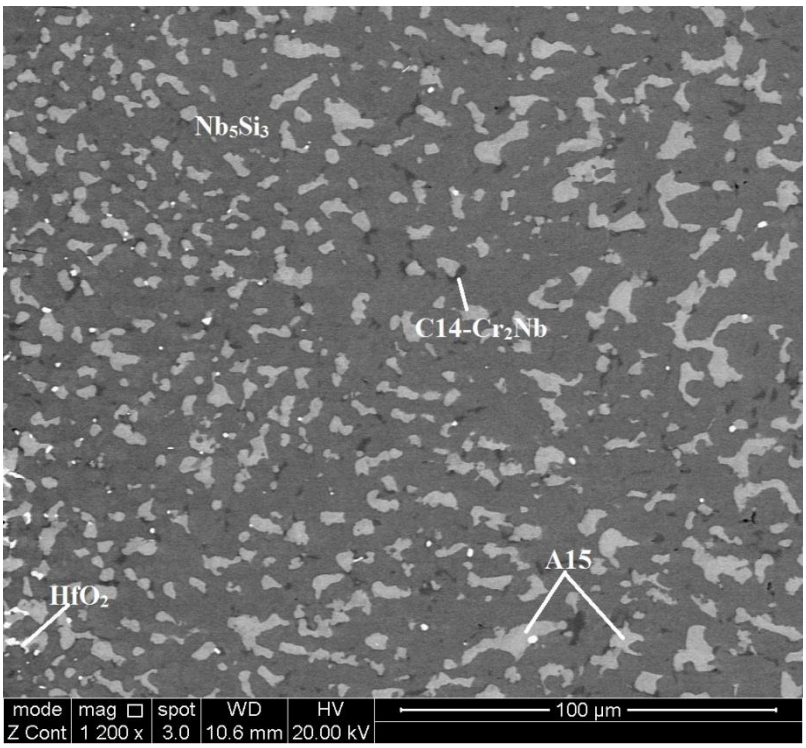
Nb5Si3
C14-Cr2Nb
A15
HfO2
mode mag spot WD HV
Z Cont 1 200 x 3.0 10.6 mm 20.00 kV
100 µm

(c)

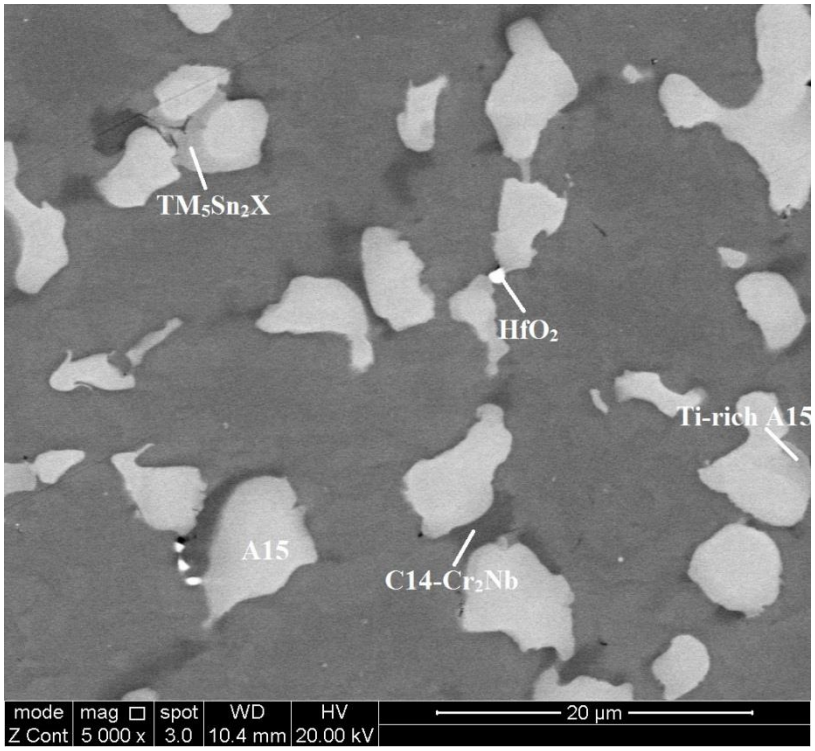

(d)

Figure 5.3 BSE images of the microstructure of the alloy JZ4-AC in the (a) top, (b) bulk, (c) bottom and (d) bulk at high magnification.

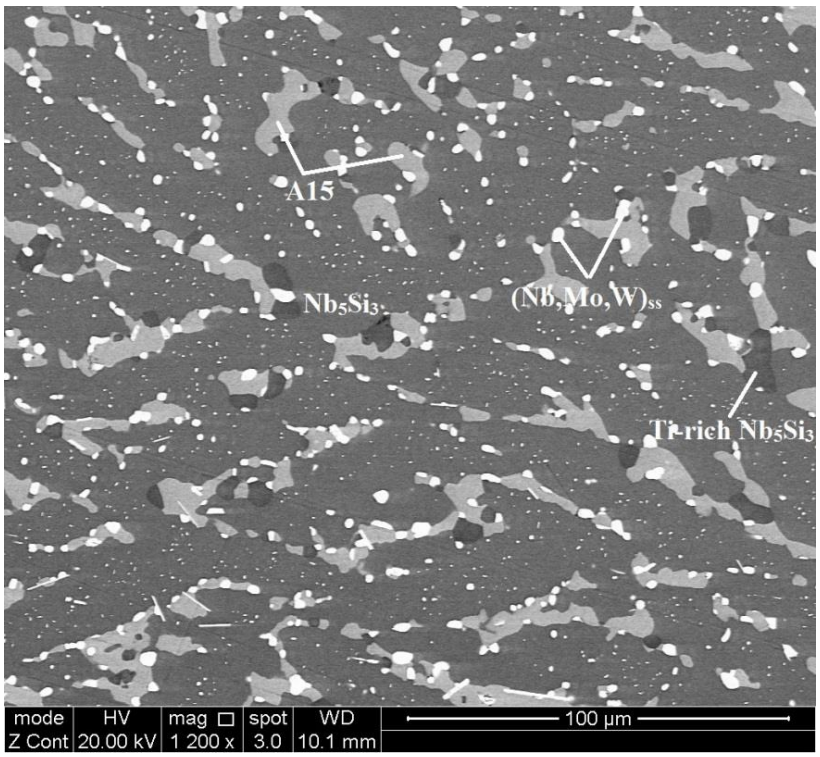

(a)

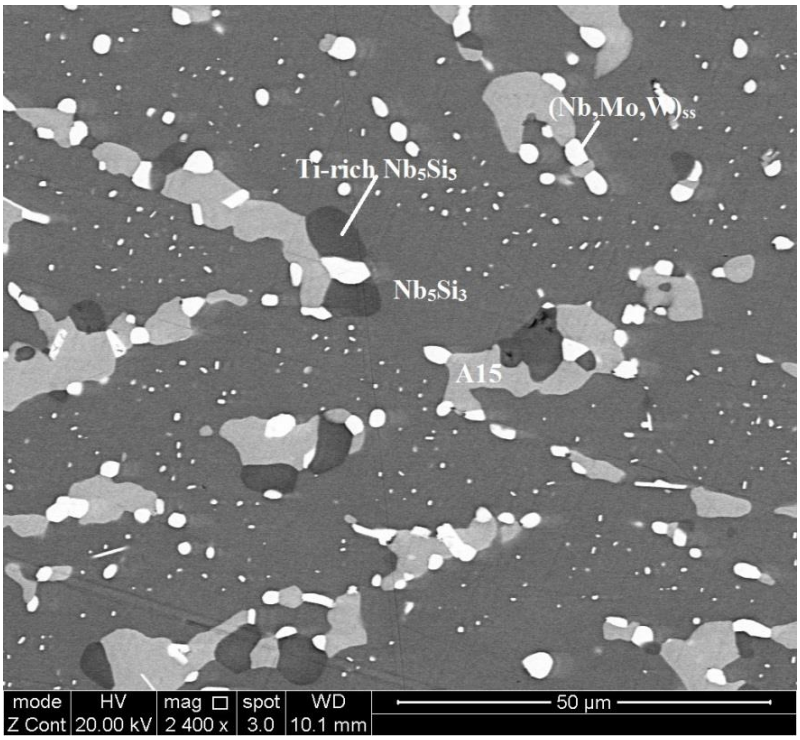

(b)

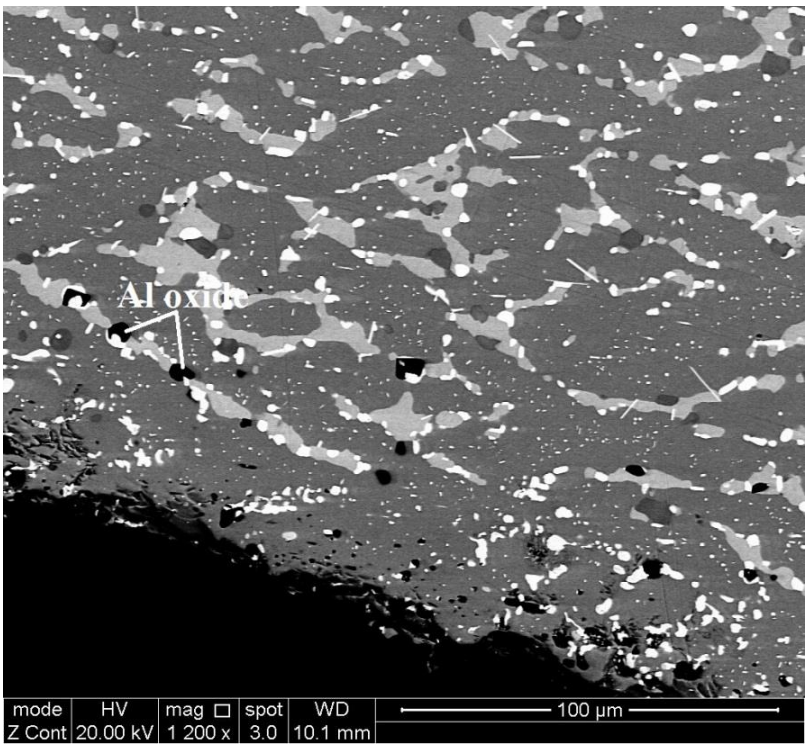

(c)

Figure 5.4 BSE images of the microstructure of the alloy JZ4-HT (a) and (b) in the bulk and (c) below the surface.

Table 5.2 The EDS analysis data (at.%) for the alloy JZ4-AC.

	Nb	Ti	Si	Mo	W	Sn	Ge	Hf	Al	Cr
Top[a]	39.4±0.3	12.4±0.3	18.2±0.7	6.0±0.3	2.5±0.1	5.3±0.3	5.2±0.2	1.1±0.1	4.9±0.3	5.0±0.3
	39.1-39.7	12.2-12.7	17.5-19.1	5.7-6.4	2.4-2.7	4.8-5.6	4.9-5.5	0.9-1.3	4.6-5.2	4.7-5.4
Bulk[a]	39.8±0.4	12.1±0.2	18.7±0.3	6.0±0.4	2.3±0.2	5.3±0.3	5.4±0.1	1.0±0.1	4.6±0.3	4.8±0.3
	39.3-40.3	11.9-12.5	18.1-19.0	5.7-6.6	2.1-2.6	4.9-5.6	5.3-5.5	0.9-1.1	4.2-5.0	4.5-5.1
Bottom[a]	38.2±0.3	12.9±0.1	16.6±0.4	6.5±0.3	1.9±0.2	6.6±0.2	5.0±0.3	1.1±0.1	5.5±0.2	5.7±0.3
	37.9-38.6	12.8-13.1	16.1-17.2	6.2-6.8	1.8-2.3	6.5-7.0	4.5-5.4	1.0-1.2	5.2-5.7	5.5-6.2
Nb_5Si_3	45.1±0.2	9.6±0.2	28.2±0.5	4.5±0.2	1.7±0.1	1.2±0.1	5.7±0.2	0.7±0.1	1.9±0.2	1.4±0.1
	44.8-45.2	9.4-10.0	27.5-28.5	4.2-4.8	1.6-1.9	1.2-1.4	5.5-5.9	0.6-0.9	1.7-2.0	1.2-1.5
Ti-rich Nb_5Si_3	40.7±1.5	12.8±1.1	20.8±1.1	4.7±0.1	1.3±0.2	5.0±1.0	5.9±0.3	1.5±0.2	4.6±0.4	2.7±0.5
	38.3-42.3	11.7-14.6	18.9-21.6	4.5-4.9	0.9-1.5	4.2-6.8	5.5-6.2	1.3-1.8	4.2-5.3	2.3-3.5
A15 phase	42.0±0.3	10.7±0.2	2.5±0.3	14.2±0.3	8.3±0.3	9.1±0.1	1.6±0.2	0.1±0.1	6.6±0.2	4.9±0.1
	41.7-42.4	10.4-10.9	2.2-3.0	13.8-14.5	8.0-8.3	9.0-9.3	1.4-1.9	0.0-0.3	6.5-7.0	4.8-5.0
Ti-rich A15	29.8±2.3	15.1±1.0	1.1±0.6	14.4±1.2	4.6±0.4	12.5±1.4	0.9±0.1	0.2±0.1	9.4±0.7	12.0±1.2
	29.0-32.6	14.1-16.3	0.4-1.9	12.8-14.9	4.3-5.4	11.2-14.5	0.6-1.0	0.0-0.4	8.7-10.4	10.7-13.8
TM_5Sn_2X[b]	27.9±2.9	22.9±2.5	8.7±3.0	4.3±0.8	0.3±0.3	16.8±3.7	4.2±1.3	2.3±0.2	7.3±0.4	5.3±0.9
	19.9-32.2	19.0-28.9	1.8-14.5	3.6-6.0	0-0.6	10.9-25.7	1.6-5.7	2.0-2.6	6.1-8.3	4.1-7.3
C14-Cr_2Nb	22.3±0.6	6.1±0.3	7.7±0.9	4.9±0.1	3.4±0.3	1.1±0.3	1.3±0.2	2.0±0.3	9.4±1.2	41.8±1
	21.6-23.2	5.6-6.5	6.9-9.0	4.7-5.0	3.0-3.7	0.7-1.4	1.1-1.5	1.6-2.3	7.3-10.4	40.4-43.1

[a] Large area analysis.

[b] Prototype W_5Si_3. TM = Nb, Ti and X = Si, Ge, Al.

Table 5.3 The EDS analysis data (at.%) for the alloy JZ4-HT.

	Nb	Ti	Si	Mo	W	Sn	Ge	Hf	Al	Cr
Large area	39.9±0.3	12.3±0.2	18.2±0.3	5.8±0.3	2.2±0.1	5.4±0.3	5.4±0.3	1.2±0.1	4.8±0.2	4.8±0.2
	39.4-40.2	11.9-12.5	17.9-18.5	5.6-6.3	2.1-2.3	5.0-5.4	5.1-5.8	1.0-1.4	4.6-4.9	4.6-5.0
$(Nb,Mo,W)_{ss}$[a]	26.7±0.2	5.4±0.1	0	21.8±0.3	29.4±0.2	0.8±0.1	0.1±0.1	0.6±0.1	3.2±0.1	12.0±0.1
	26.5-27.0	5.2-5.5		21.3-22.2	29.2-29.6	0.7-0.9	0.0-0.2	0.5-0.7	3.1-3.5	11.8-12.2
Nb_5Si_3	39.8±0.2	13.4±0.2	20.8±0.2	4.3±0.3	0.6±0.2	5.3±0.1	5.7±0.1	1.3±0.1	4.8±0.1	4.0±0.1
	39.6-40.1	13.2-13.5	20.6-21.0	4.0-4.7	0.4-0.8	5.2-5.5	5.5-5.8	1.2-1.4	4.6-5.0	3.9-4.1
Ti-rich Nb_5Si_3	34.6±0.4	15.3±0.3	24.1±0.5	3.7±0.3	0.1±0.2	1.6±0.2	6.8±0.1	4.3±0.2	5.6±0.1	3.9±0.2
	34.2-35.1	14.9-15.7	23.4-24.6	3.3-4.0	0-0.4	0.4-1.8	6.6-6.9	4.0-4.5	5.5-5.7	3.8-4.2
A15 phase	39.3±0.1	10.6±0.2	2.0±0.2	14.3±0.2	5.6±0.1	10.3±0.1	1.2±0.1	0.1±0.1	7.1±0.1	9.5±0.3
	39.2-39.5	10.4-11.0	1.7-2.2	14.1-14.3	5.4-5.7	10.2-10.5	1.0-1.4	0.0-0.1	7.0-7.0	9.0-9.8
C14-Cr_2Nb[b]	25.9±0.4	4.0±0.1	10.2±0.3	4.0±0.3	3.5±0.3	0.3±0.1	1.0±0.2	1.3±0.1	4.4±0.2	45.4±0.7
	25.4-26.2	3.8-4.1	9.8-10.5	3.7-4.2	3.3-3.7	0.2-0.3	0.9-1.2	1.2-1.4	4.2-4.7	44.7-46.1

[a] XRD data suggested the presence of $(Nb_{0.5},Mo_{0.5})_{ss}$ and the EDS showed that the solid solution was also very rich in W.

[b] Only three analyses were possible.

5.2 The alloy Nb-20Ti-18Si-6Mo-2.5W-7.5Sn-5Ge-1Hf-5Al-5Cr (alloy JZ5): Results

The EDS large area analysis from the top to bottom of the cast alloy JZ5 (JZ5-AC) is given in Table 5.4. The actual composition of JZ5-AC was 32Nb-20.4Ti-19.2Si -6.3Mo-1.1W-5.7Sn-5.2Ge-0.9Hf-4.5Al-4.7Cr. There was Sn loss due to the evaporation of Sn in the alloy preparation, and the Si and W concentrations were above and below the nominal ones, respectively. There was also macrosegregation of Si the concentration of which varied between 17.2 and 21.7 at.%. The XRD data in Figure 5.5 suggested that the same phases were present in JZ5-AC as in JZ4-AC, namely Nb_5Si_3, A15, C14-Cr_2Nb, Nb_5Sn_2Si and HfO_2. The Nb_5Si_3 was present in both the β and α forms with only two peaks corresponding to αNb_5Si_3. The XRD did not show peaks for Nb solid solution. The absence of the latter in JZ5-AC was confirmed by EDS. The higher Ti concentration in the alloy JZ5-AC, compared with the other alloys of this research, resulted to the density of the JZ5-AC dropping below 7 g/cm^3 (see Table 5.1 and compare data with Tables 3.1 and 4.1).

BSE images of the microstructure of JZ5-AC are given in Figure 5.7, and show similar microstructure in the top, bulk and bottom. The primary phase was the Nb_5Si_3 and between its grains the A15 formed. Ti rich areas were observed at the edge of grains of the former and in some regions of the latter. The partitioning behaviour of elements between the Nb_5Si_3 and the A15 phase in JZ5-AC was the same as in JZ4-AC, with increased concentration of Mo, W and Cr in the latter phase. The Si+Sn+Ge+Al contents in the normal and Ti-rich Nb_5Si_3 in JZ5-AC were 37 at.% and 36.1 at.%, respectively, almost the same as in JZ4-AC. The Si+Sn+Ge+Al contents of the A15 and Ti-rich A15 were 21.6 at.% and 24.3 at.%, respectively, slightly higher than those of JZ4-AC. The C14-Cr_2Nb formed in the interdendritic regions, and its composition was not very different from that in JZ4-AC, with slightly higher Ti and less Nb, Cr and W. The TM_5Sn_2X was observed next to the Laves phase in JZ5-AC as in the cast alloy JZ4 but was richer in Ti. As was the case for JZ4-AC, the analysis

data for TM_5Sn_2X exhibited significantly standard deviations for Nb, Ti, Si and Sn and the average Si+Sn+Ge+Al concentration was 36.8 at.%.

The average composition of the alloy JZ5 after the heat treatment at 1500 ˚C for 100 hours (JZ5-HT) is given in Table 5.5. The XRD and EDS data (Figure 5.6 and Table 5.5) would suggest the presence of the Nb_5Si_3, A15 phase, $(Nb,Mo,W)_{ss}$ and HfO_2. The 5-3 silicide was present in both the βNb_5Si_3 and αNb_5Si_3 forms with two peaks corresponding to the αNb_5Si_3. The microstructure in the bulk and near the surface of the heat treated specimen is shown in Figure 5.8. No Ti-rich regions were observed in the large Nb_5Si_3 grains and the A15 phase. Ti-rich Nb_5Si_3 formed adjacent to A15 grains. There were $(Nb,Mo,W)_{ss}$ particles dispersed in the large Nb_5Si_3 grains.

According to the EDS data, after the heat treatment the Si solubility in the 5-3 silicide was reduced to 20.3 at.% and the Sn, Al and Cr concentrations were increased whereas in the Ti-rich Nb_5Si_3 there were higher concentrations of Si and Hf and lower concentration of Sn. The Si+Sn+Ge+Al contents of the normal and Ti-rich Nb_5Si_3 were 36.9 at.% and 37.9 at.%, respectively. The solid solution exhibited white contrast and was very rich in W (18 at.%) and with no Si. There was change in the composition of the A15 phase with only a slight increase in the Cr content after the heat treatment. The Si+Sn+Ge+Al content of the A15 was 20.8 at.%. The Laves and TM_5Sn_2X phase were not observed and no contamination was found in any part of the heat treated specimen.

Table 5.4 The EDS analysis data (at.%) for the alloy JZ5-AC.

	Nb	Ti	Si	Mo	W	Sn	Ge	Hf	Al	Cr
Top[a]	31.7±0.6	20.6±0.6	19.4±1.0	6.3±0.2	1.3±0.2	5.4±0.3	5.2±0.1	0.9±0.1	4.5±0.3	4.7±0.3
	31.2-32.4	20.0-21.5	18.4-20.9	6.0-6.6	1.0-1.5	5.0-5.8	5.1-5.3	0.8-1.0	4.2-5.0	4.2-4.9
Bulk[a]	32.8±1.4	19.9±0.6	19.8±1.9	6.3±0.5	1.3±0.3	5.3±1.0	5.3±0.1	0.8±0.1	4.1±0.5	4.4±0.5
	31.1-33.9	19.3-20.7	17.2-21.7	6.0-7.1	1.0-1.6	4.5-6.4	5.2-5.5	0.7-0.9	3.6-4.7	3.9-5.1
Bottom[a]	31.5±0.7	20.6±0.5	18.3±0.9	6.3±0.1	0.8±0.1	6.5±0.4	5.1±0.4	0.9±0.1	4.8±0.4	5.2±0.7
	30.3-32.2	20.2-21.2	17.3-19.2	6.1-6.4	0.7-0.9	6.0-6.9	4.7-5.4	0.8-1.0	4.4-5.2	4.7-6.4
Nb_5Si_3	37.9±0.5	16.9±0.5	28.1±0.6	4.9±0.2	1.0±0.1	1.2±0.2	6.2±0.2	0.8±0.1	1.6±0.2	1.4±0.1
	3.73-38.6	16.3-17.4	27.5-28.8	4.5-5.1	1.0-1.1	0.9-1.5	5.7-6.3	0.7-0.9	1.4-1.8	1.3-1.4
Ti-rich Nb_5Si_3	31.1±0.6	21.9±0.6	18.3±0.3	5.3±0.2	1.3±0.1	6.2±0.2	6.6±0.1	1.3±0.2	5.0±0.1	3.0±0.2
	30.2-31.6	21.2-22.6	17.8-18.6	5.0-5.5	1.2-1.4	6.1-6.5	6.5-6.8	1.1-1.5	4.9-5.1	2.8-3.2
A15 phase	30.1±0.7	19.4±0.3	2.1±0.4	16.2±0.4	4.8±0.2	10.3±0.5	2.1±0.4	0.5±0.1	7.1±0.2	7.4±0.5
	29.2-31.2	19.1-19.9	1.8-2.7	15.9-16.8	15.9-16.8	9.5-10.7	1.8-2.7	0.4-0.5	6.9-7.5	7.0-8.1
Ti-rich A15	19.1±2.6	22.7±1.4	0.8±0.3	15.5±0.4	3.9±0.5	11.6±0.8	1.4±0.3	0.4±0.1	10.5±1.0	14.1±0.9
	16.3-22.4	21.2-24.5	0.4-1.1	15.0-15.9	3.4-4.5	10.6-12.3	1.0-1.8	0.3-0.5	9.3-11.7	13.1-15.5
TM_5Sn_2X	17.8±4.7	34.3±4.0	7.6±4.2	3.8±0.5	0	17.5±4.5	4.2±1.3	1.6±0.1	7.5±0.8	5.7±1.7
	12.1-23.2	29.0-39.6	2.3-12.8	2.9-4.0		11.5-22.8	2.6-5.5	1.3-1.8	6.6-9.0	4.3-8.9
C14-Cr_2Nb	18.5±0.3	10.5±0.2	7.5±0.7	5.0±0.4	2.3±0.2	0.9±0.4	1.4±0.2	1.4±0.1	9.3±1.3	43.2±0.4
	18.3-19.1	10.3-10.7	6.7-8.3	4.6-5.6	2.1-2.6	0.5-1.6	1.2-1.8	1.4-1.6	7.8-10.6	42.8-43.8

[a] Large area analysis.

Table 5.5 The EDS analysis data (at.%) for the alloy JZ5-HT.

	Nb	Ti	Si	Mo	W	Sn	Ge	Hf	Al	Cr
Large area	31.4±0.3	20.5±0.2	18.8±0.4	6.2±0.1	1.2±0.1	5.7±0.2	5.6±0.2	1.0±0.2	4.7±0.2	4.9±0.2
	31.1-31.8	20.4-20.8	18.4-19.3	6.0-6.4	1.0-1.3	5.4-5.9	5.4-5.9	0.8-1.3	4.6-5.0	4.7-5.1
$(Nb,Mo,W)_{ss}$	21.2±0.4	11.3±0.3	0	23.4±0.3	18.0±0.3	1.2±0.1	1.6±0.6	0.3±0.3	5.3±0.3	17.7±0.3
	20.9-21.7	10.8-11.6		22.9-23.9	17.7-18.3	1.0-1.4	0.8-2.3	0-0.8	5.1-5.8	17.2-18.0
Nb_5Si_3	31.4±0.2	21.1±0.4	20.3±0.5	5.0±0.1	0.5±0.1	5.7±0.3	6.2±0.3	1.1±0.1	4.6±0.1	4.1±0.2
	31.2-31.6	20.6-21.7	19.5-20.9	4.9-5.2	0.4-0.6	5.3-6.1	5.9-6.8	1.1-1.2	4.5-4.8	3.8-4.2
Ti-rich Nb_5Si_3	27.3±0.3	23.7±0.4	24.1±0.3	3.8±0.3	0.1±0.1	1.4±0.1	7.2±0.1	3.2±0.1	5.2±0.1	4.0±0.2
	26.9-27.7	23.1-24.2	23.6-24.4	3.6-4.4	0-0.2	1.3-1.5	7.1-7.3	3.1-3.4	5.1-5.3	3.7-4.2
A15 phase	29.9±0.4	17.4±0.3	2.4±0.2	16.3±0.3	4.7±0.1	9.2±0.1	1.8±0.1	0.2±0.1	7.3±0.1	10.8±0.6
	29.3-30.4	16.9-17.5	2.0-2.6	15.9-16.6	4.5-4.8	9.2-9.3	1.7-2.0	0.1-0.4	7.2-7.4	10.2-11.7

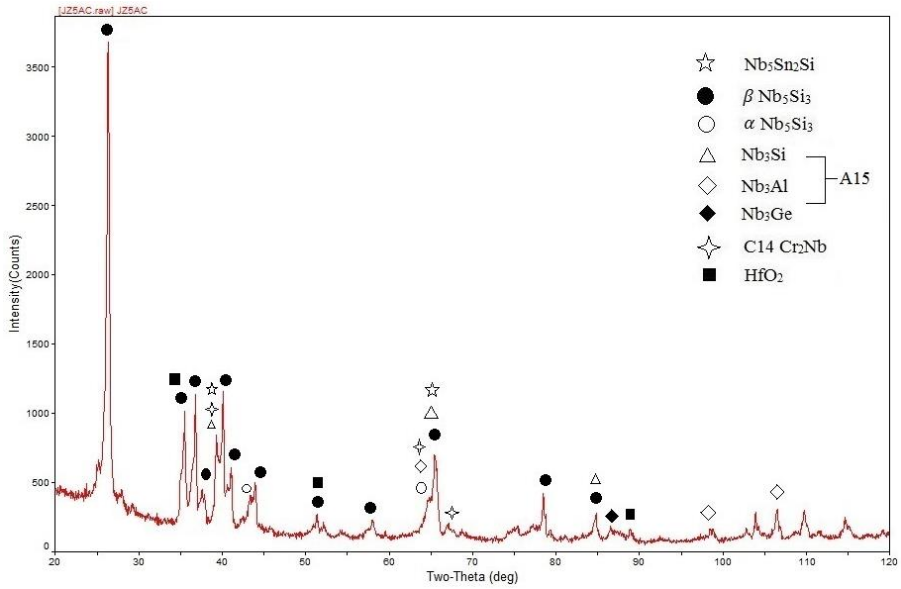

Figure 5.5 The X-ray diffractogram of the alloy JZ5-AC.

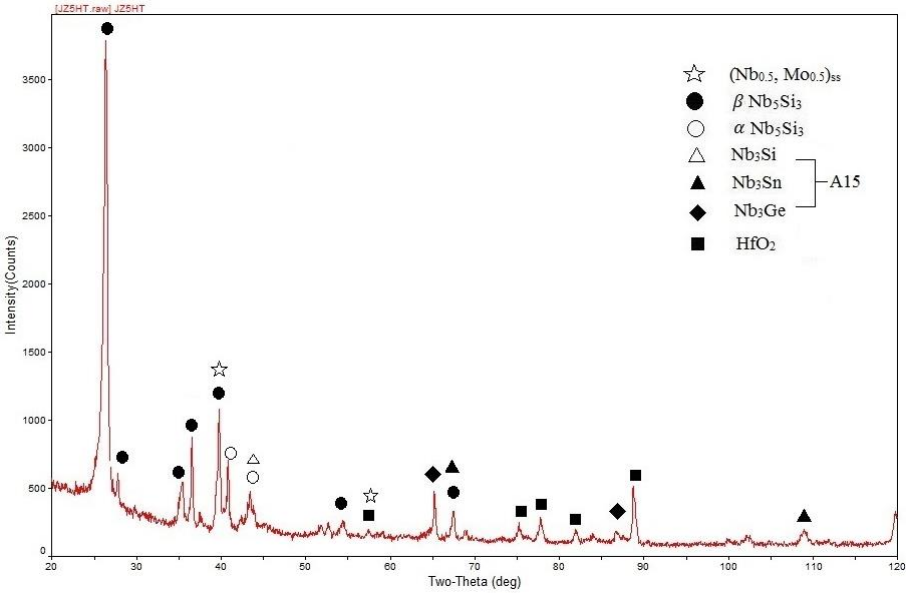

Figure 5.6 The X-ray diffractogram of the alloy JZ5-HT.

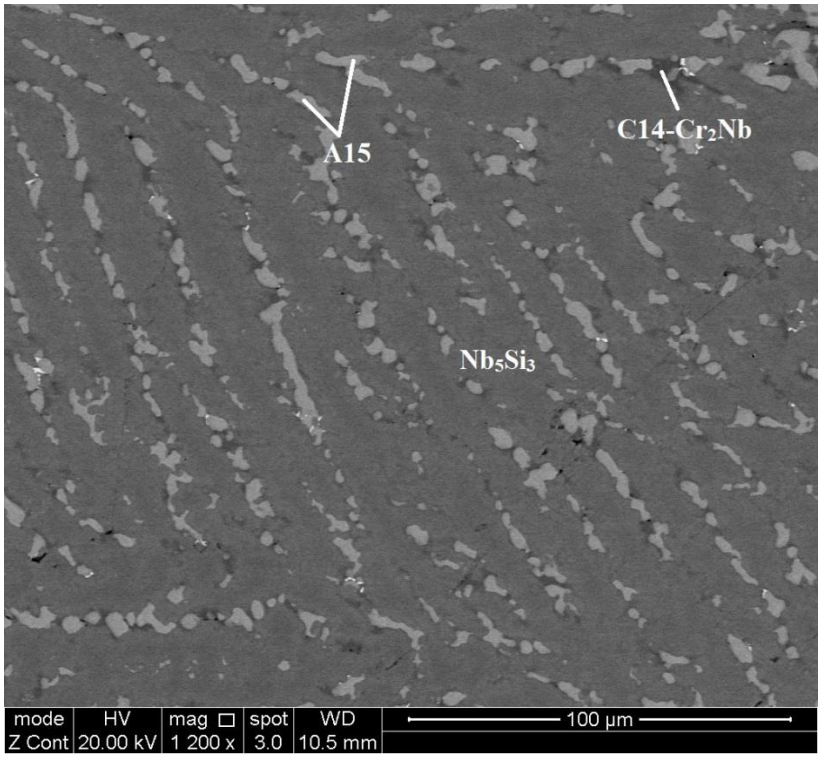
A15
C14-Cr2Nb
Nb5Si3
mode HV mag spot WD
Z Cont 20.00 kV 1 200 x 3.0 10.5 mm
100 µm

(a)

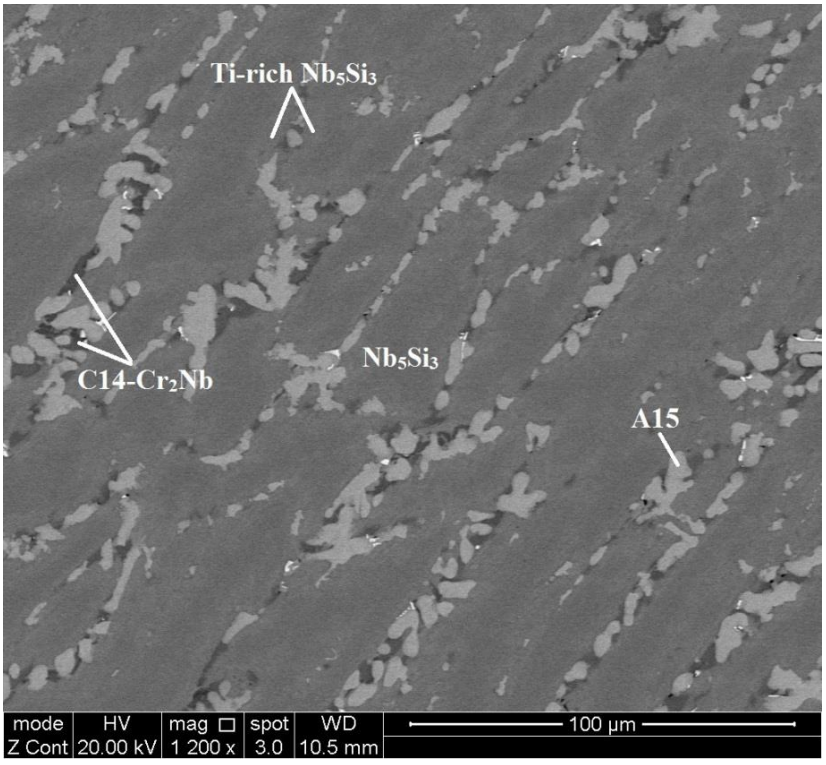
Ti-rich Nb5Si3
C14-Cr2Nb
Nb5Si3
A15
mode HV mag spot WD
Z Cont 20.00 kV 1 200 x 3.0 10.5 mm
100 µm

(b)

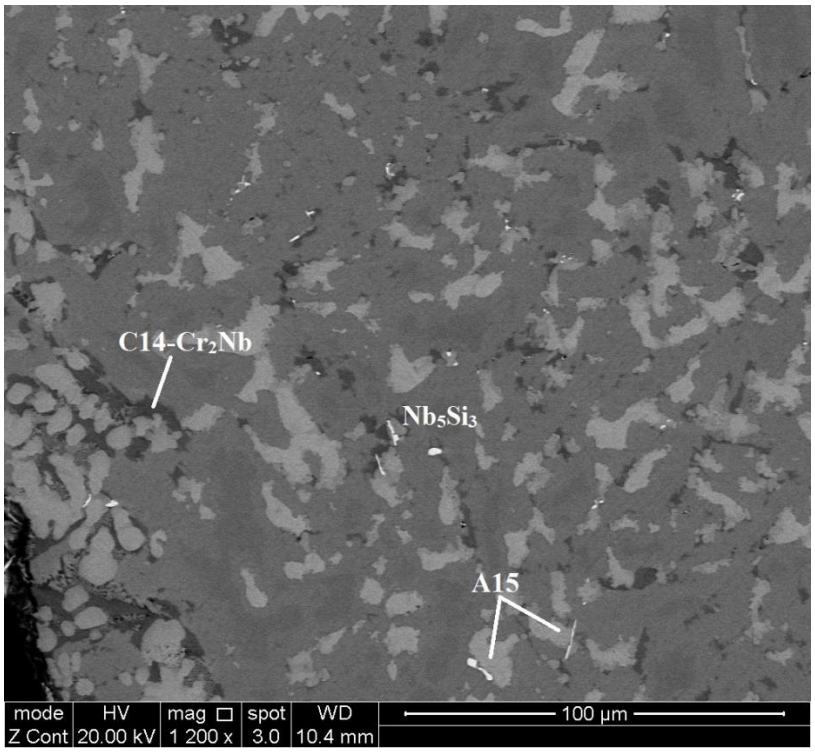

(c)

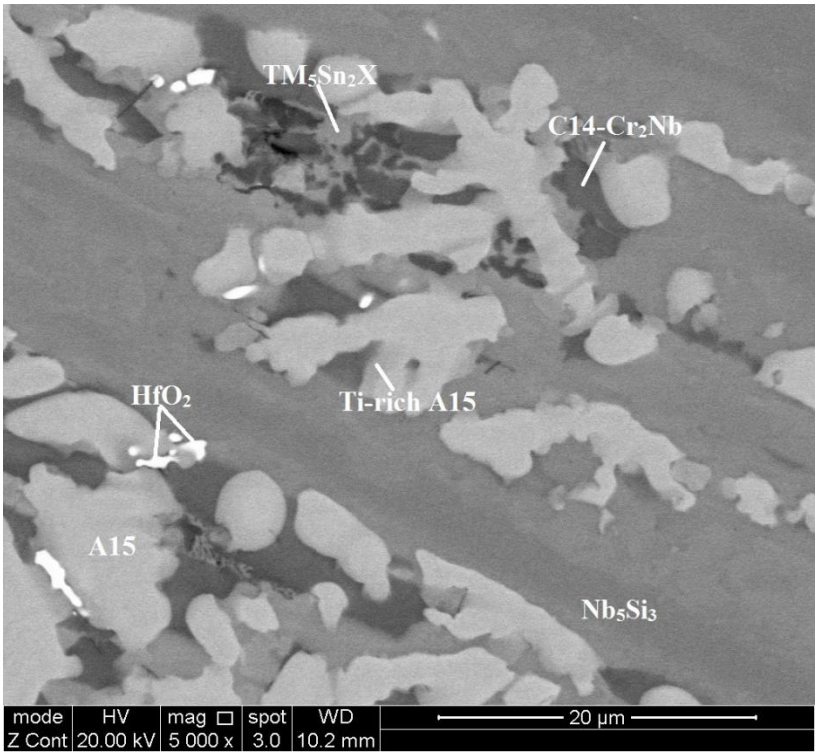

(d)

Figure 5.7 BSE images of the microstructure of the alloy JZ5-AC in the (a) top, (b) bulk, (c) bottom and (d) bulk at high magnification.

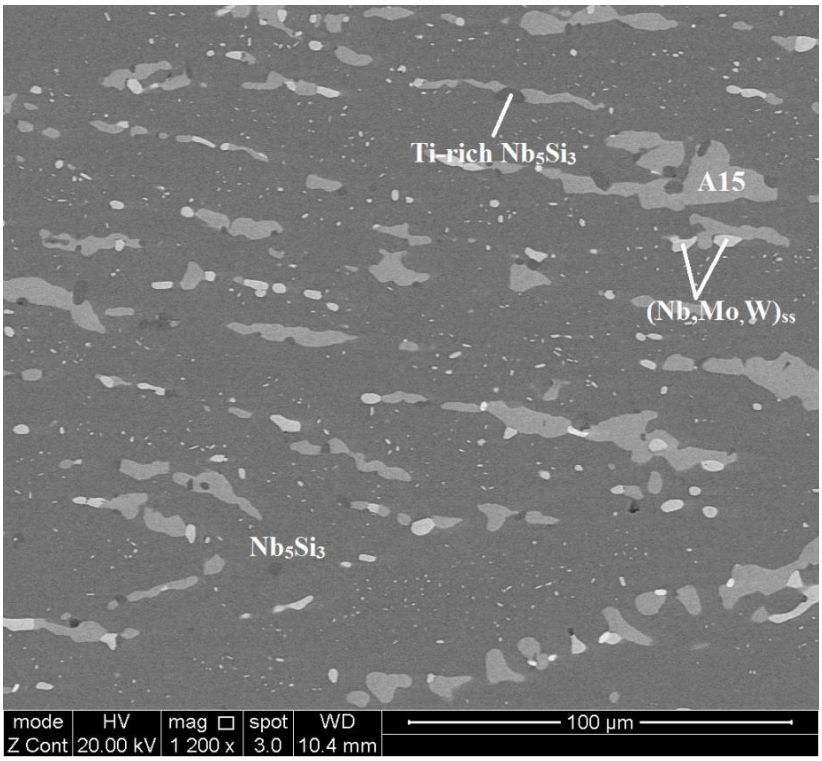
Ti-rich Nb_5Si_3
A15
$(Nb,Mo,W)_{ss}$
Nb_5Si_3
mode HV mag spot WD
Z Cont 20.00 kV 1 200 x 3.0 10.4 mm
100 µm

(a)

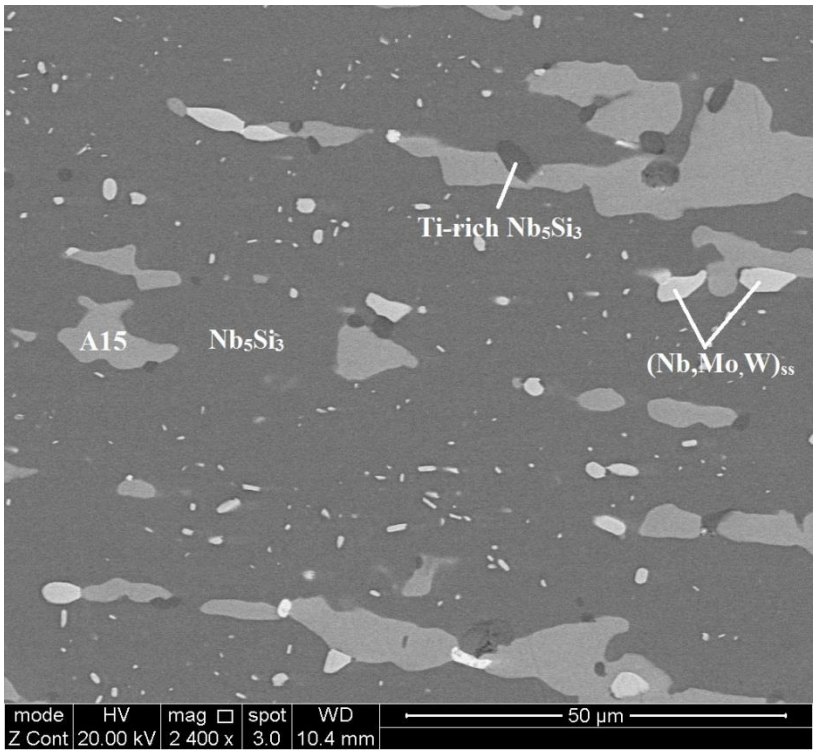
Ti-rich Nb_5Si_3
A15
Nb_5Si_3
$(Nb,Mo,W)_{ss}$
mode HV mag spot WD
Z Cont 20.00 kV 2 400 x 3.0 10.4 mm
50 µm

(b)

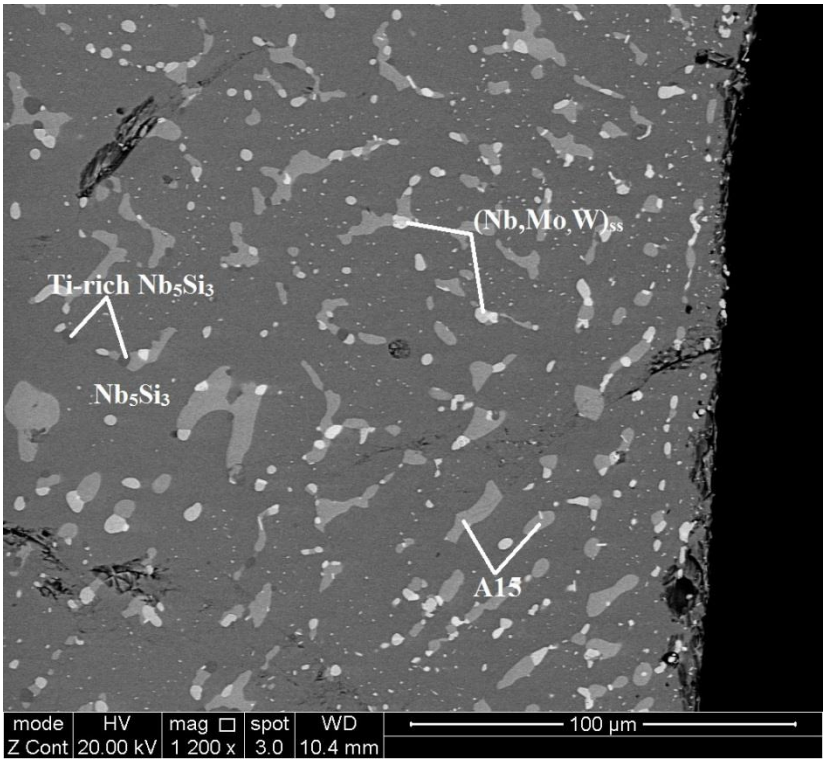

(c)

Figure 5.8 BSE images of the microstructure of the alloy JZ5-HT (a) and (b) in the bulk and (c) below the surface.

5.3 Discussion

There was Sn loss during the preparation of both alloys owing to the evaporation of Sn during the arc melting. Thus in both alloys the Sn/Ge was the same (≈1.1). In both alloys the Al and Cr contents were the same and the main difference was the higher Si and Ti concentrations in the alloy JZ5. Macrosegregation of Si existed in both alloys, and was 3 at.% in JZ4 and 4.5 at.% in JZ5 compared with calculated average MACSi values of 3.2 and 5 at.%, respectively for this two alloys. The MACSi values calculated using ΔH_m^{sd} were the closest to the measured values.

In the alloy JZ4 the addition of Mo instead of Ta did not change the architecture of the microstructure. In the interdendritic areas of the primary Nb_5Si_3 the A15 compound, the C14-Cr_2Nb and TM_5Sn_2X (where TM = Nb, Ti and X = Si, Ge, Al) formed. The

latter compound was not observed in the alloys JZ3 and JZ3+. Furthermore, the solid solution was not found in any part of the ingot. Thus, it is concluded that the addition of Mo with other elements in the alloy JZ4 did not affect the formation of the A15 compound and the Laves phase but suppressed the solid solution and promoted the formation of TM_5Sn_2X in the solidified microstructure of the alloy JZ4. The TM_5Sn_2X compound is based on the Nb_5Sn_2Si, Ti_5Sn_2Si, Nb_5Sn_2Ge, Nb_5Sn_2Al compounds which all have the tetragonal W_5Si_3 as prototype and similar lattice parameters. The Nb_5Sn_2Si compound was previously observed by *Geng et al.* (2007) and was stable at 900 ˚C and 1200 ˚C according to Sun *et al.* (2012). Bulanova *et al.* (2003) reported the $Ti_5Si_{1.2\text{-}1.6}Sn_{1.8\text{-}1.4}$ compound in Ti-Si-Sn alloys. The Nb_5Sn_2Ge and Nb_5Sn_2Al in the Nb-Ge-Si and Nb-Al-Si ternary systems have been studied by our research group. In the alloy JZ4 in the TM_5Sn_2X the solubility of Ti, Si, Sn, Ge and Al was widened with Ti substituting Nb and Ge and Al substituting either Si or Sn.

As the primary Nb_5Si_3 formed the surrounding melt became rich in Ti, Mo, W, Sn, Al and Cr. Considering the microstructure of the alloy JZ4 in which the TM_5Sn_2X and C14-Cr_2Nb Laves only existed in the interdendritic regions with small volume fractions and that the phase with the highest melting temperature should form first, in the melt surrounding the Nb_5Si_3 the A15 phase formed first followed by the TM_5Sn_2X and then the C14-Cr_2Nb. Thus, it is suggested that in the top, bulk and bottom of JZ4-AC the solidification path was $L \rightarrow L + \beta Nb_5Si_3 \rightarrow L + \beta Nb_5Si_3 + A15 \rightarrow L + \beta Nb_5Si_3 + A15 + TM_5Sn_2X \rightarrow \beta Nb_5Si_3 + A15 + TM_5Sn_2X$ + C14-Cr_2Nb. The formation of αNb_5Si_3 occurred for the same reasons as discussed in the previous chapters

The solidification path, calculated for the alloy JZ4 using the Pandat database and combining Mo with Nb, and Ge and Sn with Si (because of non-availability of phase equilibria data), was as follows: solidification started at 2255 ˚C with Nb_5Si_3 as the primary phase, then at 1820 ˚C the Nb_{ss} formed via $L \rightarrow Nb_5Si_3$ + bcc A2 (Nb), then at 1660 ˚C the Ti_5Si_3 formed via $L + Nb_5Si_3 \rightarrow$ bcc A2 (Nb) + Ti_5Si_3, then at 1316 ˚C

the Hf_2Si formed via L + Ti_5Si_3 → bcc A2 (Nb) + Hf_2Si, then at 1149 ˚C the DO22 tri-aluminide intermetallic formed via L → bcc A2 (Nb) + Hf_2Si + DO22-Al_3X, the at 1108 ˚C the hcp A3 (Ti) solid solution formed via L → bcc A2 (Nb) + Hf_2Si + DO22-Al_3X + hcp A3 (Ti), and from the last liquid at 1136 ˚C formed bcc A2 (Nb) + hcp A3 (Ti) + DO22-Al_3X + Hf_2Si.

The mole fractions of phases were predicted to be 0.724 for Nb_5Si_3, 0.236 for Nb_{ss}, 0.04 for Ti_5Si_3 with negligible mole fractions for Hf_2Si, DO22-Al_3X and hcp A3 (Ti). The calculation predicted formation of hexagonal 5-3 silicide and Hf_2Si, DO22-Al_3X and hcp A3 (Ti), which were not observed in JZ4-AC, gave Nb_5Si_3 as the primary phase, in agreement with experiments and also predicted the formation of Nb_{ss}, which was not observed in JZ4-AC. The calculation did not give the A15 phase, which was expected since the Ge and Sn (that stabilize the A15) were combined with Si and the database does not include metastable A15-Nb_3Si, and also did not predict the formation of TM_5Sn_2X compound(s) and the C14-Cr_2Nb Laves phase.

In the alloy JZ5, the increase in the content of Ti did not change the architecture of the microstructure the scale of which was slightly coarsened compared with the alloy JZ4. The phases in the microstructure were the Nb_5Si_3, A15 compound, C14-Cr_2Nb Laves and TM_5Sn_2X. The volume fraction of the latter compound was increased, indicating that Ti promoted the formation of the TM_5Sn_2X. Similar to the alloy JZ4, the Nb_{ss} formation was supressed in JZ5-AC. As the primary Nb_5Si_3 formed the surrounding melt became rich in Ti, Mo, W, Sn Al and Cr owing to the partitioning behaviour of these elements, and then the A15 formed followed by the TM_5Sn_2X compound and the C14-Cr_2Nb Laves which were formed in the interdendritic regions. Thus, it is suggested that in the top, bulk and bottom of the alloy JZ5-AC the solidification path was L → L + βNb_5Si_3 → L + βNb_5Si_3 + A15 → L + βNb_5Si_3 + A15 + TM_5Sn_2X → βNb_5Si_3 + A15 + TM_5Sn_2X + C14-Cr_2Nb.

The solidification path, calculated for the alloy JZ5 using the Pandat database and

combining Mo with Nb, and Ge and Sn with Si, was as follows: solidification started at 2170 ˚C with Nb_5Si_3 as the primary phase, then at 1897 ˚C the Ti_5Si_3 formed via L $\rightarrow$ Nb_5Si_3 + Ti_5Si_3, then at 1739 ˚C the Nb_{ss} formed via L $\rightarrow$ Nb_5Si_3 + Ti_5Si_3 + bcc A2 (Nb), then at 1433 ˚C the C14-Cr_2Nb Laves phase formed via L $\rightarrow$ Ti_5Si_3 + bcc A2 (Nb) + C14-Cr_2Nb, and from the last liquid at 1419 ˚C formed Ti_5Si_3 + bcc A2 (Nb) + C14-Cr_2Nb Laves.

The mole fractions of phases were predicted to be 0.573 for Nb_5Si_3, 0.230 for Nb_{ss}, 0.196 for Ti_5Si_3 and 0.001 C14-Cr_2Nb Laves phase. The calculation predicted formation of significant volume fraction of hexagonal 5-3 silicide and Nb_{ss}, which were not observed in JZ5-AC, gave Nb_5Si_3 as the primary phase, in agreement with experiments. The calculation did not give the A15 phase, and also did not predict the formation of TM_5Sn_2X compound(s). However, it predicted the formation of a very small volume fraction of the C14-Cr_2Nb Laves phase.

The microstructures of the heat treated alloys JZ4 and JZ5 consisted of the Nb_5Si_3, A15 phase and $(Nb,Mo,W)_{ss}$, with a very small volume fraction of the C14-Cr_2Nb Laves phase only present in the former alloy. The XRD data suggested the presence of the β and αNb_5Si_3 with only one and two peaks corresponding to the latter in JZ4-HT and JZ5-HT, respectively. Thus, it is concluded (1) that the 5-3 silicide, A15 phase and solid solution were stable in the equilibrium microstructures of JZ4 and JZ5 at 1500 ˚C with the stability of the C14-Cr_2Nb Laves phase suppressed in the alloy JZ5, (2) that the TM_5Sn_2X was unstable at 1500 ˚C in both the alloys, in agreement with Sun *et al.* (2012) and (3) that the addition of Mo and W in the two alloys to a larger extent stabilised the βNb_5Si_3 because Mo can form Mo_5Si_3 and W can form the W_5Si_3 both of which have the $D8_m$ structure, the same as the βNb_5Si_3.

The calculation of phase equilibria using the Pandat software showed that the microstructure of JZ4-HT should consist of the Nb_5Si_3 and Nb_{ss} phases with mole fractions of 0.765 and 0.235 Nb_{ss}, respectively. In other words, the calculation for

JZ4-HT did not show that the A15 and C14-Cr_2Nb are stable in this alloy.

In the case of JZ5-HT, the calculation gave a microstructure consisting of the Nb_5Si_3, Nb_{ss} and Ti_5Si_3 phases with mole fractions of 0.644, 0.230 and 0.126, respectively and failed to predict the stability of the A15 compound but correctly predicted that the C14-Cr_2Nb Laves phase is not stable in this alloy.

Very low solubility of Mo in the Nb_5Si_3 (almost zero) was reported in alloys of the Nb-Ti-Si-Mo-Al-Cr-Hf-Sn (Geng *et al.* 2007) and Nb-Si-Hf-Mo-W (Grammenos and Tsakiropoulos, 2011) systems. This was not confirmed in JZ4-HT and JZ5-HT where the contents of Mo in the 5-3 silicide were 4.3 and 5.0 at.%, respectively. Thus, it is suggested that the increase in the solubility of Mo in the Nb_5Si_3 was attributed to the addition of Ge in the alloys. The high solubility of Mo in the A15 phase which was up to 16.6 at.% was exhibited by both alloys. The solid solutions formed in JZ4-HT and JZ5-HT were very rich in refractory metals but free of Si owing to the addition of Mo and W, which were reported by Grammenos and Tsakiropoulos (2011) to promote the formation of the Si free Nb_{ss}.

Comparison of phases in alloys with/without Al and Cr and with Mo or Ta

The limited data for the compositions of the different phases that were present in the microstructures of the cast and heat treated alloys studied in this thesis indicated certain trends, from which subtle differences emerge about the alloying behaviour of Mo or Ta with Ge and Sn and with/without Al and Cr. The limited data given in the figures 5.9 to 5.21 should be used with caution.

<u>The bcc Nb solid solution</u>

In the alloys with Ta and no Al and Cr (i.e., the alloys JZ1 and JZ2) the trend of the data would suggest that the Si concentration in the normal Nb_{ss} increased as the Sn/Ge ratio in the alloy increased with the limited data indicating a maximum of Si = 4.5 at.% at Sn/Ge ≈ 0.65, see figure 5.9. In the same alloys, the trend of the data would

suggest that the Sn/Ge ratio in the normal Nb_{ss} increased as the Sn/Ge ratio in the alloy increased, with the limited data indicating a minimum of Sn/Ge ≈ 3.4 in the Nb_{ss} at Sn/Ge ≈ 0.6 in the alloy, see figure 5.10. Furthermore, the Ta/W ratio and the Ta+W sum in the normal Nb_{ss}, respectively increased and decreased with increasing Sn/Ge ratio in the alloy, see figures 5.11 and 5.12. Also, the Ti concentration in the normal Nb_{ss} decreased with increasing Ta+W sum in the normal Nb_{ss}, see Figure 5.13.

In the alloys with Ta and Al and Cr (i.e., the alloys JZ3 and JZ3+) the trend of the data would suggest (1) that the Si concentration and the Sn/Ge ratio in the normal Nb_{ss} respectively decreased and increased with increasing Sn/Ge ratio in the alloy, (2) that the Ta/W ratio and the Ta+W sum in the normal Nb_{ss}, respectively decreased and increased with Sn/Ge ratio in the alloy, (3) that the Sn/Ge and Ta/W ratios and the Ta+W sum in the normal Nb_{ss}, respectively increased and decreased with increasing Al+Cr sum in the normal Nb_{ss}, (4) that the Cr/Al ratio in the normal Nb_{ss} decreased with increasing Sn/Ge and Ta/W ratios in the normal Nb_{ss}, (5) that the Cr/Al ratio increased with Ta+W sum in the normal Nb_{ss}, (6) that the Ti concentration in the normal Nb_{ss} decreased with increasing Ta+W sum in the normal Nb_{ss} (i.e., the same trend as in the alloys without Al and Cr), (7) that the Al+Cr content of the normal Nb_{ss} decreased with increasing Ta+W sum in the normal Nb_{ss} (figure 5.14) and (8) that the Cr/Al ratio in the normal Nb_{ss} increased with decreasing Ti in the normal Nb_{ss} (figure 5.15). Figures 5.16 and 5.17 respectively would suggest a maximum of Al+Cr in the normal Nb_{ss} of about 18 at.% for Sn/Ge ≈ 5.0 and a minimum of Cr/Al of about 2.25 for Sn/Ge ≈ 5.5.

The alloys with Mo and Al and Cr additions (i.e., the alloys JZ4 and JZ5) had the same Sn/Ge and Cr/Al ratios (= 1) and the same Al+Cr sum (= 9.6 at.%) but the alloy JZ5 was richer in Ti than the alloy JZ4. In these alloys the Nb_{ss} was stable at a very low volume fraction in the heat treated microstructures. In both alloys the Nb_{ss} with no Si was formed. The data would suggest that the increase in the Ti content in the alloy JZ5 respectively decreased and increased the Sn/Ge and Mo/W ratios in the Nb_{ss}

from 8 to 0.75 and from 0.74 to 1.3 and also increased the Al+Cr sum from 15 to 23 at.%. The alloy JZ4 is directly comparable with the alloy JZ3+. The limited data for these two alloys would suggest that the Si concentration in the Nb_{ss} decreased with increasing Sn/Ge ratio and Al+Cr sum of the Nb_{ss}.

The vol% of Nb_{ss} in the alloys decreased with increasing Ge+Sn concentration in the alloys (figure 5.18) and with increasing total refractory metal content of the alloys.

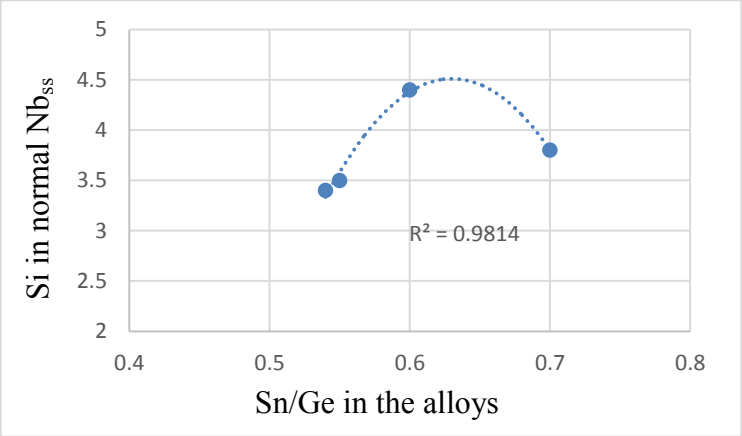

Figure 5.9 Si in normal Nb_{ss} (ordinate) versus (abscissa) Sn/Ge ratio in the alloys with Ta and no Al and Cr.

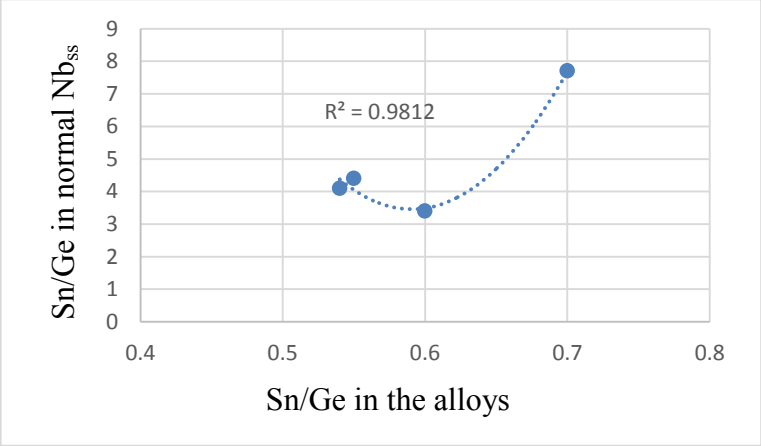

Figure 5.10 Sn/Ge ratio in normal Nb_{ss} (ordinate) versus (abscissa) Sn/Ge ratio in the alloys with Ta and no Al and Cr.

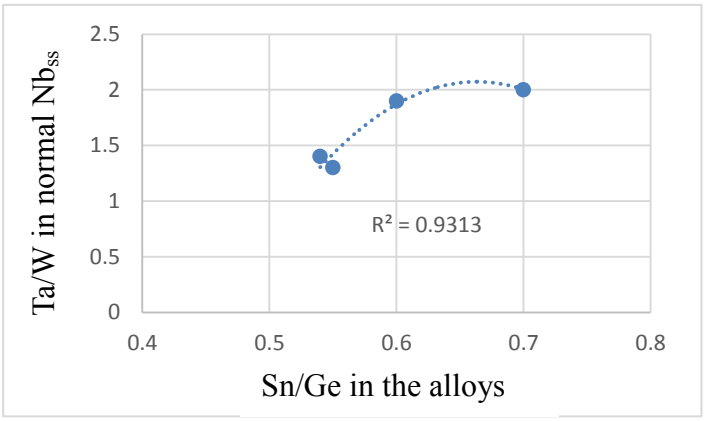

Figure 5.11 Ta/W ratio in normal Nb_{ss} (ordinate) versus (abscissa) Sn/Ge ratio in the alloys with Ta and no Al and Cr.

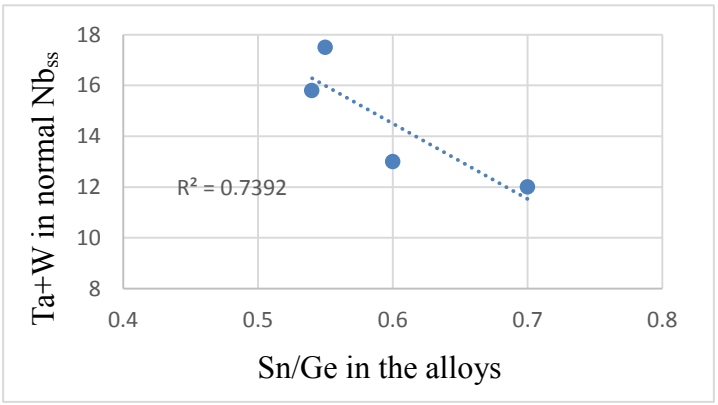

Figure 5.12 Ta+W sum in normal Nb_{ss} (ordinate) versus (abscissa) Sn/Ge ratio in the alloys with Ta and no Al and Cr.

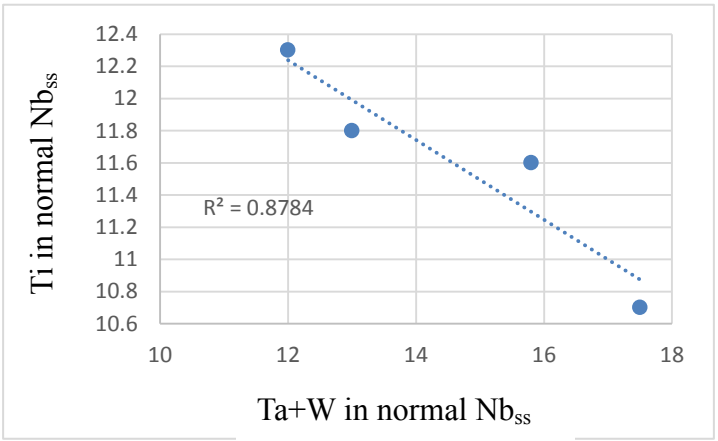

Figure 5.13 Ti in normal Nb_{ss} (ordinate) versus (abscissa) Ta+W sum in normal Nb_{ss} in the alloys with Ta and no Al and Cr.

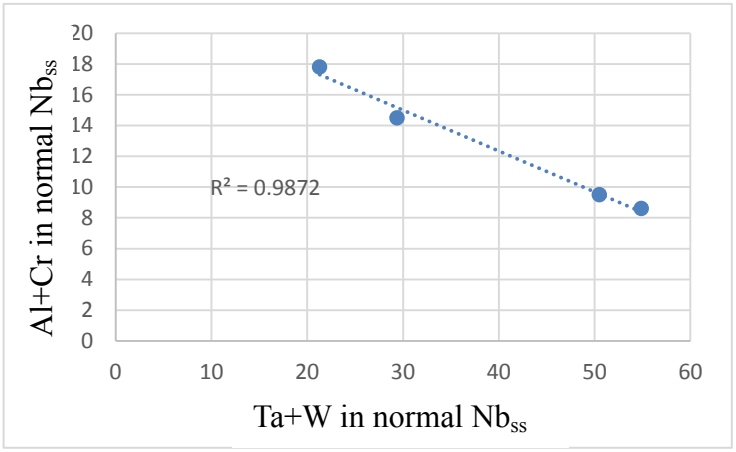

Figure 5.14 Al+Cr in normal Nb_{ss} (ordinate) versus (abscissa) Ta+W sum in normal Nb_{ss} in the alloys with Ta and with Al and Cr.

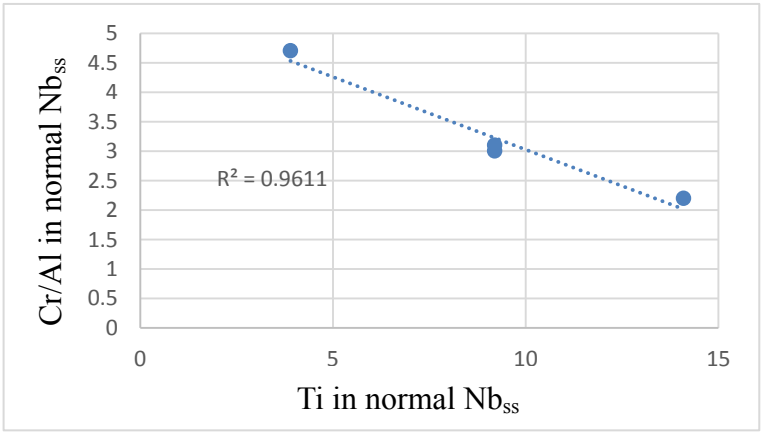

Figure 5.15 Cr/Al in normal Nb_{ss} (ordinate) versus (abscissa) Ti in normal Nb_{ss} in the alloys with Ta and with Al and Cr.

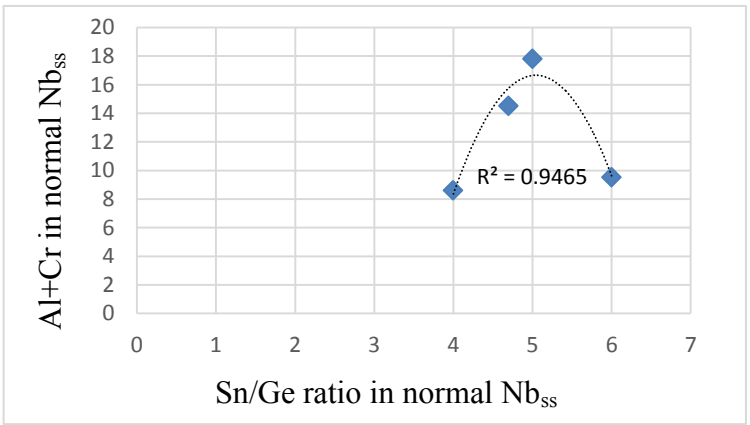

Figure 5.16 Al+Cr sum in normal Nb_{ss} (ordinate) versus (abscissa) Sn/Ge ratio in normal Nb_{ss} in alloys with Ta and with Al and Cr.

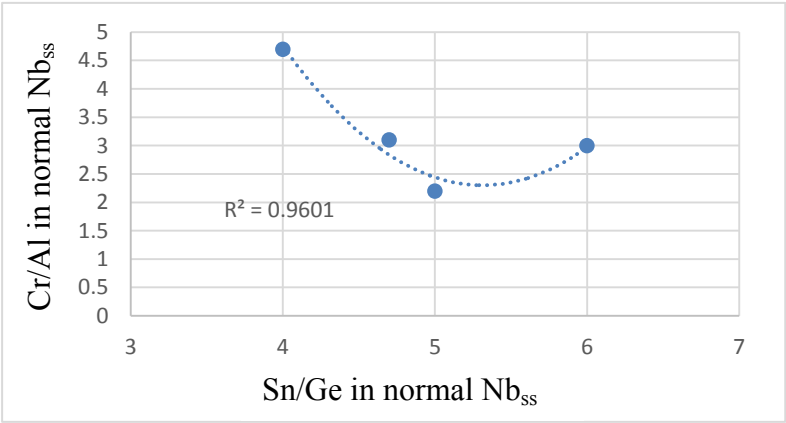

Figure 5.17 Cr/Al ratio in normal Nb_{ss} (ordinate) versus (abscissa) Sn/Ge ratio in normal Nb_{ss} in alloys with Ta and with Al and Cr.

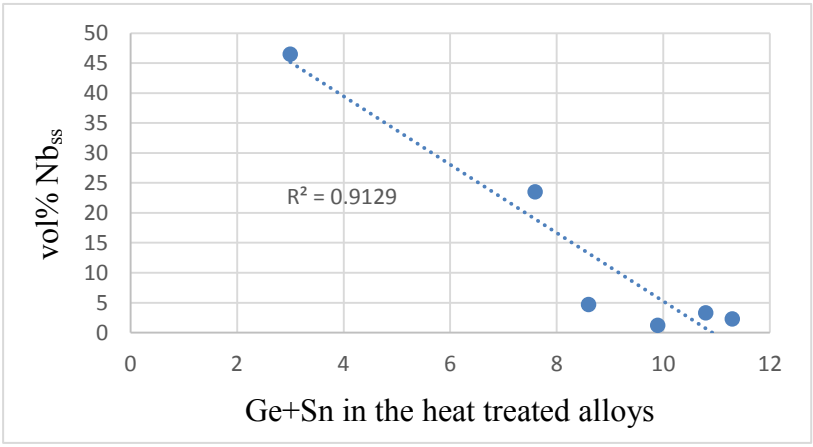

Figure 5.18 vol% Nb_{ss} (ordinate) versus (abscissa) Ge+Sn concentration in the heat treated alloys of this study.

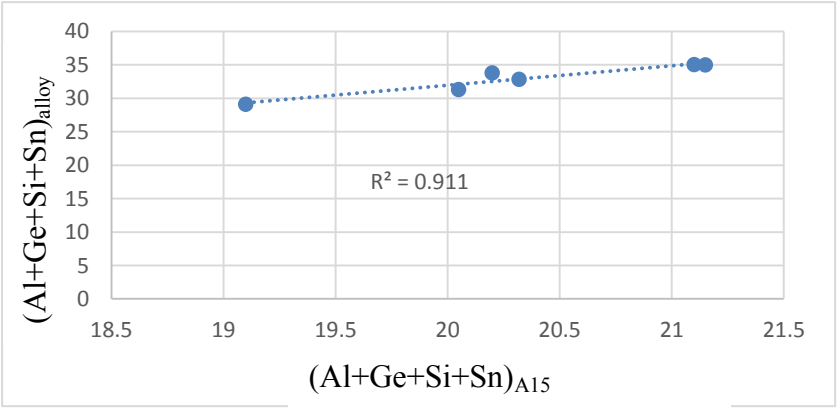

Figure 5.19 $(Al+Ge+Si+Sn)_{alloy}$ (ordinate) versus (abscissa) $(Al+Ge+Si+Sn)_{A15}$ for the alloys of this study.

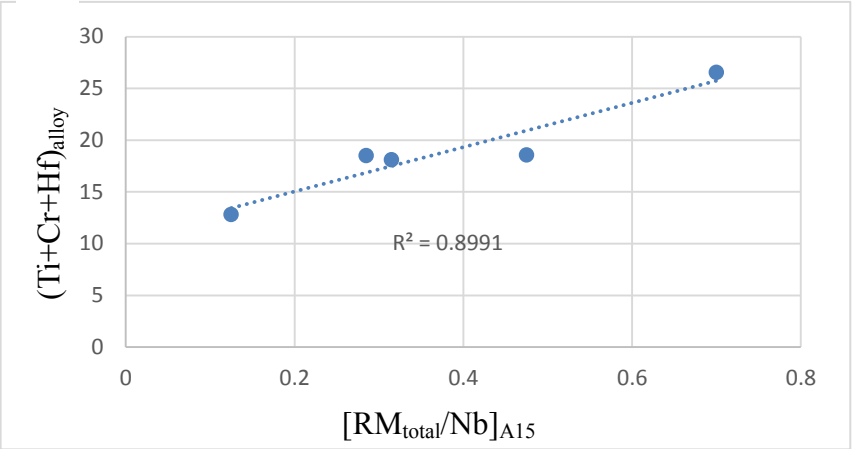

Figure 5.20 $(Ti+Cr+Hf)_{alloy}$ (ordinate) versus (abscissa) $[RM_{total}/Nb]_{A15}$ for the alloys of this study.

The A15 compound

The solute elements Al, Cr, Ge, Mo, Si, Sn, Ta and the solvent Nb can form the following A15 compounds (prototype Cr_3Si): Nb_3Al, Nb_3Ge, Nb_3Si (metastable), Nb_3Sn, Ta_3Sn, Mo_3Si, Mo_3Al, Mo_3Ge, Mo_3Sn and Cr_3Ge. No A15 compounds were stable in the alloy JZ1 owing to its low Ge+Sn concentration, which is in agreement with other research in our group and the literature. The average value of the Al+Ge+Si+Sn sum of the A15 compounds observed in the alloys of this study was 20.3, which is in agreement with other data from our research group. The relationship between the Al+Ge+Si+Sn sum of the compounds and alloys is shown in figure 5.19. The refractory metal (RM) content of the alloys was also important for the stability of the A15 compounds, as refractory metals can form A15 compounds (see above). The importance of the effect between RM and TM elements for the stability of the A15 compounds is shown in the figure 5.20.

C14-Cr_2Nb Laves phase

The solute elements Hf, Ta and Ti and the solvent Nb form with Cr the C14 Laves phase. In the alloys studied in this thesis that contained Ta the concentration of Nb in the Laves phase was essentially constant (unchanged). If the Laves phase in these alloys is written down as AB_2 where A = TM + RM and B = Cr + Al + Ge + Si + Sn

then after the heat treatment the A and B contents respectively decreased and increased (figure 5.21) and the average B content (62.7 at.%) was lower than 66.6 at%, in agreement with Geng and Tsakiropoulos (2007). Furthermore, the Ta+W content increased after the heat treatment (and was greater than the Mo+W content of the Laves phase in the Mo containing alloys).

In the Mo containing alloys studied in this thesis the Nb concentration in the Laves phase was not constant, the (A-Nb) content decreased after the heat treatment but the B and Mo+W contents were essentially the same (unchanged). In the alloys with the same Ti concentration the Laves phase had Ta/W > Mo/W (1.86 versus 1.25) but in the alloy with higher Ti content (alloy JZ5) the Laves phase had Mo/W = 2.2.

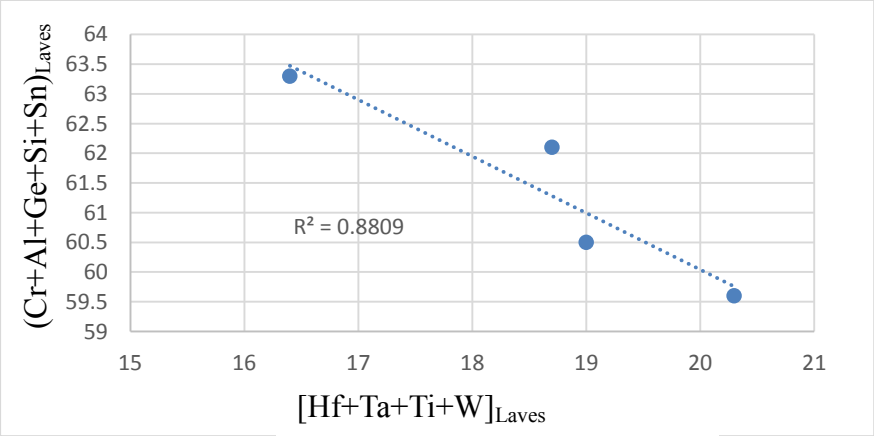

Figure 5.21 $(Cr+Al+Ge+Si+Sn)_{Laves}$ (ordinate) versus (abscissa) $[Hf+Ta+Ti+W]_{Laves}$ for the Ta containing alloys of this study.

<u>Nb_5Si_3</u>

In the alloys with 1.2 at.% < Sn < 4 at.% (JZ2 and JZ3) and only in the cast microstructure the Ti-rich Nb_5Si_3 was also richer in Sn compared with the "normal" Nb_5Si_3. In the heat treated microstructures of these alloys the Sn concentration in the Ti-rich Nb_5Si_3 was essentially the same as in the "normal" Nb_5Si_3 and at the concentrations observed in other Sn containing alloys in our group.

In the alloys with Sn > 4 at.% (JZ3+, JZ4 and JZ5) in the cast microstructure the Ti rich Nb_5Si_3 was also richer in Sn compared with the "normal" Nb_5Si_3, but in the heat treated microstructure the Ti-rich Nb_5Si_3 was poorer in Sn compared with the "normal" Nb_5Si_3, and the latter was now the Sn-rich Nb_5Si_3. This was an unexpected (and surprising) result as it has not been observed previously in our group or reported in the literature, as it is widely accepted that Sn partitions to the Nb_{ss} and Ge to the Nb_5Si_3. The high Sn concentration in the "normal" Nb_5Si_3 might be a consequence of the higher Sn concentration in the alloys JZ3+, JZ4 and JZ5, compared with previously studied alloys. It was also noted that all Sn-rich Nb_5Si_3 had lower Si concentration than the Sn poor Nb_5Si_3, which is another confirmation that Si is substituted by Sn in the silicide. If only the Ti-rich Nb_5Si_3 was rich in Sn, then this could be attributed to Ti forming Ti_5Sn_3 (prototype Mn_5Si_3, like Ti_5Ge_3). Clearly, this is not the case. Further research is required to clarify this point.

5.4 Conclusions

In this chapter the microstructures of the alloys Nb-12Ti-18Si-6Mo-2.5W-7.5Sn-5Ge -1Hf-5Al-5Cr (JZ4) and Nb-20Ti-18Si-6Mo-2.5W-7.5Sn-5Ge-1Hf-5Al-5Cr (JZ5) in the as cast and heat treatment conditions were studied. The conclusions of this chapter were as follows:

1. Macrosegregation of Si existed in both alloys.
2. The phases in the microstructures of the as cast alloys JZ4 and JZ5 were the Nb_5Si_3, A15 phase, C14-Cr_2Nb, TM_5Sn_2X and HfO_2. The Nb_5Si_3 was present in the β and α forms in both alloys.
3. The phases in the microstructures of the alloys JZ4 and JZ5 after the heat treatment at 1500 ˚C for 100 h were the βNb_5Si_3, αNb_5Si_3, A15 phase, $(Nb,Mo,W)_{ss}$ and HfO_2, with a very small vol% of the C14-Cr_2Nb Laves phase only present in the former alloy.
4. Aluminium oxide formed in the heat treated microstructure near the surface areas of the alloy JZ4.

5. The stability of C14-Cr_2Nb was suppressed when alloying with Mo instead of Ta in the alloys.
6. The βNb_5Si_3 was stabilised to a larger extent at 1500 ˚C in the alloys JZ4 and JZ5 owing to the addition of Mo and W.
7. The solubility of Mo in the Nb_5Si_3 was increased in the alloys JZ4 and JZ5 probably owing to the addition of Ge.
8. The solubility of Sn in the Nb_5Si_3 in the heat treated microstructures of the alloys JZ3+, JZ4 and JZ5 was high and up to 6.1 at.%, probably owing to the higher Sn concentration in these alloys.

Chapter 6

Isothermal oxidation at 800 ˚C and 1200 ˚C

6.1 Thermogravimetric analysis at 800 ˚C

TG curves of the alloys studied in this thesis after exposure to air for 100 h at 800 ˚C are shown in Figure 6.1, where the weight change (g/cm^2) is plotted as function of time (h). The TG results were analysed using the following equations for linear and parabolic oxidation (Schutze 2000)

$$\frac{\Delta m}{A} = k_1 t \qquad (6.1)$$

$$\left(\frac{\Delta m}{A}\right)^2 = k_p t \qquad (6.2)$$

where Δm is the weight of samples, A is the surface of samples and t is the exposure time.

The weight gain and oxidation rate constants of the alloys are listed in Table 6.1. Images of the oxidised specimens are shown in Figure 6.2. The oxidation of the alloys JZ1 and JZ2 followed linear kinetics and their oxidation rates were essentially the same. The weight gain of both alloys increased gradually before about 40 h and after about 56 and 54 h the alloys JZ1 and JZ2, respectively, showed an abrupt drop in weight gain, after which the weight increased linearly at the similar rate as before up to 40 h. The sudden weight changes could be associated with the spallation of the oxide scales and their disintegration to powder (Figure 6.2). The latter indicated that these two alloys were susceptible to pest oxidation. The weight gains of the alloys JZ1 and JZ2 after oxidation for 100 h were 33.59 mg/cm^2 and 28.93 mg/cm^2, respectively. The addition of 5 at.% Al and 5 at.% Cr in the alloy JZ3 apparently decreased the oxidation rate and did not change oxidation kinetics but reduced the linear oxidation rate by an order of magnitude. No pest oxidation and good adherence of the oxide scale were observed in the alloy JZ3, which would suggest that Al and Cr improved

the properties of the scale. Comparison of the TG data of the alloys JZ3 and JZ3+ shows that before 40 h the oxidation rate of the latter was an order of magnitude lower than that of the former but oxidised very fast after this time and finally suffered from complete disintegration to powder after exposure to air for 74 h. Considering the actual compositions of both alloys, which differ only in the Sn content, this result would suggest that in Ta and W containing alloys there is an upper limit to the concentration of Sn above which the benefit of Sn on oxidation were lost. The weight gains of the alloys JZ4 and JZ5 after 100 h exposure to air were 0.82 mg/cm^2 and 0.57 mg/cm^2, respectively. The alloys JZ4 and JZ5 exhibited the best oxidation resistance at 800 ˚C，gained the lowest weight compared with the alloys JZ1 to JZ3+ (Table 6.1), the cubic specimens retained their shape (Figure 6.2) and did not form thick oxide scales. Pest oxidation and spallation of oxide scales did not occur in these alloys (Figure 6.2). The TG curves of these two alloys can be seen in figure 6.1b. The alloy JZ5 exhibited weight loss for the first 60 hours but not the alloy JZ4. The oxidation data for the whole duration of the isothermal oxidation experiment exhibited parabolic oxidation kinetics for both of alloys (Table 6.1) but the R^2 value for JZ4 was 0.58 compared with 0.81 for JZ5. Low R^2 value was also exhibited by the alloy JZ4 from 9 to 100 hours, see Table 6.1. The oxidation of the alloys of this study at 800 ˚C was inferior to that of the single crystal Ni superalloy CMSX-4, which gained 0.05 mg/cm^2 after 50 hours and had $k_p = 4 \times 10^{-14}$ g^{2}cm^{-4}s^{-1}. The different oxidation behaviours of the alloys JZ4 and JZ5 at 800 ˚C that were shown in figure 6.1b require further study regarding their reproducibility with oxidation specimens cut from larger ingots. This will be considered in a separate PhD program in the group. Only the microstructures of the specimens of the oxidised alloys JZ3, JZ4 and JZ5 shown in figure 6.2 were subjected to further study, which is reported in the following sections.

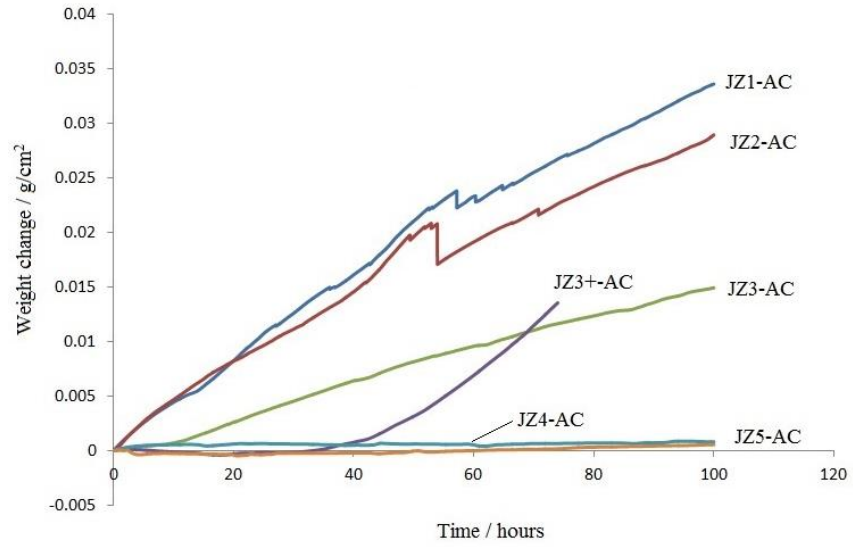

(a)

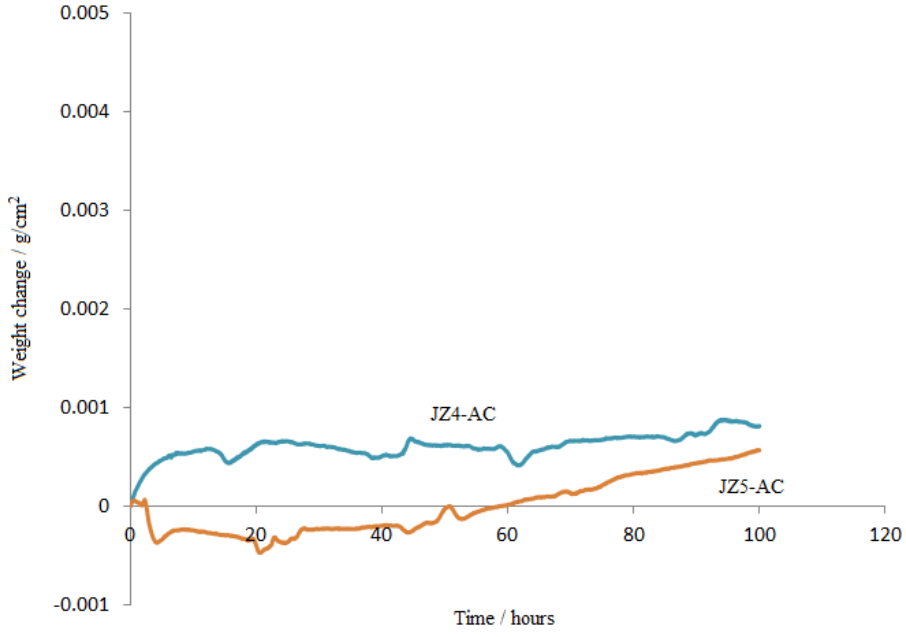

(b)

Figure 6.1 TG curves for the alloys after isothermal oxidation in air at 800 ˚C for 100 h.

Table 6.1 Weight gain and oxidation rate constants of the alloys studied in this thesis at 800 ˚C for 100 h.

Alloy	Weight gain (mg/cm^2)	800 ˚C	
		k_l ($g\ cm^{-2}\ s^{-1}$)	k_p ($g^2\ cm^{-4}\ s^{-1}$)
JZ1	33.59 (100 h)	1.14×10^{-7} (0-58 h) 7.46×10^{-8} (58-100 h)	-
JZ2	28.93 (100 h)	1.01×10^{-7} (0-53 h) 6.77×10^{-8} (53-100 h)	-
JZ3	14.92 (100 h)	4.39×10^{-8} (0-100 h)	-
JZ3+	13.93 (74 h)	6.45×10^{-9} (0-45 h) 1.15×10^{-7} (45-74 h)	-
JZ4	0.82 (100 h)	-	1.02×10^{-12} (0-100 h)$^{+}$ 9.9×10^{-12} (0-9h)* 9.4×10^{-13} (9-100h)
JZ5	0.57 (100 h)	-	7.33×10^{-12} (0-100 h)$^{+}$ 1.2×10^{-11} (45-100h)*

* $R^2>0.95$, $^{+}$ see text

JZ1

JZ2

JZ3

JZ3+

JZ4 JZ5

Figure 6.2 TG samples (3×3×3 mm^3) after isothermal oxidation in air at 800 ˚C for 100 h. Partial pesting was observed in the alloys JZ1 and JZ2 and the alloy JZ3+ suffered from complete disintegration to powder .

The alloy Nb-12Ti-18Si-6Ta-2.5W-5Sn-5Ge-1Hf-5Al-5Cr (alloy JZ3)

BSE images of a cross section of the alloy JZ3 after the TG experiment are shown in Figure 6.3. The outer layer that exhibits darker contrast is the oxide scale. The latter was severely cracked and the cracks were formed parallel to the surface. The thickness of the scale was about 150 μm. The diffusion zone that has been reported to form in some alloys by our research group was not observed in the alloy JZ3.

The chemical analyses of the phases in the bulk and oxide scale are given in Table 6.2. The phases in the bulk were Nb_5Si_3, A15 phase, Nb_{ss} and C14-Cr_2Nb Laves with Ti-rich regions in the 5-3 silicide and the A15 compound. The Cr-rich A15 phase that was observed in the cast alloy was not present. There was no noticeable change in the compositions of the phases compared with the cast alloy (Table 4.2) but the volume fraction of the Nb_{ss} was increased. Furthermore, the Ti concentrations of the Ti-rich A15 and the Nb_{ss} were closer to the compositions of these phases in the heat treated alloy (Table 4.3). The same was the case for the Ta content of the Nb_{ss}. In the oxide scale Nb-rich and Si-rich oxides were formed (Table 6.2), with the former exhibiting bright contrast and the latter dark contrast. Some remaining Nb_5S_{i3} grains were observed in the oxide scale, indicating that oxidation occurred via the inward

diffusion of oxygen. The chemical composition of Nb_5Si_3 in the scale was essentially the same as that in the bulk (Table 6.2). The average oxygen concentration of the oxide was close to that of Nb_2O_5.

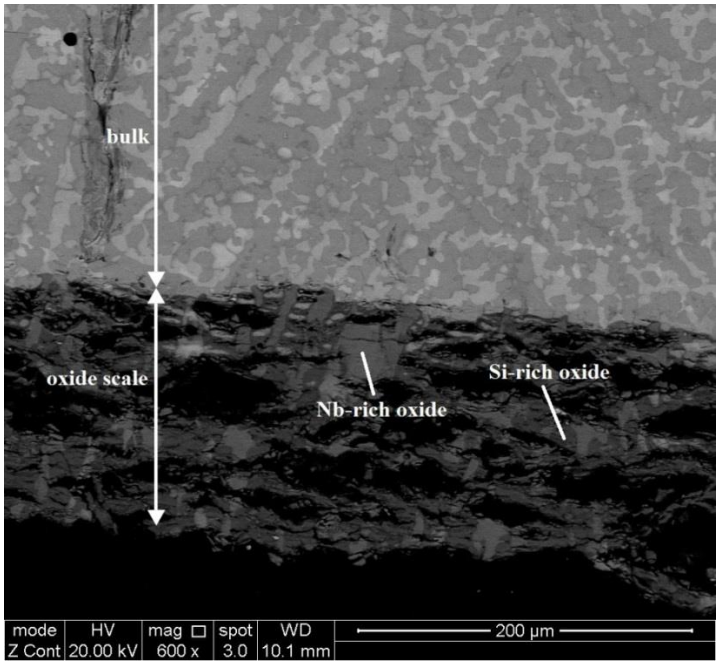

(a)

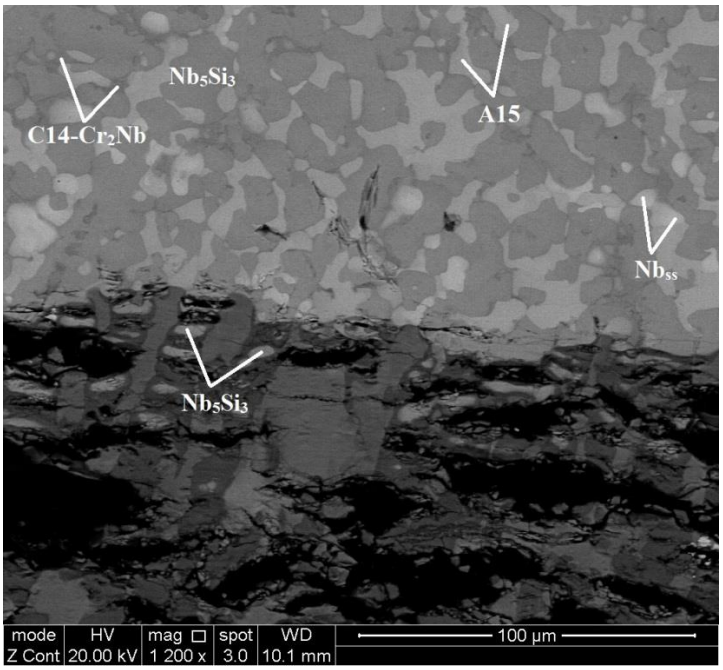

(b)

Figure 6.3 BSE images of the microstructure of a cross section of the oxidised alloy JZ3 (a) ×600 and (b) ×1200.

Table 6.2 The EDS analysis data (at.%) of phases in the alloy JZ3 after oxidation at 800 ˚C for 100 h.

Phase	O	Nb	Ti	Si	Ta	W	Sn	Ge	Hf	Al	Cr
Oxide scale											
Nb-rich oxide	73.6±0.6	14.5±0.2	2.9±0.3	1.4±0.4	2.5±0.1	1.7±0.1	0.4±0.1	0.5±0.1	0.1±0.1	1.3±0.1	1.2±0.2
	72.1-74.4	14.3-14.7	2.5-3.2	1.1-2.1	2.3-2.6	1.6-1.8	0.3-0.6	0.4-0.7	0.1-0.2	1.1-1.4	0.9-1.5
Si-rich oxide	72.3±1.2	12.3±0.6	2.9±0.4	8.1±0.3	1.6±0.1	0.3±0.1	0.2±0.1	0.6±0.3	0.3±0.1	1.0±0.1	0.3±0.1
	70.3-73.4	12.0-13.3	2.5-3.4	7.7-8.5	1.5-1.7	0.2-0.4	0.2-0.3	0.3-1.0	0.2-0.5	0.9-1.2	0.2-0.5
Nb_5Si_3	-	43.2±0.5	10.2±0.6	26.0±0.9	5.5±0.3	1.1±0.1	2.0±0.3	5.9±0.3	0.8±0.2	3.8±0.4	1.4±0.2
		42.6-43.8	9.5-10.9	25.3-27.3	5.2-5.9	1.0-1.2	1.6-2.2	5.5-6.4	0.6-1.0	3.1-4.0	1.3-1.7
Bulk											
Nb_5Si_3	-	43.5±0.4	9.6±0.4	26.8±0.8	6.0±0.3	1.0±0.2	1.7±0.5	6.1±0.3	0.7±0.2	3.2±0.3	1.4±0.1
		42.9-44.0	9.2-10.3	25.7-27.9	5.7-6.2	0.8-1.3	1.2-2.3	5.7-6.5	0.6-1.0	2.9-3.6	1.4-1.5
Ti-rich Nb_5Si_3	-	40.9±0.2	13.1±0.6	24.2±0.5	5.1±0.2	0.7±0.1	2.2±0.1	6.1±0.2	1.3±0.2	4.2±0.1	2.3±0.1
		40.7-41.1	12.3-13.8	23.4-24.8	4.8-5.4	0.6-0.8	2.0-2.2	5.9-6.4	1.0-1.4	4.1-4.3	2.2-2.4
A15	-	52.8±0.5	9.0±0.8	5.2±0.7	9.5±0.7	6.4±0.7	7.3±0.1	1.9±0.3	0.3±0.2	4.4±0.3	3.1±0.4
		52.1-53.4	8.4-10.0	4.2-6.0	9.0-10.6	5.8-7.4	7.1-7.4	1.7-2.2	0.1-0.6	4.1-4.9	2.7-3.6
Ti-rich A15	-	49.6±0.7	12.0±0.9	5.5±0.7	8.0±0.3	4.9±0.5	7.2±0.1	2.1±0.3	0.4±0.1	5.3±0.2	5.0±0.8
		48.8-50.6	11.1-13.5	4.5-6.3	7.6-8.4	4.4-5.7	7.0-7.3	1.7-2.4	0.2-0.6	5.0-5.7	3.9-5.9
Nb_{ss}	-	47.9±1.1	8.9±1.0	3.2±0.6	13.0±0.6	13.3±0.8	2.2±0.2	1.3±0.3	0.2±0.2	3.9±0.3	6.0±1.1
		46.8-49.2	7.7-10.3	2.3-3.6	12.4-13.8	12.2-14.2	2.0-2.5	0.9-1.8	0-0.4	3.5-4.2	4.6-7.5
C14-Cr_2Nb	-	21.8±1.1	9.6±1.2	9.1±0.4	6.3±0.6	2.3±0.3	0.4±0.3	1.4±0.3	1.7±0.1	4.7±0.3	42.8±2.0
		20.0-22.9	8.5-10.8	8.6-9.7	5.6-7.1	2.0-2.7	0.3-0.9	1.1-1.8	1.5-1.9	4.2-5.0	41.4-46.2

The alloy Nb-12Ti-18Si-6Mo-2.5W-7.5Sn-5Ge-1Hf-5Al-5Cr (alloy JZ4)

Figure 6.4 shows the microstructure of a cross section of the alloy JZ4 after the TG experiment and shows the bulk and oxide scale. The latter was dramatically thinner than that formed on the alloy JZ3, and was about 3 μm. Some cracks were observed in the scale.

Table 6.3 gives the chemical composition of the phases in different regions. The phases in the bulk were the same as those in JZ4-AC with the exception of the Ti-rich A15 that was not observed and with no apparent change in the compositions of the 5-3 silicide and the Laves phase. The content of W in the A15 phase was decreased by 1.6 at.% (the W content of the A15 also decreased after the heat treatment, see Table 5.3) and the content of Ti in the TM_5Sn_2X was slightly increased after the oxidation. The mixed oxide that formed the oxide scale was rich in Nb and Si but very lean in other elements and the oxygen concentration was close to that of Nb_2O_5. Its chemical composition was essentially the same as that of the Si-rich oxide formed on the alloy JZ3 (Table 6.2), if we substitute Ta with Mo. Some small regions just below the oxide scale exhibited a darker contrast, see Figure 6.4b. There were oxidised A15 phase, which indicated internal oxidation of the alloy just below the scale.

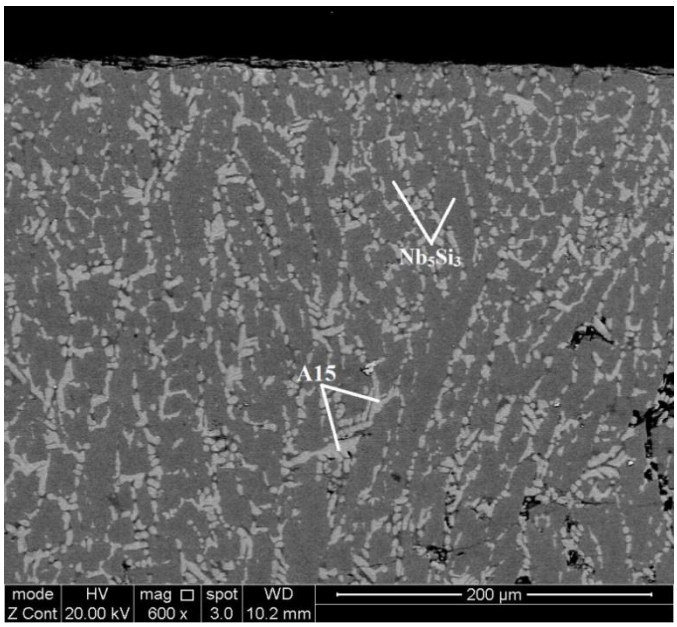

(a)

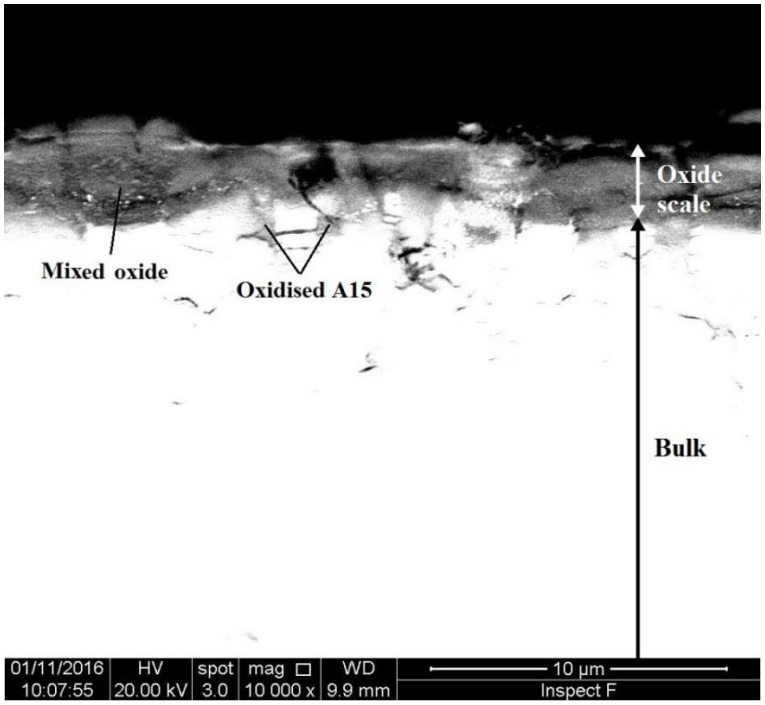

(b)

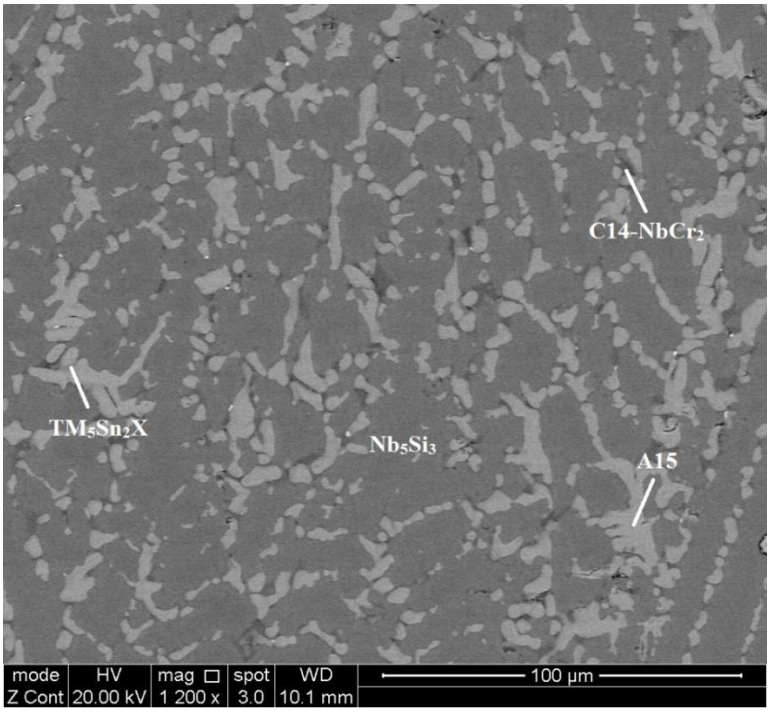

(c)

Figure 6.4 BSE images of the microstructure of a cross section of the oxidised alloy JZ4 (a) ×600, (b) ×10000 and (c) ×1200, shows the microstructure in the bulk.

Table 6.3 The EDS analysis data (at.%) of phases in the alloy JZ4 after oxidation at 800 ˚C for 100 h.

Phase	O	Nb	Ti	Si	Mo	W	Sn	Ge	Hf	Al	Cr
Oxide scale											
Mixed Si-rich oxide	70.8±1.4	13.4±0.8	3.2±0.1	7.7±0.8	1.3±0.3	0.5±0.1	0.4±0.1	0.8±0.5	0.3±0.1	0.9±0.2	0.8±0.1
	69.0-72.4	12.1-14.1	3.0-3.3	6.6-8.8	0.8-1.6	0.4-0.5	0.3-0.5	0.3-1.4	0.3-0.4	0.7-1.0	0.7-1.0
Bulk											
Nb_5Si_3	-	45.0±0.8	9.6±0.1	28.1±0.4	4.4±0.3	1.4±0.2	1.1±0.1	6.4±0.6	1.0±0.1	1.9±0.3	1.2±0.2
		44.2-45.9	9.5-9.8	27.5-28.5	3.9-4.6	1.1-1.6	0.9-1.2	6.2-7.0	0.8-1.1	1.5-2.3	0.9-1.4
Ti-rich Nb_5Si_3	-	39.9±2.2	14.2±1.6	20.1±0.5	4.4±0.1	1.0±0.3	5.1±0.9	5.9±0.6	1.6±0.2	4.9±0.2	2.9±0.6
		38.2-43.6	11.5-15.4	19.4-20.7	4.2-4.6	0.7-1.5	3.7-6.1	5.6-6.9	1.3-1.9	4.7-5.1	2.0-3.6
TM_5Sn_2X[a]	-	24.1±3.1	27.9±2.7	8.5±2.4	3.7±0.3	0	16.5±3.0	4.5±0.3	3.0±0.2	7.3±0.5	4.4±0.2
		19.6-27.7	24.9-31.4	5.4-11.7	3.3-4.3		12.7-20.6	4.1-4.7	2.8-3.3	7.0-8.1	4.1-4.6
A15	-	41.9±1.5	11.6±0.8	2.6±0.4	14.2±0.3	6.7±0.4	8.6±0.5	2.1±0.2	0.5±0.2	6.5±0.4	5.4±0.8
		39.7-43.0	10.5-12.6	2.1-3.0	13.9-14.6	6.2-7.3	8.0-9.1	1.9-2.3	0.4-0.8	5.9-6.8	4.5-6.6
C14-Cr_2Nb	-	22.2±0.3	7.4±0.4	8.1±0.6	4.8±0.2	2.6±0.2	0.6±0.1	1.7±0.2	2.9±0.1	8.2±1.0	41.6±0.8
		21.6-22.5	7.0-8.1	7.3-8.9	4.7-5.1	2.2-2.8	0.5-0.8	1.5-2.1	2.8-3.1	7.2-9.8	40.4-42.4

[a] Prototype W_5Si_3 where TM = Nb, Ti and X = Si, Ge, Al.

Table 6.4 The EDS analysis data (at.%) of phases in the alloy JZ5 after oxidation at 800 ˚C for 100 h.

Phase	O	Nb	Ti	Si	Mo	W	Sn	Ge	Hf	Al	Cr
Oxide scale											
Mixed Si-rich oxide	72.3±1.0	10.5±1.1	5.1±0.3	7.1±1.0	1.3±0.2	0.3±0.1	0.5±0.2	1.5±0.5	0.2±0.1	0.6±0.1	0.7±0.6
	71.4-74.0	8.7-11.4	4.8-5.7	5.2-7.7	1.0-1.4	0.2-0.3	0.3-0.9	1.1-2.3	0.1-0.3	0.5-0.8	0.4-1.7
Bulk											
Nb_5Si_3	-	39.8±0.2	15.7±0.2	29.4±0.5	4.8±0.2	1.0±0.1	1.0±0.1	5.3±0.2	0.7±0.1	1.2±0.2	1.0±0.1
		39.4-40.0	15.5-15.9	29.3-29.8	4.6-5.2	0.9-1.1	0.7-1.1	5.1-5.6	0.6-0.8	1.1-1.4	0.9-1.1
Ti-rich Nb_5Si_3	-	33.7±0.8	20.4±0.4	19.7±0.2	5.6±0.3	0.9±0.1	5.7±0.3	5.5±0.2	1.1±0.1	4.8±0.2	2.5±0.4
		32.5-34.3	20.1-21.0	19.5-19.9	5.3-6.1	0.7-1.0	5.3-6.2	5.3-5.7	0.8-1.2	4.6-5.1	2.3-3.1
TM_5Sn_2X	-	21.2±5.6	32.2±4.9	9.5±4.5	4.2±0.5	0.2	15.9±4.8	4.1±0.9	1.4±0.2	6.9±0.9	4.5±1.0
		15.9-30.5	23.8-37.1	4.2-16.0	3.6-5.0		11.0-21.0	2.8-5.3	1.2-1.6	5.6-8.1	3.2-5.0
A15	-	32.2±0.3	18.3±0.3	2.7±0.2	16.6±0.2	5.4±0.1	9.4±0.1	2.0±0.4	0.3±0.1	6.6±0.1	6.4±0.2
		31.6-32.5	17.9-18.8	2.5-2.9	16.5-16.9	5.3-5.5	9.3-9.5	1.6-2.5	0.1-0.4	6.5-6.8	6.2-6.7
C14-Cr_2Nb	-	20.0±0.3	10.9±0.4	8.3±0.4	5.2±0.2	2.5±0.2	0.7±0.1	1.3±0.2	1.6±0.1	8.4±0.7	41.2±0.4
		19.4-20.2	10.4-11.4	8.0-8.9	5.0-5.5	2.3-2.7	0.6-0.9	1.1-1.6	1.5-1.8	7.7-9.4	40.5-41.5

The alloy Nb-20Ti-18Si-6Mo-2.5W-7.5Sn-5Ge-1Hf-5Al-5Cr (alloy JZ5)

BSE images of a cross section of the alloy JZ5 after the TG experiment are presented in Figure 6.5. The microstructure shows the bulk and oxide scale. The thickness of the oxide scale was about 3 μm, similar to that formed on the alloy JZ4. The cracking (Figure 6.5a) observed in the bulk microstructure could be introduced during the process of the SEM sample preparation.

The EDS data of the phases in the scale and bulk is given in Table 6.4. The phases in bulk were Nb_5Si_3, A15, TM_5Sn_2X and Laves phase. The mixed oxide was rich in Nb, Ti and Si and lean in other elements in the oxide scale. The oxygen concentration of the mixed oxide was close to that of Nb_2O_5. No significant change in the compositions of the phases was observed in the bulk compared with the cast alloy. There was no evidence of internal oxidation.

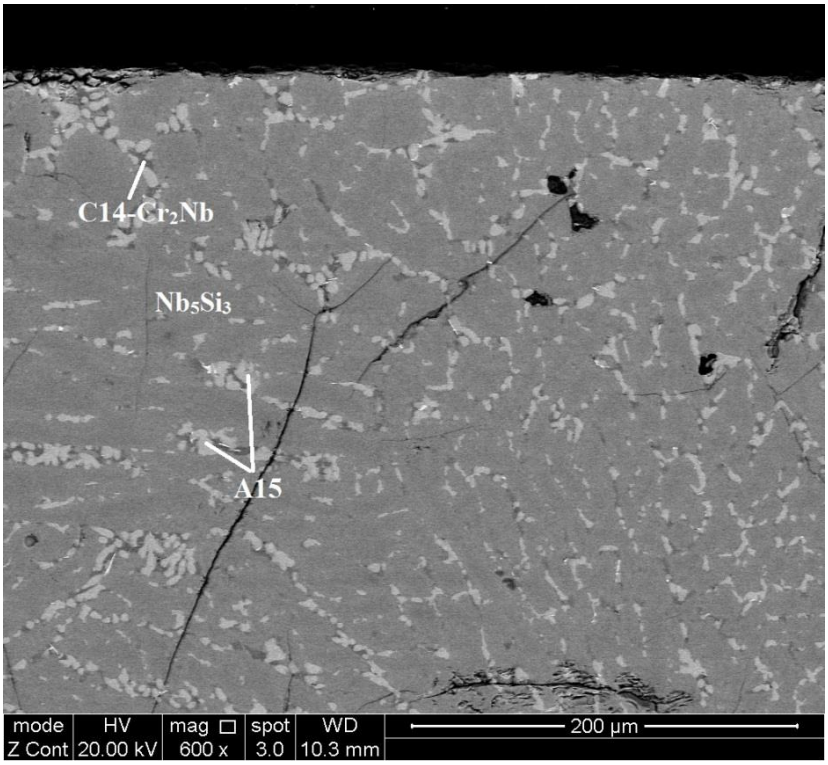

(a)

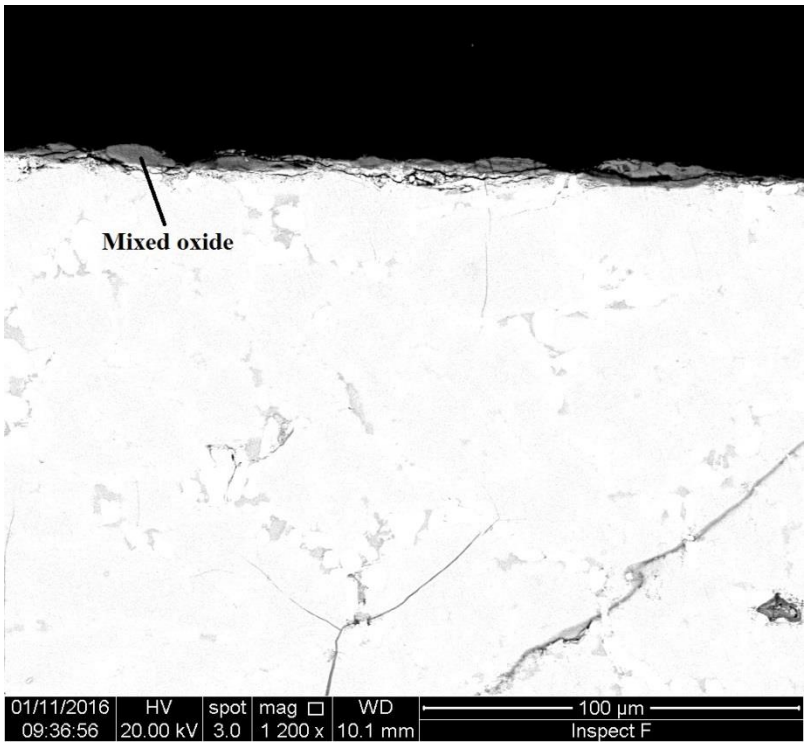
Mixed oxide
01/11/2016
09:36:56
HV
20.00 kV
spot
3.0
mag
1 200 x
WD
10.1 mm
100 µm
Inspect F

(b)

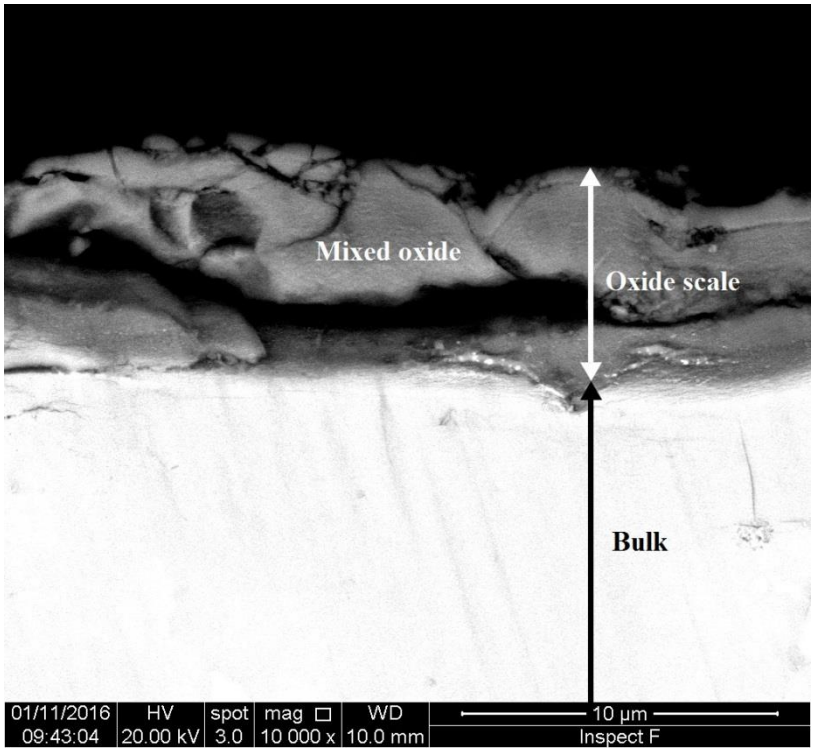
Mixed oxide
Oxide scale
Bulk
01/11/2016
09:43:04
HV
20.00 kV
spot
3.0
mag
10 000 x
WD
10.0 mm
10 µm
Inspect F

(c)

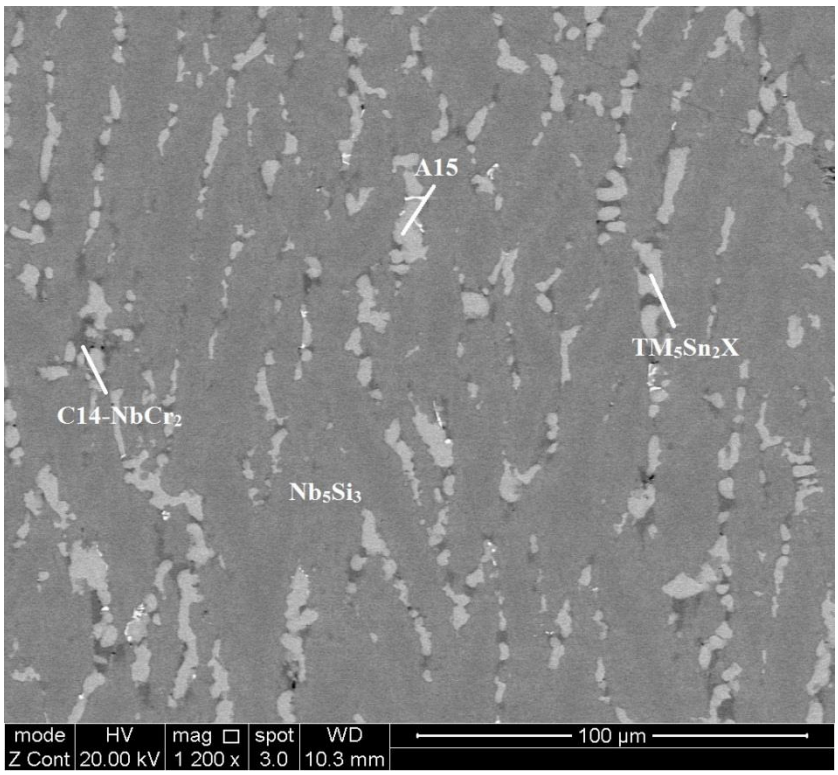

(d)

Figure 6.5 BSE images of the microstructure of a cross section of the oxidised alloy JZ5 (a) ×600, (b) ×1200, (c) ×10000 and (d) ×1200, shows the microstructure in the bulk.

6.2 Thermogravimetric analysis at 1200 ˚C

The TG curves of the alloys after exposure to air at 1200 ˚C for 100 h are shown in Figure 6.6. The weight change and oxidation rate constants of each alloy are given in Table 6.5. The alloys JZ1, JZ2 and JZ3 followed parabolic oxidation kinetics in the initial stage of oxidation that were followed by linear kinetics. The alloys JZ3+, JZ4 and JZ5 followed parabolic oxidation with lower rate in the early stage of oxidation.

The alloy JZ1 exhibited the worst oxidation behaviour, with spallation of the oxide scale and a high weight gain of 91.34 mg/cm^2. The increase in Sn and Ge contents in the alloy JZ2 slightly improved the oxidation behaviour at 1200 ˚C, presenting a lower weight change (71.39 mg/cm^2) after 100 h exposure and a better adherence of

the oxide scale. The addition of 5 at.% Al and 5 at.% Cr in the alloys JZ3 and JZ3+ dramatically reduced the oxidation rates, and the weight gains reduced to 24.21 mg/cm^2 and 14.02 mg/cm^2, respectively. There was good adhesion of the oxide scale of the latter alloy. The oxidation behaviour of the alloy JZ4 at 1200 ˚C was similar to that of the alloy JZ3+, with a weight gain of 13.43 mg/cm^2. In the case of the alloy JZ5 the oxidation rate was reduced further due to the increase in the content of Ti and the weight gain of 8.43 mg/cm^2 was the lowest in the JZ series of alloys. Good adhesion of the oxide scales was also observed in the alloys JZ4 and JZ5.

The parabolic rate constants of the polycrystalline alloys JZ3+, JZ4 and JZ5 were the closest to that of the single crystal Ni superalloy CMSX-4, which is about 1×10^{-11} g^{2}cm^{-4}s^{-1} at 1200 ˚C, and which had gained 0.4 mg/cm^2 after 50 hours. The microstructures of the oxidised alloys JZ2, JZ3, JZ3+, JZ4 and JZ5 were subjected to further study that is reported in the following sections. To date, the alloy JZ5 of this study has exhibited the best oxidation behaviour of Nb-silicide based alloys studied in our group. The reproducibility of the oxidation behaviour of the alloys JZ4 and JZ5 at 1200 ˚C using specimens from larger ingots will be subject of future research in the group.

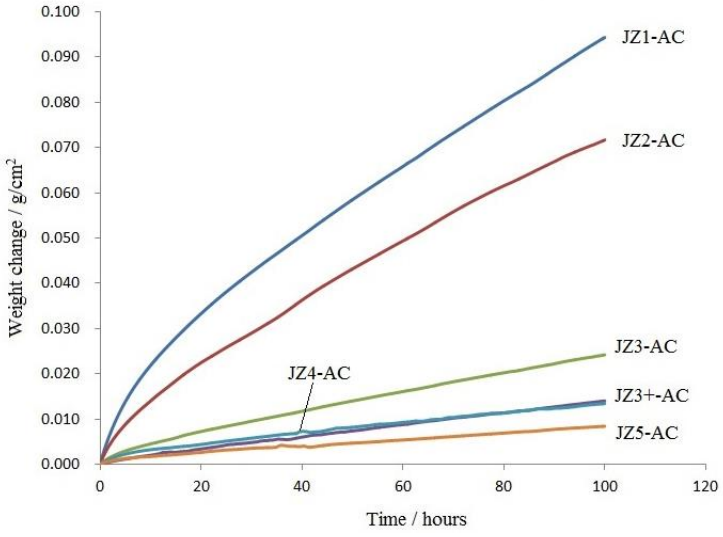

Figure 6.6 TG curves for the alloys after isothermal oxidation in air at 1200 ˚C for 100 h.

Table 6.5 Weight gain and oxidation rate constants of the alloys studied in this thesis at 1200 ˚C for 100 h.

Alloy	Weight gain (mg/cm^2)	1200 ˚C	
		k_l ($g\ cm^{-2}\ s^{-1}$)	k_p ($g^2\ cm^{-4}\ s^{-1}$)
JZ1	91.34 (100 h)	2.16×10^{-7} (9-100 h)	1.37×10^{-8} (0-9 h)
JZ2	71.69 (100 h)	1.78×10^{-7} (9-100 h)	5.52×10^{-9} (0-9 h)
JZ3	24.21 (100 h)	6.00×10^{-8} (9-100 h)	5.88×10^{-10} (0-9 h)
JZ3+	14.02 (100 h)	-	5.48×10^{-10} (0-100 h) 4.71×10^{-11} (0-6 h) 5.76×10^{-10} (6-100 h)
JZ4	13.43 (100 h)	-	5.04×10^{-10} (0-100 h) 2.92×10^{-10} (0-14 h) 5.44×10^{-10} (14-100 h)
JZ5	8.43 (100 h)	-	1.92×10^{-10} (0-100 h) 9.46×10^{-11} (0-9 h) 2.04×10^{-10} (9-100 h)

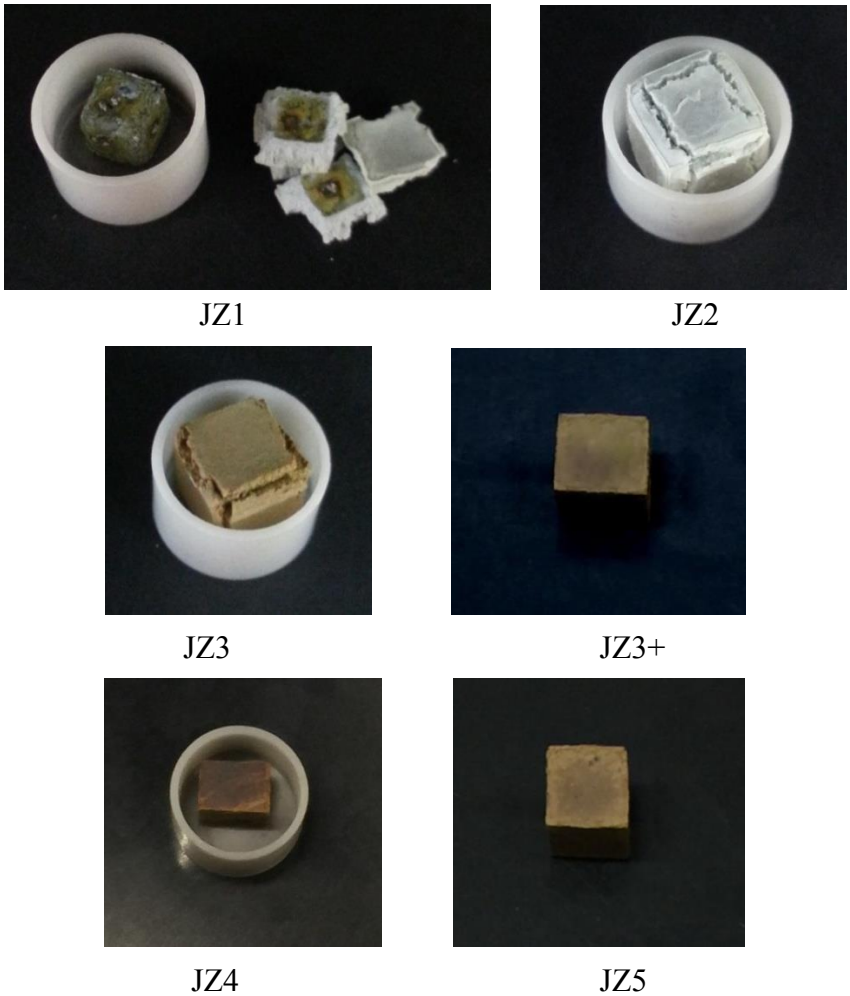

Figure 6.7 TG samples ($3\times3\times3\ mm^3$) after isothermal oxidation at 1200 ˚C for 100 h in air. The alloy JZ1 exhibited spallation of its oxide scale.

The alloy Nb-12Ti-18Si-6Ta-2.5W-5Sn-5Ge-1Hf (alloy JZ2)

BSE images of the microstructure of a cross section of the alloy JZ2 after isothermal oxidation at 1200 ˚C for 100 h are shown in Figure 6.8. There were three regions in the microstructure, namely the oxide scale, diffusion zone and bulk. Pores and cracks were observed in the oxide scale. The diffusion zone consisted of two different microstructures, which were marked as diffusion zone 1 and diffusion zone 2, in Figure 6.8.

The EDS data in Table 6.6 shows the compositions of three types of oxides that were formed in the oxide scale. There were a Nb-rich oxide (grey phase), a Ti-rich oxide (darker grey phase) and HfO_2 (white phase). There was also silicon oxide in the scale that appeared as a black phase and exhibited the same contrast with the pores and cracks under BSE imaging conditions. No Ge and Sn were detected in the oxidation products in the scale. The microstructure in the bulk of JZ2 after the oxidation was similar to that of the cast alloy (see Figure 3.8c) but the A15 compound which only formed in the bottom of the cast alloy was now present. The Ti-rich Nb_5Si_3 and A15 phase were leaner in Si and the former was richer in Ti and the Nb_{ss} was leaner in Sn, compared with JZ2-AC and JZ2-HT. The phases in the diffusion zone 2 were Nb_{ss}, Nb_5Si_3, A15, HfO_2 and Ti oxide. The latter exhibited black contrast and was formed adjacent to the Nb_5Si_3 and inside the solid solution and A15 compound where the Ti contents were reduced by 4.8 and 2.4 at.%, respectively compared with the bulk, owing to the consumption of Ti to form the oxide. This indicated contamination of the microstructure by oxygen to the depth of diffusion zone 2 below the scale (about 200 μm). The phases in the diffusion zone 1 were totally different from those in the diffusion zone 2. They were $Nb_5(Si_{1-x},Ge_x)_3$, $NbGe_2$ and HfO_2. There were W rich areas in the former compound. The *tI32*-W_5Si_3-type Nb_5Ge_3 and $NbGe_2$ are stable compounds in the Nb-Ge binary (Pappadimitriou *et al.* 2015). The former is also isomorpohous with βNb_5Si_3. Thus the $Nb_5(Si_{1-x},Ge_x)_3$ and the W-rich areas of the compound that formed in the diffusion zone 1, most likely were of the W_5Si_3-type silicides. The formation of $Nb_5(Si_{1-x},Ge_x)_3$ in the diffusion zone is in agreement with

the results of Hernandez-Negrete and Tsakiropoulos (2017).

In Figure 6.8a it should be noticed that there is a continuous layer exhibiting bright contrast that separates the diffusion zone 1 into two. The chemical analyses and the X-ray maps in Figure 6.9 suggested that the layer was extremely rich in Sn and lean in other elements as well as in oxygen. In the layer there were some regions of dark contrast, which were extremely rich in Ge (Figure 6.9). In the regions near the interface of the diffusion zones 1 and 2, a large amount of particles of white contrast (see Figure 6.8d) were dispersed in the Nb_{ss}, A15 and $Nb_5(Si_{1-x},Ge_x)_3$. These particles were too small for chemical analysis but X-ray maps suggested that some were rich in W (see Figure 6.10) and thus could be W-rich solid solution which was observed in JZ3-AC, JZ3-HT and JZ3+-HT. The maps in figure 6.10 also confirmed the enrichment in Ge and Sn towards the surface of the oxidised.

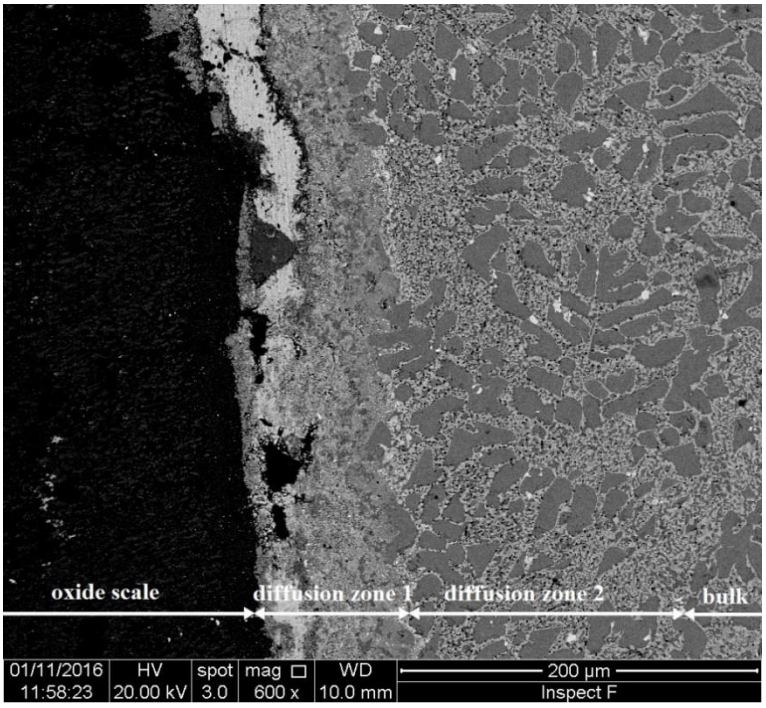

(a)

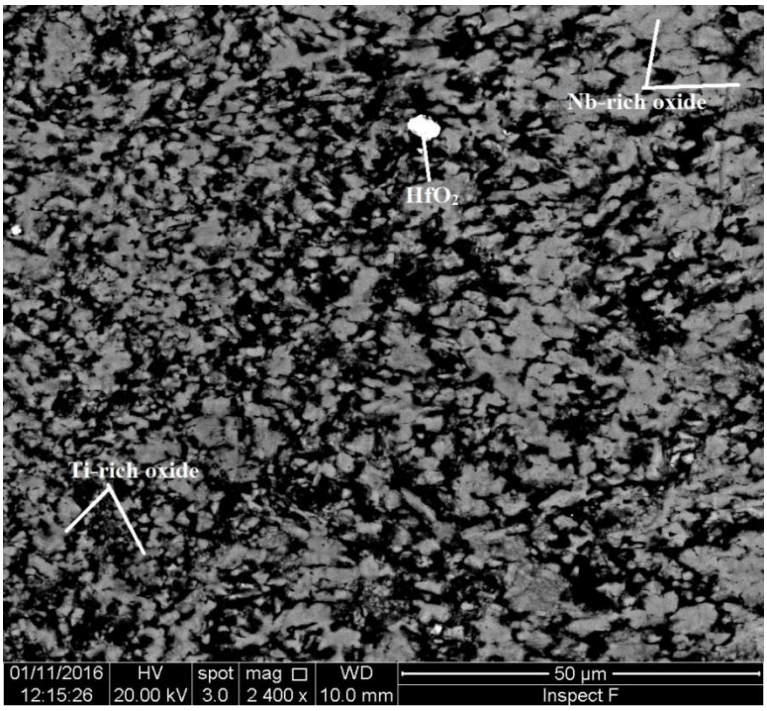
Nb-rich oxide
HfO2
Ti-rich oxide
01/11/2016 12:15:26
HV 20.00 kV
spot 3.0
mag 2 400 x
WD 10.0 mm
50 µm
Inspect F

(b)

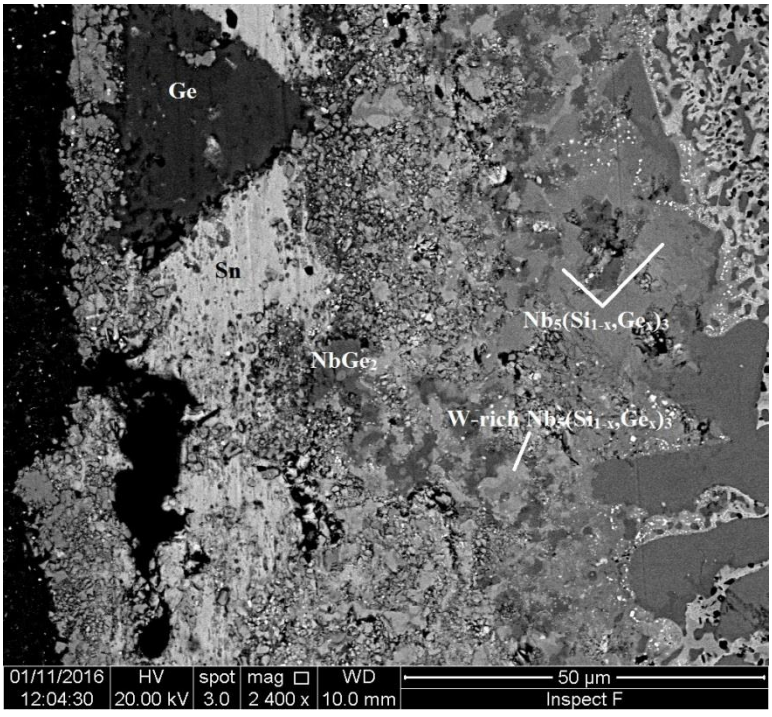
Ge
Sn
Nb5(Si1-x,Gex)3
NbGe2
W-rich Nb5(Si1-x,Gex)3
01/11/2016 12:04:30
HV 20.00 kV
spot 3.0
mag 2 400 x
WD 10.0 mm
50 µm
Inspect F

(c)

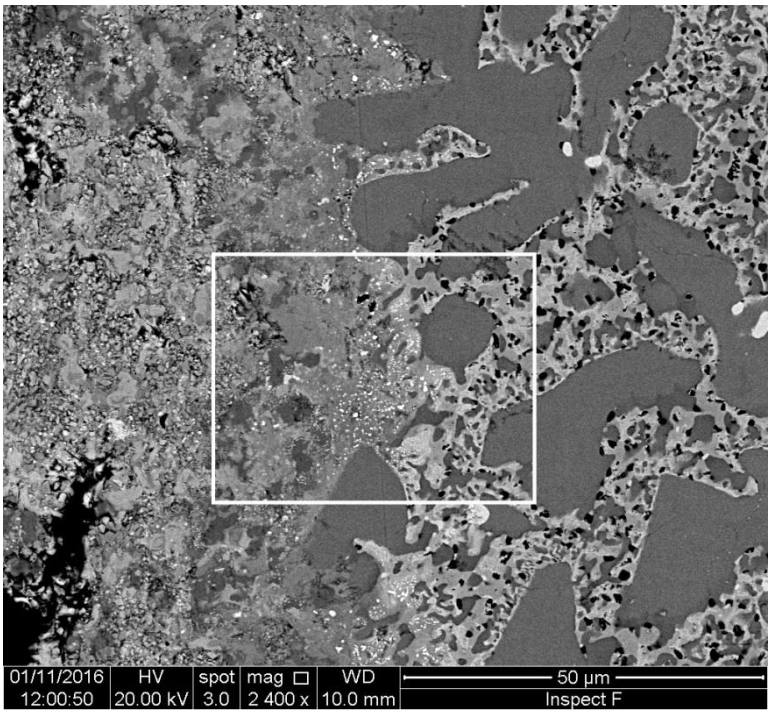

(d)

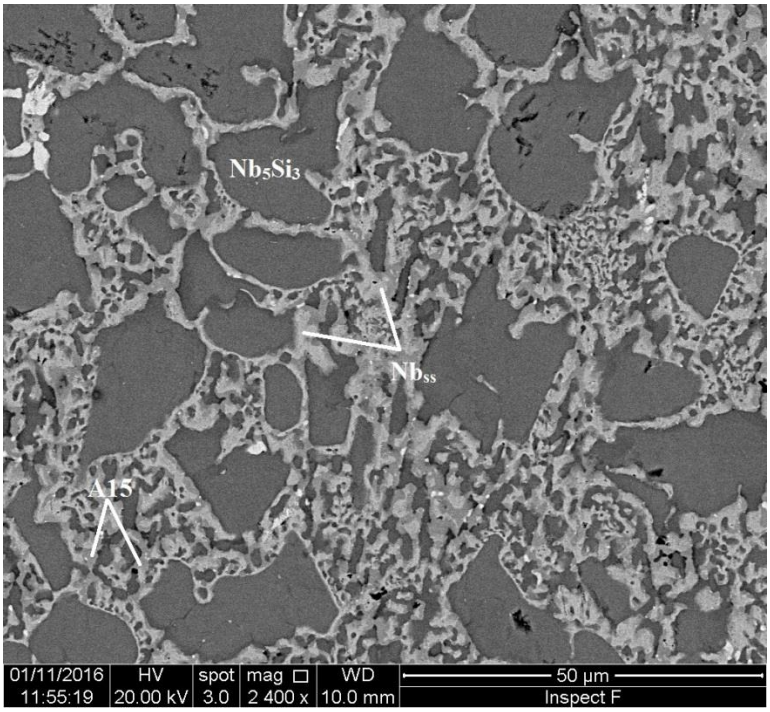

(e)

Figure 6.8 BSE images of the microstructure of a cross section of the oxidised alloy JZ2, (a) ×600, (b) ×2400, shows the microstructure of the oxide scale, (c) and (d) ×2400, show the diffusion zones 1 and 2, respectively and (e) ×2400 shows the microstructure in the bulk. For the region indicated by a rectangle in (d), see Figure 6.10 and text.

Table 6.6 The EDS anlysis data (at.%) of phases in the alloy JZ2 after oxidation at 1200 ˚C for 100 h.

	Phase	O	Nb	Ti	Si	Ta	W	Sn	Ge	Hf
Oxide scale	Nb-rich oxide	74.4±0.7	16.6±0.9	5.7±1.9	0.7±0.5	1.8±0.4	0.4±0.2	0	0	0.3±0.2
		73.3-75.0	15.6-17.7	3.6-7.5	0.3-1.4	1.3-2.3	0.3-0.7			0.2-0.6
	Ti-rich oxide	73.8±0.8	4.0±0.7	20.9±0.9	0.3±0.2	0.6±0.1	0	0	0	0.4±0.1
		72.8-74.6	3.5-5.2	19.7-22.2	0.1-0.5	0.6-0.7				0.3-0.4
	HfO_2	71.8±1.7	1.6±0.4	1.1±0.1	0.5±0.9	0	0	0	0	24.9±0.3
		69.7-73.2	1.2-1.9	1.0-1.1	0-1.6					24.6-25.1
Diffusion zone 1	$Nb_5(Si_{1-x}Ge_x)_3$	-	54.3±0.9	1.6±0.6	15.3±0.5	5.2±0.3	1.1±0.2	0	22.4±1.0	0
			52.8-54.8	1.1-2.7	14.6-15.7	4.7-5.4	0.9-1.4		21.6-24.1	
	W-rich $Nb_5(Si_{1-x}Ge_x)_3$	-	47.4±1.2	1.2±0.2	12.8±1.0	7.4±0.3	6.2±0.5	0.5±0.4	24.8±1.5	0
			45.7-48.7	1.0-1.5	12.2-14.6	7.2-7.9	5.7-6.9	0.3-1.0	22.7-26.6	
	$NbGe_2$	-	33.0±0.9	1.0±0.5	4.4±1.2	2.7±0.4	0.9±0.3	0.2±0.1	57.8±1.0	0
			32.0-34.1	0.2-1.4	2.8-5.8	2.3-3.4	0.6-1.5	0.1-0.4	56.5-5.89	
Diffusion zone 2	Nb_5Si_3	-	48.3±0.3	8.0±0.2	31.4±0.7	4.5±0.3	0.7±0.1	1.0±0.1	5.5±0.2	0.6±0.2
			47.8-48.7	7.6-8.2	30.7-32.4	4.1-4.9	0.6-0.9	0.9-1.1	5.3-5.7	0.5-0.9
	Ti-rich Nb_5Si	-	45.8±1.2	15.0±1.8	24.9±0.6	3.4±0.5	0.3±0.1	3.2±0.4	6.8±0.5	0.9±0.1
			44.1-46.6	13.7-17.7	24.2-25.6	2.7-3.7	0.2-0.4	2.8-3.7	6.3-7.4	0.7-1.0
	A15	-	61.0±0.8	14.2±1.0	4.7±0.9	4.6±0.3	2.0±0.4	10.3±0.3	3.2±0.1	0
			59.9-61.9	12.9-15.4	3.7-5.7	4.2-4.9	1.4-2.5	10.0-10.8	3.1-3.3	
	Nb_{ss}[a]	-	69.7	5.5	4.6	10.2	7.1	2.0	0.8	0.2
Bulk	Nb_5Si_3	-	47.0±1.0	8.2±0.2	31.9±0.8	4.6±0.3	0.7±0.12	1.0±0.1	5.9±0.5	0.7±0.1
			45.9-48.3	8.1-8.6	30.9-32.7	4.2-5.0	0.6-0.8	0.9-1.1	5.3-6.4	0.5-0.8
	Ti-rich Nb_5Si_3	-	42.9±1.5	17.0±2.2	26.2±0.9	2.9±0.6	0	2.4±0.4	7.6±0.7	1.1±0.1
			40.6-44.6	13.8-19.4	25.0-27.3	2.4-3.9		1.8-2.9	6.5-8.6	1.0-1.3
	A15	-	58.9±0.9	16.6±0.5	3.9±1.0	5.0±0.4	2.0±0.2	10.8±0.5	2.8±0.2	0
			57.2-59.3	16.2-17.3	3.1-5.5	4.6-5.6	1.8-2.2	10.4-11.7	2.4-2.9	
	Nb_{ss}	-	66.1±1.0	10.3±0.4	3.9±1.4	10.1±0.5	6.8±0.5	1.9±0.6	1.0±0.3	0
			64.9-67.5	9.7-10.7	2.1-5.4	9.6-10.9	6.2-7.3	1.2-2.7	0.6-1.3	

[a] many small Ti oxide particles in the phase and two analyses were possible.

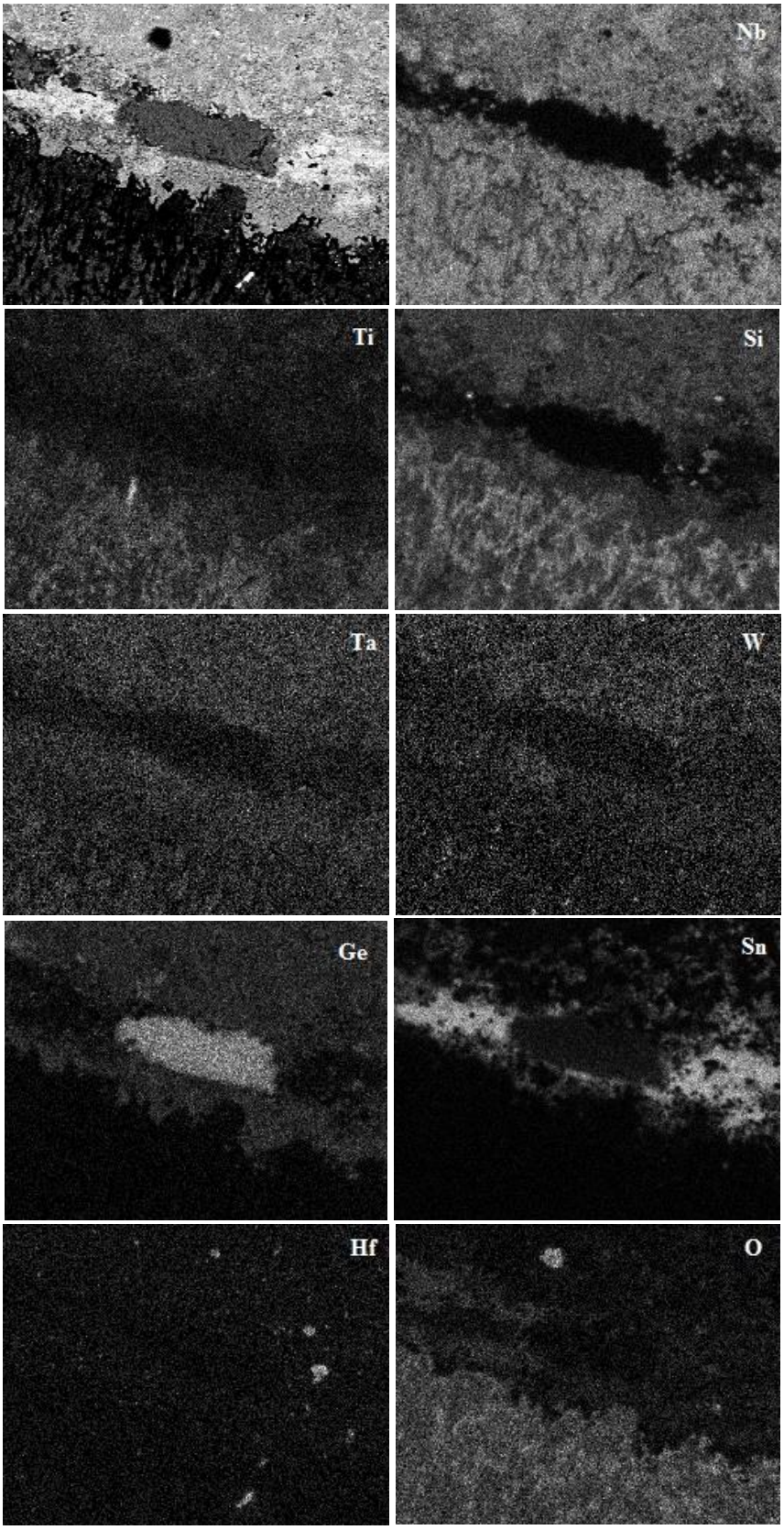

Figure 6.9 BSE image (×2500) and X-ray maps of the region where the layer formed.

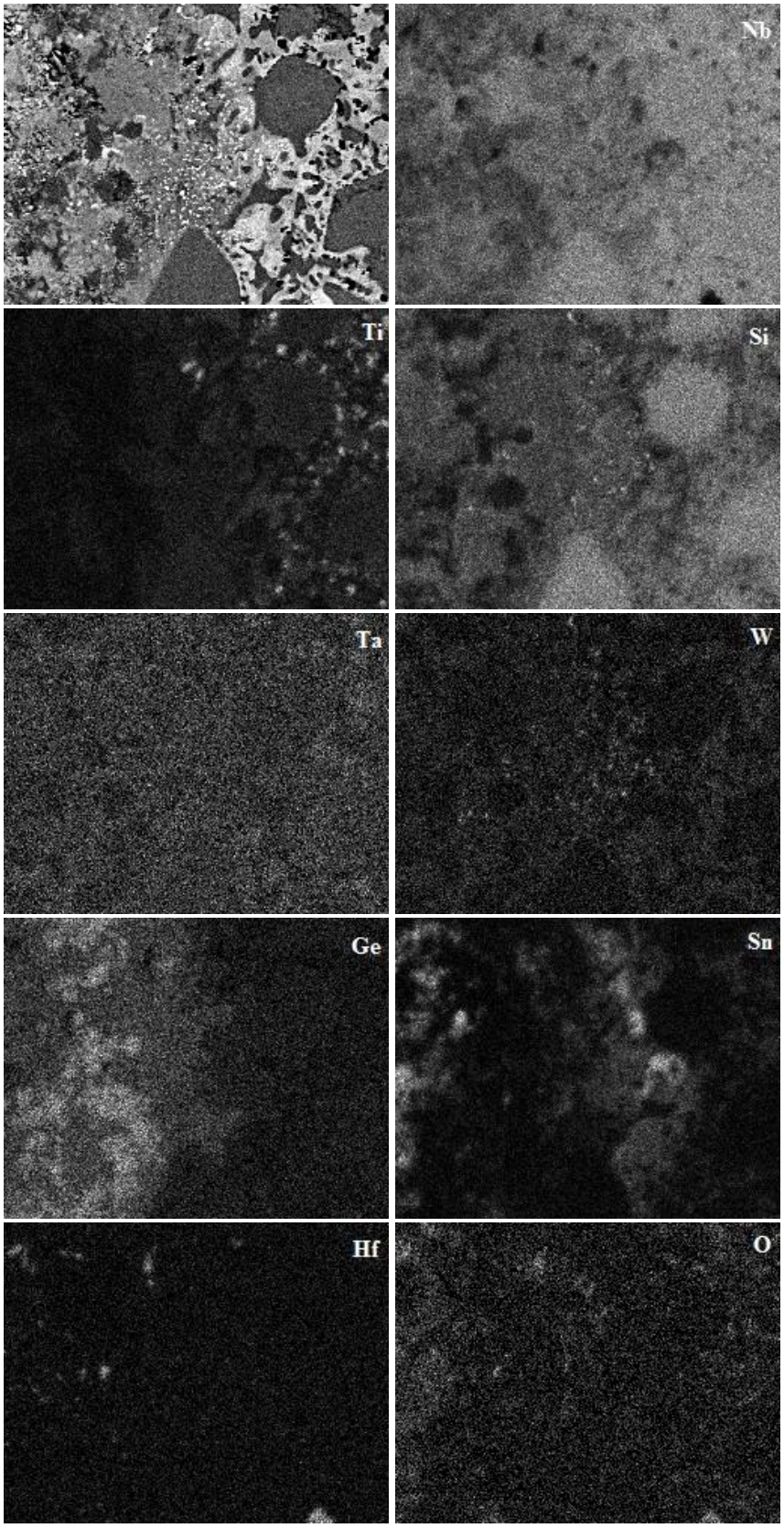

Figure 6.10 BSE image (×5000) and X-ray maps of the rectangular region marked in Figure 6.8d.

The alloys Nb-12Ti-18Si-6Ta-2.5W-5Sn-5Ge-1Hf-5Al-5Cr (alloy JZ3) and Nb -12Ti-18Si-6Ta-2.5W-7.5Sn-5Ge-1Hf-5Al-5Cr (alloy JZ3+)

The microstructures of cross sections of the alloys JZ3 and JZ3+ after the isothermal oxidation at 1200 ˚C are shown in Figures 6.11 and 6.12, which show the oxide scale, diffusion zone and bulk. Compared with the alloy JZ2, the oxide scales formed on the alloys JZ3 and JZ3+ were much thinner and contained cracks and holes. Also, only one diffusion zone was formed.

Table 6.7 gives the composition of the phases in the different regions of the oxidised alloy JZ3. In the oxide scale Nb-rich, Ti-rich and silicon oxides were formed. The composition of the latter is not given in the table for the same reason as discussed in the previous section. Hafnia was not observed in the scale and the oxides were free of Sn and Ge. The oxygen concentration of the oxides given in the table 6.7 was close to that of Nb_2O_5. The Ti-rich oxide was rich in Al and Cr compared with the Nb-rich oxide. The bulk of oxidised alloy JZ3 had similar microstructure to that of the cast alloy but no solid solution was observed. The composition of Nb_5Si_3 was the same as in the cast alloy, the A15 was richer in Ti and poorer in Si and the Laves phase was poorer in Ti and richer in Ta and Cr. There were small particles exhibiting black contrast at the interface of the Nb_5Si_3 and A15 phases. The spot chemical analyses could not give the accurate composition of these particles but suggested they were rich in Ti. In the diffusion zone, partial oxidation in the Nb_5Si_3 was observed, where needle like oxides were formed. The presence of the $Nb_5(Si,Sn)_3$, $Nb_5(Si_{1-x},Ge_x)_3$, Nb_3Sn and $(Nb,Ta,W)_{ss}$ phases in the diffusion zone were suggested by the EDS analyses, with the former 5-3 compound present in the inner regions of the zone and the latter 5-3 compound present in the outer regions. According to the EDS analysis data, these phases were all very lean in Ti and Al owing to the consumption of these elements in the formation the scale. A small volume fraction of HfO_2 was present in the diffusion zone. The hafnia exhibited the same contrast as the solid solution. Some of the black contrast phases just below the scale were Ti or Al oxide(s).

Table 6.7 The EDS analysis data (at.%) of phases in the alloy JZ3 after oxidation at 1200 ˚C for 100 h.

	Phase	O	Nb	Ti	Si	Ta	W	Sn	Ge	Hf	Al	Cr
Oxide scale	Nb-rich oxide	72.5±0.7	18.9±1.2	2.6±0.6	1.2±0.3	2.9±0.8	0.7±0.3	0	0	0.2±0.1	0.6±0.2	0.4±0.2
		71.6-73.2	17.3-20.4	1.9-3.3	0.8-1.7	2.1-4.2	0.3-1.0			0.1-0.3	0.5-0.9	0.2-0.7
	Ti-rich oxide	71.4±0.3	10.7±0.9	8.5±0.8	0.5±0.2	1.5±0.2	0.6±0.1	0	0	0.3±0.1	2.5±0.1	4.2±0.2
		71.1-71.8	9.4-11.8	7.4-9.6	0.4-0.8	1.3-1.7	0.4-0.8			0.2-0.4	2.5-2.7	3.8-4.4
Diffusion zone	Nb_5Si_3	-	43.7±0.7	9.7±0.1	25.8±1.3	6.0±0.4	1.1±0.2	1.9±0.1	6.0±0.3	0.8±0.1	3.6±0.2	1.4±0.3
			43.2-44.1	9.6-9.8	24.5-27.6	5.4-6.4	0.8-1.2	1.8-2.1	5.6-6.4	0.6-0.9	3.4-3.8	1.1-1.8
	$Nb_5(Si,Sn)_3$	-	51.5±2.0	0.5±0.4	15.0±1.9	6.4±0.7	0.4±0.1	15.4±4.3	8.2±1.4	0	0	2.6±0.3
			47.7-52.6	0.2-1.2	11.6-16.3	5.5-7.1	0.3-0.5	12.7-22.8	6.3-9.9			2.1-2.9
	$Nb_5(Si_{1-x},Ge_x)_3$	-	50.9±1.0	2.1±0.9	10.9±6.1	6.1±0.2	1.8±0.8	0.4±0.6	26.1±4.8	0	0.4±0.2	1.2±0.9
			49.4-51.9	1.0-3.1	5.8-17.9	5.9-6.3	0.7-2.8	0.1-1.5	20.8-30.6		0.1-0.6	0.7-2.8
	Nb_3Sn	-	58.1±0.4	0.9±0.3	3.2±0.2	8.4±0.5	4.0±0.5	21.3±0.3	0.7±0.3	0	0.6±0.4	2.9±0.3
			57.3-58.2	0.5-1.2	3.0-3.5	7.7-9.1	3.2-4.5	20.8-21.6	0.3-1.0		0.1-1.3	2.6-3.2
	$(Nb,Ta,W)_{ss}$	-	15.5±2.7	0.5±0.4	1.6±1.0	18.3±1.3	57.7±2.1	0.9±0.4	3.0±0.8	0	0	2.5±0.7
			13.8-20.1	0-1.2	0-2.5	16.8-20.2	54.5-60.2	0.5-1.5	2.1-4.2			1.5-3.2
Bulk	Nb_5Si_3	-	43.5±0.5	10.0±0.7	26.8±0.9	5.3±0.6	0.9±0.2	2.0±0.4	5.6±0.3	0.8±0.3	3.6±0.4	1.5±0.1
			43.0-44.4	9.2-10.8	26.0-27.9	4.6-6.1	0.6-1.1	1.5-2.5	5.4-6.0	0.4-1.1	3.1-4.2	1.3-1.6
	Ti-rich Nb_5Si_3	-	39.0±0.4	13.9±0.6	23.6±0.7	4.9±0.3	0.9±0.1	3.0±0.1	6.5±0.2	1.1±0.2	4.8±0.2	2.4±0.1
			38.5-39.5	13.2-14.6	22.9-24.7	4.4-5.2	0.8-1.0	2.9-3.1	6.1-6.7	0.8-1.4	4.5-4.9	2.2-2.5
	A15	-	48.2±0.9	12.4±0.9	3.5±1.0	8.4±0.6	6.5±0.5	8.5±0.2	1.8±0.2	0.3±0.2	5.9±0.6	4.5±1.1
			47.0-49.0	11.4-13.7	2.8-5.3	7.8-9.5	5.8-7.1	8.2-8.7	1.5-2.1	0-0.5	5.4-6.4	3.2-5.7
	C14-Cr_2Nb	-	19.9±1.3	4.8±0.4	10.4±0.8	8.9±0.5	3.4±0.5	0	0.8±0.3	1.4±0.2	2.9±0.2	47.6±1.3
			18.2-21.0	4.4-5.3	9.2-11.5	8.4-9.5	2.8-4.0		0.5-1.3	1.2-1.6	2.6-3.1	45.9-49.1

Table 6.8 The EDS analysis data (at.%) of phases in the alloy JZ3+ after oxidation at 1200 ˚C for 100 h.

	Phase	O	Nb	Ti	Si	Ta	W	Sn	Ge	Hf	Al	Cr
Oxide scale	Nb-rich oxide	73.2±1.1	17.2±1.2	3.6±0.6	1.3±0.4	2.8±0.4	0.9±0.4	0	0	0.2±0.1	0.5±0.1	0.3±0.2
		71.6-74.8	15.6-18.7	2.6-3.8	0.6-1.6	2.2-3.1	0.3-1.3			0.1-0.3	0.5-0.7	0.1-0.6
	Ti-rich oxide	72.5±0.3	8.6±1.1	9.8±1.7	0.5±0.5	1.5±0.2	0.5±0.2	0	0	0.3±0.1	2.9±0.6	3.4±0.8
		72.1-72.9	7.3-9.9	7.6-11.8	0-0.9	1.3-1.7	0.2-0.8			0.3-0.5	2.4-3.1	2.6-4.5
Diffusion zone	Nb_5Si_3	-	42.2±0.4	8.9±0.4	30.6±1.1	6.8±0.3	1.4±0.2	1.8±0.7	5.4±0.2	0.8±0.2	1.4±0.4	0.8±0.2
			41.7-42.6	8.4-9.4	29.4-31.1	6.4-7.1	1.2-1.6	1.0-2.7	5.2-5.8	0.6-1.1	0.8-2.0	0.5-1.0
	$Nb_5(Si,Sn)_3$	-	45.2±0.7	7.5±1.2	16.7±1.6	5.0±0.4	0.8±0.7	15.4±2.5	4.6±0.4	0.4±0.3	2.1±1.0	2.9±0.4
			44.4-45.8	6.1-9.2	14.4-18.9	4.5-5.5	0.3-2.0	12.3-19.1	3.9-5.1	0-0.6	0.9-3.4	2.5-3.5
	$Nb_5(Si_{1-x},Ge_x)_3$	-	49.2±1.7	1.5±0.9	17.9±2.4	7.7±0.7	2.5±0.6	0.7±0.7	18.7±2.4	0.3±0.2	1.2±1.3	0.3±0.1
			47.9-51.4	0.9-3.0	14.6-21.3	7.1-8.8	1.5-3.1	0-1.8	15.3-21.2	0.1-0.6	0.2-2.7	0.1-0.4
	$(Nb,Ta,W)_{ss}$	-	14.7±2.9	0.3±0.1	0.4±0.7	16.7±2.0	60.7±0.4	0.6±0.3	3.2±0.6	0	0	3.4±0.7
			12.2-19.1	0.2-0.5	0-1.7	13.5-19.1	60.4-61.2	0.2-1.1	2.2-3.8			2.3-4.1
Bulk	Nb_5Si_3	-	41.6±0.7	9.2±0.5	29.6±1.4	6.9±0.5	1.3±0.1	1.6±0.3	5.5±0.5	0.8±0.2	2.2±0.4	1.4±0.2
			40.7-42.6	8.4-9.8	28.1-31.3	6.3-7.6	1.2-1.5	1.3-1.9	4.6-6.0	0.5-1.0	1.5-2.6	1.1-1.6
	Ti-rich Nb_5Si_3	-	35.8±0.5	19.5±1.1	14.9±1.9	3.7±0.5	0.8±1.2	9.3±1.0	4.8±0.3	1.7±0.2	7.4±0.5	2.0±0.5
			35.0-36.2	18.7-21.0	13.1-17.9	3.2-4.2	0.5-1.2	8.2-10.6	4.5-5.3	1.5-2.0	7.2-8.1	1.4-2.6
	A15	-	45.8±0.5	12.4±1.0	2.1±0.3	7.9±0.5	8.2±0.4	10.4±0.4	1.5±0.5	0.4±0.3	6.3±0.4	5.0±0.7
			45.3-46.5	11.3-13.6	1.6-2.4	7.2-8.4	7.9-8.9	10.0-11.1	1.0-2.0	0-0.7	5.6-6.7	4.3-5.9
	C14-Cr_2Nb	-	20.1±0.7	3.9±0.6	10.4±1.0	9.6±0.4	4.5±0.4	0.3±0.2	1.3±0.1	1.2±0.2	5.4±0.4	43.4±0.6
			19.4-21.0	3.3-4.6	8.6-11.2	9.2-10.2	4.0-5.1	0.2-0.6	1.2-1.4	1.0-1.4	4.9-6.0	42.4-44.0

Similar to the alloy JZ3, the phases in the microstructure of the alloy JZ3+ after the isothermal oxidation were Nb-rich, Ti-rich and silicon oxides in the scale, Nb_5Si_3, $Nb_5(Si,Sn)_3$, $Nb_5(Si_{1-x},Ge_x)_3$, Nb_3Sn, $(Nb,Ta,W)_{ss}$, HfO_2 and Ti and Al oxides in the diffusion zone and Nb_5Si_3, A15 phase, C14-Cr_2Nb and hafnia with no solid solution in the bulk, see Table 6.8 and Figure 6.12. Sn and Ge were also not detected in the scale. The average oxygen concentration in the oxide was close to that of Nb_2O_5. The Ti-rich oxide was rich in Al and Cr compared with the Nb-rich oxide. The composition of the Nb_3Sn in the diffusion zone was not given in the table 6.5 because there were many small particles of the solid solution dispersed inside it. The solubility of Al and Ti in $Nb_5(Si,Sn)_3$ in the inner areas of the diffusion zone was not affected (in the areas no Al and/or Ti oxide were formed). The $Nb_5(Si_{1-x},Ge_x)_3$ formed in the areas just below the oxide scale was lean in Ti and Al owing to the consumption of these elements to form Ti and/or Al oxides in these regions. The same was the case for the solid solution which was very rich in W and Ta. The composition of the Nb_5Si_3 in the bulk did not change after the oxidation. However, some Nb_5Si_3 grains were severely cracked, which was not observed in the alloys JZ2 and JZ3. The A15 and Laves phase were poorer in Si and Ti, respectively and the latter phase was richer in Si and Ta.

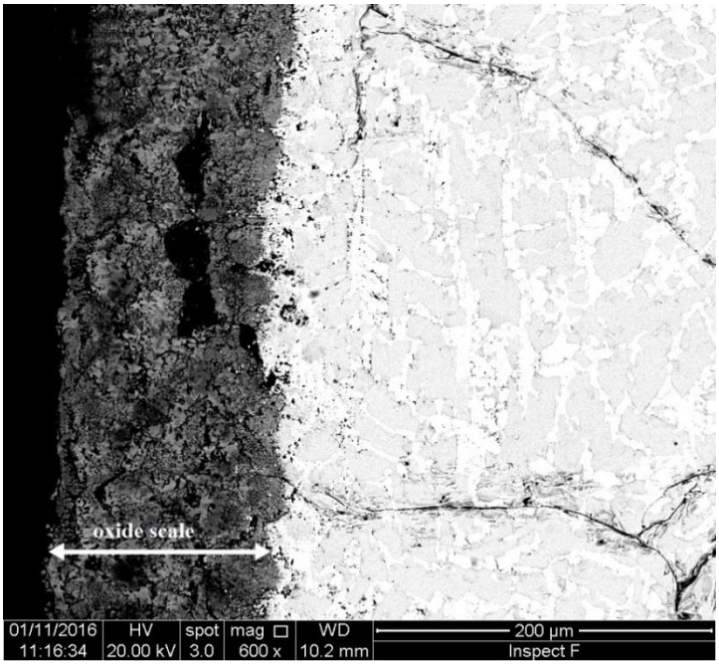

(a)

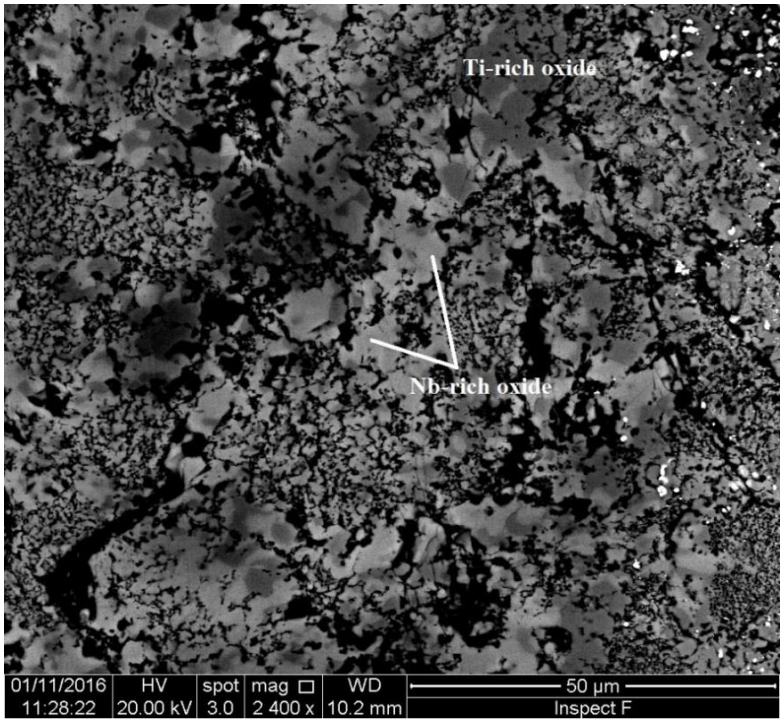
Ti-rich oxide
Nb-rich oxide
01/11/2016
11:28:22
HV
20.00 kV
spot
3.0
mag
2 400 x
WD
10.2 mm
50 µm
Inspect F

(b)

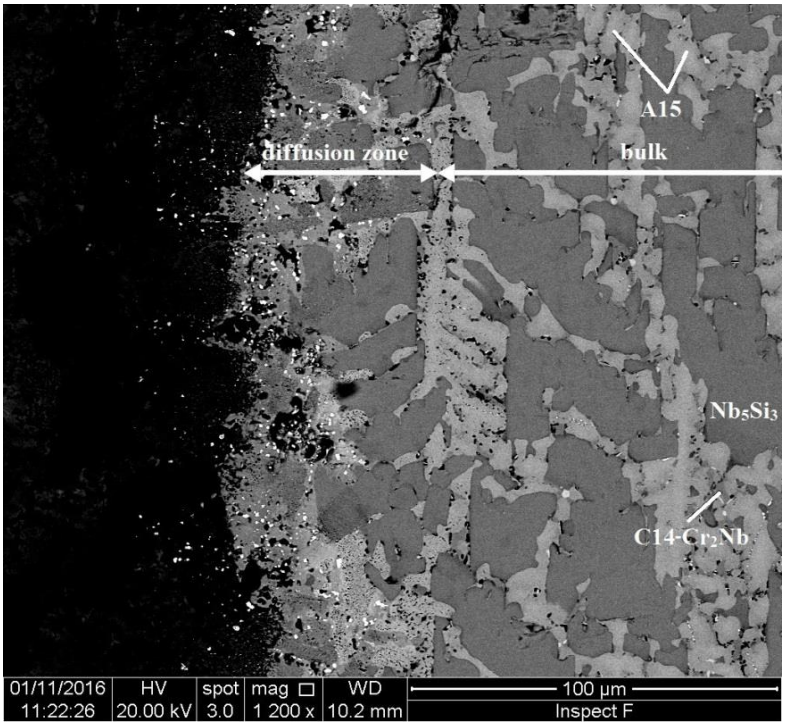
A15
diffusion zone
bulk
Nb5Si3
C14-Cr2Nb
01/11/2016
11:22:26
HV
20.00 kV
spot
3.0
mag
1 200 x
WD
10.2 mm
100 µm
Inspect F

(c)

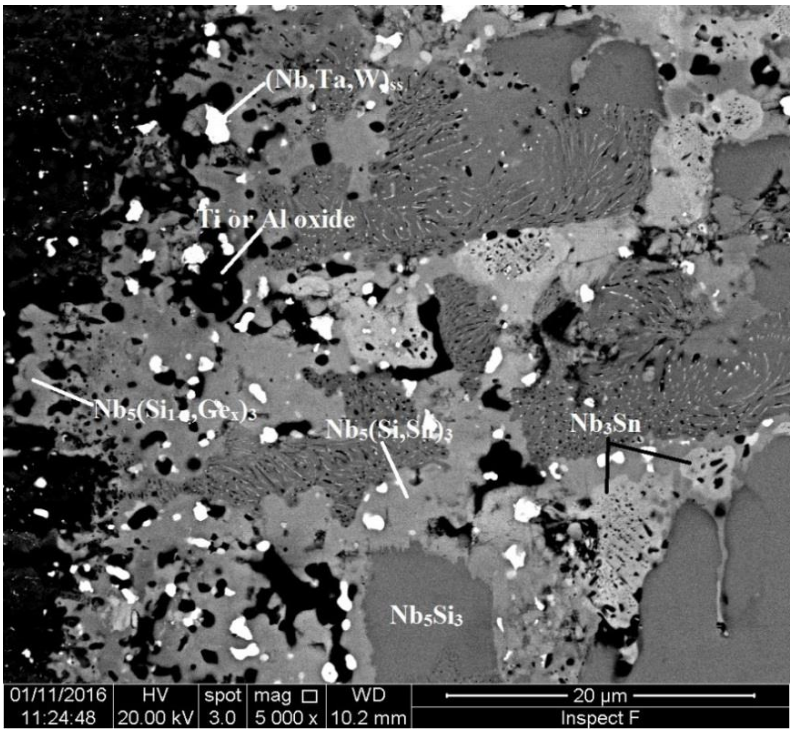
(Nb,Ta,W)ss
Ti or Al oxide
Nb5(Si1-x,Gex)3
Nb5(Si,Sn)3
Nb3Sn
Nb5Si3
01/11/2016 11:24:48
HV 20.00 kV
spot 3.0
mag 5 000 x
WD 10.2 mm
20 µm
Inspect F

(d)

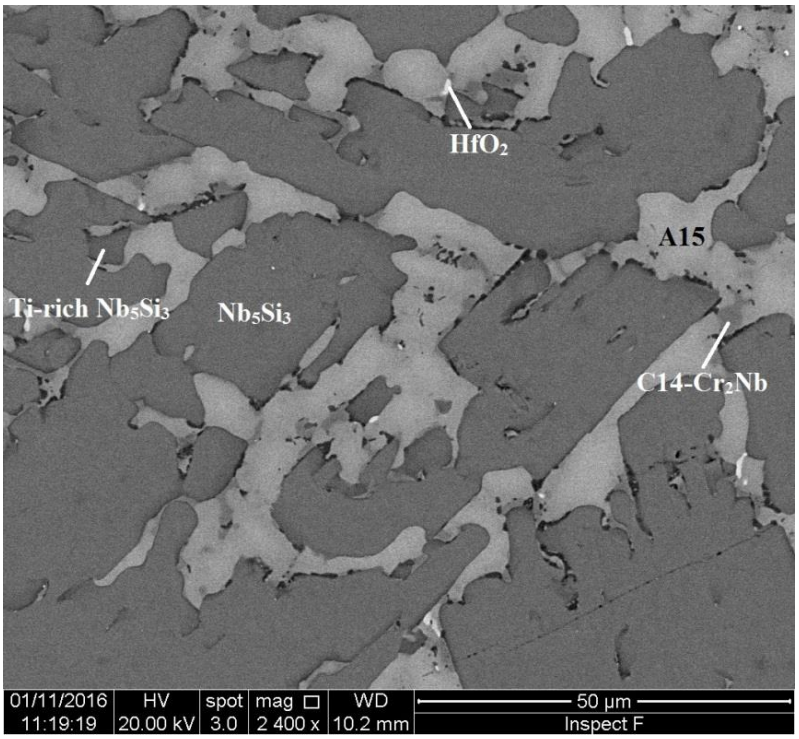
HfO2
A15
Ti-rich Nb5Si3
Nb5Si3
C14-Cr2Nb
01/11/2016 11:19:19
HV 20.00 kV
spot 3.0
mag 2 400 x
WD 10.2 mm
50 µm
Inspect F

(e)

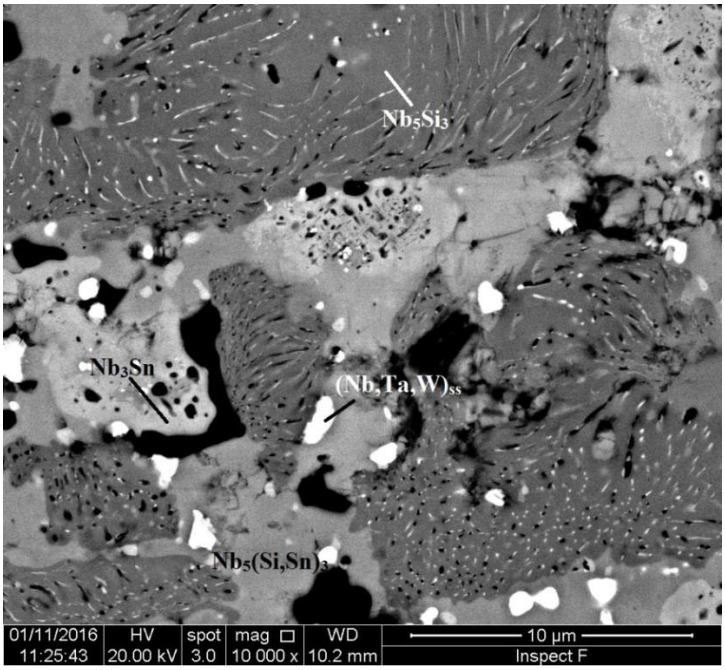

(f)

Figure 6.11 BSE images of the microstructure of a cross section of the oxidised alloy JZ3, (a) ×600, (b) ×2400, shows the microstructure of the oxide scale, (c) ×1200, shows diffusion zone and bulk, (d) ×5000, shows the microstructure of the diffusion zone, (e) ×600, shows the microstructure of the bulk and (f) ×600, shows the white-line feature in the Nb_5Si_3

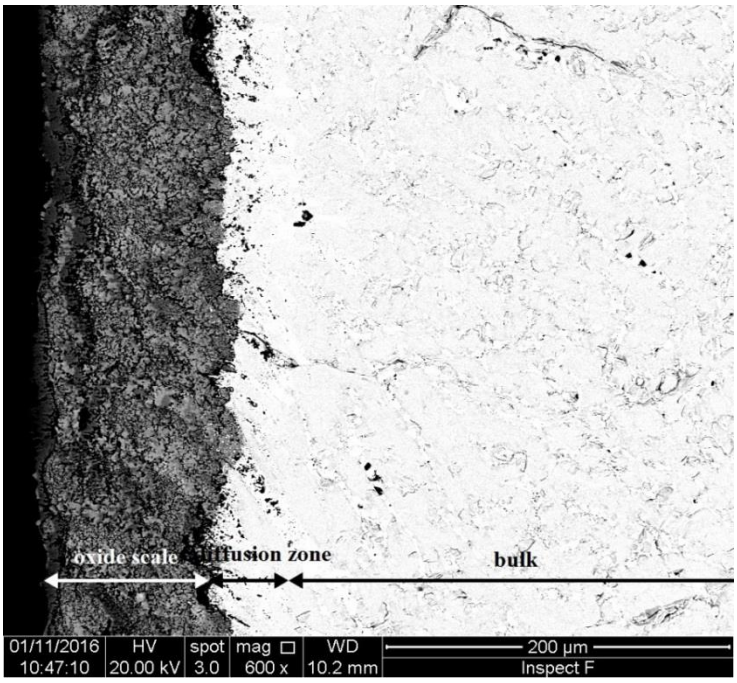

(a)

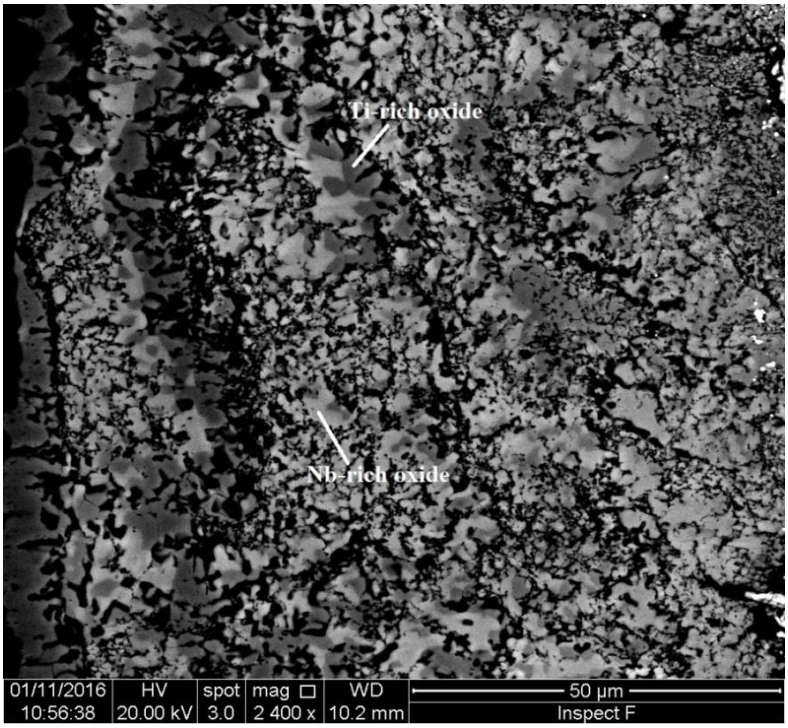
Ti-rich oxide
Nb-rich oxide
01/11/2016
10:56:38
HV
20.00 kV
spot
3.0
mag
2 400 x
WD
10.2 mm
50 µm
Inspect F

(b)

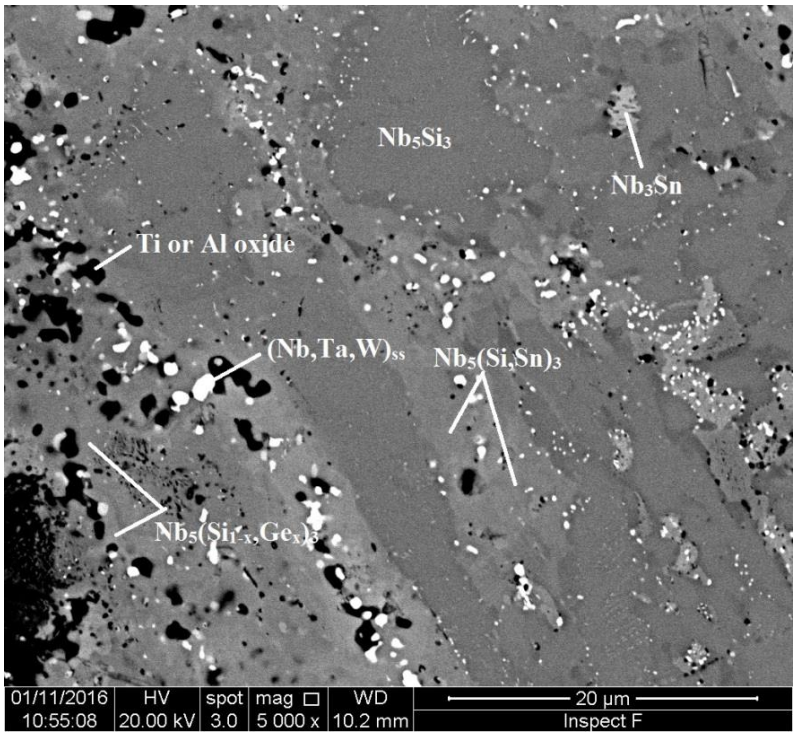
Nb5Si3
Nb3Sn
Ti or Al oxjde
(Nb,Ta,W)ss
Nb5(Si,Sn)3
Nb5(Si1-x,Gex)3
01/11/2016
10:55:08
HV
20.00 kV
spot
3.0
mag
5 000 x
WD
10.2 mm
20 µm
Inspect F

(c)

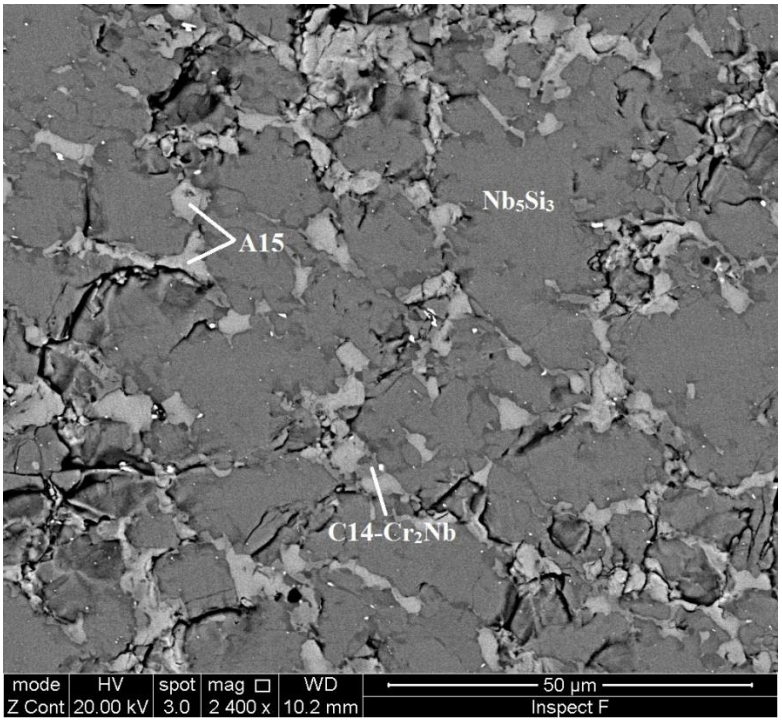

(d)

Figure 6.12 BSE images of the microstructure of a cross section of the oxidised alloy JZ3+, (a) ×600, (b) ×2400, shows the microstructure of the oxide scale, (c) ×5000, shows the microstructure of the diffusion zone and (d) × 2400, shows the microstructure of the bulk.

The alloys Nb-12Ti-18Si-6Mo-2.5W-7.5Sn-5Ge-1Hf-5Al-5Cr (alloy JZ4) and Nb -20Ti-2Si-6Mo-2.5W-7.5Sn-5Ge-1Hf-5Al-5Cr (alloy JZ5)

Figures 6.13 and 6.14 show the microstructures of cross sections of the alloys JZ4 and JZ5 after isothermal oxidation at 1200 ˚C. For each alloy three regions were observed, namely the oxide scale, diffusion zone and bulk. The oxide scale formed on the alloy JZ5 was significantly thinner than that formed on the alloy JZ4. Cracks and holes were observed in the scales of both alloys and were more severe in the alloy JZ5.

Three types of oxides, namely Nb-rich, Ti-rich (Table 6.9) and silicon oxides formed in the oxide scale of the alloy JZ4. The composition of the silicon oxide is not given in the table for the same reason as discussed previously. The concentrations of Sn and Ge in the scale were essentially zero. The Nb-rich oxide was essentially free of Mo

and the Ti-rich oxide free of W. The latter oxide was richer in Al and Cr compared with the former. The phases present in the diffusion zone were similar to those in the alloys JZ3 and JZ3+, namely Nb_5Si_3, $Nb_5(Si,Sn,Ge)_3$, $Nb_5(Si_{1-x},Ge_x)_3$, Nb_3Sn, $(Nb,Mo,W)_{ss}$ and HfO_2. The contents of Ti and Al in these phases remained relatively high owing to the significantly suppressed formation of Ti and/or Al oxides in the diffusion zone. These oxides were only observed in a few areas just below the scale. The solubility of Mo in the Nb_3Sn compound (25.2 at.%) should be noticed. The microstructure in the bulk was similar to the cast alloy and the solid solution which was not observed in JZ4-AC but present in JZ4-HT was observed after oxidation. The TM_5Sn_2X was not found in the bulk after the oxidation. In the bulk the Nb_5Si_3 and Ti-rich Nb_5Si_3 were poorer in Si and the latter was also poorer in W and richer in Ti and Sn compared with the cast alloy. The Laves phase was richer in Si and poorer in Al. Compared with the JZ4-HT, the solid solution was richer in Mo, W, Ge and poorer in Al and Cr.

The oxides in the scale formed on the alloy JZ5 were similar to those of the alloy JZ4, see Table 6.10, and the chemical analyses also suggested that the solid solution rich in Mo and W was present in the inner regions of the scale, where it exhibited white contrast, see Figure 6.14b. According the EDS analysis data, the contents of Mo, W, Sn and Ge were essentially zero in the scale. The Ti-rich oxide was richer in Al and Cr compared with the Nb-rich oxide. The phases in the diffusion zone were the same as those in the alloy JZ4 but the volume fraction of the Ti and Al oxides was increased compared with the alloy JZ4. The solid solution was present in the bulk of the alloy JZ5 after oxidation but the TM_5Sn_2X was not present. The Ti-rich Nb_5Si_3 was richer in Ti and Sn and poorer in Si and W compared with the cast alloy. The A15 phase was richer in Mo and the Laves phase was poorer in Ti and Al. The solid solution was not formed in JZ5-AC but was stable after the heat treatment. Compared with JZ5-HT, the solid solution was richer in Mo and W and poorer in Al and Cr.

Table 6.9 The EDS analysis data (at.%) of phases in the alloy JZ4 after oxidation at 1200 ˚C for 100 h.

	Phase	O	Nb	Ti	Si	Mo	W	Sn	Ge	Hf	Al	Cr
Oxide scale	Nb-rich oxide	74.2±0.4	19.7±0.5	2.9±0.1	0.7±0.5	0.2±0.1	1.0±0.1	0	0	0.3±0.1	0.7±0.1	0.2±0.1
		73.5-74.6	19.0-20.5	2.8-3.1	0-1.4	0.1-0.2	1.0-1.1			0.3-0.4	0.6-0.9	0.1-0.4
	Ti-rich oxide	71.7±0.3	9.6±0.5	8.5±0.6	1.0±0.7	1.2±1.0	0	0	0.3±0.1	0.5±0.1	3.4±0.1	3.7±0.6
		71.0-71.9	8.9-10.2	7.6-9.1	0.3-2.1	0.4-2.8			0.2-0.4	0.4-0.6	3.3-3.6	2.8-4.2
Diffusion zone	Nb_5Si_3	-	44.0±0.5	10.3±0.1	24.7±0.5	4.9±0.2	1.3±0.3	2.6±0.1	6.3±0.2	1.0±0.2	3.3±0.5	1.6±0.2
			43.3-44.5	10.2-10.5	24.1-25.4	4.7-5.1	0.8-1.6	2.5-2.8	6.1-6.4	0.7-1.1	2.7-3.7	1.4-2.0
	$Nb_5(Si,Sn,Ge)_3$	-	42.5±2.2	9.0±1.0	13.2±1.0	7.3±0.7	0.3±0.1	9.7±3.1	11.5±2.0	0.3±0.1	2.7±0.3	3.4±0.2
			39.2-45.3	7.7-10.3	11.9-14.7	6.4-8.1	0.2-0.4	7.2-14.6	8.8-13.5	0.2-0.5	2.5-3.2	3.1-3.6
	$Nb_5(Si_{1-x}Ge_x)_3$	-	42.9±2.6	8.5±0.9	11.8±5.0	7.9±1.6	1.5±0.7	0	23.8±4.8	0.8±0.3	0.5±0.1	2.4±0.6
			39.4-45.0	7.7-9.7	7.2-17.4	6.2-9.7	0.5-2.0		18.4-28.0	0.4-1.1	0.4-0.6	1.5-3.0
	Nb_3Sn	-	41.7±1.1	4.1±0.1	1.5±0.1	21.9±1.1	2.5±0.2	20.0±0.7	2.1±0.5	0	1.1±0.3	5.3±0.3
			40.2-43.2	4.0-4.2	1.4-1.7	20.5-23.2	2.2-2.8	19.1-20.9	1.4-2.9		0.7-1.4	4.8-5.7
	$(Nb,Mo,W)_{ss}$	-	16.5±2.3	1.7±0.7	0	29.3±2.7	43.3±3.6	0.8±0.4	2.6±0.4	0.2±0.2	0.9±0.3	4.8±0.4
			14.0-19.8	0.8-2.8		26.7-32.6	38.9-47.8	0.4-1.3	2.1-3.1	0-0.4	0.6-1.4	4.5-5.4
Bulk	Nb_5Si_3	-	44.4±0.2	10.3±0.2	24.9±0.9	4.9±0.3	1.6±0.1	2.1±0.1	6.2±0.5	1.0±0.2	3.0±0.2	1.6±0.1
			44.2-44.7	10.0-10.7	24.6-25.0	4.3-5.0	1.5-1.8	2.0-2.3	5.4-6.4	0.8-1.2	2.7-3.2	1.4-1.7
	Ti-rich Nb_5Si_3	-	36.1±2.0	19.4±2.1	13.9±2.3	3.6±0.5	0.4±0.3	11.5±2.3	5.0±0.4	2.0±0.3	5.5±0.3	2.6±0.3
			33.0-39.2	15.7-21.6	11.6-17.7	2.8-4.1	0-0.9	7.9-13.5	4.5-5.7	1.6-2.3	5.3-5.9	2.0-2.9
	A15	-	40.8±0.7	10.2±0.3	2.2±0.3	15.3±0.6	7.7±0.2	8.8±0.4	1.8±0.4	0.3±0.2	7.3±0.3	5.7±0.2
			39.8-41.4	9.9-10.4	1.8-2.6	14.3-15.8	7.5-8.0	8.4-9.5	1.2-2.2	0.1-0.5	7.0-7.7	5.5-6.0
	$(Nb,Mo,W)_{ss}$	-	23.9±0.8	5.1±0.3	0	24.0±0.5	33.5±1.3	0.6±0.3	1.6±0.7	0.3±0.3	1.7±0.2	9.2±1.3
			23.0-24.6	4.6-5.4		23.5-24.6	31.6-35.1	0.4-1.1	0.7-2.1	0-0.7	1.4-1.9	7.4-10.9
	C14-Cr_2Nb	-	26.8±0.7	4.7±0.2	10.5±0.3	3.9±0.2	3.1±0.5	0.5±0.3	1.4±0.2	1.8±0.2	5.1±0.2	42.1±0.6
			25.9-27.9	4.5-5.0	10.2-11.0	3.6-4.1	2.5-4.0	0.2-0.7	1.2-1.6	1.5-2.1	4.9-5.3	41.3-43.0

Table 6.10 The EDS analysis data (at.%) of phases in the alloy JZ5 after oxidation at 1200 ˚C for 100 h.

	Phase	O	Nb	Ti	Si	Mo	W	Sn	Ge	Hf	Al	Cr
Oxide scale	Nb-rich oxide	74.7±1.1	17.6±1.9	4.8±0.5	0.9±0.7	0	0.4±0.4	0	0	0.3±0.1	1.0±0.4	0.2±0.1
		73.4-76.1	15.4-18.9	4.0-5.2	0-1.4		0-1.0			0.1-0.4	0.5-1.4	0.2-0.3
	Ti-rich oxide	72.5±0.7	8.0±1.1	11.9±1.7	0.7±0.5	0	0	0.2±0.1	0	0.4±0.2	3.9±0.5	2.3±0.4
		71.5-73.6	6.7-9.6	10.4-14.6	0.1-1.2			0.2-0.3		0.2-0.6	3.3-4.5	1.9-2.8
Diffusion zone	Nb_5Si_3	-	40.8±0.2	17.4±0.3	29.4±0.4	5.2±0.2	1.1±1.3	1.3±0.1	1.0±0.3	0.7±0.1	1.5±0.2	1.4±0.2
			40.4-41.0	17.1-17.9	28.9-30.0	5.0-5.5	1.1-1.3	1.2-1.5	0.7-1.4	0.6-0.9	1.3-1.8	1.2-1.7
	$Nb_5(Si,Sn)_3$	-	31.6±1.4	20.3±1.8	13.2±1.9	5.8±0.3	0.2±0.1	16.9±1.5	4.4±0.5	0.8±0.2	2.3±0.6	4.5±0.2
			30.3-33.5	17.4-21.7	11.1-16.0	5.6-6.3	0.1-0.2	15.0-19.0	3.8-5.3	0.6-1.0	1.2-2.8	4.1-4.7
	$Nb_5(Si_{1-x},Ge_x)_3$	-	46.6±1.5	3.3±0.9	17.5±4.6	10.3±1.7	1.7±0.3	0.3±0.5	16.7±4.1	0.3±0.2	0.9±0.5	2.4±0.6
			44.4-47.8	2.5-4.5	10.8-23.3	8.6-12.6	1.4-2.3	0-1.3	11.2-22.7	0.1-0.7	0.4-1.5	1.8-3.3
	Nb_3Sn	-	30.8±1.6	9.9±0.6	1.1±0.2	25.2±0.8	3.9±0.7	19.2±0.7	1.3±0.1	0.1±0.1	1.4±0.6	7.1±0.4
			28.3-32.6	9.3-10.7	0.9-1.3	24.2-26.3	3.0-4.9	18.4-20.2	1.1-1.4	0-0.2	0.8-2.4	6.8-7.7
	$(Nb,Mo,W)_{ss}$	-	12.7±1.2	3.6±0.6	0	31.5±0.8	39.1±1.3	1.0±0.7	2.2±0.4	0.3±0.2	1.6±0.6	8.1±0.9
			11.5-14.5	2.8-4.4		30.9-32.8	38.0-41.0	0.1-1.9	1.9-2.7	0.1-0.5	0.9-2.6	7.5-9.4
Bulk	Nb_5Si_3	-	39.0±0.8	16.2±0.5	28.1±0.6	5.2±0.2	0.8±0.1	1.3±0.2	5.6±0.4	0.8±0.1	1.6±0.2	1.4±0.1
			37.9-40.0	15.6-16.9	27.4-28.8	5.0-5.4	0.7-0.9	1.1-1.6	5.1-5.9	0.7-0.8	1.5-2.0	1.3-1.6
	Ti-rich Nb_5Si_3	-	28.2±2.6	26.7±3.1	13.9±2.6	4.2±0.8	0.2±0.2	11.8±2.9	5.0±0.5	1.2±0.1	5.9±0.3	2.9±0.8
			25.6-32.3	25.8-29.9	10.8-17.7	3.4-5.3	0-0.3	7.7-14.8	4.3-5.7	1.0-1.4	5.4-6.2	2.1-3.7
	A15	-	27.1±0.9	18.6±0.9	1.4±0.3	19.9±0.8	4.2±0.5	10.6±0.3	1.4±0.3	0.2±0.1	8.9±0.3	7.6±1.1
			25.9-28.1	17.7-19.8	1.1-1.9	18.8-20.9	3.6-4.9	10.3-11.2	1.2-1.8	0.1-0.3	8.5-9.2	6.4-9.0
	$(Nb,Mo,W)_{ss}$	-	19.5±0.8	9.7±0.5	0	27.9±0.7	30.0±2.0	1.6±0.6	2.0±0.4	0.4±0.1	2.2±0.4	6.8±0.5
			18.4-20.6	9.2-10.2		27.1-28.8	27.7-31.6	1.1-2.3	1.5-2.6	0.1-0.5	1.8-2.8	6.3-7.3
	C14-Cr_2Nb	-	22.9±0.4	7.8±0.3	8.7±0.3	4.6±0.1	3.3±0.1	0.4±0.1	1.0±0.1	1.3±0.1	7.0±0.5	43.0±0.4
			22.5-23.4	7.2-8.1	8.5-9.2	4.5-4.6	3.1-3.5	0.3-0.5	0.9-1.1	1.2-1.5	6.1-7.3	42.4-43.2

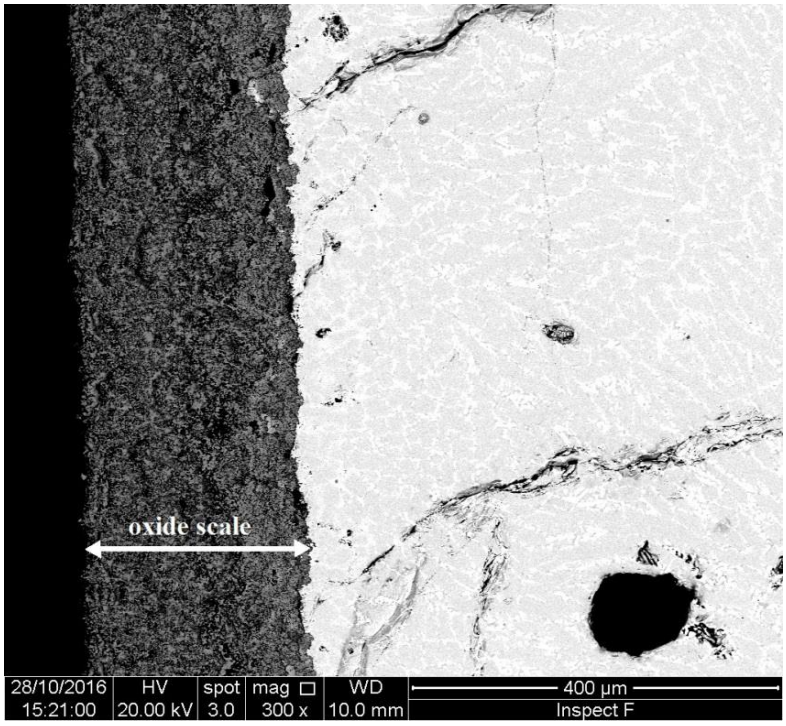
oxide scale
28/10/2016
15:21:00
HV
20.00 kV
spot
3.0
mag
300 x
WD
10.0 mm
400 µm
Inspect F

(a)

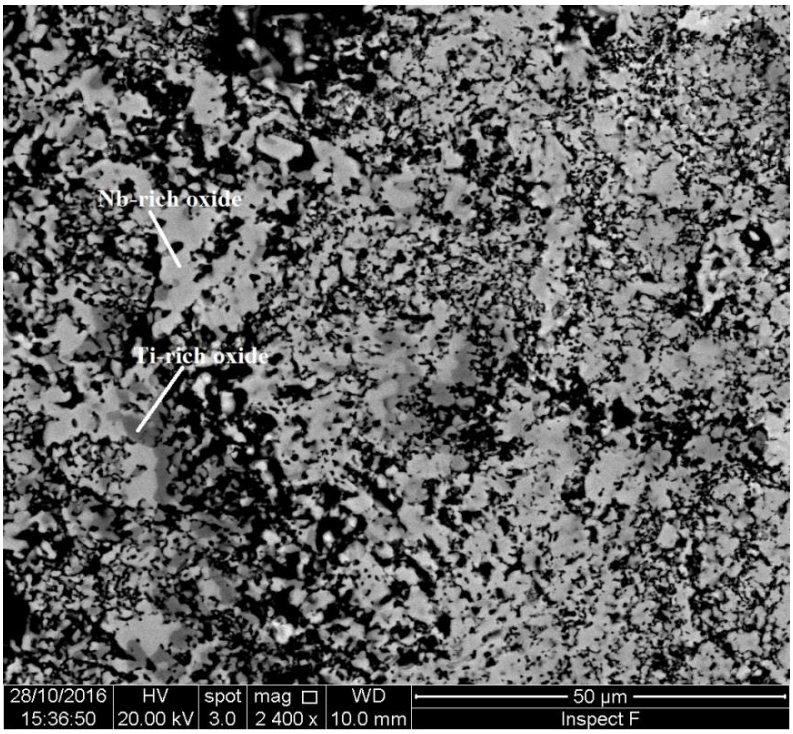
Nb-rich oxide
Ti-rich oxide
28/10/2016
15:36:50
HV
20.00 kV
spot
3.0
mag
2 400 x
WD
10.0 mm
50 µm
Inspect F

(b)

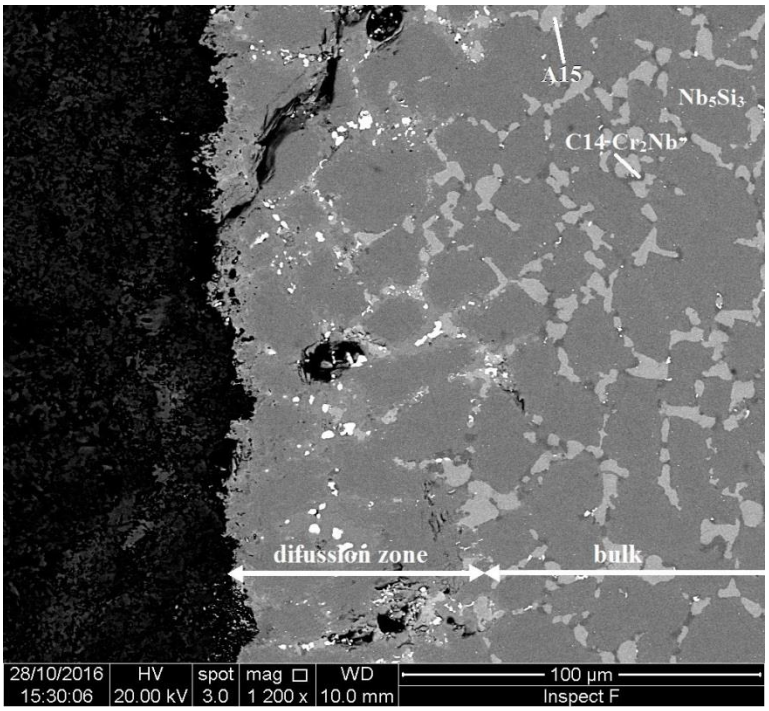
A15
Nb5Si3
C14-Cr2Nb?
difussion zone
bulk
28/10/2016
15:30:06
HV
20.00 kV
spot
3.0
mag
1 200 x
WD
10.0 mm
100 µm
Inspect F

(c)

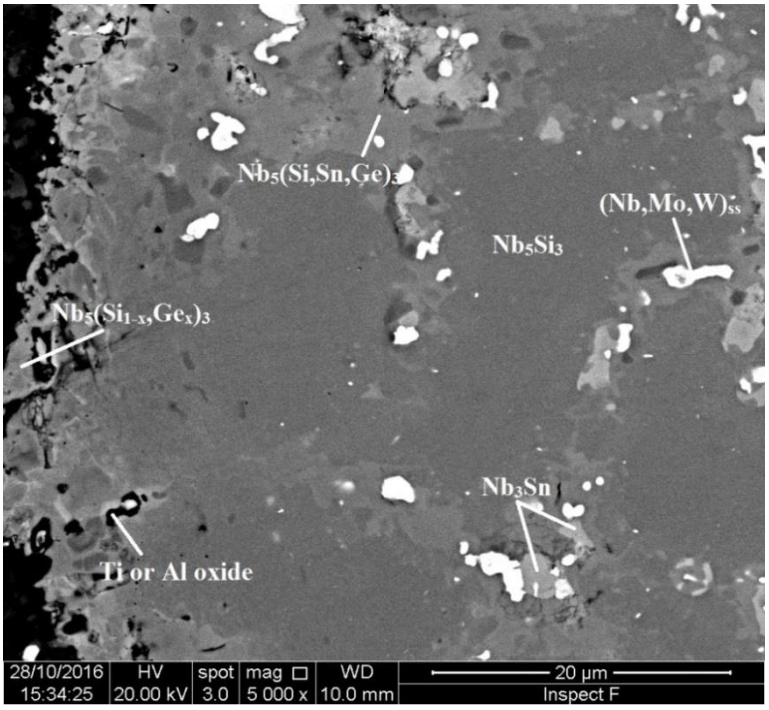
Nb5(Si,Sn,Ge)3
(Nb,Mo,W)ss
Nb5Si3
Nb5(Si1-x,Gex)3
Nb3Sn
Ti or Al oxide
28/10/2016
15:34:25
HV
20.00 kV
spot
3.0
mag
5 000 x
WD
10.0 mm
20 µm
Inspect F

(d)

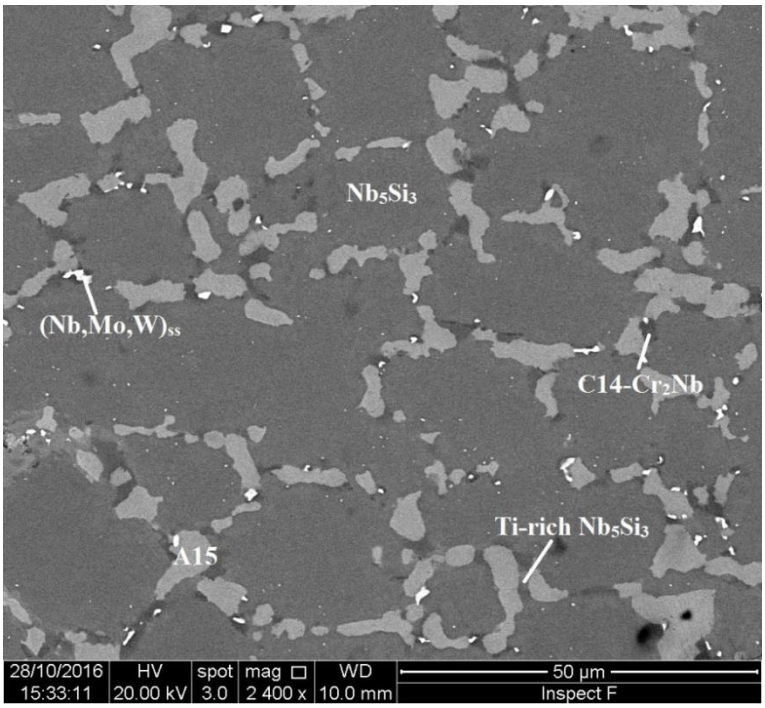

(e)

Figure 6.13 BSE images of the microstructure of a cross section of the oxidised alloy JZ4, (a) ×600, (b) ×2400, shows the microstructure of the oxide scale, (c) ×1200, shows the diffusion zone and bulk, (d) ×5000, shows the microstructure of the diffusion zone and (e) ×2400, shows the microstructure of the bulk.

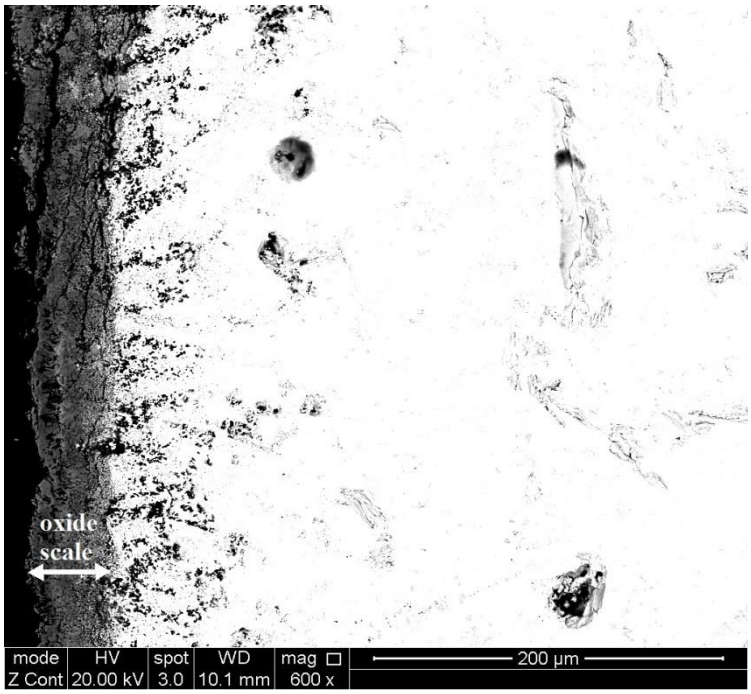

(a)

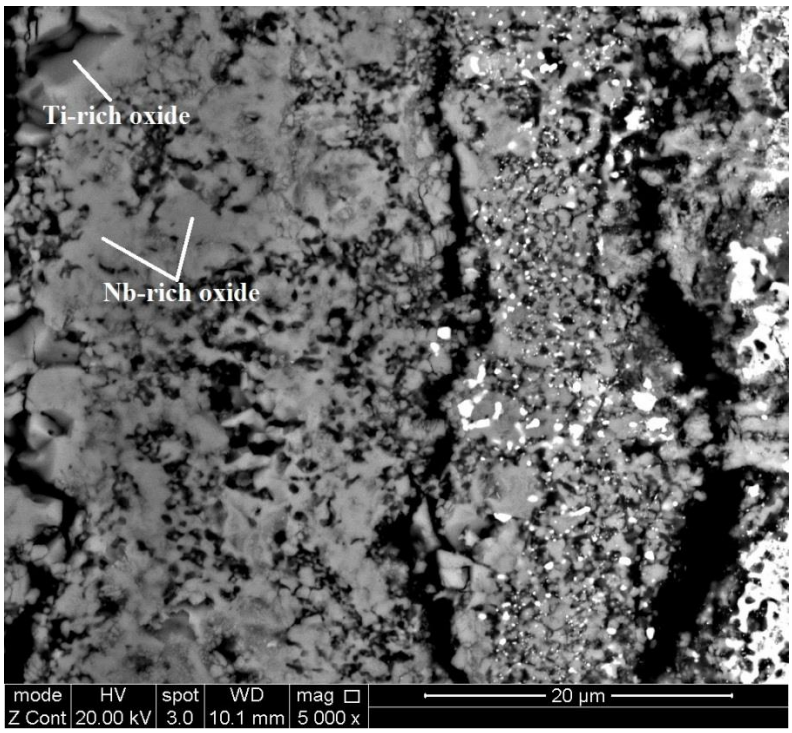
Ti-rich oxide
Nb-rich oxide
mode HV spot WD mag
Z Cont 20.00 kV 3.0 10.1 mm 5 000 x
20 µm

(b)

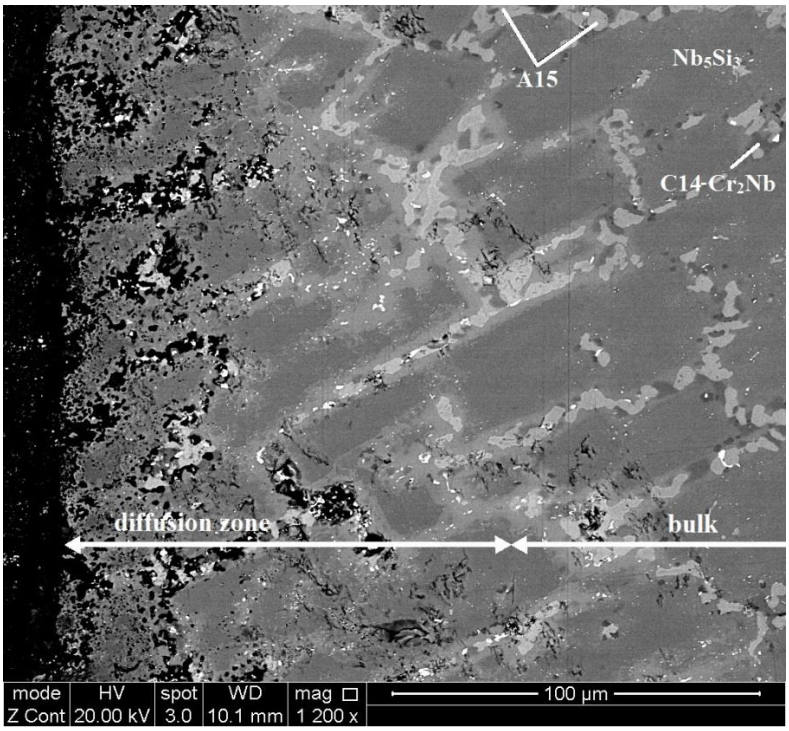
A15
Nb5Si3
C14-Cr2Nb
diffusion zone
bulk
mode HV spot WD mag
Z Cont 20.00 kV 3.0 10.1 mm 1 200 x
100 µm

(c)

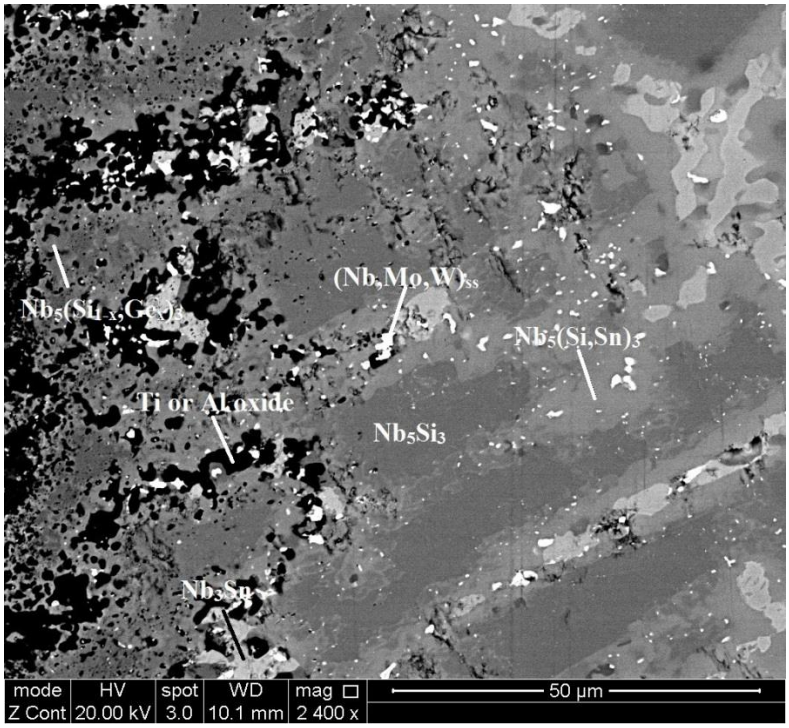

(d)

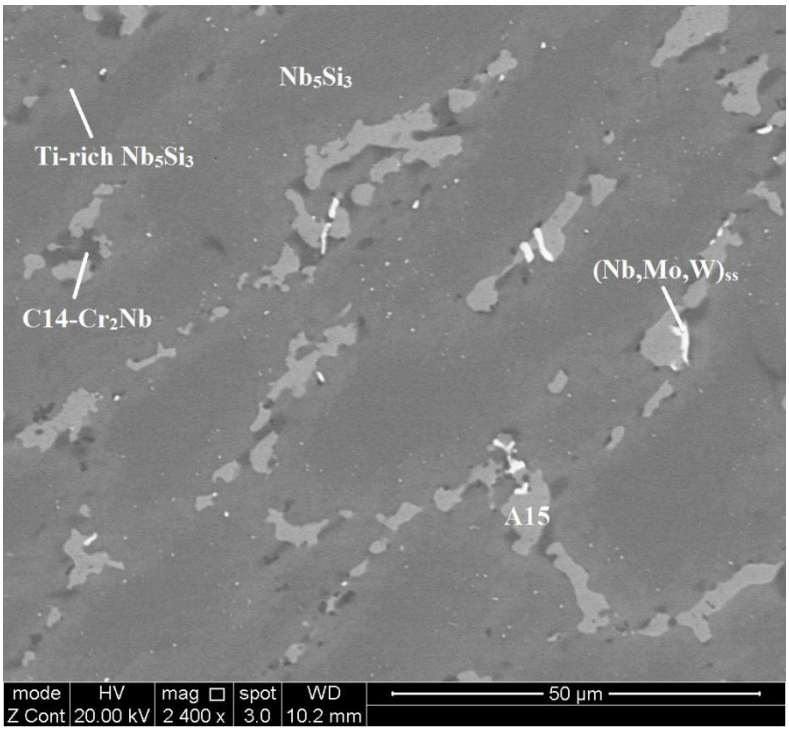

(e)

Figure 6.14 BSE images of the microstructure of a cross section of the oxidised alloy JZ5, (a) ×600, (b) ×5000, shows the microstructure of the oxide scale, (c) ×1200, shows the diffusion zone and bulk, (d) ×2400, shows the microstructure of the diffusion zone and (e) ×2400, shows the microstructure of the bulk.

6.3 Discussion

Oxidation behaviour at 800 ˚C

Pest oxidation of intermetallics or alloys occurs at intermediate temperatures, usually in the range 600 to 900 ˚C and has been considered to occur as the rapid diffusion of oxygen along the grain boundaries results in internal oxidation and the oxide(s) formed induce internal stresses that cause the disintegration of intermetallics or alloys along the grain boundaries (Westbrook and Wood 1964). Zelenitsas and Tsakiropoulos (2006), Geng *et al*. (2006, 2007) and Geng and Tsakiropoulos (2007) showed that the volume fraction of the Nb_{ss} is critical for the oxidation of Nb-silicide based alloys where the Nb_5Si_3 is cracked below the substrate/scale interface with the cracks running parallel to the interface. The latter was attributed to the low fracture toughness of the Nb_5Si_3 (about 3 MPa $m^{0.5}$ for the unalloyed silicide and up to about 10 MPa $m^{0.5}$ for Ti alloyed silicide with ≈ 30 at.% Ti) and the stresses arising from the oxidation of the Nb_{ss}. The cracking of Nb_5Si_3 below the substrate/scale interface also had been reported in conferences by USA researchers (Menon *et al.* 2001) working on Nb-silicide based alloys. Mathieu *et al.* (2012) suggested that the mechanical stresses in the silicide, which were induced by the volume expansion of the oxidised Nb_{ss} as the oxygen diffused in and oxides formed with reactive elements such as Ti, Hf and Al, could be responsible for pesting in Nb_{ss}/Nb_5Si_3 alloys and indicated that the volume expansion of the solid solution was possible toward the surface, leading to the cracks observed in the Nb_5Si_3 below the oxide scale always being parallel to the substrate-scale interface. Thus, control of the volume fraction of the Nb_{ss} and the oxygen diffusion toward the bulk of the alloy are critical for the pest oxidation of Nb_{ss}/Nb_5Si_3 alloys.

At 800 ˚C, the alloys JZ1 and JZ2 suffered from the spallation of the oxide scales of which parts disintegrated into powder after oxidation. Both alloys presented linear oxidation kinetics and no protective oxide scales formed on them. The weight change of the alloy JZ2 was slightly lower than that of the alloy JZ1. As mentioned above, the

Nb_{ss}, which is very susceptible to the oxygen attack, plays the key role in pesting behavour of the Nb_{ss}/Nb_5Si_3 alloys. The alloys JZ1 and JZ2 had similar microstructures and the volume fractions of the Nb_{ss} were 46.5 % in the former and 34.5 % in the latter. Vellios and Tsakiropoulos (2008) showed that at 800 ˚C the alloy Nb-18Si-5Sn (at.%, nominal composition) suffered from complete disintegration to powders (pesting) after isothermal oxidation at 800 ˚C and the alloy Nb-24Ti-18Si-5Sn (at.%, nominal composition) did not pest but instead formed a thin scale that cracked along all the edges of the cube shaped specimen. Li and Tsakiropoulos (2012) showed that the alloy Nb-24Ti-18Si-5Ge (at.%, nominal composition) suffered from complete disintegration to powders (pesting) after isothermal oxidation at 800 ˚C. The above results would suggest that the addition of 5 at.% Sn with 24 at.% Ti is more effective than that of 5 at% Ge with 24 at% Ti regarding the control of pest oxidation at 800 ˚C.

The alloys JZ1 and JZ2 had lower Ge and Sn (Ge + Sn = 3 and 8 at.%, respectively) and the same but lower Ti concentrations than the alloys studied by Vellios and Tsakiropoulos (2008) and Li and Tsakiropoulos (2012) and did not suffer from complete disintegration to powders, instead the scale formed on them spalled off and the scale fragments disintegrated into powder. This would suggest that the simultaneous presence of Ge and Sn in the alloys “controlled and improved” the effect of Ge and that the addition of these two elements with Hf, Ta, Ti and W were also beneficial regarding the control of pest oxidation. The oxidation resistance of the alloy JZ2 at 800 ˚C was slightly improved owing to the lower volume fraction of the Nb_{ss} and higher Sn+Ge content compared with the alloy JZ1.

The weight gain of the alloy JZ3 after oxidation at 800 ˚C for 100 h was reduced to 14.92 mg/cm^2 and no pesting was observed. Similar to the alloys JZ1 and JZ2, linear oxidation kinetics was exhibited by the alloy JZ3 on which a cracked oxide scale formed, see figure 6.3. Comparison of the results of the alloys JZ1, JZ2 and JZ3 shows that the addition of Sn and Ge with Al, Cr and the refractory metals Ta and W

and the transition metals Hf and Ti eliminated pest oxidation. However, the nature of the oxide scale could not protect the substrate.

Zelenitsas and Tsakiropoulos (2006) reported (1) that the scales were thinner in alloys when Al and Cr were present simultaneously, (2) that Cr and Al with/without Ta had impeded the diffusion of oxygen toward the bulk of the alloys and (3) the addition of 6 at.% Ta in the alloy Nb-24Ti-18Si-5Al-5Cr was slightly detrimental to its oxidation resistance at 800 ˚C owing to the increased volume fraction of Nb_{ss} and the high solubility of Ta in the the solid solution. They also suggested that the C14 Laves was not beneficial regarding the oxidation behaviour at 800 ˚C. Vellios and Tsakiropoulos (2008) showed that the improved oxidation behaviour of Sn containing alloys at 800 ˚C and the suppression of pesting was linked (1) with the lower vol% of Nb_{ss} and (2) with the enrichment in Sn of the substrate just below the substrate/scale interface, where Nb-Sn intermetallic(s) formed. Geng *et al.* (2007) showed that the addition of Sn in Nb-24Ti-18Si-5Al-5Cr-2Mo-5Sn suppressed pest oxidation at 800 ˚C. This was linked with the stability of Nb_3Sn in the alloy (this phase was referred to as Sn-rich Nb solid solution in the paper, but subsequent research in the group (Vellios and P Tsakiropoulos 2008, Zacharis and Tsakiropoulos 2013, Xu and Tsakiropoulos 2016) confirmed that the Sn-rich Nb solid solution actually was the A15-Nb_3Sn compound). A very thin diffusion zone formed in the alloy Nb-24Ti-18Si-5Al-5Cr-2Mo-5Sn.

Xu and Tsakiropoulos (2016) showed that the stability or not of A15-Nb_3Sn in Sn containing Nb-Si alloys depends on the Sn concentration in the alloys as well as the other alloying additions and that there is a “critical” Sn concentration below which the A15-Nb_3Sn is not stable. The alloys Nb-24Ti-18Si-5Al-5Cr-2Sn and Nb-24Ti-18Si -5Al-5Cr-5Sn (at.%, nominal composition) did not pest after isothermal oxidation at 800 ˚C, both alloys followed parabolic oxidation kinetics in the early stages of oxidation followed by linear kinetics with the rate constant of the latter alloy similar to that of the alloy JZ3 and an order of magnitude lower for the former alloy. In both alloys the A15-Nb_3Sn was stable and the C14-Cr_2Nb Laves phase was stable only in

the latter alloy. In both alloys there was enrichment in Sn of the substrate just below the substrate/scale interface with formation of Nb-Sn intermetallic(s). The diffusion zone formed in the alloy with low Sn was significantly thicker than that formed in the alloy with high Sn.

Zacharis and Tsakiropoulos (2013) showed that the alloys Nb-24Ti-18Si-5Sn-5Hf and Nb-24Ti-18Si-5Al-5Cr-5Sn-5Hf (at.%, nominal compositions) did not suffer from pest oxidation at 800 ˚C and followed parabolic oxidation kinetics for the first 24 h followed by linear oxidation kinetics with rate constant an order of magnitude lower than that of the alloy JZ3. In both alloys the Nb_{ss} was stable in their cast microstructures and its vol% was lower in the latter alloy. In both alloys the A15-Nb_3Sn was stable and the C14-Cr_2Nb Laves phase was stable in the latter alloy.

Li and Tsakiropoulos (2012) showed that at 800 ˚C the alloy Nb-24Ti-18Si-5Al-5Cr -5Ge (at.%, nominal composition) did not suffer from disintegration to powders (pest oxidation) after isothermal oxidation at 800 ˚C and instead followed parabolic oxidation kinetics. The same was the case when 5 at.% Hf was added to the alloy. No A15 compound was present in the microstructures of these alloys. Furthermore, the C14-Cr_2Nb was formed at small vol% in their cast microstructures but was not stable after heat treatment. The exceptional oxidation behaviour of the alloys at 800 ˚C was attributed to their low vol% of Nb_{ss}. No diffusion zone was observed in both alloys.

Hernandez-Negrete and Tsakiropoulos (2016) showed that the alloy Nb-24Ti-18Si -5Al-5Cr-5Ge-5Sn (at.%, nominal composition) did not suffer from disintegration to powders (pesting) after isothermal oxidation at 800 ˚C and instead followed parabolic oxidation kinetics with rate constant comparable to that of the alloys studied by Li and Tsakiropoulos (2012) and formed a thin scale. In the cast microstructure the A15-Nb_3Sn and Ti-rich A15-Nb_3Sn was present and the former was stable after heat treatment. Enrichment in Ge and Sn of the substrate just below the substrate/scale interface was observed. There was also evidence for some internal oxidation in the

substrate just below the substrate/scale interface.

Knittel *et al*. (2014) investigated the effect of Sn addition (2-8 at.%) on the oxidation behaviour at 800 ˚C of the alloy Nb-25Ti-16Si-8Hf-2Al-2Cr. This is essentially the basis of the alloy known as MASC, developed by GE. The actual MASC composition is said to include Sn and/or Ge and/or B additions, the latter however have not been specified in the open literature. Vellios and Tsakiropoulos (2008) showed that the scale formed on the alloy Nb-25Ti-16Si-8Hf-2Al-2Cr after isothermal oxidation at 800 ˚C was in the shape of Maltese cross (this was also reported by Zelenitsas and Tsakiropoulos (2006) for their alloy KZ4 (= Nb-24Ti-18Si-5Cr) and that the alloy followed linear kinetics with rate constant an order of magnitude higher than that of JZ3. Knittel *et al*. (2014) reported that the Sn effect on oxidation behaviour was enhanced as its concentration in the alloy increased and the improvement in oxidation was linked with the formation of a Sn-rich layer below the scale that was suggested to act as barrier to inward diffusion of oxygen. Diffusion zone was observed in the alloys studied by Knittel *et al.* (2014).

The above results from our group and the literature would suggest (1) that the addition of Ge or Sn with Al and Cr (and Hf and Ti) is effective at suppressing pest oxidation at 800 C, (2) that the addition of Ge with Al and Cr (and Hf and Ti) is more effective than that of Sn with the same elements at 800 ˚C (parabolic kinetics versus parabolic and linear kinetics), (3) that the addition of Ge and Sn (meaning both elements are simultaneously present in the alloy) with Al and Cr (and Hf and Ti) is also beneficial (parabolic kinetics), (4) that suppression of pest oxidation is linked with enrichment of the substrate just below the substrate/scale interface with Sn and Ge (the latter when both elements are simultaneously present in the alloy) and the formation of A15 compound(s) and (5) that the C14-Cr_2Nb Laves phase probably does not benefit oxidation at 800 ˚C in alloys where Sn is added with Al and Cr (and Hf and Ti).

The Nb_{ss}, C14-Cr_2Nb and A15 phases were stable in the microstructure of the alloy

JZ3 with the A15 forming Ti and Cr rich compounds of which only the former was stable in the bulk of the oxidised alloy at 800 ˚C where the vol% of the Nb_{ss} increased compared with the cast alloy. There was no diffusion zone in JZ3 and the scale formed was thinner than that formed on the alloy KZ6 in Zelenitsas and Tsakiropoulos (2006) (KZ6 = Nb-24Ti-18Si-5Al-5Cr-6Ta). The oxidation kinetics of the alloy JZ3 were linear for the whole duration of the isothermal oxidation experiment and there was no enrichment in Ge and/or Sn at the substrate just below the substrate/scale interface (A15 and Ti rich A15 was already present in the microstructure). Considering the work of Zelenitsas and Tsakiropoulos (2006) for Ta containing alloys and the work of Hernandez-Negrete and Tsakiropoulos (2016), see above, it is concluded that the linear oxidation kinetics of the alloy JZ3 should be attributed to the presence of the refractory metals Ta and W, meaning these alloying additions reduced the effect of Ge and Sn with Al and Cr (and Hf and Ti). The suppression of pest oxidation in the alloy JZ3 is attributed to the addition of Ge and Sn, the stability of A15 and the low vol% of Nb_{ss} in the alloy.

The alloy JZ3+ suffered complete disintegration after 74 h exposure in air at 800 ˚C, with a very low mass gain for the first 40 h of oxidation and an increasing oxidation rate after this time. The same phases were present in the microstructure of the alloys JZ3+ and JZ3. However, there were some important differences in the compositions of the phases.

The Nb_{ss} in the alloy JZ3+ was significantly richer in W with W/Ta = 2.3 and this ratio increased slightly after exposure to high temperature. As a consequence of its high refractory metal content the Ti concentration in the Nb_{ss} in JZ3+ was significantly lower than that in the solid solution in the alloy JZ3. The lower Ti concentration in the Nb_{ss} in the alloy JZ3+ meant lower Al and Cr concentrations in the solid solution compared with the alloy JZ3. The same was also the case for the Sn and Ge concentrations in the Nb_{ss} in JZ3+ that also decreased after exposure to high temperature. Thus, even though the alloy JZ3 had four times the vol% of Nb_{ss}

compared with the alloy JZ3+, the solid solution in the cast microstructure of the latter was poorer regarding the elements that are known to improve the oxidation resistance of the solid solution and to decrease the diffusivity of oxygen in it and became even poorer after exposure to high temperature, as the data for the heat treated [JZ3+]-HT shows (see Tables 4.4 and 4.5).

The A15 phase in the alloy JZ3 formed as “normal”, Ti-rich and Cr-rich. The former two had lower W/Ta ratios, lower Ti, Cr and Sn and higher Ge content compared with the alloy JZ3+ in which the Cr-rich A15 did not form. The latter was also rich in Ti, Al, Ge and Hf. After exposure to high temperature the compositions of the A15 in both alloys were essentially the same with the exception of the concentrations of Sn and Ge that increased and decreased respectively in [JZ3+]-HT. Furthermore, after exposure to high temperature the vol% of A15 increased in the alloy JZ3 but did not change in the alloy JZ3+.

The concentration of Cr in the C14-Cr_2Nb Laves phase was lower in JZ3+ compared with the alloy JZ3 and Sn rich Nb_5Si_3 formed in the alloy JZ3+, however, this phase was also poor in Si compared with the normal Nb_5Si_3. In other words, both these phases were poorer in the elements Cr and Si that are known to improve oxidation.

The vol% Nb_{ss} in the alloy JZ3+ was lower than that in the alloys JZ3, JZ4 and JZ5. In the early stages of oxidation at 800 ˚C the weight change was lower than all these alloys, see figure 6.1, and it followed parabolic kinetics. Thus, the better oxidation behaviour of the alloy JZ3+ for the first 40 h of exposure to 800 ˚C compared with the alloy JZ3 is attributed to its lower vol% of Nb_{ss}. After this time the chemical composition of the Nb_{ss} (see above) and to a lesser extent those of the other phases (see above) were not able to maintain the low weight change, and instead the weight gain increased dramatically, following linear kinetics.

The addition of Mo instead of Ta in the alloy JZ4 strongly improved the oxidation

resistance at 800 ˚C in air in the 100 h oxidation test with a weight gain of 0.85 mg/cm^2 after 100 h. The increase in the content of Ti in the alloy JZ5 gain reduced the weight further to 0.57 mg/cm^2. Both the alloys with Mo followed parabolic oxidation kinetics and did not pest. The effect of Mo with Al and Cr but without Sn and Hf additions on the oxidation resistance at 800 ˚C of Nb-24Ti-18Si based alloys was reported by Geng and Tsakiropoulos (2007), who showed that the addition of 2 at.% Mo was more beneficial to the oxidation resistance than 5 at.%. Pest oxidation was only eliminated in the Nb-24Ti-18-Si-2Mo-5Al-5Cr-5Hf-5Sn alloy with the addition of Hf and Sn. The total weight gain was 2 mg/cm^2. Comparison of the TG data of the JZ and JG series of alloys (Geng and Tsakiropoulos, 2007) shows (1) that the beneficial effect of Mo with Sn, Ge, Al, Cr, Ti and Hf and the refractory metal W was stronger than that of Ta and (2) that the detrimental effect of Mo addition at high concentration on the oxidation behaviour of the Nb-25Ti-18Si-5Al-5Cr based alloys can be compensated via the addition of Sn and Ge with Hf, Ti and the refractory metal W. This is good news because Mo has a stronger solid solution strengthening effect at high temperatures compared with Ta.

The alloy JZ4 is comparable with the alloy JZ3+. The former had significantly better oxidation behaviour at 800 ˚C than the latter. In both alloys the Nb_{ss} played a key role in oxidation behaviour. It should be noted that the Nb_{ss} in the alloy JZ4 (better oxidation) was (1) Si free, (2) richer in Al+Cr (15.2 at% vs 8.6 at%, both elements are important for oxidation), (3) richer in Al (Cr/Al ratios of 3.75 and 4.7, respectively, Al is important for oxidation in the pest regime (Zelenitsas and Tsakiropoulos (2006)), (4) richer in Sn (Sn/Ge ratios of 8 and 4, respectively, Sn improves the oxidation of the Nb_{ss} (Geng *et al*. (2007)) and (5) even though the total refractory element content in the two alloys was similar the Mo/W > Ta/W (0.74 vs 0.38), which would suggest that a low W concentration in the Nb_{ss} is beneficial for oxidation.

The microstructures of the alloys JZ4 and JZ5 were slightly different compared with the alloysJZ3 and JZ3+, in that the TM_5Sn_2X compound formed adjacent to the Laves

phase the volume faction of which was higher than those in the alloys JZ3 and JZ3+. However, the C14-Cr_2Nb Laves phase was not stable in the alloy JZ4 after the heat treatment. The severe cracking of the Nb_5Si_3 observed in the JG series of alloys (Geng *et al.*, 2006 and 2007) was not found in JZ4 and JZ5, indicating the improved ductility of the Nb_5Si_3. There was no apparent change in the compositions of the phases in the alloys JZ4 and JZ5 after the oxidation. Considering that the Laves phase is believed not to play the key role in the oxidation of Nb-silicide based alloys at 800 ˚C and the TM_5Sn_2X compound was present only in a small volume fraction, it is suggested that the good oxidation resistance of the alloys JZ4 and JZ5 at 800 ˚C is attributed to the low volume fractions of the Nb_{ss} and A15 phase.

It should be noted that some of the A15 phase below the oxide scale was attacked by oxygen in the alloy JZ4 (see figure 6.4b). This was not observed in the alloy JZ5. Thus, it is suggested that the better oxidation resistance of the A15 phase in the alloy JZ5 at 800 ˚C was attributed to the increase in its content of Ti that might be linked with the higher Ti concentration in the alloy.

Oxidation behaviour at 1200 ˚C

The TG curves of the alloys JZ1, JZ2, JZ3, JZ3+, JZ4 and JZ5 all exhibited parabolic kinetics at the beginning of the exposure followed by linear kinetics for the alloys JZ1, JZ2 and JZ3, which implied that in the initial stages of oxidation before 9 h for the alloys JZ1, JZ2, JZ3 and JZ5, 6h for JZ3+ and 14 h for JZ4 the oxidation kinetics were controlled by solid-state diffusion and then the cracks and pores that appeared during oxide growth resulted in an scale/atmosphere interfacial reaction making the oxidation kinetics linear.

A high weight gain (91.34 mg/cm^2) after 100 h at 1200 ˚C was recorded for the alloy JZ1 and complete spallation of the oxide scale occurred after oxidation. The spallation of the oxide scale was not observed in the alloy JZ2 the mass gain of which was slightly reduced to 71.69 mg/cm^2. Thus, it is concluded (1) that the increase in Sn and

Ge content in the alloy JZ2 improved oxidation behaviour and adherence of the oxide scale to the substrate and (2) that the slightly lower volume fraction of the Nb_{ss} in JZ2 also contributed to the improvement of the oxidation resistance of this alloy.

The alloying with 5 at.% Al and 5 at.% Cr of the alloy JZ3 led to a reduction of an order of magnitude of the oxidation rate of the alloy JZ3 at 1200 ˚C and the increased content of Sn in the alloy JZ3+ further improved the oxidation resistance and the adhesion of the scale. The weight gains of these two alloys after 100 h exposure were 24.21 mg/cm^2 and 14.02 mg/cm^2 respectively. The oxidation rate of the alloy JZ4 was of the same order as that of JZ3+, which indicated that the substitution of Ta by Mo did not have a significant effect on the oxidation behaviour at 1200 ˚C and did not destroy the good adherence of the scale seen in JZ3+. The reduction by 37 % in the weight gain of the alloy JZ5 compared with the alloy JZ4 was attributed to the beneficial effect of the increased concentration of Ti on the oxidation resistance at 1200 ˚C, in agreement with Geng and Tsakiropoulos (2007). Furthermore, the increase in Ti did not affect the adherence of the scale.

Knittel *et al.* (2014) reported the limited effect of Sn addition (2-8 at.%) on the oxidation resistance of the MASC type alloy Nb-25Ti-16Si-8Hf-2Al-2Cr at 1200 ˚C (all alloys exhibited more than 50 mg/cm^2 after 50 h exposure). A mass gain of about 40 mg/cm^2 was observed in the alloy Nb-24Ti-18Si-5Ge-5Al-5Cr after 100 h (Li and Tsakiropoulos 2012). Addition of 5 at.% Sn to Nb-24Ti-18Si-2Mo-5Al-5Cr-5Hf reduced the oxidation rate at 1200 ˚C but a high weight gain of about 90 mg/cm^2 was observed after 100 h exposure. Comparison of the data of the alloys mentioned above and JZ3+, JZ4 and JZ5 shows (1) that the good adherence of the oxide scale at 1200 ˚C could also be gained in the presence of Al and Cr with either Ta or Mo, (2) that the oxidation resistance of the Nb-silicide based alloys at 1200 ˚C was enhanced dramatically when Sn and Ge were added with refractory metals Ta or Mo and W and Hf was present at low (≤ 1 at.%) concentration, (3) that oxidation improved with the increase in the content of Sn or Ti in the alloys and (4) that, even though Sn or Ge

individually has been reported to have a dramatic effect on oxidation at 1200 ˚C, their simultaneous presence in the alloys improved oxidation behaviour significantly.

At 1200 ˚C, Geng *et al.* (2007) and Knittel *et al.* (2014) reported that in their Sn-containing alloys Sn segregated at the oxide scale/diffusion zone boundary where Nb_3Sn and Nb_5Sn_2Si formed. The latter intermetallic is not stable at 1200 ˚C according to the limited available phase equilibria for the Nb-Si-Sn ternary system (Sun *et al*. 2012). The Nb_5Sn_2Si compound has W_5Si_3 as prototype, the same as βNb_5Si_3, and its stability has also been confirmed in oxidised Nb-24Ti-18Si-5Al-5Cr -5Hf-5Sn-2Mo (Geng *et al*. 2007) and Nb-24Ti-18Si-5Al-5Cr-xSn (Xu and Tsakiropoulos 2016) alloys, i.e., in only Sn containing Nb-silicide based alloys with Al and Cr, which would suggest that contamination by oxygen can stabilise the Nb_5Sn_2Si compound at high temperatures in such alloys. It should be noted that the TM_5Sn_2X compound, which also has W_5Si_3 as prototype, was formed in JZ4-AC and JZ5-AC but was not stable in the heat treated alloys and in the oxidised alloys at 1200 ˚C. The Nb_5Sn_2Si and TM_5Sn_2X compounds were not observed in any of the oxidised alloys of this research, which could suggest that the addition of Ge and Sn with refractory metals did not stabilise them at 1200 ˚C.

A common observation in the alloys JZ2, JZ3, JZ3+, JZ4 and JZ5 was that the oxide scale was free of Sn and Ge and the formation of Sn and Ge containing intermetallic phases in the diffusion zone. In the alloy JZ2 two diffusion zones were observed but in the other four alloys only one diffusion zone formed. In the alloy JZ2 the $Nb_5(Si_{1-x},Ge_x)_3$ and $NbGe_2$ formed in the diffusion zone 1 (which was the zone formed below the scale) and in the other alloys the Nb_5Si_3, $Nb_5(Si,Sn)_3$, $Nb_5(Si_{1-x},Ge_x)_3$, A15-Nb_3Sn and $(Nb,Ta,W)_{ss}$ or $(Nb,Mo,W)_{ss}$ were formed. The solid solution was particularly rich in W and its Ti content was very low. The experimental data suggested that Ge and Sn segregated to the substrate just below the scale/substrate interface. Further strong evidence for such segregation was provided by the alloy JZ2 where Sn rich or very Ge rich areas formed in the said region, see figures 6.9 and 6.10.

Segregation of solutes at the substrate just below the scale/substrate interface has been studied in our research group by Geng *et al.* (2007), Vellios and Tsakiropoulos (2008) and more recently by Xu and Tsakiropoulos (2016) and Hernandez-Negrete and Tsakiropoulos (2016). The former three studies concentrated on Sn containing alloys and the latter on Ge and Sn alloys. Xu and Tsakiropoulos (2016) also studied "why Sn segregates to the surface of Nb-silicide based alloys?". Their study showed that the elements shown in the Table 6.11 are predicted to segregate to the surfaces of binary Nb-X alloys.

Table 6.11: Solutes in Nb-X binary alloys predicted to segregate to the surface

Theory	Surface segregating element							
A	Al	Cr	Si	Sn	Ge	Mo	Hf	Ti
B	Al			Sn	Ge			Ti
C		Cr	Si	Sn	Ge*			
D	Al	Cr	Si	Sn	Ge		Hf	Ti

*small freezing range

In the table 6.11 according to theory A the solute of the alloy with lower heat of sublimation should segregate to the surface, according to theory B the larger the solute atom relative to the solvent the higher the degree of surface segregation, according to theory C the surface segregation is related with the partitioning of solute to the melt of the alloy and surface segregation should occur when owing to distribution (partitioning) of solute the melt is richer in solute than the solid, according to theory D the element with the lower surface energy segregates.

The predictions of theories A to D are supported by the results of this research for the aforementioned alloys that show the formation of Ge and Sn containing intermetallics and Nb_{ss} rich in refractory metals. The theories however fail to predict the segregation of W or Ta to the surface and thus it is likely that the formation of $(Nb,RM)_{ss}$ in the diffusion zone might be the result of the changed phase equilibria in the presence of

oxygen.

In the alloy JZ2 the microstructure in the diffusion zone 2 was essentially the same as in the bulk and the Ti oxide formed either at the interface or inside the solid solution and A15 compound, which indicated that the Nb_{ss} and A15 compound were more susceptible to oxygen attack than the Nb_5Si_3 at 1200 ˚C.

Similar to the alloy JZ2, the oxides formed in the oxide scales of JZ3, JZ3+, JZ4 and JZ5 after exposure to air at 1200 ˚C all exhibited zero concentrations of Sn and Ge. These alloys had the similar phases in their diffusion zones where the segregation of Sn and Ge also occurred but the Sn or Ge rich layers that were formed in the alloy JZ2 were not observed. Ge segregated in the outer regions of their diffusion zones to form the $Nb_5(Si_{1-x},Ge_x)_3$ and Sn was enriched in the inner regions of their diffusion zones where formed the Sn-rich 5-3 compound and Nb_3Sn. In the Sn-containing alloys of Geng *et al.* (2007) and Knittel *et al.* (2014) the oxide scales were easily separated after oxidation, indicating minimal contribution of Sn to the adherence of the oxide scales. Li and Tsakiropoulos (2012) also observed the spallation of the oxide scales formed on the Ge-containing alloys. Thus, it is suggested that the good adherence of the oxide scales in the alloys JZ3, JZ3+, JZ4 and JZ5 at 1200 ˚C was the result of the relatively thinner oxide scales, with relatively lower stresses in the scales, and the presence of the $Nb_5(Si_{1-x},Ge_x)_3$ and Sn-rich 5-3 compound probably with more deformation capability.

Considering that the microstructures of the alloys JZ3, JZ3+, JZ4 and JZ5 mainly consist of Nb_5Si_3 and the A15 compound, different from that of the alloy JZ2, it is suggested that the formation the A15 compound instead of the solid solution contributed to the improvement on the oxidation behaviour of these alloys at 1200 ˚C compared with JZ2 and indicated the better inherent oxidation resistance of the A15 compound than the solid solution. However, even the A15 phase could oxidise. The alloys JZ3+, JZ4 and JZ5 exhibited further improved oxidation resistance owing to

the increased volume faction of the silicide in their microstructures.

6.4 Conclusions

In this chapter the oxidation behaviour of the JZ series of cast alloys at 800 ˚C and 1200 ˚C was studied. The conclusions are as follows:

1. The presence of Ge and Sn in the alloys with Ti, Hf and the refractory metals Ta and W was beneficial regarding the oxidation behaviour at 800 ˚C but did not completely eliminated pesting in the alloys JZ1 and JZ2.
2. The addition of Al and Cr in the alloy JZ3 suppressed pest oxidation but the presence of the refractory metals Ta and W reduced the effect of Ge and Sn with Al Cr, Hf and Ti that benefited oxidation in the alloy Nb-24Ti-18Si-5Al-5Cr-5Ge-5Sn (parabolic oxidation kinetics).
3. Alloying with Mo instead of Ta in the alloys JZ4 and JZ5 led to good oxidation behaviour at 800 ˚C, with the formation of thin scales (about 3 μm thick) and no pesting.
4. The reported detrimental effect of the Mo addition at high concentration on the oxidation behaviour of Nb-25Ti-18Si-5Al-5Cr based alloys at 800 ˚C was compensated via the addition of Sn and Ge with Hf, Ti and the refractory metal W in the alloys JZ4 and JZ5.
5. The increase in Ti concentration in the alloy and the A15 compound led to the better oxidation resistant of the latter in the alloy JZ5 at 800 ˚C.
6. Spallation of the oxide scale was only observed in the alloy JZ1 after the oxidation test at 1200 ˚C. The increase of the Sn and Ge contents in the alloy JZ2 improved the adherence of the oxide scale at 1200 ˚C. The good adherence of the oxide scale at 1200 ˚C was also possible in the presence of Al and Cr with either Ta or Mo in the alloys JZ3, JZ3+, JZ4 and JZ5.
7. The oxidation resistance of the alloys at 1200 ˚C was enhanced dramatically when Sn and Ge were added with refractory metals Ta or Mo and W and Hf was

present at low (≤ 1 at.%) concentration.

8. The addition of Sn or Ge individually had been reported to have a dramatic effect on oxidation at 1200 ˚C but their simultaneous presence in the alloys improved oxidation behaviour significantly.
9. At 1200 ˚C the oxide scales of the alloys JZ2, JZ3, JZ3+, JZ4 and JZ5 all exhibited zero concentrations of Sn and Ge and these two elements segregated to the substrate just below the scale/substrate interface to form Sn and Ge containing intermetallic phases in the diffusion zone.
10. The Nb_{ss} and A15 compound were more susceptible to oxygen attack than the Nb_5Si_3 at 1200 ˚C and the A15 phase exhibited better inherent oxidation resistance than the solid solution.

Chapter 7

Conclusions and suggestions for future work

7.1 Conclusions

The aim and objectives of this research, which were given in the introduction, were achieved. The conclusions of the research were as follows:

Alloy preparation

The JZ series of alloys with Ge, Sn, Ti, Hf, Ta or Mo and W additions with/without Al and Cr were prepared using arc melting. The control of alloy composition was difficult owing to the loss of Sn by evaporation during melting.

Alloy microstructure

Macrosegregation of Si (MACSi) existed in all the alloys. The alloy JZ1 had the highest MACSi value, which was 5.6 at.%. The lowest MACSi value was exhibited by the alloy JZ4, which was 3 at.%.

$\underline{Nb_{ss}}$

The Nb_{ss} was present in the alloys JZ1, JZ2, JZ3 and JZ3+ but was suppressed in the cast microstructures of the alloys JZ4 and JZ5. The solid solution was only stable in the heat treated (1500 for 100 h) and oxidised (1200 ˚C) microstructures of the alloys JZ4 and JZ5, with a very low vol%. The vol% of the solid solution in the alloys decreased with increasing Ge+Sn concentration and with increasing total refractory metal content in the alloys.

In the alloys with Ta and no Al and Cr (JZ1 and JZ2) the Si concentration and Ta+W sum in the normal Nb_{ss}, respectively increased and decreased as the Sn/Ge ratio in the alloy increased with a maximum of Si = 4.5 at.% at Sn/Ge ≈ 0.65. In the alloys with

Ta and Al and Cr (JZ3 and JZ3+) the Si concentration and Ta+W sum in the normal Nb_{ss}, respectively increased and decreased as the Sn/Ge ratio in the alloy increased with the increased Al+Cr sum. In the alloys with Mo and Al and Cr additions (JZ4 and JZ5) the Nb_{ss} was free of Si and the increase in the Ti content in the alloy JZ5 increased the Al+Cr sum of the solid solution from 15 to 23 at.%.

In the alloys with high concentration of Sn > 4 at.% (JZ3+, JZ4 and JZ5) the solubility of W in the solid solution was high and up to 40.2 at.% in [JZ3+]-HT. The solubility of Mo in the solid solution of the alloys JZ4 and JZ5 was high and up to 28.8 at.% in oxidised microstructure of JZ5 at 1200 ˚C.

Nb_5Si_3

In all the alloys (JZ1, JZ2, JZ3, JZ3+, JZ4 and JZ5) the Nb_5Si_3 was the primary phase, and was present in its β and α forms in both the as cast and heat treated conditions. The βNb_5Si_3 was stabilised to a larger extent at 1500 ˚C in the alloys JZ4 and JZ5 owing to the addition of Mo and W compared with the alloys JZ1, JZ2, JZ3 and JZ3+.

The solubility of Mo in the Nb_5Si_3 of the alloys JZ4 and JZ5 was increased significantly compared with the other Mo containing alloys studied in our research group, probably owing to the addition of Ge.

The solubility of Sn in the Nb_5Si_3 in the heat treated microstructures of the alloys JZ3+, JZ4 and JZ5 was high and up to 6.1 at.%, probably owing to the higher Sn concentration in these alloys.

Nb_5Si_3 + Nb_{ss} eutectic

In the cast microstructures in the top and bulk of the alloys JZ1 and JZ2 the Nb_5Si_3 + Nb_{ss} eutectic formed surrounding the primary Nb_5Si_3 grains. The Si+Ge+Sn contents of the eutectic were 20.7 at.% and 23.3 at.% in the alloys JZ1 and JZ2, respectively. In the bottom of the ingot of the alloy JZ1 an anomalous microstructure formed owing

to the decoupled growth of the two phases of the eutectic.

The formation of the Nb_{ss} + βNb_5Si_3 eutectic was completely suppressed in the alloys JZ3, JZ3+, JZ4 and JZ5.

Nb_3Si

The tetragonal (i.e., the stable) Nb_3Si was only observed in parts of the bottom of the ingot of JZ1-AC. The concentrations of Ta and W were relatively high in the Nb_3Si compared with the Nb_5Si_3 of JZ1-AC, respectively at 6.5 at.% and 1.5 at.%, and the Sn solubility in the Nb_3Si was extremely low, close to zero. This phase was unstable after the heat treatment.

The A15 phase

The A15 phase was not stable only in the alloy JZ1 owing to its low Ge+Sn concentration and was stabilised in the alloys JZ2, JZ3, JZ3+, JZ4 and JZ5 in the as cast and heat treated conditions as the higher Sn concentration in the alloys had a strong effect on promoting the formation of the A15 phase.

The average value of the Al+Ge+Si+Sn sum of the A15 compounds observed in the alloys of this research was 20.3 at.%, which is in agreement with other data from our research group. The A15 phase exhibited relatively high solubility of the refractory metals, especially the solubility of Mo in the alloy JZ5 was up to 20.9 at.% after oxidation at 1200 ˚C.

C14-Cr_2Nb Laves phase

The C14-Cr_2Nb Laves phase was observed in the alloys JZ3, JZ3+, JZ4 and JZ5 and after the heat treatment it became rare in JZ4-HT and unstable in JZ5-HT. It is suggested that the addition of 5 at.% Cr was capable of stabilising the Laves phase in the alloys JZ3 and JZ3+ where Cr was added with Al, Ge, Sn, Ti, Hf, Ta and W.

In the alloys with Ta (JZ3 and JZ3+) the average Cr+Al+Ge+Si+Sn of the Laves

phase was 62.7 at.%, lower than 66.6 at%, and the Ta+W content increased after the heat treatment and oxidation at 1200 ˚C. In the alloys with Mo (JZ4 and JZ5) the Mo+W content of the Laves phase was essentially the same.

TM_5Sn_2X

The TM_5Sn_2X (based on the Nb_5Sn_2Si, Ti_5Sn_2Si, Nb_5Sn_2Ge and Nb_5Sn_2Al compounds, which have the tetragonal W_5Si_3 as prototype and similar lattice parameters) was stabilised in the solidified microstructure of the alloys JZ4 and JZ5 This phase was unstable at 1200 ˚C and 1500 ˚C but present at 800 ˚C. The vol% of the TM_5Sn_2X compound was increased in the alloy JZ5, indicating that Ti promoted the formation of the TM_5Sn_2X.

In the TM_5Sn_2X the solubility of Ti, Si, Sn, Ge and Al was widened with Ti substituting Nb and Ge and Al substituting either Si or Sn.

HfO_2, TiO_2 and aluminium oxide

Hafnia was stable in all of the alloys. TiO_2 formed near the surface of the specimens of the alloys JZ1, JZ2 and JZ3 during the heat treatment and aluminium oxide formed near the surface of the specimen of the alloy JZ4 during the heat treatment.

After oxidation at 1200 ˚C titanium oxide formed in the diffusion zone 2 of the alloy JZ2 and in the alloys JZ3, JZ3+, JZ4 and JZ5 both titanium and aluminium oxides formed just below the scales.

Isothermal oxidation at 800 ˚C

The alloys with Mo (JZ4 and JZ5) had better oxidation resistance at 800 ˚C compared with the alloys with Ta (JZ1, JZ2, JZ3 and JZ3+), and both exhibited parabolic oxidation kinetics. The k_p of the alloys JZ4 and JZ5 was two orders of magnitude higher than the k_p of the single crystal Ni superalloy CMSX-4.

The thickness of the scale formed on the alloy JZ3 at 800 ˚C was about 150 μm, with severe cracking parallel to the surface. Thin oxide scales (about 3 μm thick) formed on the alloys JZ4 and JZ5 at 800 ˚C. The average oxygen concentrations of the oxides of these three alloys were close to that of Nb_2O_5.

The alloys JZ1 and JZ2 did not suffer from complete disintegration to powders. The addition of Al and Cr in the alloy JZ3 suppressed pest oxidation owing to the addition of Ge and Sn, the stability of A15 and the low vol% of Nb_{ss} in the alloy. The alloy JZ3+ suffered complete disintegration after 74 h exposure in air at 800 ˚C, with a very low mass gain for the first 40 h of oxidation and an increasing oxidation rate after this time, owing to the solid solution of the alloy JZ3+ being poorer regarding the beneficial elements Al, Cr and Ti even though its low vol% of Nb_{ss} and the A15 phase (compared with the alloy JZ3) improved the oxidation resistance for the first 40 h. No pesting was observed in the alloys JZ4 and JZ5 that exhibited good oxidation behaviour at 800 ˚C owing to the stronger beneficial effect of Mo with Sn, Ge, Al, Cr, Ti and Hf and the refractory metal W, than that of Ta.

Some of the A15 phase below the oxide scale was attacked by oxygen in the alloy JZ4 and this was not observed in the alloy JZ5. Thus, the increase in Ti concentration in the alloy and the A15 compound led to the better oxidation resistant of the latter in the alloy JZ5 at 800 ˚C.

Isothermal oxidation at 1200 ˚C

The alloys JZ1, JZ2 and JZ3 followed parabolic oxidation kinetics in the initial stage of oxidation that were followed by linear kinetics. The alloys JZ3+, JZ4 and JZ5 followed parabolic oxidation with lower rate in the early stage of oxidation. The parabolic rate constants of the alloys JZ3+, JZ4 and JZ5 (in particular JZ5) were the closest to that of the single crystal Ni superalloy CMSX-4.

Spallation of the oxide scale was only observed in the alloy JZ1 after oxidation at

1200 ˚C. The increase of the Sn and Ge contents in the alloy JZ2 improved the adherence of the oxide scale at 1200 ˚C. The alloys JZ3, JZ3+, JZ4 and JZ5 exhibited better adherence of the oxide scale at 1200 ˚C owing to the presence of Al and Cr with either Ta or Mo in the alloys. The oxide scale formed on the alloy JZ5 was much thinner compared with the alloys JZ2, JZ3, JZ3+ and JZ4. Pores and cracks were observed in the oxide scales of the alloys JZ2, JZ3, JZ3+, JZ4 and JZ5. The EDS analysis data suggested the presence of Nb-rich, Ti-rich and silicon oxides in their scales and that the scales of these alloys were free of Sn and Ge.

The formation of Sn and Ge containing intermetallic phases in the diffusion zone was observed in the alloys JZ2, JZ3, JZ3+, JZ4 and JZ5, with two diffusion zones in the alloy JZ2 but only one diffusion zone formed in the other four alloys. In the alloy JZ2 the $Nb_5(Si_{1-x},Ge_x)_3$ and $NbGe_2$ formed in the diffusion zone 1 and in the other alloys the Nb_5Si_3, $Nb_5(Si,Sn)_3$, $Nb_5(Si_{1-x},Ge_x)_3$, A15-Nb_3Sn and $(Nb,Ta,W)_{ss}$ or $(Nb,Mo,W)_{ss}$ were formed owing to the Ge and Sn segregation to the substrate just below the scale/substrate interface. In the diffusion zone 2 of the alloy JZ2 the Ti oxide formed either at the interface or inside the solid solution and A15 compound. The Nb_{ss} and A15 compound were more susceptible to oxygen attack than the Nb_5Si_3 at 1200 ˚C and the A15 phase exhibited better inherent oxidation resistance than the solid solution.

7.2 Suggestions for future work

1. Surfaces of the oxidised alloys at 800 ˚C and 1200 ˚C need to be studied using glancing angle XRD to determine phases in the scales and compare the data with the literature.

2. Ti is beneficial to the oxidation resistance of Nb-silicide based alloys. It is suggested that the Ti concentration in the alloy JZ3+ is increased to 20 at.% to

study whether the relatively poor oxidation of the alloy JZ3+ can be eliminated and whether the TM_5Sn_2X can form as was the case in the alloy JZ5.

3. The $Nb_5Si_3 + Nb_{ss}$ eutectic, which formed in the alloys JZ1 and JZ2, was believed to be beneficial to the mechanical properties of Nb-silicide based alloys, especially their fracture toughness. It is suggested to study two alloys with the same compositions as the alloys JZ1 and JZ2 but with Mo instead of Ta to study whether the Nb_3Si and eutectic can form/are stable and whether the oxidation behaviour improves or deteriorates.

Appendix

X-ray diffraction data of the as cast and heat treated JZ alloys

Table 1 PDF cards used for XRD analysis.

Phase	Structure	Reference
Nb_{ss}	Cubic	00-035-0789
$(Nb_{0.5},W_{0.5})_{ss}$	Cubic	04-004-7560
$(Nb_{0.5},Mo_{0.5})_{ss}$	Cubic	04-006-3535
βNb_5Si_3	Tetragonal	00-030-0875
αNb_5Si_3	Tetragonal	00-030-0874
Nb_5Sn_2Si	Tetragonal	00-024-0813
Nb_3Si	Tetragonal	00-034-1217
Nb_3Si (A15)	Cubic	00-037-1170
Nb_3Sn	Cubic	00-017-0909
Nb_3Ge	Cubic	00-033-0576
Nb_3Al	Cubic	00-012-0085
C14-Cr_2Nb	Hexagonal	00-047-1638
HfO_2	Monoclinic	00-043-1017
TiO_2	Tetragonal	00-021-1276

Table 2 XRD data for the alloy JZ1-AC.

2θ measured	d (Å) measured	I/I_0 measured	d (Å) reference	I/I_0 reference	hkl	Phase
24.206	3.6738	1.9	3.6760	15	011	HfO_2
26.404	3.3727	35.0	3.3610	25	211	βNb_5Si_3
31.305	2.8550	18.3	2.8540	25	211	αNb_5Si_3
35.750	2.4965	5.2	2.5070	14	400	βNb_5Si_3
36.756	2.4431	4.0	2.4400	80	321	βNb_5Si_3
			2.4400	30	112	Nb_3Si
38.058	2.3625	88.1	2.3650	11	411	βNb_5Si_3
38.547	2.3336	100	2.3379	100	110	Nb_{ss}
40.850	2.2072	12.1	2.2040	30	204	αNb_5Si_3
43.550	2.0764	27.6	2.0770	40	310	αNb_5Si_3
45.596	1.9879	3.2	1.9820	16	006	αNb_5Si_3
55.704	1.6487	13.1	1.6484	11	013	HfO_2
			1.6532	16	200	Nb_{ss}
58.437	1.5780	2.2	1.5809	10	213	βNb_5Si_3
59.704	1.5475	3.8	1.5488	4	330	αNb_5Si_3
61.903	1.4977	1.3	1.4961	10	541	βNb_5Si_3
62.810	1.4782	7.5	1.4780	16	413	αNb_5Si_3
64.937	1.4349	3.6	1.4336	17	631	βNb_5Si_3
68.247	1.3731	11.2	1.3731	13	334	αNb_5Si_3
69.857	1.3454	23.8	1.3499	20	211	Nb_{ss}
			1.3443	1	622	βNb_5Si_3
			1.3465	12	112	TiO_2
78.265	1.2205	1	1.2196	15	642	βNb_5Si_3
79.065	1.2102	1.2	1.2085	6	318	αNb_5Si_3
81.398	1.1813	4.4	1.1800	30	324	Nb_3Si
			1.1820	5	660	βNb_5Si_3
82.798	1.1648	8.9	1.1648	1	024	HfO_2
			1.1688	5	220	Nb_{ss}
			1.1656	4	750	βNb_5Si_3
86.389	1.1254	4.5	1.1267	4	530	αNb_5Si_3
89.509	1.0940	1.4	1.0950	3	600	αNb_5Si_3
95.350	1.0419	6.7	1.0456	4	310	Nb_{ss}
98.359	1.0179	1.5	1.0171	2	419	αNb_5Si_3

Table 3 XRD data for the alloy JZ1-HT (1500 ˚C for 100 hours).

2θ measured	d (Å) measured	I/I_0 measured	d (Å) reference	I/I_0 reference	hkl	Phase
26.519	3.3583	100	3.3610	25	211	βNb_5Si_3
31.440	2.8430	6.5	2.8540	25	211	αNb_5Si_3
38.161	2.3564	11.9	2.3650	11	330	βNb_5Si_3
38.679	2.3260	23.8	2.3379	100	110	Nb_{ss}
			2.3250	13	220	αNb_5Si_3
40.940	2.2026	2.7	2.2040	30	204	αNb_5Si_3
43.659	2.0715	5.2	2.0770	40	310	αNb_5Si_3
45.721	1.9828	1.9	1.9820	16	006	αNb_5Si_3
54.580	1.6800	2.7	1.6801	1	422	βNb_5Si_3
55.839	1.6451	5.3	1.6532	16	200	Nb_{ss}
59.840	1.5443	1.2	1.5488	4	330	αNb_5Si_3
62.940	1.4755	2.6	1.4780	16	413	αNb_5Si_3
65.003	1.4336	1.6	14338	17	316	αNb_5Si_3
68.377	1.3708	1.3	1.3731	13	334	αNb_5Si_3
69.978	1.3433	7.1	1.3499	20	211	Nb_{ss}
			1.3443	1	622	βNb_5Si_3
77.479	1.2309	1.5	1.2313	1	-141	HfO_2
83.081	1.1615	4	1.1688	5	220	Nb_{ss}
			1.1623	10	417	αNb_5Si_3
86.518	1.1240	2.8	1.1237	7	802	βNb_5Si_3
95.440	1.0411	3.2	1.0456	5	310	Nb_{ss}
			1.0408	1	034	HfO_2

Table 4 XRD data for the alloy JZ2-AC.

2θ measured	d (Å) measured	I/I_0 measured	d (Å) reference	I/I_0 reference	hkl	Phase
26.545	3.3552	100	3.3610	25	211	βNb_5Si_3
28.045	3.1790	4	3.1720	30	310	βNb_5Si_3
31.949	2.7989	4.4	2.8230	74	111	HfO_2
35.465	2.5291	7.9	2.5360	30	002	βNb_5Si_3
36.791	2.4409	13	2.4400	80	321	βNb_5Si_3
38.693	2.3252	54.2	2.3379	100	110	Nb_{ss}
			2.3250	13	220	αNb_5Si_3
39.58	2.2599	41.5	2.2630	40	202	βNb_5Si_3
41.051	2.1969	62.2	2.1930	100	411	βNb_5Si_3
			2.2040	30	204	αNb_5Si_3
43.900	2.0607	77.6	2.0625	60	222	βNb_5Si_3
55.850	1.6448	9.1	1.6532	16	200	Nb_{ss}
			1.6420	1	400	αNb_5Si_3
61.793	1.5001	1.8	1.5009	6	113	HfO_2
64.483	1.4439	1.8	1.4469	1	325	αNb_5Si_3
			1.4438	2	023	HfO_2
65.467	1.4245	6.2	1.4229	14	532	βNb_5Si_3
			1.4280	16	320	Nb_3Ge
67.393	1.3884	6.4	1.3878	30	413	βNb_5Si_3
70.046	1.3422	14.3	1.3499	20	211	Nb_{ss}
			1.3443	1	622	βNb_5Si_3
74.908	1.2667	3.8	1.2672	8	004	βNb_5Si_3
			1.2646	2	406	αNb_5Si_3
78.161	1.2219	3.3	1.2196	15	642	βNb_5Si_3
82.905	1.1636	3.6	1.1688	5	220	Nb_{ss}
			1.1623	10	417	αNb_5Si_3
85.759	1.1320	2.0	1.1313	3	404	βNb_5Si_3
95.644	1.0394	4.9	1.0456	4	310	Nb_{ss}
105.694	0.9664	2.5	0.9660	14	521	Nb_3Sn
107.848	0.9530	1.5	0.9546	1	222	Nb_{ss}

Table 5 XRD data of for the alloy JZ2-HT (1500 ˚C for 100 hours).

2θ measured	d (Å) measured	I/I_0 measured	d (Å) reference	I/I_0 reference	hkl	Phase
26.453	3.3666	100	3.3610	25	211	βNb_5Si_3
31.304	2.8550	7.8	2.8540	25	211	αNb_5Si_3
34.269	2.6145	4	2.6080	25	002	HfO_2
35.008	2.5610	3.2	2.5580	11	200	Nb_3Si (A15)
35.763	2.5087	4.8	2.5040	25	114	αNb_5Si_3
36.531	2.4576	2.2	2.4500	30	002	TiO_2
38.054	2.3627	27.3	2.3600	100	213	αNb_5Si_3
			2.3670	100	210	Nb_3Sn
38.694	2.3251	32.5	2.3379	100	110	Nb_{ss}
			2.3250	13	220	αNb_5Si_3
40.848	2.2073	10.2	2.2040	30	204	αNb_5Si_3
42.356	2.1322	14	2.1520	30	102	TiO_2
43.508	2.0783	10.6	2.0770	40	310	αNb_5Si_3
45.607	1.9874	5.7	1.9820	16	006	αNb_5Si_3
			1.9960	60	112	TiO_2
54.594	1.6796	2.2	1.6833	22	202	HfO_2
55.907	1.6432	6	1.6532	16	200	Nb_{ss}
			1.6420	1	400	αNb_5Si_3
58.362	1.5798	2.7	1.5809	10	213	βNb_5Si_3
			1.5792	8	411	αNb_5Si_3
59.743	1.5466	2.4	1.5488	4	330	αNb_5Si_3
63.197	1.4701	4.8	1.4699	20	217	αNb_5Si_3
			1.4680	20	320	Nb_3Sn
64.250	1.4485	3.2	1.4464	1	325	αNb_5Si_3
64.845	1.4367	4	1.4376	9	404	αNb_5Si_3
66.996	1.3957	6.3	1.3953	18	602	βNb_5Si_3
			1.3960	60	311	TiO_2
68.155	1.3747	4.6	1.3731	13	334	αNb_5Si_3
			1.3760	20	321	Nb_3Ge
70.098	1.3413	11	1.3499	20	211	Nb_{ss}
74.939	1.2662	2.2	1.2646	2	406	αNb_5Si_3
77.499	1.2306	1.5	1.2313	1	-141	HfO_2
78.207	1.2213	2.3	1.2201	4	336	αNb_5Si_3
83.046	1.1619	7.3	1.1688	5	220	Nb_{ss}
			1.1623	10	417	αNb_5Si_3
85.045	1.1397	3	1.1400	1	442	αNb_5Si_3
89.389	1.0952	2.6	1.0950	3	600	αNb_5Si_3
95.701	1.0390	4.3	1.0456	4	310	Nb_{ss}

Table 6 XRD data for the alloy JZ3-AC.

2θ measured	d (Å) measured	I/I_0 measured	d (Å) reference	I/I_0 reference	hkl	Phase
26.404	3.3727	100	3.3610	25	211	βNb_5Si_3
27.846	3.2012	7	3.1720	30	310	βNb_5Si_3
34.636	2.5877	4.1	2.5850	15	200	Nb_3Al
35.314	2.5395	15.8	2.5360	30	002	βNb_5Si_3
36.613	2.4523	43.2	2.4400	80	321	βNb_5Si_3
37.701	2.3840	8	2.3870	14	112	βNb_5Si_3
38.852	2.3160	63.6	2.3250	13	220	αNb_5Si_3
39.799	2.2631	14.3	2.2630	40	202	βNb_5Si_3
40.812	2.2092	43.8	2.2040	30	204	αNb_5Si_3
42.791	2.1115	40.5	2.1130	35	211	Nb_3Al
			2.1170	100	112	C14-Cr_2Nb
43.712	2.0691	20.1	2.0625	60	222	βNb_5Si_3
54.550	1.6809	1.7	1.6801	1	600	βNb_5Si_3
			1.6808	1	203	C14-Cr_2Nb
57.604	1.5988	3.2	1.5964	1	211	C14-Cr_2Nb
61.408	1.5086	1.9	1.5077	1	226	αNb_5Si_3
			15095	7	105	C14-Cr_2Nb
62.052	1.4944	1.7	1.4950	15	222	Nb_3Al
64.349	1.4465	16.7	1.4437	18	323	βNb_5Si_3
65.199	1.4297	16.5	1.4280	16	320	Nb_3Ge
67.158	1.3927	6.8	1.3953	18	602	βNb_5Si_3
			1.3927	33	213	C14-Cr_2Nb
67.705	1.3828	10	1.3840	15	321	Nb_3Al
76.407	1.2455	9.7	1.2446	2	651	βNb_5Si_3
			1.2441	22	220	C14-Cr_2Nb
77.995	1.2241	10.1	1.2231	1	-133	HfO_2
80.887	1.1874	4	1.1888	1	0010	αNb_5Si_3
81.838	1.1760	2.3	1.1772	5	314	βNb_5Si_3
83.802	1.1534	11.1	1.1510	5	420	Nb_3Ge
			1.1526	2	240	HfO_2
86.150	1.1279	15.9	1.1267	4	530	αNb_5Si_3
			1.1280	10	332	Nb_3Sn
88.548	1.1034	6.7	1.1033	14	424	βNb_5Si_3
108.949	0.9465	5.8	0.9466	7	521	Nb_3Al
110.745	0.9361	4.8	0.9340	8	440	Nb_3Sn
115.292	0.9118	22.3	0.9096	6	440	Nb_3Ge

Table 7 XRD data for the alloy JZ3-HT (1500 ˚C for 100 hours).

2θ measured	d (Å) measured	I/I_0 measured	d (Å) reference	I/I_0 reference	hkl	Phase
26.447	3.3673	100	3.3610	25	211	βNb_5Si_3
34.571	2.5924	15.2	2.5910	21	020	HfO_2
35.443	2.5305	3.7	2.5360	30	002	βNb_5Si_3
36.560	2.4558	14.9	2.4500	30	002	TiO_2
37.630	2.3884	2.3	2.3870	14	112	βNb_5Si_3
38.655	2.3273	7.1	2.3250	13	220	αNb_5Si_3
39.339	2.2884	4.7	2.2797	87	103	C14-Cr_2Nb
39.901	2.2575	12.2	2.2630	40	202	βNb_5Si_3
40.820	2.2088	26.5	2.2040	30	204	αNb_5Si_3
42.690	2.1163	12.6	2.1130	35	211	Nb_3Al
			2.1170	100	112	C14-Cr_2Nb
			2.1180	60	121	TiO_2
43.753	2.0673	3.8	2.0625	60	222	βNb_5Si_3
54.592	1.6797	2.6	1.6801	1	422	βNb_5Si_3
			1.6808	1	203	C14-Cr_2Nb
61.799	1.5000	2.3	1.4982	2	332	αNb_5Si_3
			1.5009	6	113	HfO_2
64.456	1.4444	10.5	1.4464	1	325	αNb_5Si_3
64.855	1.4365	22.9	1.4376	9	404	αNb_5Si_3
			1.4365	9	300	C14-Cr_2Nb
			1.4350	20	320	Nb_3Al
67.699	1.3829	37.8	1.3878	30	413	βNb_5Si_3
			1.3840	15	321	Nb_3Al
71.486	1.3186	4	1.3170	1	424	αNb_5Si_3
			1.3190	40	400	Nb_3Sn
73.104	1.2934	13.6	1.2940	10	400	Nb_3Al
			1.2905	26	205	C14-Cr_2Nb
84.006	1.1511	6.9	1.1519	1	1110	αNb_5Si_3
			1.1530	40	421	Nb_3Sn
			1.1510	5	420	Nb_3Ge
88.490	1.1040	4.8	1.1033	14	424	βNb_5Si_3
			1.1050	5	332	Nb_3Al
97.941	1.0211	3.3	1.0224	2	653	βNb_5Si_3
106.601	0.9607	10.6	0.9620	10	422	TiO_2
108.913	0.9467	2.5	0.9466	7	521	Nb_3Al

Table 8 XRD data for the alloy [JZ3+]-AC.

2θ measured	d (Å) measured	I/I_0 measured	d (Å) reference	I/I_0 reference	hkl	Phase
26.504	3.3602	99.5	3.3610	25	211	βNb_5Si_3
27.906	3.1945	5.5	3.1720	30	310	βNb_5Si_3
35.474	2.5285	11.1	2.5360	30	002	βNb_5Si_3
			2.5250	21	200	HfO_2
36.551	2.4564	10.6	2.4400	80	321	βNb_5Si_3
37.605	2.3899	2.9	2.3870	14	112	βNb_5Si_3
38.898	2.3134	21.9	2.3090	100	210	Nb_3Al
			2.3050	100	210	Nb_3Ge
39.619	2.2729	4.1	2.2698	100	110	$(Nb_{0.5},W_{0.5})_{ss}$
			2.2630	40	202	βNb5Si3
40.752	2.2123	100	2.2040	30	204	αNb_5Si_3
42.701	2.1157	7.9	2.1130	35	211	Nb_3Al
			2.1170	100	112	C14-Cr_2Nb
43.657	2.0716	5.2	2.0625	60	222	βNb_5Si_3
			2.0770	40	310	αNb_5Si_3
			2.0817	65	201	C14-Cr_2Nb
54.705	1.6765	2	1.6721	1	600	βNb_5Si_3
62.040	1.4947	3.4	1.4961	10	541	βNb_5Si_3
			1.4950	15	222	Nb_3Al
64.900	1.4356	38.9	1.4336	17	631	βNb_5Si_3
			1.4338	17	316	αNb_5Si_3
			1.4365	9	300	C14-Cr_2Nb
65.640	1.4212	47.9	1.4229	14	532	βNb_5Si_3
			1.4200	63	320	Nb_3Si (A15)
			1.4256	1	230	HfO_2
67.650	1.3838	22.8	1.3840	15	321	Nb_3Al
73.050	1.2942	4.1	1.2940	10	400	Nb_3Al
			1.2929	1	213	HfO_2
78.438	1.2182	14.3	1.2196	15	642	βNb_5Si_3
			1.2201	4	336	αNb_5Si_3
83.354	1.1584	3.7	1.1580	5	420	Nb_3Al
85.901	1.1305	6.4	1.1313	3	404	βNb_5Si_3
			1.1310	20	421	Nb_3Al
105.806	0.9657	9.1	0.9660	14	521	Nb_3Sn
106.208	0.9632	8.1	0.9628	25	520	Nb_3Al

Table 9 XRD data for the alloy [JZ3+]-HT (1500 ˚C for 100 hours).

2θ measured	d (Å) measured	I/I_0 measured	d (Å) reference	I/I_0 reference	hkl	Phase
26.449	3.3671	77.7	3.3610	25	211	βNb_5Si_3
27.802	3.2063	19.7	3.1720	30	310	βNb_5Si_3
34.889	2.5695	3.4	2.5780	40	200	Nb_3Ge
36.467	2.4618	100	2.4400	80	321	βNb_5Si_3
39.649	2.2713	20..6	2.2698	100	110	$(Nb_{0.5},W_{0.5})_{ss}$
			2.2797	87	103	C14-Cr_2Nb
40.746	2.2126	8.9	3.2040	30	204	αNb_5Si_3
42.301	2.1348	20.1	2.1490	100	211	Nb_3Sn
43.663	2.0713	4.7	2.0770	40	310	αNb_5Si_3
			2.0817	65	201	C14-Cr_2Nb
57.406	1.6038	23.3	1.6050	14	200	$(Nb_{0.5},W_{0.5})_{ss}$
			1.6009	24	212	HfO_2
61.295	1.5111	6	1.5077	1	226	αNb_5Si_3
			1.5095	7	105	C14-Cr_2Nb
63.444	1.4650	10.7	1.4630	30	320	Nb_3Sn
64.158	1.4504	48.9	1.4526	9	442	βNb_5Si_3
64.904	1.4355	23.8	1.4336	17	631	βNb_5Si_3
			1.4338	17	316	αNb_5Si_3
			1.4350	20	320	Nb_3Al
			1.4365	9	300	C14-Cr_2Nb
67.199	1.3938	6.6	1.3953	18	602	βNb_5Si_3
			1.3927	33	213	C14-Cr_2Nb
72.005	1.3104	2.7	1.3104	24	211	$(Nb_{0.5},W_{0.5})_{ss}$
77.500	1.2306	24.4	1.2313	1	-141	HfO_2
81.261	1.1829	4.1	1.1820	5	660	βNb_5Si_3
			1.1820	5	514	αNb_5Si_3
83.596	1.1557	5	1.1530	40	420	Nb_3Sn
96.047	1.0361	21.8	1.0362	3	216	C14-Cr_2Nb
			1.0374	2	-143	HfO_2
98.644	1.0157	3.3	1.0170	3	510	Nb_3Al
108.254	0.9506	11.3	0.9509	100	520	Nb_3Si (A15)

Table 10 XRD data for the alloy JZ4-AC.

2θ measured	d (Å) measured	I/I_0 measured	d (Å) reference	I/I_0 reference	hkl	Phase
26.455	3.3664	77	3.3610	25	211	βNb_5Si_3
35.011	2.5608	29.9	2.5580	11	200	Nb_3Si (A15)
35.444	2.5305	11.6	2.5360	30	002	βNb_5Si_3
36.751	2.4434	18.3	2.4400	80	321	βNb_5Si_3
37.652	2.3870	8.2	2.3870	14	112	βNb_5Si_3
39.307	2.2903	100	2.2880	100	411	Nb_5Sn_2Si
			2.2797	87	103	C14-Cr_2Nb
39.784	2.2639	54.8	2.2630	40	202	βNb_5Si_3
			2.2695	1	210	HfO_2
40.147	2.2442	69.1	2.2430	55	420	βNb_5Si_3
40.758	2.2120	20.3	2.2040	30	204	αNb_5Si_3
43.344	2.0858	9.2	2.0890	40	211	Nb_3Si (A15)
			2.0817	65	201	C14-Cr_2Nb
65.149	1.4307	13	1.4338	17	316	αNb_5Si_3
			1.4280	16	320	Nb_3Ge
65.604	1.4219	20	1.4229	14	532	βNb_5Si_3
68.494	1.3688	4.4	1.3680	56	321	Nb_3Si (A15)
74.034	1.2794	34.9	1.2800	36	400	Nb_3Si (A15)
			1.2823	3	106	C14-Cr_2Nb
			1.2795	2	312	HfO_2
78.153	1.2220	8	1.2196	15	642	βNb_5Si_3
			1.2220	3	411	Nb_3Al
84.501	1.1456	13	1.1435	14	831	βNb_5Si_3
			1.1450	24	420	Nb_3Si (A15)
			1.1457	5	215	C14-Cr_2Nb
			1.1458	4	331	HfO_2
87.051	1.1185	4.3	1.1170	81	420	Nb_3Si (A15)
			1.1135	1	142	HfO_2
98.784	1.0146	2.6	1.0150	8	912	βNb_5Si_3
108.355	0.9500	5.5	0.9509	100	520	Nb_3Si (A15)
110.954	0.9349	2	0.9340	8	440	Nb_3Sn

Table 11 XRD data for the alloy JZ4-HT (1500 ˚C for 100 hours).

2θ measured	d (Å) measured	I/I_0 measured	d (Å) reference	I/I_0 reference	hkl	Phase
26.499	3.3608	100	3.3610	25	211	βNb_5Si_3
37.697	2.3843	8.6	2.3870	14	112	βNb_5Si_3
39.355	2.2875	15	2.2900	95	210	Nb_3Si (A15)
39.717	2.2675	22.7	2.2627	100	110	$(Nb_{0.5},Mo_{0.5})_{ss}$
			2.2630	40	202	βNb_5Si_3
			2.2695	1	210	HfO_2
40.765	2.2116	62.6	2.2040	30	204	αNb_5Si_3
43.301	2.0878	18.2	2.0890	40	211	Nb_3Si (A15)
43.811	2.0647	31.2	2.0625	60	222	βNb_5Si_3
54.586	1.6799	3.1	1.6801	1	422	βNb_5Si_3
58.162	1.5848	2.9	1.5854	14	620	βNb_5Si_3
59.276	1.5576	5.4	1.5538	13	512	βNb_5Si_3
64.498	1.4436	33.2	1.4437	18	323	βNb_5Si_3
			1.4438	2	023	HfO_2
67.354	1.3891	30.3	1.3878	30	413	βNb_5Si_3
			1.3840	15	321	Nb_3Al
68.518	1.3683	5.8	1.3680	56	321	Nb_3Si (A15)
73.012	1.2948	4.2	1.2940	10	400	Nb_3Al
76.358	1.2462	38.5	1.2446	2	651	βNb_5Si_3
83.857	1.1528	6.5	1.1530	40	420	Nb_3Sn
			1.1510	5	420	Nb_3Ge
85.798	1.1316	4.4	1.1314	64	220	$(Nb_{0.5},Mo_{0.5})_{ss}$
			1.1313	3	404	βNb_5Si_3
			1.1310	20	421	Nb_3Al
88.557	1.1033	6.6	1.1050	5	332	Nb_3Al
97.703	1.0229	4	1.0227	3	015	HfO_2
102.965	0.9845	4.6	0.9830	40	520	Nb_3Sn
108.257	0.9506	7.9	0.9509	100	520	Nb_3Si (A15)
111.020	0.9346	5.9	0.9354	28	521	Nb_3Si (A15)
			0.9360	20	440	Nb_3Sn

Table 12 XRD data for the alloy JZ5-AC.

2θ measured	d (Å) measured	I/I_0 measured	d (Å) reference	I/I_0 reference	hkl	Phase
26.397	3.3736	100	3.3610	25	211	βNb_5Si_3
35.544	2.5236	21.9	2.5360	30	002	βNb_5Si_3
			2.5250	21	220	HfO_2
36.843	2.4376	24	2.4400	80	321	βNb_5Si_3
37.942	2.3694	4.5	2.3650	11	330	βNb_5Si_3
39.356	2.2875	19.5	2.2880	100	411	Nb_5Sn_2Si
			2.2900	40	211	Nb_3Si (A15)
			2.2797	87	103	C14-Cr_2Nb
40.147	2.2443	21	2.2430	55	420	βNb_5Si_3
41.141	2.1923	13.2	2.1930	100	411	βNb_5Si_3
43.555	2.0762	6.3	2.0770	40	310	αNb_5Si_3
43.998	2.0563	9.4	2.0625	60	222	βNb_5Si_3
51.395	1.7764	3.4	1.7824	3	402	βNb_5Si_3
			1.7728	5	-221	HfO_2
58.089	1.5866	3.4	1.5854	14	620	βNb_5Si_3
64.849	1.4366	6.9	1.4376	9	404	αNb_5Si_3
			1.4350	20	320	Nb_3Al
			1.4365	9	300	C14-Cr_2Nb
65.507	1.4237	17.9	1.4230	3	413	Nb_5Sn_2Si
			1.4229	14	532	βNb_5Si_3
			1.4200	63	320	Nb_3Si (A15)
67.187	1.3922	2.5	1.3927	33	213	C14-Cr_2Nb
78.546	1.2168	8.5	1.2162	15	820	βNb_5Si_3
84.838	1.1419	5.2	1.1435	14	831	βNb_5Si_3
			1.1450	24	420	Nb_3Si (A15)
86.600	1.1232	2.1	1.1230	12	421	Nb_3Ge
88.944	1.0995	2.2	1.0968	6	313	HfO_2
98.812	1.0144	2.3	1.0170	3	510	Nb_3Al
106.587	0.9608	6.4	0.9628	25	520	Nb_3Al

Table 12 XRD data for the alloy JZ5-HT (1500 ˚C for 100 hours).

2θ measured	d (Å) measured	I/I_0 measured	d (Å) reference	I/I_0 reference	hkl	Phase
26.403	3.3728	100	3.3610	25	211	βNb_5Si_3
27.844	3.2014	5.6	3.1720	30	310	βNb_5Si_3
35.495	2.5270	8.8	2.5360	30	002	βNb_5Si_3
36.605	2.4529	19.4	2.4400	80	3213	βNb_5Si_3
39.807	2.2626	24.2	2.2627	100	110	$(Nb_{0.5},Mo_{0.5})_{ss}$
			2.2630	40	202	βNb_5Si_3
40.861	2.2067	13.1	2.2040	30	204	αNb_5Si_3
43.460	2.0805	7.3	2.0770	40	310	αNb_5Si_3
			2.0890	40	211	Nb_3Si (A15)
54.450	1.6837	3.3	1.6801	1	422	βNb_5Si_3
57.555	1.6000	1.5	1.6000	14	200	$(Nb_{0.5},Mo_{0.5})_{ss}$
			1.6009	24	212	HfO_2
65.254	1.4286	10.4	1.4280	16	320	Nb_3Ge
67.497	1.4286	6.3	1.4229	14	532	βNb_5Si_3
			1.4140	45	321	Nb_3Sn
75.248	1.2618	3.8	1.2623	2	400	HfO_2
77.809	1.2265	5.4	1.2259	2	410	HfO_2
81.958	1.1746	2.8	1.1725	2	-124	HfO_2
86.699	1.1221	2	1.1230	12	421	Nb_3Ge
88.802	1.1009	12.7	1.1007	4	124	HfO_2
108.998	0.9462	3.2	0.9340	8	440	Nb_3Sn

References

Balsone, S.J., Bewlay, B.P., Jackson, M.R., Subramanian, P.R., Zhao, J.C., Chatterjee, A. and Heffernan, T.M., (2001). In: K.J. Hemker, D.M. Dimiduk, H. Clemens, R. Darolia, M. Inui, J.M. Larsen, V.K. Sikka, Thomas, and J.D. Whittenberger, Eds. *Structural Intermetallics*. TMS, Warrendale. pp. 99-108.

Bendersky, L., Biancaniello, F.S., Boettinger, W.J. and Perepezko J.H., (1987). Microstructural characterization of rapidly solidified Nb-Si alloys. *Mater. Sci. Eng.*, 89, 151-159.

Bewlay, B.P. and Jackson M.R., (2003). Chapter 3.22 High-temperature in situ composites: processing and properties. In: A. Kelly, and C. Zweben, Eds. *Comprehensive Composite Materials*. Elsevier. pp. 579-615.

Bewlay, B.P., Jackson, M.R. and Gigliotti, M.F.X., (2001). Niobium silicide high temperature in situ composites. In: R.L. Fleischer, and J.H. Westbrook, eds. *Intermetallic Compounds: Principles and Practice*. New York: John Wiley. pp. 541–560.

Bewlay, B.P., Jackson, M.R. and Lipsitt, H.A., (1997). *J. Phase Equilibria*, 18(3), 264-278.

Bewlay, B.P., Jackson, M.R. and Subramanian, P.R., (1999). Processing high-temperature refractory-metal silicide in-situ composites. *JOM*, 51(4), 32-36.

Bewlay, B.P., Jackson, M.R., Zhao, J.C. and Subramanian, P.R., (2003). A review of very-high-temperature Nb-silicide-based composites. *Metall. Mater. Trans. A*, 34, 2043-2052.

Bewlay, B.P., Jackson, M.R., Zhao, J.C. and Subramanian, P.R., (2003). A review of very-high-temperature Nb-silicide-based composites. *Metall. Mater. Trans. A*, 34, 2043-2052.

Bewlay, B.P., Jackson, M.R., Zhao, J.C., Subramanian, P.R., Mendiratta, M.G. and Lewandowski, J.J., (2003). Ultrahigh-temperature Nb-silicide-based composites. *MRS Bulletin*, 28(9), 646-653.

Bewlay, B.P., Yang, Y., Casey, R.L., Jackson, M.R. and Chang, Y.A., (2009). Experimental study of the liquid-solid phase equilibria at the metal-rich region of the Nb-Cr-Si system. *Intermetallics*, 17, 120-127.

Brukl, C., Nowotny, H. and Benesovsky, F., (1961). *Monatsh. Chem.*, 92, 967-980.

Chan, k.S., (2002). Alloying effects on fracture mechanisms in Nb-based intermetallic in-situ composites. *Mater. Sci. Eng. A*, 329-331, 513-522.

Chan, k.S. and Davidson, D.L., (2003). Improve the fracture toughness of constituent phases and Nb-based in-situ composites by a computational alloy design approach, *Metall. Mater. Trans. A*, 34, 1833-1849.

Chang, K.M., Bewlay, B.P., Sutliff, J.A. and Jackson, M.R., (1992). Cold-crucible directional solidification of refractory metal-silicide eutectics. *JOM*, 44(6), 59-63.

Chattopadhyay, K., Balachandran, G. and Ray, K., (2006). Effect of Mo on microstructure and mechanical behaviour of as-cast Nb_{ss}-Nb_5Si_3 in situ composites. *Intermetallics*, 14, 1452-1460.

Chen, Z. and Yan, Y., (2006). Influence of sintering temperature on microstructure of Nb/Nb_5Si_3 in situ composites synthesized by spark plasma sintering. *J. Alloys and Compd.*, 413, 73-76.

Devantay, H., Jorda, J., Decroux, M., Muller, J. and Flukiger, R., (1981). The physical and structural properties of superconducting A15-type Nb-Sn alloys. *J. Mater. Sci.*, 16, 2145-2153.

Geng, J. and Tsakiropoulos, P., (2006). A study of the microstructures and oxidation of Nb-Si-Cr-Al-Mo in situ composites alloyed with Ti, Hf and Sn. *Intermetallics*, 15, 382-395.

Geng, J., Tsakiropoulos, P. and Shao, G.S., (2007). A study of the effects of Hf and Sn additions on the microstructure of Nb_{ss}/Nb_5Si_3 based in situ composites. *Intermetallics*, 15, 69-76.

Geng, J., Tsakiropoulos, P. and Shao, G.S., (2006). Oxidation of Nb-Si-Cr-Al in situ composites with Mo, Ti and Hf additions. *Mater. Sci. Eng.*, 441, 26-38.

Geng, J., Tsakiropoulos, P. and Shao, G.S., (2007). A thermo-gravimetric and

microstructural study of the oxidation of (Nb)/Nb_5Si_3-based in situ composites with Sn addition. *Intermetallics*, 15, 270-281.

Geng, T., Li, C., Zhao, X., Xu, H., Du, Z. and Guo, C., (2010). Thermodynamic assessment of the Nb-Si-Mo system. *GALPHAD*, 34, 363-376.

Grammenos, I. and Tsakiropoulos, P., (2010). Study of the role of Mo and Ta additions in the microstructure of Nb-18Si-5Hf silicide based alloys. *Intermetallics*, 18, 1524-1530.

Grammenos, I. and Tsakiropoulos, P., (2011). Study of the role of Hf, Mo and W additions in the microstructure of Nb-20Si silicide based alloys. *Intermetallics*, 19, 1612-1621.

Han, X. and Wei, B., (2002). Microstructural characteristics of Ni-Sb eutectic alloys under substantial undercooling and containerless solidification conditions. *Metall. Mater. Trans. A*, 33A, 1221–1228.

Henshall, G.A., Strum, M.J., Subramanian, P.R. and Mendiratta, M.G., (1995). *Mat. Res. Soc. Symp. Proc.*, 364, 937-942.

Hernandez-Negrete, O.C. and Tsakiropoulos, P., (2016). Unpublished research. *University of Sheffield*.

Jackson, M.R., Bewlay, B.P., Rowe, R.G., Skelly, D.W. and Lipsitt, H.A., (1996). High-temperature refractory metal intermetallic composites. *JOM*, 48(1), 39-44.

Kim, Y.M., Tanaka, H., Kasama, A. and Hanada, S., (2001). Microstructure and room temperature fracture toughness of Nb_{ss}/Nb_5Si_3 in situ composites. *Intermetallics*, 9, 827-834.

Kim, Y.M., Tanaka, H., Kasama, A. and Hanada, S., (2001). Microstructure and high temperature strength at 1773 K of Nb_{ss}/Nb_5Si_3 composites alloyed with molybdenum. *Intermetallics*, 10, 625-634.

Knittel, S., Mathieu, S., Portebois, L. and Vilasi, M., (2014). Effect of tin addition on Nb-Si-based in situ composites. Part II: oxidation behaviou'. *Intermetallics*, 47, 43-52.

Li, M. and Kuribayashi, K., (2003). Further discussion on the free growth behaviour in the solidification of undercooled eutectic melts. *Metall. Mater. Trans. A*, 34,

1393-1396.

Li, Y., Li C., Du, Z. and Guo, C., (2013). Thermodynamic optimization of the Nb-Si-W ternary system. *GALPHAD*, 43, 112-123.

Li, Z. and Tsakiropoulos, P., (2012). Unpublished research. *University of Sheffield*.

Li, Z. and Tsakiropoulos, P., (2010). Study of the effects of Ge addition on the microstructure of Nb-18Si in situ composites. *Intermetallics*, 18, 1072-1078.

Li, Z. and Tsakiropoulos, P., (2011). Study of the effects of Ti and Ge in the microstructure of Nb-24Ti-18Si-5Ge in situ composites. *Intermetallics*, 19, 1291-1297.

Liu, W. and Sha, J.B., (2016). Failure mode transition of Nb phase from cleavage to dimple/tear in Nb-16Si-based alloys prepared via spark plasma sintering. *Materials and Design*, 111, 301-311.

Ma, C., Li, J., Tan, Y., Tanaka, R. and Hanada, S., (2004). Microstructure and mechanical properties of Nb/Nb_5Si_3 in situ composites in Nb-Mo-Si and Nb-W-Si systems. *Mater. Sci. Eng. A*, 386, 375-383.

Ma, C., Tan, Y., Kasama, A. and Hanada, S., (2002). Phase equilibria in Nb-W-rich zone of the Nb-W-Si ternary system, *Mater. Trans.*, 43(4), 688-693.

Mathieu, S., Knittel, S., Berthod, P. and Vilasi, M., (2012). On the oxidation mechanism of niobium-base in situ composites. *Corrosion Science*, 60, 181-192.

Matstakova, A.A. and Lazarev, B.G., (1973). Peculiarities of the constitution phase diagram of the system nioubium-tin, *Fiz. Metalloved i metallovedenie*, 35(5), 148-156.

Menon, E.S.K., Mendiratta, M.G. and Dimiduk, D.M., (2001). High temperature oxidation mechanisms in Nb-silicide bearing multicomponent alloys. *Structural Intermetallics,* 591-600.

Murakami, T., Sasaki, S., Ichikawa, K. and Kitahara, A., (2001). Mircostructure, mechanical properties and oxidation behaviour of Nb-Si-Al and Nb-Si-N powder compacts prepared by spark plasma sintering. *Intermetallics*, 9, 621–627 and 629–635.

Pan, V.M., Latysheva, V.I., Kulik, O.G. and Popov, A.G., (1982). Influence of alloying

with germanium and copper on the conditions of formation of the superconducting compound Nb_3Si. *Russ. Metall.*, 3, 167-171.

Pope, D.P., Shah, D.M., Romanow, W. and Huntley, M., (1994). Directional solidification of refractory intermetalics-single crystals and composites. *Mat. Res. Soc. Symp. Proc.*, 322, 461-472.

Sha, J., Hiral, H., Tabaru, T., Kitahara, A., Ueno, H. and Hanada, S., (2004). High-temperature strength and room-temperature toughness of Nb-W-Si-B alloys prepared by arc-melting. *Mater. Sci. Eng. A*, 364, 151-158.

Sha, J., Yang, C. and Liu, J., (2010). Toughening and strengthening behavior of an Nb-8Si-20Ti-6Hf alloy with addition of Cr. *Scripta Mater.*, 62, 859-862.

Schachner, H., Cerwenka, E. and Nowotny, H., (1954). New silicides of M_5Si_3-type with $D8_8$-structure. *Monatsh. Chem.*, 85, 245-254.

Schlesingcr, M.E., Okamoto, H., Gokhalc, A.B. and Abbaschian, R., (1993). The Nb-Si (niobium-silicon) system. *J. Phase Equilibria*, 14(4), 502-509.

Schlesinger, M.E., (1994). The Si-Ta (silicon-tantalum) system. *J. Phase Equilibria*, 15, 90-95.

Schutze, M., (2000). In: R.W. Cahn, P. Haasen, and E.J. Kramer, eds. *Material science and technology: corrosion and environmental degradation, vol I*. Germany: Wiley-VCH. pp 83.

Stewart, G., Newkirk, L.R. and Valencia, F.A., (1980). Impurity stabilized A15 Nb_3Nb – a new superconductor. *Phys. Rev. B*, 21, 5055-5064.

Straumanis, M. and Zyszczynsk, S., (1970). *J. Appl. Cryst.*, 3, 1-6.

Subramanian, P.R., Parthasarathy, T.A., Mendiratta, M.G. and Dimiduk, D.M., (1995). Compressive creep-behavior of Nb_5Si_3. *Scripta Metal.*, 32(8), 1227-1232.

Sun, Z., Guo, X. and Zhang, C., (2012). Thermodynamic modeling of the Nb-rich corner in the Nb-Si-Sn system. *GALPHAD*, 36, 82-88.

Tafto, J., Suenaga, M. and Welch, D., (1984). Crystal site determination of dilute alloying elements in polycrystalline Nb_3Sn superconductors using a transmission electron microscope. *J. Applied Physics*, 55, 4330-4333.

Toffolon, C., Gachon, J.C. and Sundman, B., (2002). Reassessment of the Nb-Sn

system. *J. Phase Equilibria*, 23(2), 134-139.

Tsakiropoulos, P., (2014). On the macrosegregation of silicon in niobium silicide based alloys. *Intermetallics*, 55, 95-101.

Tsakiropoulos, P., (2015). Private communication. *University of Sheffield*.

Utton, C., Papadimitriou, I., Kinoshita, H. and Tsakiropoulos, P., (2017). Experimental and thermodynamic assessment of the Ge-Nb-Si ternary phase diagram. *J. Alloys and Compd.*, 717, 303-316.

Utton, C. and Tsakiropoulos, P., (2017), Private communication. *University of Sheffield*.

Vellios, N. and Tsakiropoulos, P., (2007). The role of Sn and Ti additions in the microstructure of Nb-18Si base alloys. *Intermetallics*, 15, 1518-1528.

Vellios, N. and Tsakiropoulos, P., (2008). Unpublished research. *University of Surrey*.

Westbrook, J. and Wood, D., (1964). Pest degradation in beryllides, silicides, aluminides, and related compounds. *J. Nucl. Mater.*, 12, 208-215.

Xiong, B., Cai, C. and Wang, Z., (2014). Microstructures and room temperature fracture toughness of Nb_{ss}/Nb_5Si_3 composites alloyed with W, Mo and W-Mo fabricated by spark plasma sintering. *J. Alloys Compd.*, 604, 211-216.

Xiong, B., Cai, C., Wan, H. and Zheng, Y., (2009). Effects of Si, W and W-Mo on isothermal oxidation behavior of Nb/Nb_5Si_3 in situ composites at high temperature. *J. Alloys Compd.*, 604, 211-216.

Xu, Z. and Tsakiropoulos, P., (2016). Unpublished research. *University of Sheffield*.

Yao, D., Zhou, C., Yang, J. and Chen, H., (2009). Experimental studies and modeling of the oxidation of multiphase niobium-base alloys. *Corrosion Science*, 51, 2619-2627.

Zacharis, E. and Tsakiropoulos, P., (2013). Unpublished research. *University of Sheffield*.

Zelenitsas, K. and Tsakiropoulos, P., (2005). Study of the role of Al and Cr additions in the microstructure of Nb-Ti-Si in situ composites. *Intermetallics*, 13, 1079-1095.

Zelenitsas, K. and Tsakiropoulos, P., (2006). Effect of Al Cr and Ta additions on the

oxidation behaviour of Nb-Ti-Si in situ composites at 800 ˚C. *Mater. Sci. Eng. A*, 416,269-280.

Zelenitsas, K. and Tsakiropoulos, P., (2006). Study of the role of Ta and Cr additions in the microstructure of Nb-Ti-Si-Al in situ composites. *Intermetallics*, 14, 639-659.

Zhang, S. and Guo, X., (2016). Alloying effects on the microstructure and properties of Nb-Si based ultrahigh temperature alloys. *Intermetallics*, 70, 33-44.

Zhao, J.C., Bewlay, B.P. and Jackson, M.R., (2004). Determination of Nb-Hf-Si phase equilibria. *Intermetallics*, 9, 681-689.

Zhao, J.C., Jackson, M.R. and Peluso, L.A., (2003). Determination of the Nb-Cr-Si phase diagram using diffusion multiples, *Acta Mater.*, 6395-6405.

Zhao, J.C., Jackson, M.R. and Peluso, L.A., (2004). Mapping of the Nb-Ti-Si phase diagram using diffusion multiples. *Mater. Sci. Eng. A*, 372, 21-27.

Zhao, J.C., Peluso, L.A., Jackson, M.R. and Tan, L.Z., (2003). Phase diagram of the Nb-Al-Si ternary system. *J. Alloys and Compd.*, 360, 183-188.